THE UNIVERSITY OF HULL

Synthesis and surface modification of nanorods for investigation into organic-inorganic hybrid materials.

being a Thesis submitted for the Degree of

in the University of Hull

by

Richard William Bourne, MChem

September 2012

Acknowledgements

I would first like to thank my supervisors, Professor Stephen M. Kelly and Dr. Jay D. Wadhawan, for their support, understanding, advice and guidance, and to my colleagues in the organophotonics group for their helpful input. Thanks also to everyone in labs F305 and C314, in particular to Dr. Stuart Kitney for his help and guidance with the organic synthesis and many useful discussions. Padina Alaei was a pleasure to work with and contributed greatly to the synthesis of gold nanorods as part of her MSc studies.

Extra thanks go to Carol Kennedy for combustion analysis, Ann Lowry for TEM and EDS and Steve Myers for photoluminescence measurements.

From a personal perspective I would like to thank my parents, family and friends for their support throughout the past four years and beyond. Also Marie, for not letting me fail my PhD!

Finally I would like to thank the University of Hull for funding this research as part of the 80th Anniversary PhD Scholarships.

Abstract

The research presented in this thesis is focused towards the synthesis of a new kind of giant hybrid liquid crystal consisting of organic semiconductor molecules surrounding an inorganic semiconductor with a nanorod shape with the potential for use in photovoltaic solar cells. It is intended that such materials will combine the good processing properties of liquid crystals, such as low cost, alignment and photolithographic patterning, with the efficient light emission and electrical conductivity of inorganic semiconductors.

Several syntheses of gold and cadmium sulphide nanorods were performed and optimised in order to increase the yield, aspect ratio and monodispersity of nanorods formed. Localised alignment according to Onsager theory was observed for nanorods produced with sufficient aspect ratio and concentration.

Investigations into the formation of self-assembled monolayers were carried out using gold nanorods and alkanethiols. Organic synthesis of thiol-terminated ligand groups for attachment to both gold and cadmium sulphide nanorods was performed, and such materials were used for investigations into surface modification of the synthesised nanorods. However, no liquid crystallinity was observed for the organic-functionalised nanorods produced during these investigations.

Metal (II) phthalocyanines were used to investigate the formation of chromonic liquid crystalline phases and demonstrated the possibility for an alternative route in producing hybrid inorganic-organic nanorod-like systems.

Contents

List of Abbreviations

Common abbreviations used in this report are given below:

ABCN	-	1,1'-Azobis(cyclohexanecarbonitrile)
acac	-	Acetylacetone
AR	-	Aspect ratio
BDAC	-	Benzyldimethylammonium chloride
CMC	-	Critical micelle concentration
CTAB	-	Cetyltrimethylammonium bromide
CV	-	Cyclic voltammetry
DCM	-	Dichloromethane
DDA	-	Discrete dipole approximation
DIBAL-H	-	Diisobutylaluminium hydride
DMF	-	N,N-Dimethylformamide
DSC	-	Differential scanning calorimetry
EDS	-	Energy dispersive X-ray spectroscopy
FT-IR	-	Fourier transform-infrared
GC	-	Gas chromatography
LC	-	Liquid crystal
Lit.	-	Literature
LPB	-	Longitudinal plasmon band
MS	-	Mass spectrometry
N	-	Nematic phase
NIR	-	Near-infrared
NMR	-	Nuclear magnetic resonance

NR	-	Nanorod
ODA	-	Octadecylamine
Pd/C	-	Palladium on carbon
PL	-	Photoluminescence
PV	-	Photovoltaic
rpm	-	Revolutions per minute
%RSD	-	Relative standard deviation
RT	-	Room temperature
SAM	-	Self-assembled monolayer
SD	-	Standard deviation
Sm	-	Smectic phase
TDAB	-	Tetradodecylammonium bromide
TEM	-	Transmission electron microscopy
THF	-	Tetrahydrofuran
TLC	-	Thin layer chromatography
TPB	-	Transverse plasmon band
TOP	-	Trioctylphosphine
TOPO	-	Trioctylphosphine oxide
UV-vis	-	Ultraviolet-visible
XRD	-	X-ray diffraction

1 Introduction

1.1 Liquid Crystals

A liquid crystal is a phase of matter with properties between those of isotropic liquids, and those of crystalline solids. Liquid crystals may flow like liquids, but with their molecules exhibiting positional and/or orientational ordering in a crystal-like manner. There are various different types of liquid crystal phases, see below, known as mesophases, with anisotropic, and therefore directionally dependent, material properties such as permittivity, refractive index, elasticity, viscosity, thermal and electrical conductivity.

Liquid Crystals were first observed in 1888 by Reinitzer,[1] who found that cholesteryl benzoate did not melt like other compounds, but instead had two melting points. At 145.5 °C the crystalline solid melted into a cloudy liquid, then at 178.5 °C it melted again and the cloudy liquid became clear, furthermore this phenomenon was found to be reversible.

The Onsager theory for the isotropic-nematic phase transition was developed by Lars Onsager in 1949.[2] In a three-dimensional gas of hard rods there are two contributions to the entropy: a part due to translation and a part due to orientation. Onsager theory considers the volume excluded from the centre-of-mass of one idealised cylinder as it approaches another. If the cylinders are oriented parallel to each other, there is less volume excluded from the centre-of-mass of an approaching cylinder than if the cylinders are at an angle to one another. In the latter scenario there is a larger volume surrounding the cylinder which the centre-of-mass of an approaching cylinder cannot enter due to hard-rod repulsion between the two cylinders. Therefore the latter arrangement leads to a decrease in the positional entropy of the approaching cylinder as there are fewer states available to it.[3] From the point of view of the translational component of the entropy, a parallel configuration of the rods is favoured as the excluded volume is effectively zero. However, from an orientational point of view a gas of perfectly aligned rods is a very low entropy configuration. At very low densities the orientational term dominates; there is very little gain in entropy to be made by reducing the excluded volume *via* parallel alignment. However, at higher densities a perfectly aligned system will be more favourable. Therefore at some point a transition must take place between the isotropic and nematic phases.

In 1969, the photovoltaic effect was discovered in smectic liquid crystals,[4] and this was followed by ionic photovoltaic effects in nematic liquid crystals[5] in 1972. At the University of Hull in 1973, Gray discovered the first stable, room temperature nematic liquid crystals used

for liquid crystal displays.[6] Charge transport in liquid crystals, necessary for their use in photovoltaic devices, see below, was first reported in 1994 with the use of discotic liquid crystals,[7] and in 2006, the Hull Group reported the first liquid crystal solar cells using a nematic gel template.[8]

1.1.1 Liquid Crystal Mesophases

Liquid crystals can be divided into thermotropic and lyotropic liquid crystals, as illustrated in figure 1.1. Thermotropic liquid crystals exhibit a phase transition from a crystalline solid to the liquid crystal phase as temperature is changed. There are two main types of thermotropic liquid crystals based on the molecular shape; calamitic liquid crystals have rod-shaped molecules containing rigid sections known as mesogens, and discotic or columnar liquid crystals have disc-shaped molecules. Lyotropic liquid crystal phases are formed by amphiphilic molecules in certain concentration ranges in the presence of a suitable solvent. At low concentrations, the molecules will be dispersed randomly without any ordering. As the concentration is increased, the amphiphilic molecules spontaneously assemble into micelles which at higher concentrations form ordered phases such as the hexagonal columnar phase, in which amphiphiles form long cylinders that arrange themselves into a roughly hexagonal lattice. Further increases in concentration may lead to phases such as the lamellar phase, in which extended sheets of amphiphiles are separated by thin solvent layers.

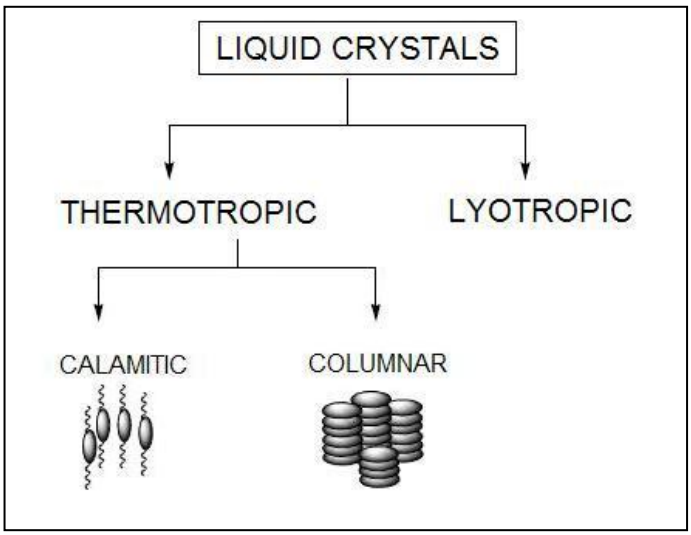

Figure 1.1 Basic classification of liquid crystals.

Calamitic liquid crystal molecules typically contain rigid 'rod-like' cores consisting of, for example, aromatic rings, with flexible end groups such as alkyl chains. The nematic phase consists of molecules with orientational alignment, roughly parallel to each other in a direction known as the director (n), but without positional ordering, and so is able to exhibit a high degree of fluidity. The smectic phase is more ordered than the nematic and consists of molecules with orientational alignment as well as a layered structure as illustrated in figure 1.2. The smectic A and smectic C phases show orientational but not positional order and are therefore more fluid than other existing smectic phases which have positional order within the layers.

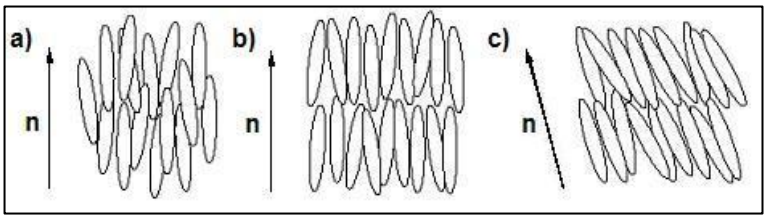

Figure 1.2 Liquid crystal phases: a) nematic, b) smectic A, c) smectic C.

Chiral nematic and smectic liquid crystal phases are also observed; see figure 1.3. The chiral nematic phase exhibits chirality and is often called the cholesteric phase because it was first observed for cholesterol derivatives. This phase exhibits a twisting of the molecules perpendicular to the director, with the molecular axis parallel to the director. The twist angle between adjacent molecules is due to their asymmetric packing, which results in longer-range chiral order. In the smectic C chiral phase the molecules have positional ordering in a layered structure as in the other smectic phases, with the molecules tilted by an angle with respect to the layer normal. The chirality induces a twist from one layer to the next, producing a spiral twisting of the molecular axis along the layer normal.

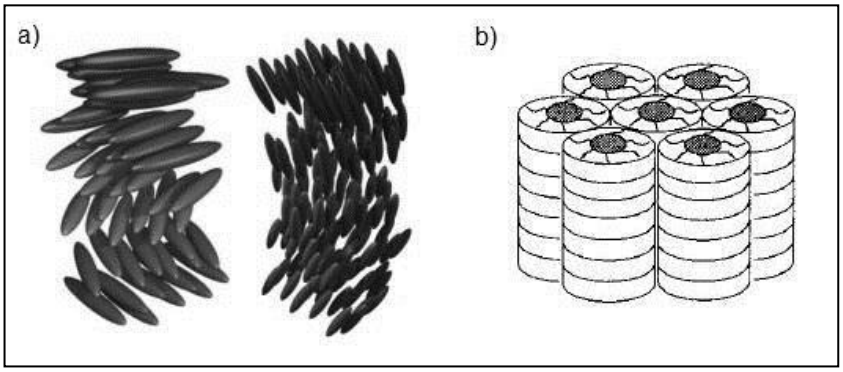

Figure 1.3 a) chiral nematic phase (left), chiral smectic C phase (right). b) discotic columnar phase.[9]

Disc-shaped mesogens can orient themselves in layers to form the discotic nematic phase, which when packed in stacks is called the discotic columnar phase. The columns may be organized into rectangular or hexagonal arrays with positional and orientational order within a discotic domain, some which have exhibited promising conductive properties.[10] There are also chiral discotic phases, similar to the chiral nematic phase.

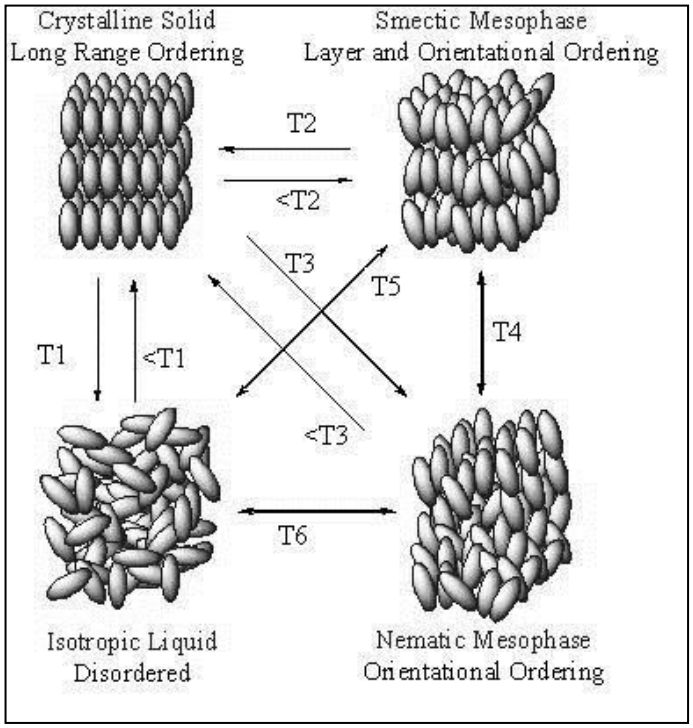

Figure 1.4 Calamitic liquid crystal phases and possible melting sequences.[9]

Figure 1.4 indicates the different transitions between thermotropic liquid crystal phases described below.

T1 - melting point. The thermal energy available is enough to overcome the attractive forces between the molecules of the crystalline solid and so long-range orientational and positional ordering is lost to form an isotropic liquid.

T2 - crystal to smectic transition. The attractive forces between the ends of the molecules are overcome, while interaction between their long molecular axes is maintained. This leads to formation of the smectic phase, a layered structure in which the molecules are still parallel to each other.

T3 - crystal to nematic transition. The attractive forces between the molecules as well as the interaction between their long molecular axes are overcome, leading to the formation of a non-layered structure of molecules with statistically parallel orientational order.

T4 - smectic to nematic transition. Once in the smectic phase the lateral interaction between the molecules may be overcome if more thermal energy is provided leading to formation of a nematic phase.

T5, T6 - clearing point, or smectic or nematic to isotropic transitions. If all remaining attractive forces are overcome then ordering is lost giving rise to the isotropic liquid.

1.1.2 Mesophase Identification

The different liquid crystal mesophases may be distinguished using techniques such as optical polarising microscopy, differential scanning calorimetry and X-ray analysis.

When viewed under an optical microscope using a polarised light source, different liquid crystal phases will appear to have different and distinctive textures. Contrasting areas within these textures correspond to domains in which the liquid crystal molecules are oriented different directions; however, within these domains the molecules are well ordered. A small amount of the material is placed between a glass slide and cover slip then inserted into a hotstage in order to finely control the temperature and observed under the microscope. In the case of lyotropic liquid crystals any temperature change will have implications on the solvent concentration and liquid crystalline phase formed, therefore microscopy is typically carried out at without heating or cooling and other methods of identification must be more heavily relied upon.

Differential scanning calorimetry is typically used as in conjunction with optical microscopy and measures the enthalpy changes of phase transitions in order to reveal the different liquid crystal mesophases. Two furnaces are linked together, one containing a reference material and the other the sample under investigation, and bother are heated at an identical rate. At melting phase transitions extra energy is supplied to the sample in order to maintain an identical heating rate and this is converted to a value for the change in enthalpy (ΔH). The enthalpy change varies with the degree of structural change and is useful for the identification of phase transitions which can then be further investigated using optical microscopy. Figure 1.5 illustrates a typical differential scanning calorimetry curve, showing examples of different phase transitions.

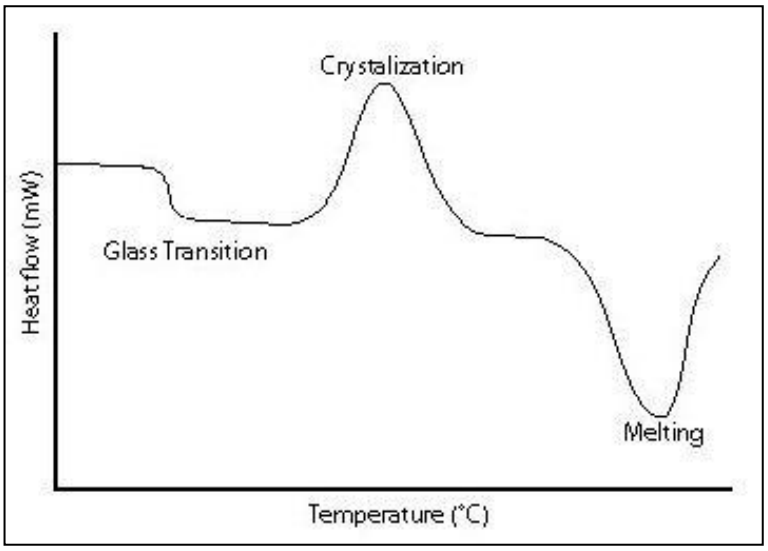

Figure 1.5 Illustration of a typical differential scanning calorimetry curve.

X-ray analysis of a liquid crystal can be used to map the position of molecules within a phase and thereby determine the phase structure. Aligned samples are required and so this technique is most useful for the more ordered phases.

1.1.3 Physical Properties

The majority of liquid crystals are organic and therefore have properties characteristic of organic compounds; they are often liquids or solids with low melting points; they are soluble in organic solvents; they are insulators or weak semiconductors and they absorb and refract light. It is often possible to process liquid crystals at room temperature and they can be applied to large surfaces using low-cost processes such as spin coating, in which an excess of material in solution is placed on a substrate and rotated at high speeds in order to spread the fluid into a thin film *via* centrifugal force.[11]

Liquid crystals in the nematic phase align parallel to each other as long molecular threads, which are easily and spontaneously aligned by surface forces, for example microgrooves. Although organic semiconductors are being developed, including liquid crystal semiconductors, the majority of commercial semiconductors are inorganic and have completely physical properties; they are high melting point solids, *e.g.*, silicon substrates doped with boron or phosphorous; they are insoluble; they conduct electricity and may emit light and they are typically processed at high temperatures under vacuum conditions in a batch-by-batch process. The high cost of semiconductor production and the inability to manufacture large areas of photovoltaic cells on cheap and flexible plastic substrates are important factors in restricting the uptake of semiconductor-based photovoltaics as an alternative energy source.

1.2 Nanoparticles

Nanoparticles typically have at least one characteristic dimension in the range of 1-100 nm and possess size and shape dependent properties which differ to those of the same material in bulk form. Gold, for example, has a yellowish colour when in bulk, but colloidal solutions of gold nanoparticles are typically red, purple or blue in colour due to their interaction with light, with particle sizes smaller than the wavelength of light causing Mie scattering to occur.[12] The material properties can be altered by fine-tuning of the nanoparticle size and shape, and according to Onsager theory,[2] rod-like particles may exhibit alignment and form liquid crystalline phases.

1.2.1 Gold Nanoparticles

The current level of interest in gold nanoparticles is largely due to advances and improvements in the understanding of their synthesis and properties[13, 14] as well as the potential for their use in many applications such as chemical[15] and biological sensors,[16] the treatment of cancer,[17] catalysts,[18] electronics[19] and photonics.[20]

A colloidal dispersion consists of particles typically 1 nm to 10 µm in size which keep the dispersed phase suspended *via* Brownian motion. Colloidal dispersions of gold nanoparticles, i.e. particles with at least one characteristic dimension in the nanometre scale, were used as dyes in ruby glass and ceramics in the days of the Roman Empire and even earlier.[21] Early work by Faraday[22] on dispersions of gold particles in water, formed by the reduction of gold chloride, produced red coloured solutions and the understanding that such colours were due to the presence of dispersed gold particles. Zsigmondy went on to develop Faraday's methods into a two-step synthesis[23] which forms the basis of the 'seed-mediated' methods found in the present-day literature, as well as devising the ultramicroscope[24] which allowed observation of colloidal gold nanoparticles as small blurry dots, due to the scattering of light.

Svedberg introduced electrochemical methods of gold nanoparticle synthesis, and in a similar fashion to Faraday's work, used an extensive range of reducing agents.[25] In addition he created the ultracentrifuge which allowed for the size separation of particles and gave insight into the roles of size and shape in sedimentation velocity.[26] Ostwald, famous for his work on

colloids, made significant contributions on the importance of size in allowing particles to stay in the dispersed form.

Mie's theory[12] on the absorption and scattering of spherical particles described experimental deviations from his theoretical predictions as being due to non-spherical particles, and this was further investigated by Gans[27] who showed that small, anisotropic particles are able to absorb at longer wavelengths than equivalently-sized spherical particles.

The special optical properties of gold (and other metal) nanoparticles are due to localised surface plasmon resonance, the excitation of surface plasmons by light. Surface plasmons are electron oscillations that occur at an interface between two materials, electromagnetic radiation interacts with conduction band electrons to induce a coherent oscillation of electrons and as a result a strong absorption band is observed in the electromagnetic spectra, with the wavelength dependent on particle size. It is notable that this effect is absent for the material in bulk as well as at an individual atom level, and that an anisotropic nanoparticle may have multiple different absorbances, as described below.[28]

Recent technological advances in areas such as optical and electronic microscopy, coupled with greater understanding and control of both their properties and synthesis, has propagated interest in gold nanoparticles and it seems likely that they will have an important role to play in chemical and technological developments in the coming years.

1.2.2 Characterisation and Properties of Gold Nanorods

Metal nanorods, such as gold and silver, are suitable as model nanorods due to their extensively investigated number of synthetic procedures, commercial availability and high reactivity with binding groups such as thiols.[29] The aspect ratio of a nanorod is often used in simply defining the nanorod type and is calculated by dividing the nanorod length by the diameter, typically varying from 1 to 15 with lengths of up to several hundred nanometres.[30]

UV-vis absorbance spectra of gold nanorods exhibit both a transverse plasmon band (TPB) and longitudinal plasmon absorption band (LPB), shown in figure 1.6b below. The TPB is due to the coherent electronic oscillation along the short nanorod axis, and the LPB is due to the coherent electronic oscillation along the long nanorod axis and is observed at a longer wavelength as well as being of greater intensity. The absorption maximum wavelength of the latter band is sensitive to the rod length and aspect ratio, typically red-shifting as the aspect ratio

increases,[28] therefore it is possible to obtain an indication of nanorod aspect ratio by examining the UV-vis absorption spectra.

Research into simulations of UV-vis absorbance spectra for gold nanorods has also been carried out using extensions of Gans theory[31] as well as the discrete dipole approximation method.[32] The latter provides the following equation for the variation of the wavelength of maximum absorption (λ_{max}) for the LPB with the nanorod aspect ratio:

$$\lambda_{max} = 96AR + 418$$

(Equation 1.1)

By inserting values for λ_{max} from the UV-vis absorbance spectra of gold nanorods it is possible to obtain an estimate of their aspect ratio in good agreement with experimental data. Another example of investigations performed in calculating the distribution of nanorod aspect ratios was carried out by El-Sayed *et al*.[33] and yielded the equation:

$$\lambda_{max} = 96.9AR + 385$$

(Equation 1.2)

Their motivation for using the observed LPB absorbance was down to the observation of statistically incorrect values for size determination carried out using TEM due to distortions during sample preparation and the difficulty associated with counting large numbers of nanorods. In addition, by comparing the relative absorbance values of the LPB and TPB, the "absorbance max ratio," A_{LPB}/A_{TPB} can be calculated, providing an indication of the nanorod yield relative to spherical particles.[34]

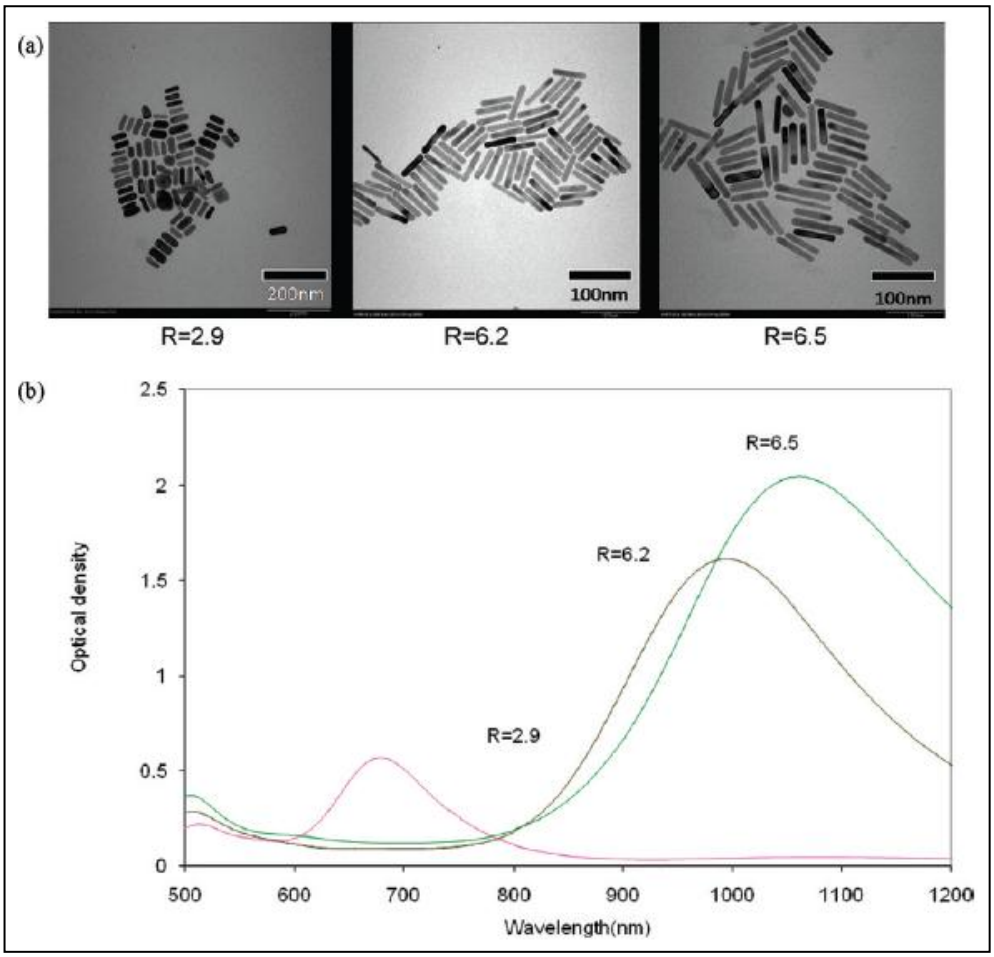

Figure 1.6 (a) TEM of gold nanorods of various aspect ratios (R) exhibiting localised orientational ordering. (b) UV-vis absorbance spectra of gold nanorods showing red-shifting of LPB (seen around 1000 nm) as nanorod aspect ratio increases.[35]

Figure 1.6a above shows gold nanorods visualised using transmission electron microscopy (TEM), a technique in which an electron beam is transmitted through a sample, typically deposited onto a copper grid, interacting as it passes through. The electrons interact with the sample, forming an image which is magnified and focused onto an imaging device. From TEM images, accurate measurements of nanorod dimensions can be made, as well as accurate estimates of the relative yields of different nanoparticles and the variation in aspect ratio distribution. TEM can also be used to observe modulations in the chemical identity, crystal orientation and electronic structure of samples. Often used alongside TEM, energy dispersive X-ray spectroscopy (EDS) is an analytical technique used for elemental analysis, allowing investigation of a sample through interactions between electromagnetic radiation and matter by analysis of the X-rays emitted by the sample after being hit with charged particles. The unique atomic structure of different elements allows X-rays that are characteristic of an element's atomic structure to be identified.

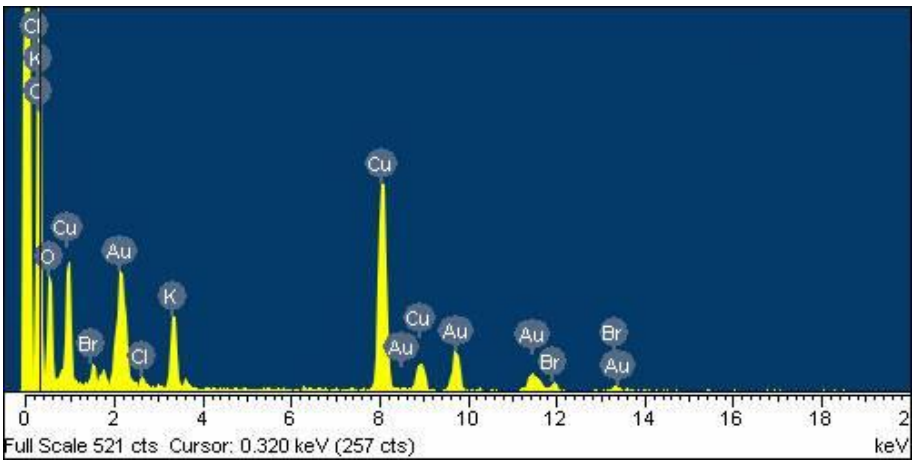

Figure 1.7 Typical EDS spectrum of gold nanorods in which Au peaks are clearly observed along with Cu peaks due to the copper grid used in mounting the samples for TEM.

In order to stimulate the emission of X-rays from a specimen, a high-energy beam of electrons or X-rays, is focused into the sample. The energy and number of X-rays emitted from a sample are measured by an energy dispersive spectrometer, and since the energies of the X-rays are characteristic of the atomic structure of the element from which they originate, this allows the elemental composition of the sample to be determined.

1.2.3 Synthesis of Gold Nanorods

The synthesis of anisotropic nanoparticles is far more complex than the reduction of gold salts to produce spherical nanoparticles as the surface energy as well as the formation of different crystal faces, surface roughnesses and atomic arrangements affects the chemical and physical properties of nanoparticles. Spherical particles are thermodynamically favourable as they have the minimum surface area per volume; it takes energy to create a new interface and energy is gained from creating new volume. Nanoparticles can be synthesised using either physical, top-down approaches such as evaporation and arc discharge, or chemical, bottom-up approaches based on the reduction of metal salts in the presence of different additives.[14] Reduction can occur by chemical,[36] photochemical[37] or electrochemical[38, 39] processes; nanoporous templating,[40] sonochemical, thermal decomposition, and hydrochemical methods may also be used.[41]

In addition, anisotropic nanoparticles may be defined by one of three different growth types. For one dimensional nanoparticles, growth is restricted to two directions leading to the

formation of rods, wires and similar structures. Two dimensional nanoparticles exhibit growth confined in one dimension, leading to the formation of planar structures such as triangles and platelets. Finally, nanoparticle growth can occur in three dimensions, leading to shapes such as tetrahedral, cubes, prisms and branched nanoparticles. The field of controlled anisotropic nanoparticle synthesis is still in development and many examples exist in the literature of particles with the same or similar morphology being synthesised under different experimental conditions, as well as differing morphologies from almost identical synthetic procedures. The investigations carried out below will focus on the bottom-up, solution-based, seed-mediated synthesis of gold nanorods.

Seed-Mediated Nanorod Growth

Probably the most widely-used method, in seeded growth, nanosized metal particles, known as "seeds", are initially formed *via* the reduction of metal salts using an appropriate reducing agent. These seeds are then added to a growth solution containing additional metal salt and reducing agent, along with other additives such as surfactants and ligands. Metal ions are reduced at the seed surface *via* heterogeneous nucleation during the particle growth process, and by varying the seed properties such as concentration and size, it is possible to obtain different nanoparticle structures.

Nucleation is the creation of a new phase and typically occurs *via* "embryos" which are small clusters of the new phase. Creation of a new surface at the nucleus boundaries costs energy, however there is also an energy release associated with the formation of a new volume, and depending on the surface to volume ratio of the developing particle there will be an energy barrier which must be overcome in order for nucleation to occur. The equilibrium shape of a seed is one that minimises the surface energy for a given enclosed volume; if surface energy is isotropic the equilibrium shape will be spherical in order to provide the minimum surface area for the new volume produced. In the case of crystalline solids, the surface energy is anisotropic and influenced by the nature of surface faces as well as the area and so the equilibrium shape is commonly an octahedron at the nanometre scale.[14] Anisotropic shapes can be induced by tuning the growth rates of different faces, for example, by modification of surface energy *via* the adsorption of various additives such as cetyltrimethylammonium bromide (CTAB) and silver ions, however the exact roles of most additives are not fully understood. Mass-transport-limited growth can also produce anisotropic nanoparticles; if the interfacial processes are extremely fast during crystal growth then the growth rate may be controlled by mass transport.

It is also possible to perform *in situ* seed-mediated nanorod growth by adding a small amount of relatively strong reducing agent to a reaction mixture in which a weaker reducing agent is already present. The strong reducing agent initiates homogeneous nucleation and the weak reducing agent allows for anisotropic growth leading to the production of various different nanoparticle shapes.[42]

Murphy *et al*. developed a three-step seeded gold nanorod synthesis method using CTAB,[36] which forms cylindrical micelles that may act as a template to nanorod growth, above the 2nd critical micelle concentration (CMC), and had previously been used in the electrochemical synthesis of gold nanorods.[38] Citrate-capped gold seeds were prepared *via* the reduction of hydrogen tetrachloroaurate with sodium borohydride and added to a growth solution containing CTAB, ascorbic acid and sodium hydroxide. Nanorod growth occurred through preferential adsorption along the long axis [110] crystal face, the ascorbate monoion is believed to adsorb better to the 5-fold [111] end faces[43] where it is able to reduce Au^{III} and Au^{I}. Nanorod aspect ratios of up to 20 were obtained and could be controlled by varying the ratio of seed to metal salt, as well as the addition of heptane to the growth solution. Alkanes can solubilise CTAB in water with a dependence on chain length, allowing for an extension of the cylindrical micelles formed and consequently an increase in the aspect ratios of nanorods produced.[44]

Ag(I)-assisted nanorod growth is capable of producing nanorods with yields above 90% in respect to other nanoparticle shapes.[45] Silver ions adsorb selectively to Au [110] faces, inhibiting the deposition of gold on those surfaces and allowing deposition on [100] and [111] surfaces, leading to nanorod growth in the [100] direction, illustrated in figure 1.8b. In contrast, nanorods formed from gold seeds in the absence of $AgNO_3$ have a [110] growth direction with pentatwinned crystal faces at the nanorod ends,[36] illustrated in figure 1.8a. It has also been noted that trisodium citrate may assist the formation of nanoplates, larger two-dimensional nanoparticles shapes, and so citrate is typically replaced by CTAB as the capping agent for the preparation of gold seeds, which as a result are smaller in diameter than those produced with citrate.[46]

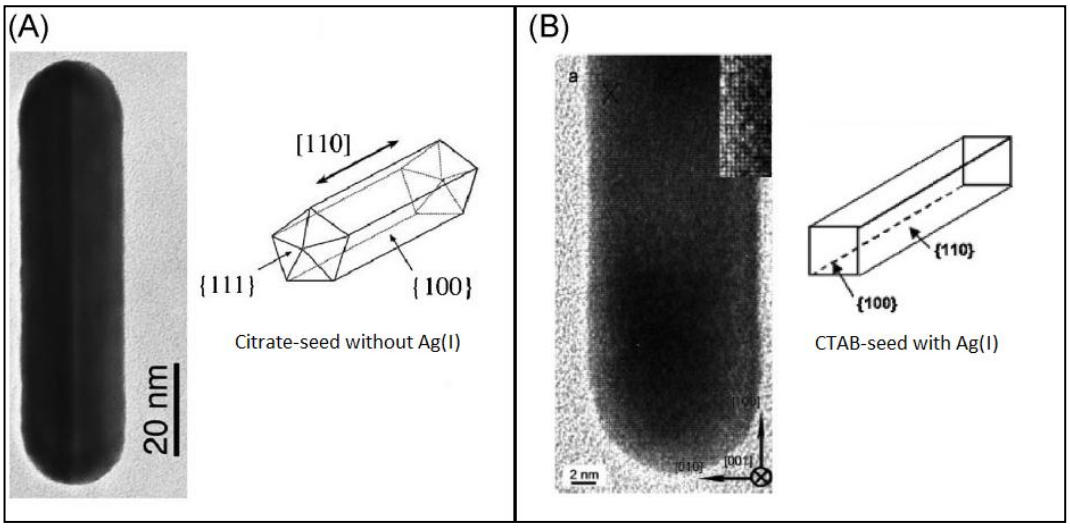

Figure 1.8 (a) Nanorod growth using citrate-capped seeds in the absence of Ag(I). Nanorods have side faces of Au [100] or [110] and pentatwinned end faces of [111].[47] (b) Nanorod growth using CTAB-capped seeds in the presence of Ag(I). Nanorods are single crystal with [110] side faces and [100] end faces.[48]

CTAB stabilises gold nanorods in aqueous solutions *via* the formation of a bilayer; polar headgroups attach to the nanorod surface and due to the bilayer structure allow interaction with surrounding water molecules and therefore aqueous dispersity. The CTAB seed-mediated approach to nanorod synthesis has been difficult to reproduce due to low concentration impurities in different commercially available CTAB batches - iodide concentrations greater than 50 ppm have been found to prevent nanorod formation as reduction of Au(III) to Au(0) is slowed and iodide absorption on Au [111] surfaces inhibits nanorod growth.[49] Korgel *et al.* investigated the effect of iodide concentration on nanorod growth by adding potassium iodide in controlled amounts to a series of growth solutions containing purified CTAB.[34] A decrease in nanorod aspect ratio was observed as the concentration of iodide increased and at concentrations above 0.57 µM no nanorods were formed. These results were compared with those of nanorods produced using CTAB from a range of different suppliers and a good correlation was observed between measured iodide content and the relative yield of nanorods produced. Addition of potassium iodide to CTAB-stabilised gold nanorod solutions instigated a transformation to spherical particles, as well as aggregation of nanoparticles due to competition with CTAB in adsorption on the gold surface.

However, there is some conflict with the findings of Mirkin *et al.* who report that iodide is necessary for nanorod formation.[50] The investigations in this case use the stepwise addition growth method described above and not the Ag(I)-assisted growth method investigated by Korgel. Greater proportions of gold nanorods are typically obtained using the Ag(I)-assisted approach, however it is more difficult to achieve aspect ratios greater than 5, the use of co-surfactants, solubilisates or other additives becoming necessary.[45] The stepwise addition

approach can provide nanorods with aspect ratios of 20 and above,[51] however the proportion of nanorods compared to total nanoparticles including spheres and other shapes is usually much lower, as demonstrated by A_{LPB}/A_{TPB} values of 0.65 and 2.66 respectively for nanorods produced in the absence and presence of Ag(I).

The two methods are believed to have different growth mechanisms, as discussed above, a relatively low quantity of nanorods is obtained from the stepwise synthesis and this further decreases with iodide addition. It is possible that iodide may affect the formation of gold nanorods due to preferential binding to Au [111] surfaces, thereby preventing further gold deposition. It has been found that gold deposition is significantly slower when [111] facets are terminated by iodide,[34] illustrating why the use of CTAB with a relatively high iodide impurity concentration is detrimental to the synthesis of gold nanorods. Nanorods with low aspect ratios may still form with low iodide concentrations and only partial coverage of Au [111] surfaces, therefore since a smaller area of the tip is [111] in the Ag(I)-assisted method the procedure is more sensitive to iodide than the stepwise method less iodide is required to completely cover the Au [111] facets.

Various different reducing agents can be used in the synthesis of gold nanorods, the most common being a combination of sodium borohydride and ascorbic acid. Sodium borohydride is typically used as a relatively strong reducing agent in the preparation of seed solutions, with ascorbic acid as a weaker reducing agent to reduce Au(III) in growth solutions. Tollan *et al.* have also developed a gold nanorod synthesis using a single reducing agent, acetylacetone, in a one-step procedure.[52]

The majority of published procedures for the synthesis of gold nanorods are carried out on a relatively small scale, with reagents and products typically in the microgram to milligram range. Several attempts have been made at producing nanorods on a milligram to gram scale, for example, Zubarev *et al.* simply scaled up the previously-developed stepwise addition approach,[53] and Drezek *et al.* investigated the effects of increasing the gold content of growth solutions,[54] achieving nanorod yields of approximately 0.1 g with a low proportion of spherical nanoparticles. Jana investigated the nucleation-growth kinetics in order to devise a gram-scale procedure for gold nanorod synthesis,[55] using standard reagents such as CTAB, ascorbic acid and sodium borohydride in a one-pot reaction.

Other factors, such as pH and the addition of additives such as nitric acid,[56] modifications to seed-mediated procedures,[51] or alternative surfactants[57] have been investigated, although it is necessary to note that the reaction kinetics and nucleation and growth processes with respect to nanorod synthesis are far from fully understood,[58] and further research is required in order to fully understand and control these processes.

1.2.4 Purification of Nanorods

The most common procedure for the purification of nanorods is *via* centrifugation, in which nanoparticles undergo Brownian motion under an external field and move with different sedimentation velocities determined by their Svedberg coefficients, leading to separation of particles of different shape and size. Typically reported are precipitates of nanorods at the bottom of centrifuge tubes with the supernatants containing mostly smaller, spherical particles. Sharma *et al.*[59] examined the hydrodynamic behaviour of different nanoparticle shapes and the effects of shape-dependant drag on their sedimentation behaviour. It was noted that the nanorods formed a precipitate on the 'side wall' of centrifuge tubes and that the precipitate at the very bottom was a mixture of spheres and lower AR nanorods, as indicated in figure 1.9 below.

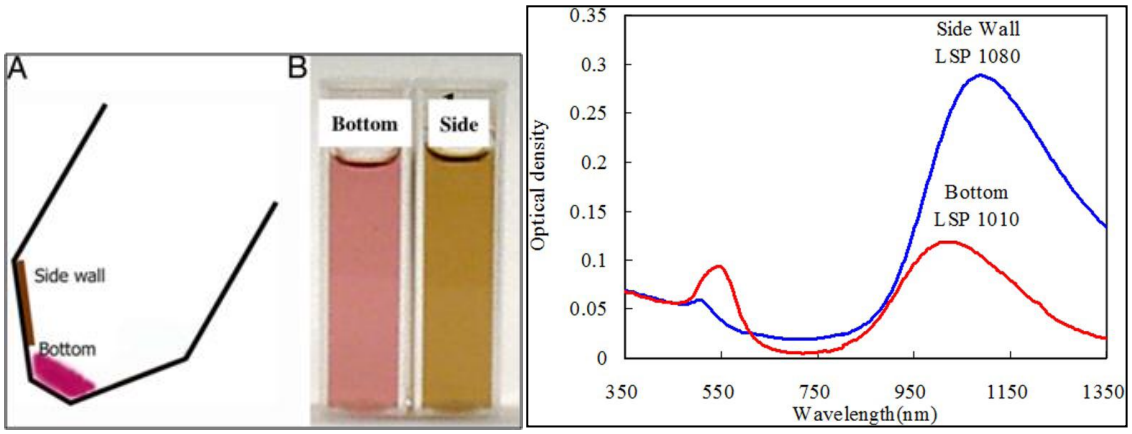

Figure 1.9 Left: A) diagram of side wall and bottom nanoparticle precipiates in a centrifuge tube. B) different colours of dispersed nanoparticles from the two precipitates. Right: UV-vis spectra of centrifuged gold nanorods.[59]

It can be clearly seen that the side wall precipitate gives a considerable increase in the absorbance max ratio in the UV-vis spectrum compared to that of the bottom precipitate, implying an increase in the concentration of nanorods. There is also a noticable red-shift of 70 nm in the LPB, indicating that the side wall precipiate contains higher aspect ratio nanorods and that the bottom precipitate is a mixture of lower aspect ratio nanorods and spherical nanoparticles.

An alternative method of removing spherical nanoparticles from gold nanorod solutions was developed by Huang *et al.* who claimed that the addition of sodium phosphate monobasic to aqueous nanorod solutions allowed for the selective oxidation of gold nanospheres, leading to higher relative yields of nanorods. [60]

1.3 Semiconductor Nanorods

Semiconductor nanocrystals show great potential as components in electronic devices as many of their physical properties can be adjusted through modification of the particle diameter and shape. Optoelectronic devices such as photovoltaic solar cells are able to take advantage of the dependence of the band gap of nanocrystals on particle radius in order to absorb and emit light with tuneable wavelengths.[61] In addition inorganic or metallic nanorod molecules are able to form liquid crystalline phases with both orientational and positional order observed in lyotropic systems.[30] II-VI semiconductor nanorods, such as cadmium sulphide and cadmium selenide, are relatively straightforward to synthesise with excellent monodispersity and high aspect ratio, for example by the pyrolysis of organometallic precursors of cadmium and selenium,[62] and may be suitable for organic photovoltaic applications.[30]

In general, semiconductor nanoparticles have attracted considerable interest due to their dimension-dependent optical and electrical properties which can be tailored by particle size and shape due to quantum confinement effects.[63] Synthetic routes include vapour-liquid-solid (VLS), template-assisted,[64] solvothermal[65] and hydrothermal[66] methods, allowing for shape-controlled synthesis of colloidal semiconductor nanoparticles. However, the most common synthetic routes are based on the high-temperature thermolysis of organometallic precursors, which are toxic, expensive and unstable.[67] There are three main methods for the growth of semiconductor nanorods in solution, metal particle-seeded growth,[68] oriented attachment,[69] and kinetically controlled ligand-assisted growth.[70] Although there has been considerable progress in the understanding of these chemical processes, there is still much to determine, particularly the systematic control of nanorod length while maintaining narrow diameters and diameter distributions with the intention of obtaining monodisperse nanorods of high aspect ratio.

1.3.1 Cadmium Chalcogenide Nanorods

Cadmium sulphide[71] and cadmium selenide[72] were the first materials systems observed to generate high nanorod yields *via* kinetically controlled ligand-assisted growth. Since initial investigations, experimental factors such as surfactant used, reactant composition, variance of addition of reactants and temperature have been examined in order to better understand and achieve control over nanorod formation and growth and obtain nanorods of increased aspect

ratio in high yield. It is understood that capping ligands are critical to the formation of nanorods due to the inhibited growth at particular crystal faces. In the case of cadmium chalcogenides, phosphonic acids with long alkyl chains are known to promote this effect.[73]

Another important aspect of solution-based nanorod growth is achieving kinetic control which favours anisotropic crystallization without homogeneous particle nucleation. This aspect is one of the most difficult to understand and control, and there have been many different approaches investigating how best to inject reactants and adjust temperature; however, the complete understanding of how to do this effectively remains elusive.

1.3.2 Characterisation and Properties of Cadmium Chalcogenide Nanorods

Typical analytical techniques used to characterise cadmium chalcogenide nanoparticles seen throughout the literature include UV-vis absorbance spectrometry, photoluminescence (PL) emission, TEM imaging, EDS, and X-ray diffraction (XRD).[74]

Figure 1.10A below shows characteristic absorbance for cadmium chalcogenide nanorods within the range 400 - 600 nm, which corresponds to the region of the electromagnetic spectrum responsible for giving the yellow colouration observed in solid and solution-based nanoparticle samples. In an identical manner to gold nanoparticles, semiconductor nanoparticles may be visualised using TEM as seen in figure 1.10B, which again allows for direct analysis of particle dimensions and yields.

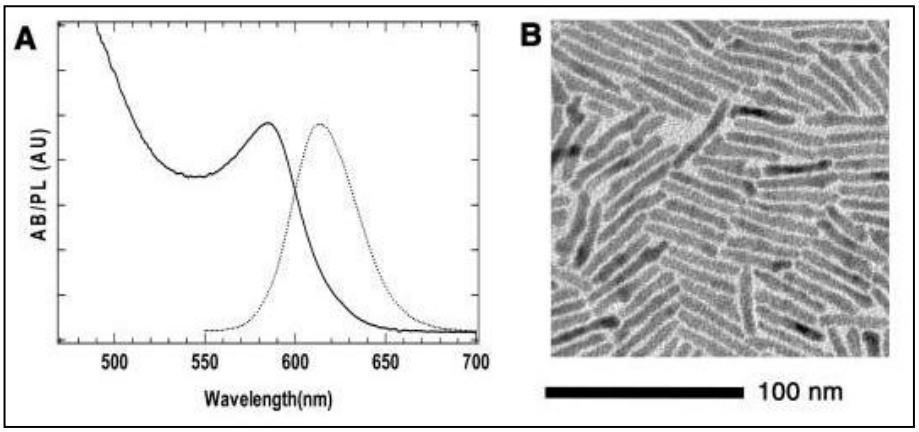

Figure 1.10 (A) TEM image and (B) absorbance (solid line) and PL emission (dotted line) spectra for CdSe nanorods.[62]

X-ray diffraction (XRD) is based on the scattering of X-rays from the electron clouds of atoms in a system and can be used to illustrate the atomic structure of the materials under investigation. XRD, also referred to as powder diffraction, may be used to determine the crystallographic structure, crystal size and preferred orientation in polycrystalline or powdered solid samples. Furthermore, powder diffraction allows for the identification of unknown substances *via* comparison with diffraction patterns of similar compounds taken from an international database.

1.3.3 Synthesis of Cadmium Sulphide Nanorods

The balance between kinetic and thermodynamic control determines the shape of cadmium sulphide nanoparticles. At relatively high temperatures and low precursor concentrations, both surface diffusion and monomer desorption are favoured and therefore nuclei grow isotropically leading to the formation of spherical structures that minimise surface energy for a given nanoparticle volume. At longer reaction times and higher temperatures, at which monomer desorption is possible, the average nanoparticle size continues to increase *via* Ostwald ripening as larger particles draw material from smaller particles even after the precursor is depleted from the solution. In contrast, at relatively low temperatures and higher precursor concentrations the nanoparticle morphology is kinetically controlled and growth occurs preferentially in the kinetically most favourable direction, *i.e.* the one with the smallest activation barrier to any rate-limiting steps occurring in the growth process.[75]

Cadmium sulphide has two distinct crystalline phases, a cubic zinc blend phase stable below 250 °C and a hexagonal wurtzite phase formed at high growth temperatures of 300 °C and above. Low temperatures of around 100 °C may be employed to produce cadmium sulphide nanorods *via* kinetically controlled growth.

A number of advances have been made in the synthesis of cadmium sulphide nanorods allowing for the use of less harmful precursors and lower reaction temperatures. Wan *et al.* investigated the use of hexagonal lyotropic liquid crystalline systems as templates for the synthesis of cadmium sulphide[76] *via* the controlled addition of hydrogen sulphide to aqueous Cd^{2+}. Nanorods were formed showing a degree of parallel alignment within the gaps between cylindrical surfactant micelles in the aqueous phase. Chen *et al.* developed a solution-phase synthesis of soluble cadmium sulphide nanorods,[64] using the surfactant CTAB as a shape-directing template in a similar way to the syntheses of gold nanorods mentioned above. It was

observed that crystal growth was terminated at certain planes which were found to be more stable than others. Prasad *et al.* prepared cadmium sulphide nanoparticles with a variety of morphologies using oleylamine as a surfactant and capping agent and varying reaction conditions such as temperature, growth time and cosurfactant addition.[75] Trioctylphosphine oxide and hydrochloric acid were also used as additives in order to modify the shape, aspect ratios and monodispersity of prepared nanorods. Zhang *et al.* developed a gold nanoparticle-catalysed colloidal synthesis of cadmium sulphide nanorods,[77] first preparing thiol-coated gold nanospheres using the Schiffrin-Brust method.[29] It is believed that gold particles stay in a molten or near-molten state during the reaction, due to the dependence of melting point on particle size,[78] and that cadmium sulphide precursor atoms dissolve inside the seeds allowing cadmium sulphide nanoparticles to grow at the metal surface. Finally, a method in which trioctylphosphine acts as both solvent and stabiliser was developed by Zhang *et al.*[79]

1.4 Surface Modification of Nanoparticles

Self-assembled monolayers (SAMs) on gold surfaces, which are typically prepared by mixing with a thiol-terminated ligand in solutions of ethanol, have been studied extensively,[80] and the surface modification of spherical gold nanoparticles can be easily carried out by a variety of methods.[81] The introduction of functional groups onto gold nanorods is of great interest as specific physical and chemical affinities such as covalent or non-covalent interactions may be exploited to achieve self-assembly of nanorods. However, the instability of such nanoparticles upon removal of surface groups such as CTAB and the fact that typically only partial functionalisation is achieved at the nanorod ends due to preferential binding to the Au [111] surface, leads to irreversible aggregation, and therefore the surface modification of gold nanorods is relatively non-trivial.[82]

Ikeda *et al*. examined the behaviour of spherical gold nanoparticles covered with a liquid-crystalline compound, formed using a modified version of the Brust synthesis,[83] using NMR, DSC and optical microscopy to confirm the presence of an Au-S bond as well as phase transitions suggesting mesomorphic behaviour. Progressing in a similar path, investigations into thermotropic nematic gold nanoparticles were performed[84] using aromatic thiol-terminated ligands in order to induce the formation of rod-like particles and therefore an ordered, liquid crystalline phase. Along with further studies this work demonstrates the potential for influencing the mesomorphic properties of inorganic nanoparticles coated with organic materials through the design and manipulation of the molecules attached to the nanoparticle surface.

Ligand-exchange reactions typically involve mixing CTAB-coated gold nanorods with an alkanethiol in a mixture of aqueous and organic solvent.[85] Modifications such as repeating of the functionalisation process several times,[86] use of ion exchange resins,[87] multiple step functionalisations[82] and DNA hybridisation[88] have been utilised with the objective of producing SAMs on gold nanorods. However, issues with incomplete surface coverage due to preferential adsorption,[89] irreversible aggregation and solubility create a need for further research, and similar issues are faced in the surface modification of cadmium sulphide nanorods.[90]

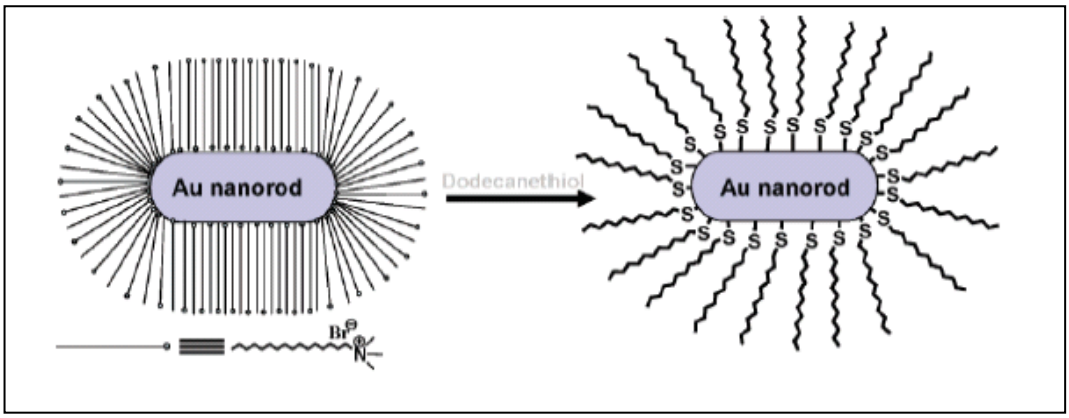

Figure 1.11 Surface modification of gold nanorods with dodecanethiol.[85]

As described above, cadmium chalcogenide nanorods can typically be synthesised with an organic surface coating already in place, and liquid crystalline phases have indeed been observed in cadmium selenide nanorods within organic solvents,[30] with characteristic Schlieren features and birefringence, and localised nematic-like alignment observed using polarising optical microscopy and TEM respectively. Reactions in which the surface modification of cadmium selenide nanorods is accomplished *via* the use of thiol-substituted oligothiophenes[91] have demonstrated that the thiol group, in a similar manner to the surface modification of gold nanoparticles, may be well-suited in the functionalisation of cadmium chalcogenide nanorods.

In addition to direct substitution of the molecules coating the surface of inorganic nanoparticles, a great deal of work has been done on inorganic nanorods within liquid crystalline systems,[92, 93] as well as the use of electric fields to align nanoparticles into organised phases[94] and allow 'switching' between aligned states.[95]

Finally, investigations have been carried out into the preparation of zinc sulphide nanorods encapsulated in organic surfactants in order to promote localised ordering and improved miscibility in nematic liquid crystal hosts.[96] Such an approach for synthesis of alkylamine-functionalised nanorods shows potential for application to different II-VI semiconductor nanorods and alternative amine-terminated organic ligands.

1.5 Energy Concerns

Worldwide energy consumption has increased significantly through the last century; a trend which looks set to continue in the foreseeable future as the energy demands of the population continues to increase with yearly growth rates consistently above 2%.[97] As illustrated by figure 1.12, the majority of current energy sources are from fossil fuels such as coal, oil and natural gas; these however, are finite resources. In addition, carbon dioxide produced from the combustion of fossil fuels is damaging to the environment, for example in the United States, over 90% of greenhouse gas emissions come from the combustion of fossil fuels.[98] Other combustion products such as sulphur can lead to acid rain which has harmful effects on plants, aquatic animals, and marble or limestone structures.

There is therefore a great need for alternative and renewable sources of energy. Wind, thermal, hydroelectric, and solar power are examples of promising alternative energy sources which are both renewable and produce less harmful by-products than fossil fuels. There is also the option of nuclear power which through nuclear fusion in particular has the potential to supply the world with energy for millions of years, though nuclear power plants have high initial costs and there are also concerns over safety.

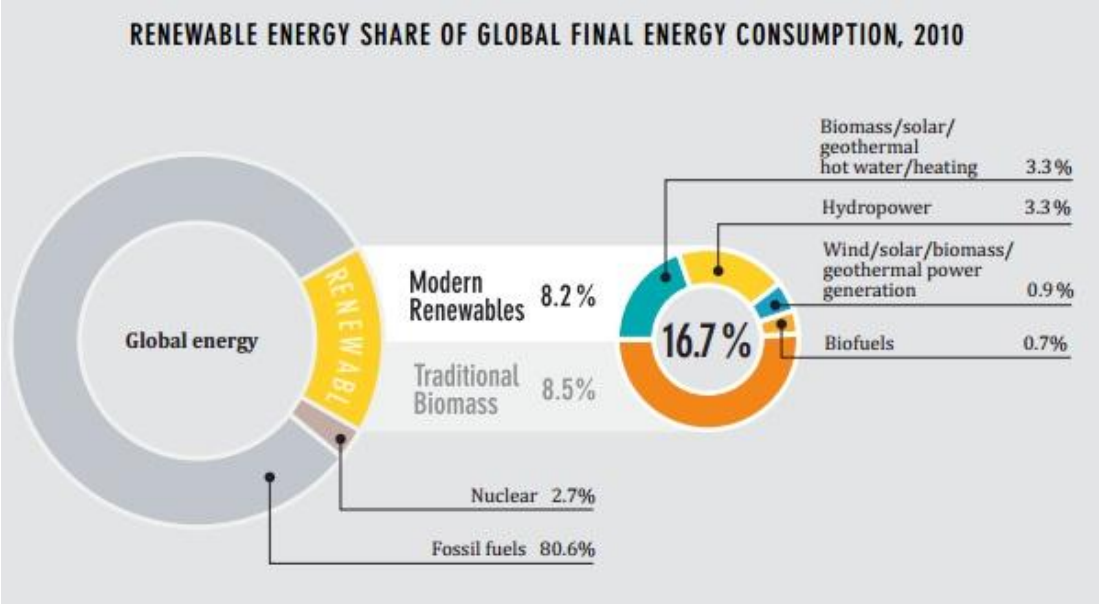

Figure 1.12 Global Energy Consumption 2010.[97]

Solar power has the potential to provide a major contribution to the energy requirements of the world; $3x10^{24}$ joules of energy reaches the Earth from the Sun each year, approximately 10000 times more than the amount currently used by the global population.[99] Photovoltaic solar cells which can harness this solar power could present a suitable replacement for fossil fuels; however the cost of manufacturing silicon-based inorganic semiconductor solar cells is currently very high, with energy costs still greater than those from fossil fuels. The power conversion efficiency of conventional solar cells made from inorganic materials has reached up to 24%, using expensive materials of high purity and energy intensive processing techniques.[100]

Photovoltaic devices based on organic materials show a great deal of promise as the synthesis of the organic materials is less expensive than the inorganic materials used in conventional semiconductors.[101] They may be processed at room temperature *via* processes such as spin coating from solution, allowing for the production of solar cells covering large, flexible, plastic surfaces. Power conversion efficiencies of approximately 5% have been achieved using cells incorporating organic materials such as small molecule and conjugated polymers.[102] Photovoltaic production has been almost doubling every two years, increasing by an average of 48 % per year since 2002, making it the world's fastest-growing energy technology.[103]

1.6 The Photovoltaic Effect

The photovoltaic effect was first reported in 1839 by Becquerel[104] who observed that certain materials produce small amounts of electric current when exposed to light using a silver-coated platinum electrode immersed in an electrolyte. This effect was explained by Einstein in 1905 whose quantum theory described the electromagnetic waves of light as consisting of discrete packets of energy known as photons.[105] The energy of the photon depends only on the frequency of the electromagnetic wave as demonstrated in the below equation:

$$E = hv$$

(Equation 1.3)

E = energy of a photon (J)

h = Planck's constant (6.626068×10^{-34} J s)

v = frequency of electromagnetic wave (s^{-1})

The Highest Occupied Molecular Orbital (HOMO) is the highest-energy molecular orbital containing an electron, the molecular ground state. The Lowest Unoccupied Molecular Orbital (LUMO) is the lowest-energy molecular orbital not containing an electron, the molecular excited state. The difference in energy between the HOMO and LUMO is known as the band gap, E_g and in an organic semiconductor corresponds to the band gap between the valence band (VB) and conduction band (CB) as illustrated in figure 1.13.

The valence band is defined as the highest range of electron energy where electrons are usually present at absolute zero. The conduction band is the range of electron energy where electrons are free to accelerate under the influence of an applied electric field and thereby generate an electric current.

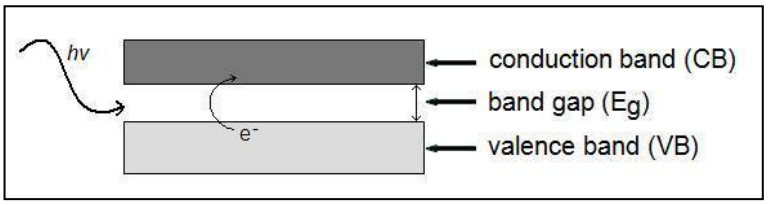

Figure 1.13 An electron is promoted from the valence to the conduction band if the energy of the incident radiation, *hv*, is greater than that of the band gap, E_g.

When an electron crosses the energy gap into the conduction band an unoccupied state, known as a hole, is created in the valence band. The electron-hole pair acts as a negative-positive charge pair which can be delivered to an external circuit *via* an applied potential. The potential difference is typically supplied by exploiting the difference in electrical properties of two materials, generally referred to as *n*-type and *p*-type. An electric field forms at the interface as electrons and holes cross the junction forming a narrow layer of opposing charges. The photoelectric effect is induced at this interface; each absorbed photon of incident light with sufficient energy promotes an electron from the valence band into the conduction band creating a positively-charged hole to form an excited state. The electric field then separates the electron/hole pair and the electron and hole move in opposite directions towards the electrodes; current flows through the circuit under the action of the electric field. The layers of silicon are typically several microns thick in order to absorb enough light across the visible part of the electromagnetic spectrum.

Metallic conductors contain moveable electric charges and have conduction and valence bands which overlap. Metals may be considered as a lattice of cations surrounded by a 'sea' of delocalised electrons. Solid semiconductors have relatively small band gaps, typically E_g ~ 1-2 eV, and have low electrical conductivity; intrinsic semiconductors are pure materials whereas extrinsic semiconductors are doped with electron acceptors or donors. Finally, dielectric materials have large band gaps, typically greater than 4 eV, and are insulators.

1.7 Organic Solar Cells

The majority of commercial semiconductors are inorganic with vastly differing properties to liquid crystals, *e.g.* they are solids with high melting points, they are insoluble, conduct electricity and emit light, and are difficult and expensive to process, requiring high temperatures inside vacuum chambers.

Silicon is the most common material for photovoltaic devices, with reported efficiencies of up to 25% as mentioned above. However, despite these high efficiencies the cost and energy intensive manufacturing process makes these devices very expensive. An important factor to be considered when considering solar cell efficiency is the time taken for the solar cell to produce as much energy as was used in its manufacture. The high cost of semiconductor manufacture is a major factor in restricting the use of solar power. An approach in which large areas of solar cells are fabricated on light, cheap and flexible plastic substrates would be one solution to this problem.

The first organic photovoltaic devices were based on a single layer of organic, hole-conducting material sandwiched between two metal electrodes, giving power conversion efficiencies of below 1%.[106] Following this, bilayer devices were made with two layers of organic materials, one a hole conductor and one an electron conductor, again sandwiched between two metal electrodes. In 1986 a power conversion efficiency of 1% was reported using a bilayer device;[107] this has since been improved to 5% with bulk heterojunction devices, in which two organic materials are blended together to form a single layer, containing both electron and hole conducting material.[108]

Figure 1.14 shows a schematic view of a typical photovoltaic solar cell; the organic bulk heterojunction blend layer is sandwiched between a transparent conducting substrate such as indium tin oxide (ITO) and a metal electrode.

In organic photovoltaic devices photons falling onto a semiconductor can excite an electron from the HOMO to the LUMO, creating a bound electron/electron-hole pair, known as an exciton, which diffuses to the interface between the electron and acceptor. Excitons which reach the interface without undergoing recombination are dissociated into the electron acceptor and donor layers where they are transported to the appropriate electrode. The difference in the HOMO and LUMO energies of donor and acceptor must exceed the exciton binding energy in order for exciton separation to occur.[106]

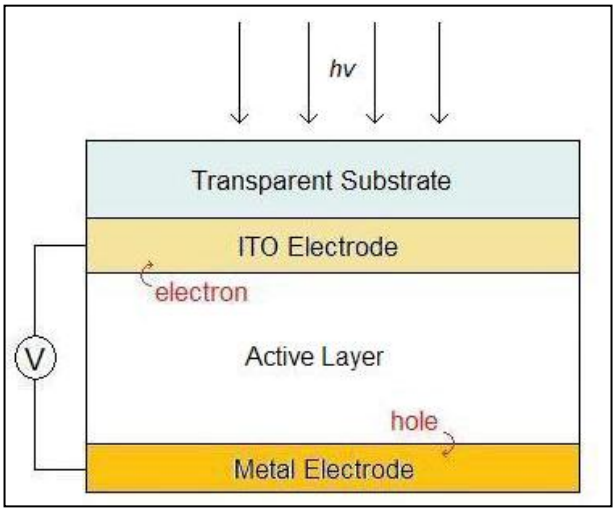

Figure 1.14 Illustration of hybrid liquid crystal solar cell in which the active layer is typically a blend of electron donor and acceptor organic materials.

The external quantum efficiency, η_{EQE}, of a photovoltaic solar cell based on exciton dissociation at a donor-acceptor interface is given by equation 1.4 in which η_A is the absorption efficiency, the exciton diffusion efficiency, η_{ED}, is the fraction of photogenerated excitons that reach the donor-acceptor interface before recombining and the carrier collection efficiency, η_{CC}, is the probability that a free carrier, generated at the interface by dissociation of an exciton, reaches its corresponding electrode.[109]

$$\eta_{EQE} = \eta_A \times \eta_{ED} \times \eta_{CC}$$

(Equation 1.4)

Some advantages of the use of organic materials in photovoltaic devices are:

- They can be processed at room temperature *via* processes such as spin coating, which allows the production of solar cells covering large surfaces.
- The valence band, conduction band, and band gap energies as well as other structural and electronic properties can be altered by chemical modification of materials.
- Small amounts of organic material, typically 50 nm thick layers may be used.[110]

1.8 Dynamic Electrochemistry

Dynamic electrochemistry is the study of electron transfer processes across a solid | liquid interface between electrodes and molecules of an electroactive species, typically in solution phase. A potential difference, *E*, is applied between the electrode and solution, with any electroactive species undergoing oxidation or reduction *via* electron transfer with the electrode, leading to the generation of a current.

$$O_{(aq)} + ne^- \rightleftharpoons R_{(aq)}$$

(Equation 1.5)

The above equation demonstrates a typical electron transfer reaction in which an oxidised species, *O*, gains *n* electrons, e^-, to form the reduced species, *R*, in a reversible, single step process. Nernst demonstrated that the potential at the electrode under equilibrium conditions, is given by the equation:

$$E_{eqm} = E^0 + \frac{RT}{nF} ln \frac{[O]}{[R]}$$

(Equation 1.6)

where *R* is the gas constant (8.314472 J mol^{-1} K^{-1}), *T* is the absolute temperature (K) and *F* is the Faraday constant (96485 C mol^{-1}); the equilibrium potential, E_{eqm}, of the electrode is obtained from the standard electrode potential for the reaction, E^0, and the concentrations of *O* and *R*, which, at equilibrium, will be equal at both electrode surface and bulk solution.[111]

If, however, a potential difference is applied to the electrode versus a suitable reference, such that electrolysis in either a forward or backward direction is driven, then a current will be passed. For such a reaction the magnitude of the current, *i*, is given by the following equation:

$$i = nAFj$$

(Equation 1.7)

where *A* is the electrode surface area (m^2) and *j* is the flux of electroactive species, *O*, towards the electrode | solution interface (mol m^{-2} s^{-1}).

When an electrode comes into contact with an electrolytic solution, the charge of the electrode surface attracts oppositely charged ions from the solution to form a double layer at the interface resembling a parallel plate capacitor, as shown in Figure 1.15.

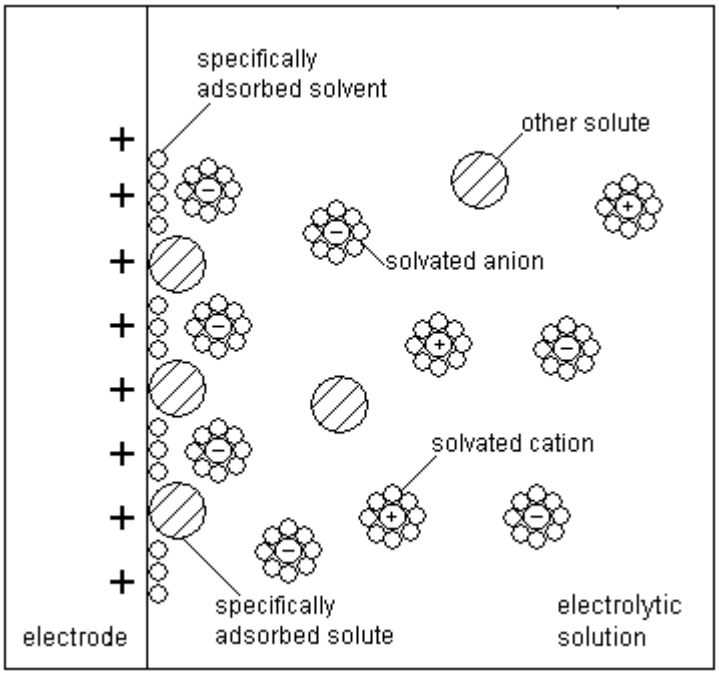

Figure 1.15 Electrode double layer. (Adapted from D.C. Harris, *Quantitative Chemical Analysis 6th Edition*, W. H. Freeman and Company, New York, 2003, p392)

The applied potential causes a breakdown in the electroneutrality of the solution at close proximity to the electrode surface, with solvated ions forming a sheet of ionic charge known as the outer Helmholtz plane (OHP) along the surface. Ions that discard their solvating molecules and become attached to the electrode surface by chemical bonds are considered to form the inner Helmholtz plane (IHP). These combined with the idea of a diffuse double layer further away from the electrode surface form the basis of the Grahame model.[112]

As *O* is reduced to *R* at the electrode-solution interface the concentration of *O* at the electrode surface will decrease compared to the concentration in bulk solution and will need to be replenished *via* mass transport. Consequently, the current observed will depend upon both the rate of heterogeneous electron transfer at the electrode surface and mass transport of reactant molecules from bulk solution to the electrode | solution interface.

1.8.1 Mass Transport

There are three forms of mass transport of electroactive species between the electrode | solution interface and bulk solution; diffusion, convection and electric migration. For the majority of investigations into electrochemical reactions diffusion plays a key role, as it is

possible to eliminate convection and migration through modification of the experimental conditions.

Convection and Migration

Convection refers to the movement of currents within fluids, and may be either natural or forced. Natural convection is caused by density gradients existing within the fluid due to variations in temperature or pressure. As natural convection is generally both irreproducible and difficult to predict, it is obviously undesirable in electrochemical investigations. Typically, natural convection effects are observed when the experimental timescale of voltammetric measurements using conventional electrodes exceeds 10-20 seconds.[113] Forced convection is movement imposed onto the fluid by deliberate agitation *via* stirring, pumping, or bubbling of gas, and can therefore be eliminated by ensuring that the solution is kept stationary for the duration of any voltammetric measurements. Forced convection may also be deliberately introduced into an electrochemical investigation in order to either dictate mass transport to the electrode or to render any natural convection effects negligible.

Electric migration occurs when an external electrical field is applied, causing movement of charged species in solution, for example a positively charged particle will move towards a negatively charged electrode surface. In order to suppress the migration of electroactive species, an excess of electrochemically-inert supporting electrolyte is added, for example 0.1 M electrolyte compared with 1.0 mM electroactive species. This virtually eliminates migration of the electroactive species by ensuring that there are sufficient background ions to prevent the build-up of electric fields in the solution and reducing the relative extent of migration, therefore allowing for electrochemical experimentation under diffusion-only conditions.

Diffusion

Electrochemical investigations are normally carried out under diffusion-only conditions, as outlined above, in order to simplify the analysis of the experimental data obtained. Diffusion is caused by unequal concentration distribution and proceeds in order to maximise entropy by levelling out any inhomogeneity within the system. For simple charge transfer reactions the voltammetric signal is proportional to the flux of electroactive species towards the electrode | solution interface, as described by Fick's first law (Equation 1.8). For uniform, planar potential distribution, Fick's second law (Equation 1.9) describes the time-dependent change in the concentration of electroactive species at the electrode surface caused by the flux.[113]

$$j = -D\frac{\partial c}{\partial x}$$

(Equation 1.8)

$$\frac{\partial c}{\partial t} = D\frac{\partial^2 c}{dx^2}$$

(Equation 1.9)

where D is the diffusion coefficient of the electroactive species ($m^2 s^{-1}$), c is the concentration of electroactive species (mol m^{-3}), x is distance (m) and t is time (s).

Application of a potential in order to oxidise or reduce an electroactive species at the surface of an electrode depletes the concentration of the species and it is therefore necessary for it to be replenished from the bulk solution in order for further reaction to occur. This leads to the generation of a concentration gradient between the electrode surface and bulk solution, the distance of which increases over time due to the diffusion. The solution volume within this concentration gradient is labelled as the diffusion layer thickness, δ (m), and is related to the diffusion coefficient and experimental timescale by the Einstein-Smoluchowski equation:[113]

$$\delta = \sqrt{2Dt}$$

(Equation 1.10)

1.8.2 Kinetics of Heterogeneous Electron Transfer

Considering the simple reaction above (Equation 1.5) for which k_{red} and k_{ox} (cm s^{-1}) are the first order heterogeneous rate constants for the oxidative (forward, occurring at the cathode) and reductive (back, occurring at the anode) electron transfer reactions, the current for both the oxidative and reductive components can be predicted.

$$i_{red} = -nFAk_{red}[O]_0$$

(Equation 1.11)

$$i_{ox} = nFAk_{ox}[R]_0$$

(Equation 1.12)

where $[O]_0$ and $[R]_0$ (mol m^{-3}) are the respective concentrations of oxidised and reduced species at the electrode surface and $k_{red}[O]_0$ and $k_{ox}[R]_0$ are the respective fluxes of material to

the electrode surface. The total current is the sum of the oxidative and reductive currents and is therefore given by the equation

$$i = nFA(k_{ox}[R]_0 - k_{red}[O]_0)$$

(Equation 1.13)

In a similar manner to homogeneous solution kinetics, parabolic energy profiles may be used for reagents and products, with the region in which they intersect, which corresponds to the activated complex, being of most interest. In the Butler-Volmer model, the energy parabolas are linearised, see Figure 1.16.

In this transition state region the curves are assumed to be straight lines, so that a change of *x* in the Gibbs free energy, *G* (J mol^{-1}), of the oxidised species translates to a change of $\alpha_{red}x$ in the activation energy, $\Delta G^{\neq}_{red}$, for the reductive process. Altering the electrode potential can radically change the rates of the forwards and backwards reactions. By adjusting the applied potential, *E*, to a value different from a potential at which there is no current flow is to change the oxidation and reduction free energy barriers in relation to each other.

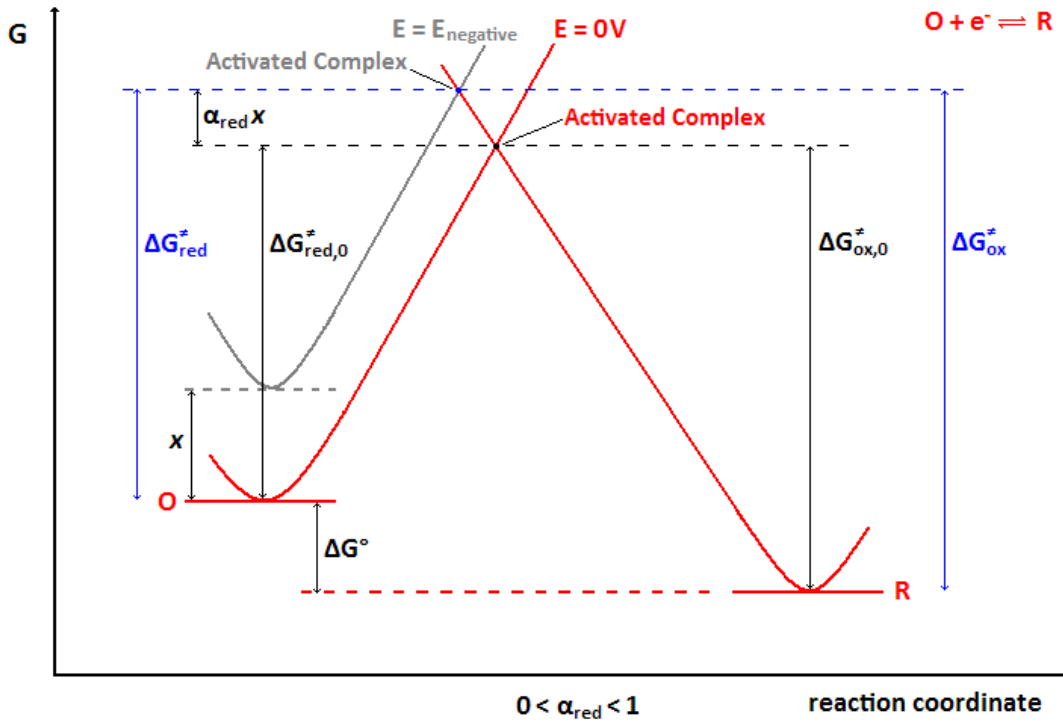

Figure 1.16 Energy-reaction coordinate diagram for electrolysis where *E* is the potential applied to the electrode and the transfer coefficient, *α*, is a measure of the slope of the energy profiles in the transition state region and reflects the sensitivity of the transition state to the decrease in potential between electrode and solution. If *α* is close to 0 then the activated complex resembles the reactants in its potential dependence, whereas when *α* approaches 1 the behaviour is product-like. Commonly values close to 0.5 are observed, inferring that activated complexes possess intermediate behaviour.

Assuming that the concentrations of the reactants at the electrode surface are equal to their bulk values allows the Butler-Volmer equation to describe how the current varies as a function of the potential.[114, 115]

$$i = FAk^0 \left\{ [R]_0 exp\left[\frac{(1-\alpha)nF}{RT}(E - E_{eqm})\right] - [O]_0 exp\left[\frac{-\alpha nF}{RT}(E - E_{eqm})\right]\right\}$$

(Equation 1.14)

where the standard rate constant, k^0 (cm s^{-1}), is independent of potential.

When the standard rate constant is large, little or no applied potential is required in order for oxidation or reduction to take place and the electrode reaction is said to be 'reversible'. This allows the Butler-Volmer equation to be simplified to:

$$\ln i = constant + \frac{(1-\alpha)F}{RT}(E - E_{eqm})$$

(Equation 1.15)

When the standard rate constant is small, a large applied potential is required in order for oxidation or reduction to take place and the electrode reaction is said to be 'irreversible'. This allows the Butler-Volmer equation to be simplified to

$$\ln(-i) = constant - \frac{\alpha F}{RT}(E - E_{eqm})$$

(Equation 1.16)

Equations 1.15 and 1.16 can be used to obtain α experimentally through knowledge of the current-potential characteristics of an irreversible electrode reaction using Tafel analysis.[116]

Marcus Theory

Considering a reduction of *O* to *R*, electron transfer is thought to take place on a timescale of 10^{-15} to 10^{-16} s, whereas nuclear vibrations within *O* occur on a timescale of 10^{-13} s. Consequently when the electron transfer occurs, *R* must still be of the same molecular shape and solvation as *O* preceding the electron transfer and so the Franck-Condon Principle is followed.[117, 118] Secondly, since there is no loss or gain of energy accompanying the electron transfer, *R* must be formed by an energy equal to the sum of the energy of *O* and of the electron in its Fermi Level in the metal electrode instantly before the electron transfer occurs. These two constraints imply that for electron transfer to occur, both *O* and *R* must be in an

energetically excited transition state, representing the structure in which *O* and *R* have the same shape and solvation as well as satisfying the above energy conservation restriction.

The energy required for the initial activation of *O* is expected to be larger for greater differences in molecular geometry (bond angles, bond lengths, degree of solvation, *etc.*), and subsequently the free energy of activation ($\Delta G^{\neq}_{red}$) will be larger for these 'inner sphere' reactions. For simple 'outer sphere' electron transfer reactions, free from adsorption effects, fast, reversible electrode processes will be observed when both species *O* and *R* have comparable shapes and salvation.

1.8.3 Cyclic Voltammetry using Macroelectrodes

Cyclic voltammetry is an electrochemical technique employed to analyse the redox properties of compounds in order to obtain information on the thermodynamic standard redox potentials[119] and the kinetics of heterogeneous charge transfer. It is also possible to determine the transfer coefficient and the transfer rate, along with the thermodynamic standard redox potential (E^o) from the voltammograms when employing microelectrodes of varying size.[119] In a conventional experiment such as the reversible process described in Equation 1.5, the potential of the working electrode is swept at a constant scan rate, v (V s^{-1}), typically in the range of a few millivolts per second up to several megavolts per second,[120] from an initial potential, E_1, at which no electron transfer takes place to a potential, E_2, at which the electron transfer is driven rapidly.

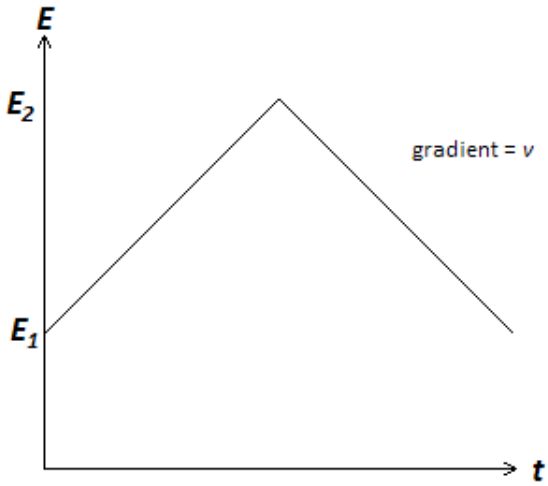

Figure 1.17 Dependence of applied potential as a function of time for cyclic voltammetry.

Experiments are conducted in stationary solutions with an excess of supporting electrolyte, therefore only diffusional mass transport of electroactive species to the electrode surface is observed, allowing calculation *via* the used of Fick's second law (Equation 1.9). The current, which is a function of the applied potential, is recorded after each increment in potential and the data is displayed as a voltammogram, an example of which is shown in Figure 1.18 below.

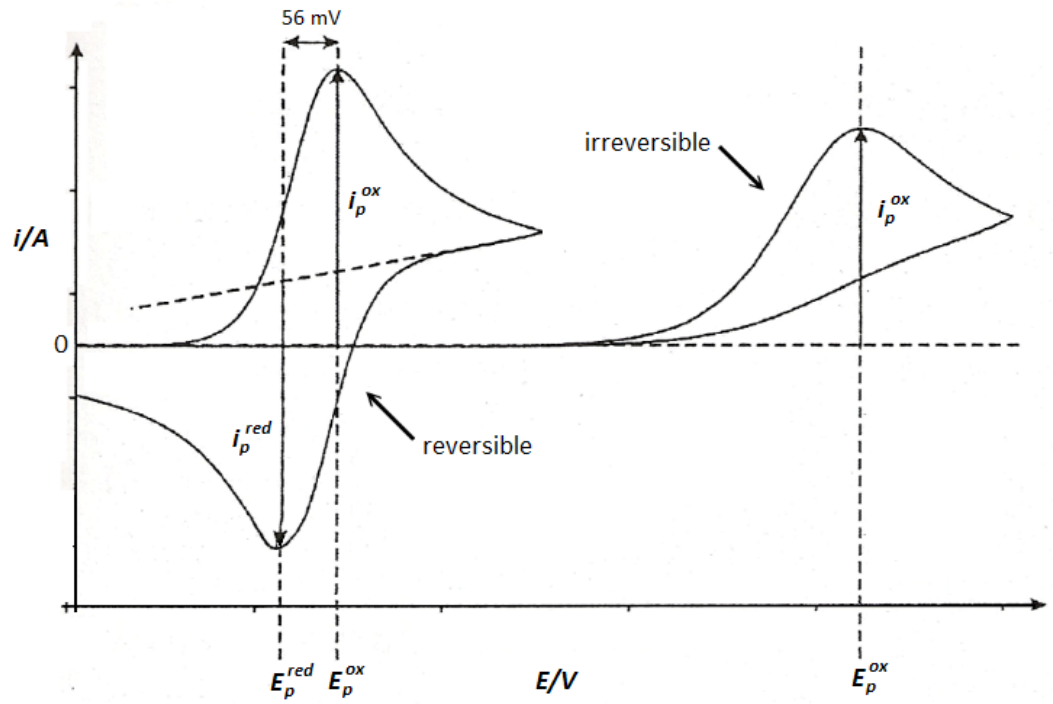

Figure 1.18 Example cyclic voltammograms for the reaction $R \rightleftharpoons O + e^-$ showing a reversible system with fast electrode kinetics relative to rate of mass transport and an irreversible system with slower electrode kinetics. The important features are the peak currents, i_p^{ox} and i_p^{red}, their corresponding peak potentials, E_p^{ox} and E_p^{red}, as well as the peak-to-peak potential separation, ΔE_{pp}. (Adapted from R. G. Compton, C. E. Banks, *Understanding Voltammetry*, World Scientific Publishing, Singapore, 2007)

The observed current-voltage response will depend upon both the rate of heterogeneous electron transfer at the electrode surface and the rate of diffusional mass transport of the electroactive species.

When the standard rate constant is large the electrode kinetics will be much faster than the rate of diffusional mass transport and so the system is said to be 'electrochemically reversible'. As the potential is increased during the potential sweep, k_{ox} increases and *R* is converted to *O*, causing the concentration of *R* at the electrode surface to decrease and require replenishment *via* diffusion from the bulk solution. Therefore the peak current reflects a balance between the increasing heterogeneous rate constant and the decreasing surface concentration of electroactive species. There is then a fall in current after the peak as diffusion is not rapid enough to replenish *R* from the bulk solution. When the potential reaches the value E_2 the

sweep is reversed and the potential decreases, increasing k_{red}. This leads to the reduction of species *O*, formed at the electrode during the forward scan, back to *R*. Initially there will be a high concentration of *O* at the electrode surface and so the current will again increase to a peak value and then decrease to zero as all of the species *O*, in the diffusion layer, is converted to *R*. These peak potentials are independent of the scan rate and for a reversible process are separated by approximately 56/*n* mV (at 298 K).

When the standard rate constant is small the electrode kinetics will be much slower than the rate of diffusional mass transport and so the system is said to be 'electrochemically irreversible'. Figure 1.18 shows a typical voltammogram for an irreversible system. Since the standard rate constant is small, a higher potential is required in order for electron transfer to occur, resulting in broader peak widths. No reverse peak is observed as the reverse reaction does not occur at a sufficient rate in the potential range under investigation.

As shown by the Randles-Sevčik equation below, if electron transfer at the electrode surface is fast and the current is limited by the diffusion of electroactive species to the electrode surface, then the current peak will be directly proportional to the square root of the scan rate:

$$i_p = 0.4463nFAc\left(\frac{nF}{RT}\right)^{1/2} v^{1/2}D^{1/2}$$

(Equation 1.17)

This makes sense as increasing the scan rate will decrease the experimental timescale, with the Einstein- Smoluchowski equation (Equation 1.10) inferring that this will result in a smaller diffusion layer thickness; hence the concentration gradient will increase with the scan rate.

1.8.4 Microelectrodes

The term *microelectrode* is used to define an electrode with at least one dimension in the micrometre range. An operational definition, based on function within a particular environment, may be that a microelectrode possesses a characteristic dimension similar to or smaller than the diffusion layer thickness, typically in the micrometre range.

Microelectrodes possess several advantages over standard electrodes when used for electrochemical investigations. The decrease in electrode size leads to a vast increase in the mass transport rates of redox-active species from the bulk solution to the electrode surface as the diffusion changes from predominantly one-dimensional linear diffusion to two dimensional

convergent diffusion.[121] This allows investigation of processes in which the current achieves a diffusion-limited steady-state value using cyclic voltammetry. Also, because this steady-state is achieved more quickly as the electrode size decreases, it is possible to follow very fast electrode processes along with reactions involving unstable reactants and products, or short-lived intermediates.[122] Microelectrodes are much less affected by Ohmic drop, caused by solution resistance,[123] with high current densities observed at the electrode even for low measuring currents; consequently experiments may be performed using low concentration or poorly conducting electrolytes.

Diffusion

The geometry of an electrode can be represented by the theory of an infinitely large planar electrode for which the flux occurs perpendicular to and is homogeneous over the electrode surface, and the concentration of electroactive species reaches the bulk value at a distance of a few multiples of the diffusion layer thickness.[124] When the electrode radius, r_0, is much greater than the diffusion layer thickness the infinite electrode model is followed and linear diffusion dominates, as illustrated in Figure 1.19.

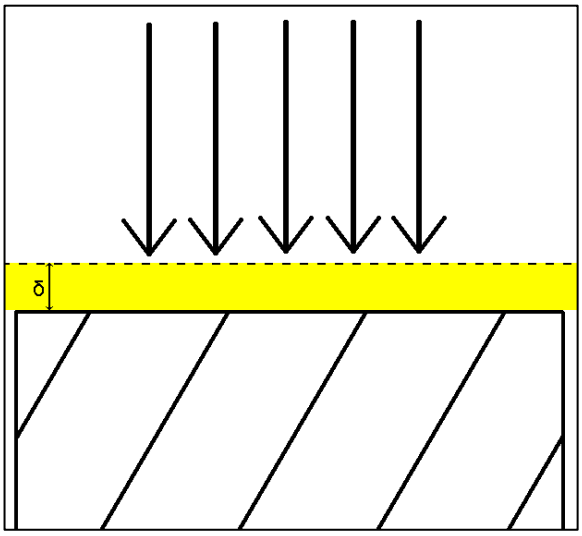

Figure 1.19 Linear, one-dimensional diffusion at a macroelectrode for which the diffusion layer thickness is much smaller than the electrode radius.

Conversely, when the electrode radius is much smaller than the diffusion layer thickness, the diffusional flux of electroactive species towards the electrode is constant with time but inhomogeneous over the electrode surface, increasing as the distance from the edge of the

electrode decreases. This is due to the vastly increased convergent diffusion in addition to linear diffusion, as illustrated in Figure 1.20.

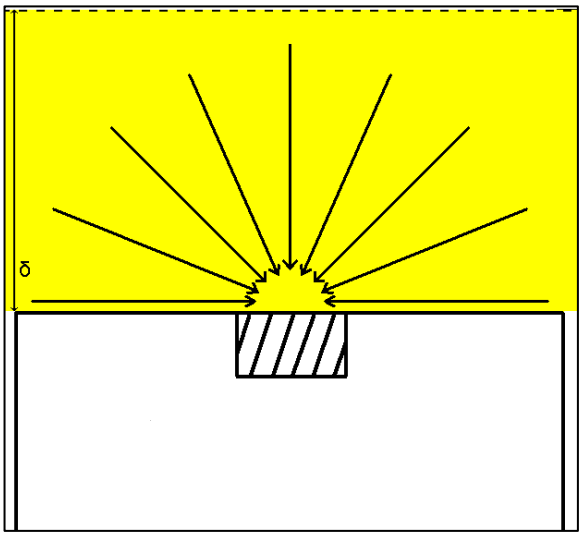

Figure 1.20 Convergent, two-dimensional diffusion at a microelectrode for which the diffusion layer thickness is much greater than the electrode radius.

As diffusion to the electrode becomes predominantly convergent and non-uniform, the current observed no longer scales with the electrode area; instead a time-independent steady-state current is achieved which is dependent on the electrode radius.

$$i_{lim} = 4nFDr_0c$$

(Equation 1.18)

Since the current measured at an electrode is a function of its radius, the current measured at a microelectrode is significantly lower than that from a conventional macroelectrode, leading to a vastly reduced amount of electrolysis in solution. Therefore it follows that the diffusion layers of such electrodes will be very thin, typically on a micrometer scale, and that the concentration gradients across them will be correspondingly high; therefore the rate of mass transport will be greatly increased when compared to macroelectrodes. Since the diffusion layer thickness depends on time (Equation 1.10), the mass transport process is also controlled by the experimental timescale. As the timescale is reduced to small enough values the diffusion layer thickness will become much smaller than the electrode radius and so planar electrodes of any size will follow the infinite electrode model of linear diffusion. Equally, as the timescale is increased the diffusion layer thickness will become much greater than the electrode radius meaning that even macroelectrodes will tend towards radial diffusion and the formation of a steady-state at sufficiently long experimental timescales.

The increased rate of mass transport to microelectrodes is useful for the investigation of electrolysis mechanisms for very fast processes which normally would be limited by the slowest step, the rate of diffusion. Using microelectrodes this limitation is less probable to occur and much faster chemical steps are accessible to investigation by electrochemical techniques and consequently important information concerning the thermodynamics and kinetics of both homogeneous and heterogeneous electron-transfer steps can be obtained.[125]

Cyclic voltammetry may be utilised in measuring the band gap - between the HOMO and LUMO, or as discussed above, between the valence band and conduction band in organic semiconducting materials - and in this way ought to be suitable for determining whether materials are suitable or not for use in photovoltaic devices.

1.9 Organometallic Lyotropic Chromonic Liquid Crystals

An alternative approach to those discussed above towards the formation of hybrid inorganic-organic nanorods capable of forming liquid crystalline phases may be through the use of organometallic lyotropic chromonic materials. As advances in nanotechnology have been made, the development of lightweight, self-assembling and flexible molecular wires, over which long-range electron transport may occur, has become of greater interest.[126] Organometallic lyotropic chromonic materials show great potential in this field and may prove useful in various technologies such as molecular computing,[127] high-speed communications[128] and redox-based security systems.[129]

Chromonic systems are lyotropic liquid crystalline phases that form from soluble aromatic materials through face-to-face aggregation of the molecules into columns. There are two fundamental chromonic phases as illustrated in figure 1.21 - the nematic N phase, consisting of an array of columns, and the M phase, observed at higher concentrations, in which the columns are assembled in a hexagonal array. Chromonic phases typically form from a range of multi-ring aromatic compounds with flat cores combined with hydrophilic side groups which will aggregate in linear stacks. As concentration increases a transition occurs from monomers to eventually form liquid crystalline phases.

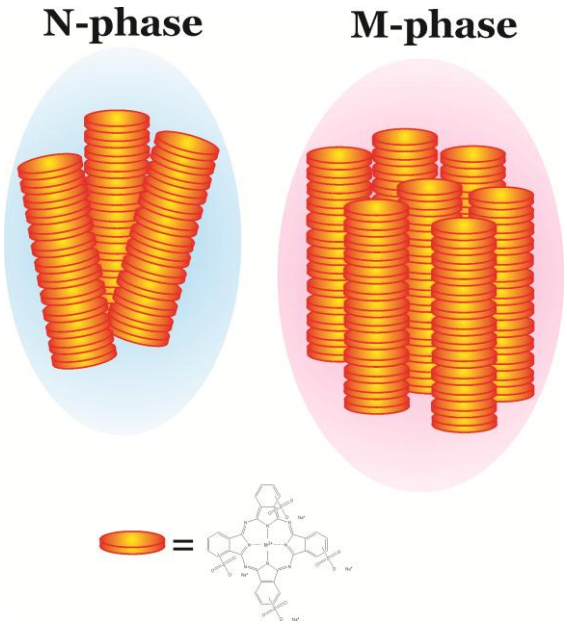

Figure 1.21 Schematic illustration of the N and M phases of chromonic liquid crystals based on tetrasulfonated phthalocyanines along with the general structure of individual mesogens.

Recent studies have demonstrated that the combination of facile alignment, self-ordering, sensitivity to changes in the local environment, along with their optical and electro-optical properties, gives chromonic materials great potential for use in technologies such as polarisers, light-harvesting devices and biosensors.[130]

Chromonic lyotropic liquid crystals[130] based on transition metal phthalocyanines represent an appealing class of metal-organic liquid nanomaterials which may be capable of providing a framework for long-range electron transport.[131-133] Such systems exhibit neither a Kraft point or CMC, and may assemble through π-stacked H-aggregates at high monomer concentrations in water to form a nematic phase or, at higher concentrations, the hexagonal (M) phase. Aggregates within these systems are generally considered to be single molecular columnar stacks, with charge transport thought to occur in one dimension only.[126, 128]

Electrochemical investigation of such systems is therefore possible, with the phase alignment determined through the anisotropy of diffusive mass transport relative to the electrode surface. Such materials should therefore have the potential for investigation into the formation of self-assembled, hybrid inorganic-organic, nanorod-like molecules capable of charge transport as described in a similar manner to the materials described above.

1.10 Project Aims

Using a biomimetic self-assembly approach mimicking that of rods of tobacco mosaic virus,[134] a new kind of liquid crystal will be produced which at the same time will also be a new kind of semiconductor with the potential for application in photovoltaic solar cells. Such a giant hybrid liquid crystal is anticipated to be composed of a thermotropic liquid crystalline phase of semiconductor nanorods with a high aspect ratio consisting of an inorganic II-VI or III-V semiconductor, or metal nanorod "core" surrounded by a "shell" of organic semiconductor molecules, as illustrated in figure 1.22.

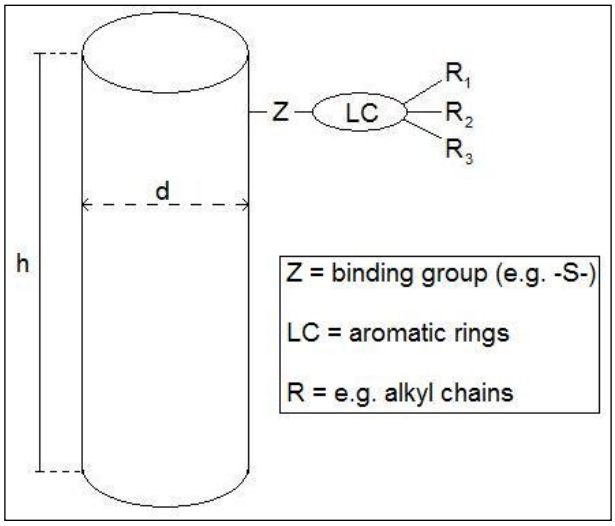

Figure 1.22 Schematic representation of a liquid crystal nanorod consisting of calamitic organic semiconductor ligands attached to a rigid inorganic nanorod semiconductor core.

The Onsager theory dictates that as the density of rods increases, an aligned system will become more favourable, and so a transition between isotropic and nematic phases will occur. Therefore, if inorganic nanorods can be synthesised in high enough yields and without the repulsive effects of charged surface groups, they should be able to align in nematic-like arrangements, giving a liquid crystalline-structured material.[2]

Initially, gold nanorods along with alkanethiols and synthesised organic ligands will be used in a proof-of-concept investigation into the synthesis and properties of such hybrid compounds. Synthesis of gold nanorods is desirable due to the high cost and relatively low concentration of commercially available nanorods, as well as the need to examine different nanorod sizes and aspect ratios. The solution-based, seed-mediated synthesis of gold nanorods will be carried out using optimised literature methods in order to reproducibly synthesise nanorods of high

yield, high aspect ratio and good monodispersity on a milligram to gram scale. Initially, II-VI semiconductor cadmium sulphide nanorods will be synthesised using literature methods, again optimising to improve yields, aspect ratios and monodispersity. Synthesised nanorods will be functionalised using both commercially available thiol-terminated ligands such as alkanethiols and synthesised organic ligands.

Liquid crystals have good processing properties (spontaneous alignment, photolithographic patterning, low cost, and solubility in organic solvents) as well as good semiconducting properties.[135] Inorganic semiconductors have good optical and electronic properties (efficient light absorption and emission and good electrical conductivity).[136]

It is envisaged that these liquid crystal core-shell semiconductor nanorods will form a new class of liquid crystals which will exhibit birefringence, biaxiality, polarity, dichroism and anisotropic thermal and electrical conductivity. They will be used to generate, conduct and direct light and electric current in a controlled direction in electronic and electro-optic devices. The potential of such nano-materials is expected to be demonstrated in low-cost organic solar cells with optical photovoltaic power conversion efficiencies of >5 % using an ideal photovoltaic configuration.[102, 108] Such materials and devices are desirable as a potential route towards low-cost, mass production of higher efficiency photovoltaic devices which may enable solar energy to meet the demands outlined in section 1.5.

Figure 1.23 illustrates a liquid crystal core-shell semiconductor nanorod and an example of how they may be incorporated into a photovoltaic solar cell. The device thickness will be determined by the length of the liquid crystal nanorods which will form a monolayer, ensuring that there are no dead ends in charge transport. The cylindrical structure will provide a large interfacial area between the organic and inorganic semiconductors for highly-efficient exciton generation, charge separation, voltage generation and very fast and anisotropic one-dimensional charge transport to the electron-donor/electron-blocker and electron acceptor/hole-blocker without charge recombination.[137] The direct pathways for the dissociated charge carriers within separate electron and hole transporting materials, the organic shell is an electron donor and the inorganic core an electron acceptor, will ensure that charge recombination is minimised.

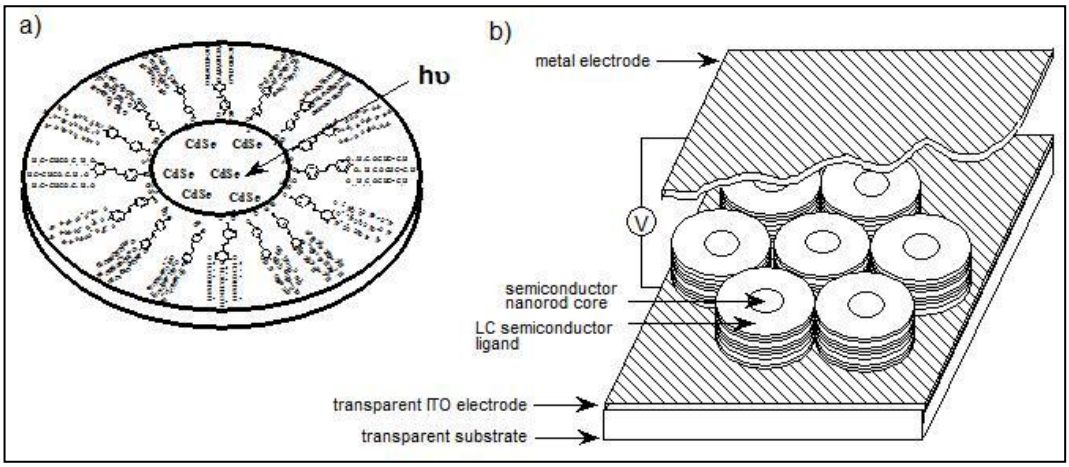

Figure 1.23 Illustration of cross sections of a) an electron accepting inorganic core encased in an organic electron donor; b) a photovoltaic cell, incorporating the material shown in (a) as a hybrid organic-inorganic liquid crystal active layer.

In addition, investigations into 'nanorods' formed through the self-assembly of metal core porphyrins in lyotropic liquid crystalline phases will be carried out. Such systems may provide an alternative route towards the formation of hybrid inorganic-organic nanorod-like systems, capable of forming liquid crystalline phases.

2 Experimental

2.1 Material Evaluation

2.1.1 Nuclear Magnetic Resonance Spectrometry

The structures of start materials, intermediates and final products were verified by ^{1}H NMR and ^{13}C NMR spectroscopy using a JEOL Eclipse 400 MHz spectrometer. Deuterated chloroform with an internal standard of tetramethylsilane was typically used as the solvent. The following abbreviations are an example of those used to describe the splitting patterns:

s	- singlet	d	- doublet	t	- triplet
quart	- quartet	quint	- quintet	sext	- sextet
sept	- septet	dd	- double doublet	m	- multiplet

2.1.2 Infrared Spectrometry

Infrared spectroscopy was used for the confirmation of certain functional groups. The analysis was carried-out using a Perkin-Elmer PARAGON 1000 Fourier Transform (FT-IR) spectrophotometer.

2.1.3 Chromatography

The progress of reactions was monitored by thin layer chromatography (TLC) using 0.25 mm aluminium backed TLC plates coated with silica gel (60 F_{254} Merck) and compounds were visualised with ultraviolet light (254 nm).

Purification of intermediates and final products was achieved using column chromatography, using silica gel 60 (230 - 400 mesh) and appropriate solvent mixtures, followed by recrystallisation from a suitable solvent.

2.1.4 Optical Microscopy and Melting Points

Images of surface textures were observed using an Olympus BH-2 polarising optical microscope and captured using a digital camera connected to a computer. Melting points of intermediates and final products were measured using a Mettler Toledo FP82HT hotstage and FP90 Central Processor in conjunction with the above microscope.

2.1.5 Cyclic Voltammetry

For electrochemical investigations, unless specifically noted, an Autolab potentiostat (PGSTAT 30, Eco Chemie, Netherlands) controlled by a Pentium III computer was used. The electrochemical cell consisted of a gold ball microelectrode, a platinum counter electrode, and either a silver or saturated calomel reference electrode (all made in house). All experiments were carried out at a temperature of 295 ± 2 K.

2.1.6 Centrifugation

Centrifugation was carried out using a Sigma Laborzentrifugen 2-15 Howe centrifuge in combination with Fisher oak ridge 28 mL centrifuge tubes.

2.1.7 UV-vis Spectrometry

UV-vis spectra were acquired using a Perkin Elmer Lambda 25 UV/VIS Spectrometer in conjunction with UV WinLab software. Samples were measured in CEL 1600 UV quartz cuvettes with a 10 mm path length.

2.1.8 Thermal Analysis

Melting points and transition temperatures were determined using a Perkin-Elmer Differential Scanning Calorimeter 7 connected to a computer running Pyris software *via* a TAC 7/3 instrument controller.

2.1.9 Transmission Electron Microscopy

Transmission electron microscopy was carried out using a Jeol 2010 running at 200 kV. Images were acquired using a Gatan Ultrascan 4000 digital camera and EDS analysis was performed using an Oxford Instruments Inca analyser. Measurements of nanoparticle dimensions for statistical analysis were performed using Digital Micrograph software.

2.1.10 Reagents and Reaction Solvents

Reagents that were purchased were used without further purification unless stated otherwise. Tetrahydrofuran was dried and distilled over sodium wire before use and then stored over

molecular sieves (4Å). Other solvents were used as purchased. For any reaction steps requiring deionised, water with resistance greater than 18 MΩ cm was used. All reactions were performed under an atmosphere of dry nitrogen unless stated otherwise.

Supplier	Chemical
Acros	1-dodecanethiol n-butyllithium 2,5-dibromoaniline cadmium chloride cadmium oxide oleylamine phenyl ether potassium phosphate dibasic potassium phosphate monobasic sodium borohydride sodium phosphate dibasic sodium phosphate monobasic succinic acid trioctylphosphine oxide Triton-X100
Aldrich	1,1'-azobis(cyclohexanecarbonitrile) 1,4-dibromobutane 1,6-dibromohexane 1,8-dibromooctane 10-bromo-1-decanol 1-octadecanethiol 5-bromopent-1-ene 8-bromo-1-octanol 9-bromo-1-nonanol acetylacetone bromine cadmium acetate carbon tetrabromide copper(II) phthalocyanine tetrasulfonic acid tetrasodium salt cyclohexane diisobutylaluminium hydride lithium chloride magnesium turnings nickel(II) phthalocyanine tetrasulfonic acid tetrasodium salt palladium on carbon sodium carbonate sodium citrate sodium hydroxide thioacetic acid triethylamine trioctylphosphine triphenylphosphine
Alfa Aesar	ascorbic acid 4-bromophenol hydrogen tetrachloroaurate

	silver nitrate
BDH Laboratory Supplies	sodium sulphide
Euriso-top	deuterated chloroform
Fisher	dimethyl formamide acetone ethanol ethyl acetate hexane hydrochloric acid hydrogen peroxide magnesium sulphate methanol methyl ethyl ketone nitric acid oleic acid potassium carbonate sodium chloride sulphuric acid tetrahydrofuran toluene
Fluka	tetradodecylammonium bromide
Kingston Chemicals	4-bromo-4'-pentylbiphenyl 4-pentylphenylboronic acid
Lancaster	sodium metabisulphite trimethyl borate
Merck	4-(4-pentylcyclohexyl)phenol silica gel (60 F254) 4-(4-propylcyclohexyl)phenol
Prime Chemicals	sulphur
Sigma	6-(ferrocenyl) hexanethiol benzyldimethylammonium chloride cetyltrimethylammonium bromide perchloric acid

Commercially obtained gold nanorods were Nanorodz™ NIR Absorbing Nanorods 30-10-750 purchased from *www.nanopartz.com*, having an axial diameter of 10 nm and a length of 35 nm and provided in dilute aqueous solution.

2.2 Synthetic Discussion

2.2.1 Synthesis of 5-(4'-pentylbiphenyl-4-yloxy)pentane-1-thiol

(3) 4'-pentylbiphenyl-4-ol

The Suzuki-Miyaura reaction couples organo-boronic acids to halides in the presence of a palladium catalyst.[138]

The phenol (3) was produced from 4-pentylphenylboronic acid (1) and 4-bromophenol (2) in a Suzuki-Miyaura coupling reaction as illustrated in figure 2.1.

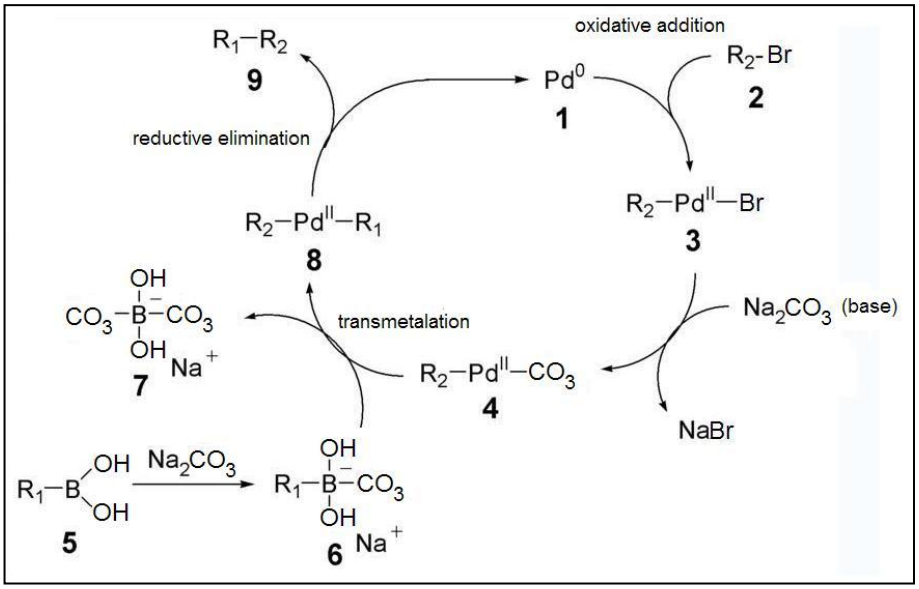

Figure 2.1 Proposed Suzuki-Miyaura coupling mechanism (adapted from reference).[139]

The first step is the oxidative addition of palladium to the halide **2** to form the organo-palladium species **3**. Reaction with a base gives intermediate **4**, which *via* transmetalation with the boron-ate complex **6**, forms the organo-palladium species **8**. Reductive elimination forms the product **9** in good yield (65%) and restores the palladium catalyst **1**.

(4) 4-(pent-4-enyloxy)-4'-pentylbiphenyl[9]

The base deprotonation of 4'-pentylbiphenyl-4-ol (3) was followed by an S_N2 electrophilic substitution with 5-bromopent-1-ene in dimethylformamide *via* a Williamson ether synthesis.[140] The product (4) was obtained in good yield (85%).

(5) S-5-(4'-pentylbiphenyl-4-yloxy)pentyl ethanethioate[141]

The radical addition of thioacetic acid using the radical initiator ABCN was carried out under reflux leading to formation of 5 in good yield (79%).

(6) 5-(4'-pentylbiphenyl-4-yloxy)pentane-1-thiol[142]

The acid hydrolysis of 5 was carried out to produce 5-(4'-pentylbiphenyl-4-yloxy)pentane-1-thiol in good yield (94.4%).

2.2.2 Synthesis of 8-(4'-pentylbiphenyl-4-yloxy)octane-1-thiol

(3) 4'-pentylbiphenyl-4-ol[143, 144]

A boronic acid was generated in high yield *via* the lithiation of 4-bromo-4'-pentylbiphenyl (7) and then oxidised to the phenol (3) (85%) *via* addition of hydrogen peroxide in diethyl ether without further purification.

(9) S-8-hydroxyoctyl ethanethioate[145]

The ethanethioate was synthesised in good yield *via* nucleophilic substitution of the bromide group of 8 with thioacetic acid.

(10) S-8-bromooctyl ethanethioate[146, 147]

Figure 2.2 illustrates the Appel reaction for converting an alcohol to an alkyl bromide using triphenylphosphine and carbon tetrabromide.

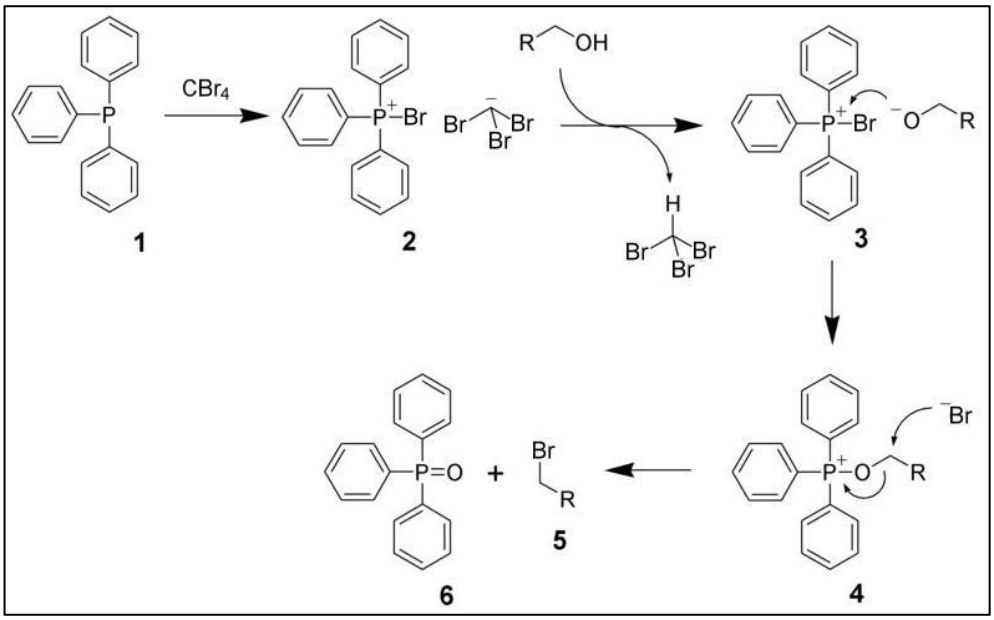

Figure 2.2 Conversion of alcohol to alkyl bromide in the Appel reaction (adapted from reference).[147]

The initial step is the formation of the phosphonium salt pair **2**. Deprotonation of an alcohol yields an alkoxide ion pair **3**. Nucleophilic substitution of the bromide by the alkoxide yields intermediate **4**. The bromide anion reacts *via* an S_N2 nucleophilic substitution forming the alkyl bromide **5** and the solid triphenylphosphine oxide **6** which phase separates from the reaction mixture.

(11) S-8-(4'-pentylbiphenyl-4-yloxy)octyl ethanethioate[9]

The base deprotonation of 4'-pentylbiphenyl-4-ol (3) was followed by an S_N2 electrophilic substitution with S-8-bromooctyl ethanethioate (10) in dimethylformamide *via* a Williamson ether synthesis.[140] The product (11) was obtained in good yield.

(12) 8-(4'-pentylbiphenyl-4-yloxy)octane-1-thiol

The acid hydrolysis of 11 was carried out to produce 5-(4'-pentylbiphenyl-4-yloxy)pentane-1-thiol.

2.2.3 Synthesis of 4-(4-propylcyclohexyl)phenol-based ligands

(15) (a) 1-(4-bromobutoxy)-4-(4-propylcyclohexyl)benzene, (b) 1-((6-bromohexyl)oxy)-4-(4-propylcyclohexyl)benzene, (c) 1-((8-bromooctyl)oxy)-4-(4-propylcyclohexyl)benzene[9]

The base deprotonation of 4-(4-propylcyclohexyl)phenol (13) was followed by an S_N2 electrophilic substitution with the appropriate dibromoalkane (14a, b, c) in dimethylformamide *via* a Williamson ether synthesis.[140] The product was obtained in good yield except in the case of b where yields were significantly lower.

(16) (a) S-(4-(4-(4-propylcyclohexyl)phenoxy)butyl) ethanethioate, (b) S-(6-(4-(4-propylcyclohexyl)phenoxy)hexyl) ethanethioate, (c) S-(8-(4-(4-propylcyclohexyl)phenoxy)octyl) ethanethioate[145]

The ethanethioate was synthesised in good yield *via* nucleophilic substitution of the bromide group of 15 with thioacetic acid. Again the yields were lower in the case of compounds b with a C_6 alky spacer.

(17) (a) 4-(4-(4-propylcyclohexyl)phenoxy)butane-1-thiol, (b) 6-(4-(4-propylcyclohexyl)phenoxy)hexane-1-thiol, (c) 8-(4-(4-propylcyclohexyl)phenoxy)octane-1-thiol

The acid hydrolysis of 16 was carried out to produce 17 in good yield (>90%).

2.3.4 Synthesis of 4-(4-pentylcyclohexyl)phenol-based ligands

(19) (a) 1-(4-bromobutoxy)-4-(4-pentylcyclohexyl)benzene, (b) 1-((6-bromohexyl)oxy)-4-(4-pentylcyclohexyl)benzene, (c) 1-((8-bromooctyl)oxy)-4-(4-pentylcyclohexyl)benzene[9]

The base deprotonation of 4-(4-hexylcyclohexyl)phenol (18) was followed by an S_N2 electrophilic substitution with the appropriate dibromoalkane (14a, b, c) in dimethylformamide *via* a Williamson ether synthesis.[140] The product was obtained in good yield except in the case of b where yields were significantly lower.

(20) (a) S-(4-(4-(4-pentylcyclohexyl)phenoxy)butyl) ethanethioate, (b) S-(6-(4-(4-pentylcyclohexyl)phenoxy)hexyl) ethanethioate, (c) S-(8-(4-(4-pentylcyclohexyl)phenoxy)octyl) ethanethioate[145]

The ethanethioate was synthesised in good yield *via* nucleophilic substitution of the bromide group of 19 with thioacetic acid. Again the yields were lower in the case of compounds b with a C_6 alky spacer.

(21) (a) 4-(4-(4-pentylcyclohexyl)phenoxy)butane-1-thiol, (b) 6-(4-(4-pentylcyclohexyl)phenoxy)hexane-1-thiol, (c) 8-(4-(4-pentylcyclohexyl)phenoxy)octane-1-thiol

The acid hydrolysis of 20 was carried out to produce 21 in good yield (>90%).

2.3 Reaction Schemes

2.3.1 Scheme 1 - Synthesis of 5-(4'-pentylbiphenyl-4-yloxy)pentane-1-thiol

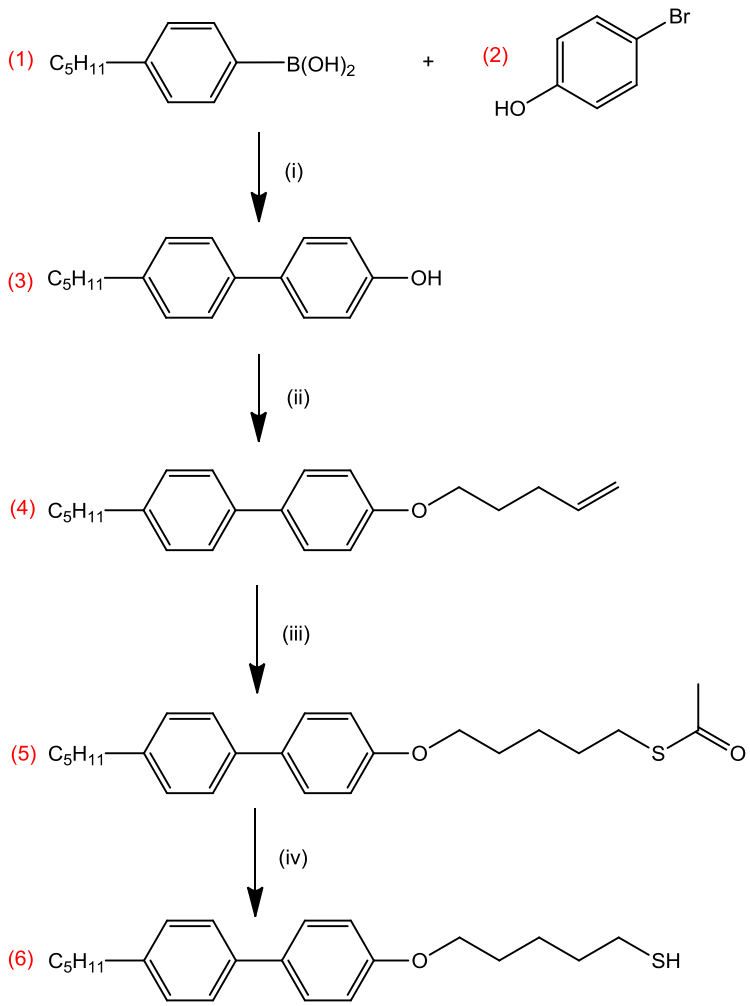

(i) 10% Pd/C, Na_2CO_3, EtOH:H_2O (1:1); (ii) 5-bromo-pent-1-ene, K_2CO_3, DMF; (iii) CH_3COSH, ABCN, THF; (iv) HCl, EtOH.

2.3.2 Scheme 2 - Synthesis of 8-(4'-pentylbiphenyl-4-yloxy)octane-1-thiol

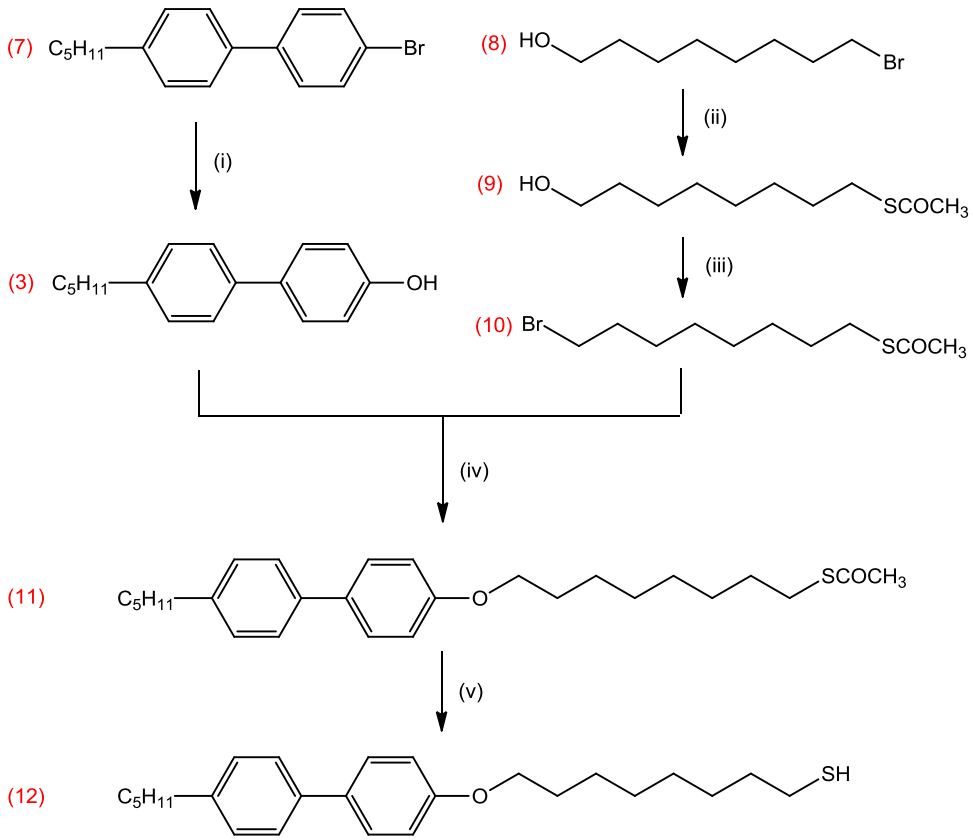

(i) *n*-BuLi, THF; $B(OCH_3)_3$; HCl; H_2O_2, ether; (ii) Et_3N, CH_3COSH, THF; (iii) CBr_4, PPh_3, DCM; (iv) K_2CO_3, DMF; (v) HCl, EtOH.

2.3.3 Scheme 3 - Synthesis of 4-(4-propylcyclohexyl)phenol-based ligands

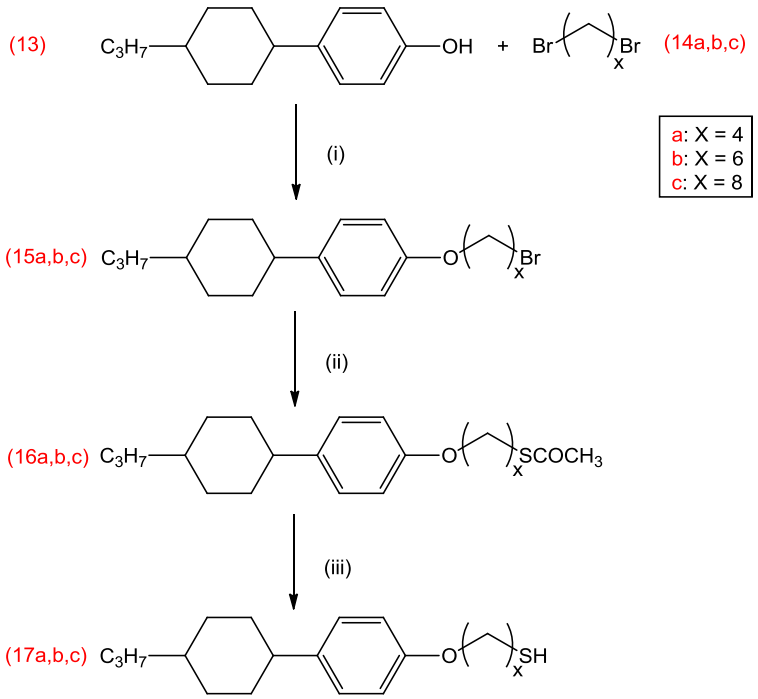

(i) K_2CO_3, Methyl ethyl ketone; (ii) Et_3N, CH_3COSH, THF; (iii) HCl, EtOH.

2.3.4 Scheme 4 - Synthesis of 4-(4-pentylcyclohexyl)phenol-based ligands

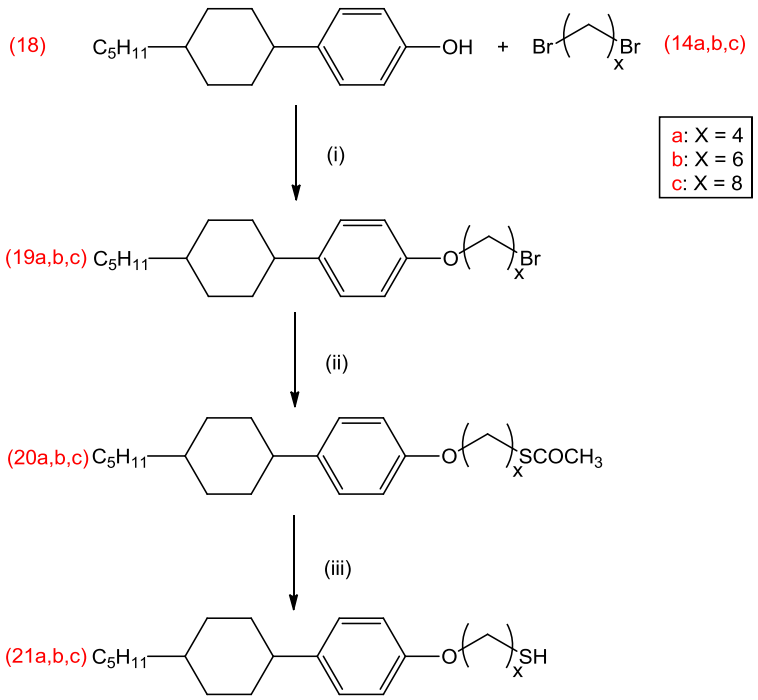

(i) K_2CO_3, Methyl ethyl ketone; (ii) Et_3N, CH_3COSH, THF; (iii) HCl, EtOH.

2.4 Synthetic procedures

2.4.1 Synthesis of 5-(4'-pentylbiphenyl-4-yloxy)pentane-1-thiol

(3) 4'-pentylbiphenyl-4-ol

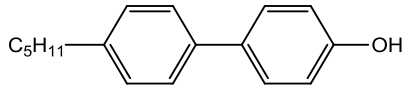

A mixture of 4-pentylphenylboronic acid (1) (5 g, 0.026 mol), 4-bromophenol (2) (6.12 g, 0.035 mol), sodium carbonate (4.60 g, 0.043 mol) and 10% palladium on activated carbon (0.46 g) was stirred in a 1:1 mixture of ethanol and water (120 mL) under air for 2 h at room temperature. The mixture was extracted with dichloromethane and filtered using a celite-packed sinter before washing with hexane followed by dichloromethane to yield a white crystalline solid (4.50 g, 65%).

Melting point: 126.0 – 128.0 °C

^{1}H NMR (400 MHz, $CDCl_3$) δ:

0.90 (3H, t, J = 7 Hz), 1.32 – 1.37 (2H, sext, J = 7 Hz), 1.32 – 1.37 (2H, quint, J = 7 Hz), 1.64 (2H, quint, J = 7 Hz), 2.63 (2H, t, J = 7 Hz), 6.89 (2H, d, J = 8.2 Hz), 7.23 (2H, t, J = 8.2 Hz), 7.42 – 7.48 (4H, m).

^{13}C NMR (100 MHz, $CDCl_3$) δ:

14.04 (1C, *CH_3*), 22.55 (1C, *CH_2*), 31.19 (1C, *CH_2*), 31.54 (1C, *CH_2*), 35.52 (1C, *CH_2*), 115.56 (2C, *Ar*), 126.52 (2C, *Ar*), 128.18 (2C, *Ar*), 128.76 (2C, *Ar*), 133.99 (1C, *Ar*), 138.04 (1C, *Ar*), 141.51 (1C, *Ar*), 154.77 (1C, *Ph*)

Combustion analysis:

Expected: C: 84.96%; H: 8.39%; O: 6.66%

Obtained: C: 84.52%; H: 8.12%; O: 6.44%

(4) 4-(pent-4-enyloxy)-4'-pentylbiphenyl

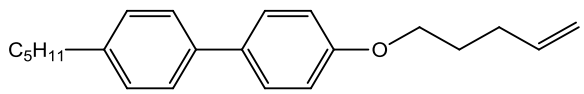

A solution of 4'-pentylbiphenyl-4-ol (3) (2.40 g, 0.01 mol) and potassium carbonate (2.07 g, 0.015 mol) in dimethylformamide (100 mL) was stirred under reflux for 2 h before the addition of 5-bromopent-1-ene (1.86 g, 0.148 mL, 0.0125 mol),after which the solution was stirred under reflux overnight. The mixture was allowed to cool to room temperature before removal of potassium carbonate *via* filtration and the addition of water (500 mL). The product was extracted into diethyl ether (3 x 100 mL) washed with brine (100 mL), dried over magnesium sulphate, and the solvent removed under reduced pressure. The crude product was purified *via* column chromatography (silica gel, ethyl acetate : hexane, 1 : 4) to yield a white crystalline solid (2.61 g, 85%).

Melting point: 88.0 – 89.0 °C

^{1}H NMR (400 MHz, $CDCl_3$) δ:

0.90 (3H, t, J = 7 Hz), 1.26 – 1.42 (2H, sext, J = 7 Hz), 1.26 – 1.42 (2H, quint, J = 7 Hz), 1.64 (2H, quint, J = 7 Hz), 1.90 (2H, quart, J = 7 Hz), 2.25 (2H, quint, J = 7 Hz), 4.00 (2H, t, J = 7 Hz), 5.04 (2H, d, J = 7 Hz), 5.87 (1H, quint, J = 6.60 Hz), 6.95 (2H, d, J = 8.2 Hz), 7.23 (2H, t, J = 8.2 Hz), 7.45 – 7.51 (4H, m).

Combustion analysis:

Expected: C: 85.66%; H: 9.15%; O: 5.19%

Obtained: C: 84.98%; H: 9.24%; O: 4.97%

(5) S-5-(4'-pentylbiphenyl-4-yloxy)pentyl ethanethioate

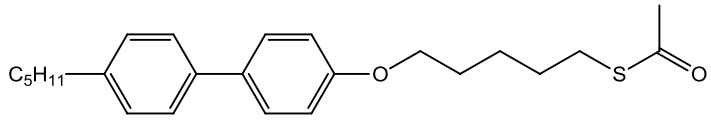

A solution of 4-(pent-4-enyloxy)-4'-pentylbiphenyl (4) (0.15 g, 0.5 mmol), thioacetic acid (0.05 mL, 0.6 mmol) and ABCN (0.025 g, 0.1 mmol) in dry tetrahydrofuran was stirred under reflux for 10 h. The solution was extracted with diethyl ether, washed with sodium carbonate and dried over magnesium sulphate before removal of solvent under reduced pressure. The crude product was purified *via* column chromatography (silica gel, ethyl acetate : hexane, 1 : 9) to yield a white crystalline solid (0.15 g, 79%).

Melting point: 64.2 - 64.8 °C

^{1}H NMR (400 MHz, $CDCl_3$) δ:

0.90 (3H, t, J = 7 Hz), 1.34 – 1.36 (2H, sext, J = 7 Hz), 1.34 – 1.36 (2H, quint, J = 7 Hz), 1.56 - 1.59 (2H, quint, J = 7 Hz), 1.56 - 1.59 (2H, quint, J = 7 Hz), 1.63 - 1.66 (2H, quint, J = 7 Hz), 1.80 - 1.84 (2H, t, J = 7 Hz), 2.33 (3H, s), 2.60 - 2.65 (2H, t, J = 7 Hz), 2.89 - 2.93 (2H, t, J = 7 Hz), 3.99 (2H, t, J = 6.8 Hz), 6.95 (2H, d, J = 8.2 Hz), 7.23 (2H, t, J = 8.2 Hz), 7.45 – 7.50 (4H, m).

Combustion analysis:

Expected: C: 74.95%; H: 8.39%; O: 8.32%; S: 8.34%

Obtained: C: 74.66%; H: 8.52%; O: 8.41%

(6) 5-(4'-pentylbiphenyl-4-yloxy)pentane-1-thiol

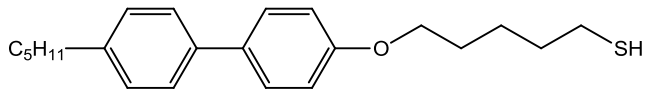

To a solution of S-5-(4'-pentylbiphenyl-4-yloxy)pentyl ethanethioate (5) (0.12 g, 0.3 mmol) in ethanol (50 mL) was added hydrochloric acid (2 mL, 36 %) and the mixture stirred under reflux in a nitrogen atmosphere for 5 h. The solution was extracted with diethyl ether, washed with sodium carbonate and dried over magnesium sulphate before removal of solvent under reduced pressure. The crude product was purified *via* column chromatography (silica gel, ethyl acetate : hexane, 1 : 9) to yield a white solid (0.097g, 94%).

Melting point: 99.2 - 102.1 °C

^{1}H NMR (400 MHz, $CDCl_3$) δ:

0.90 (3H, t, J = 7 Hz), 1.33 – 1.36 (2H, sext, J = 7 Hz), 1.33 – 1.36 (2H, quint, J = 7 Hz), 1.57 - 1.64 (2H, quint, J = 7 Hz), 1.57 - 1.64 (2H, quint, J = 7 Hz), 1.74 - 1.86 (2H, quint, J = 7 Hz), 2.60 - 2.64 (2H, t, J = 7 Hz), 2.71 - 2.75 (2H, t, J = 7 Hz), 3.99 (2H, t, J = 6.8 Hz), 6.95 (2H, d, J = 8.2 Hz), 7.23 (2H, t, J = 8.2 Hz), 7.45 – 7.50 (4H, m).

^{13}C NMR (100 MHz, $CDCl_3$) δ:

14.04 (1C, *CH_3*), 22.55 (1C, *CH_2*), 24.49 (1C, *CH_2*), 24.71 (1C, *CH*), 28.76 (1C, *CH_2*), 31.19 (1C, *CH_2*), 31.54 (1C, *CH_2*), 33.96 (1C, *CH_2*), 35.52 (1C, *CH_2*), 68.33 (1C, *O-CH_2*), 115.56 (2C, *Ar*), 126.52 (2C, *Ar*), 128.18 (2C, *Ar*), 128.76 (2C, *Ar*), 133.99 (1C, *Ar*), 138.04 (1C, *Ar*), 141.51 (1C, *Ar*), 157.54 (1C, *Ar-O*)

Combustion analysis:

Expected: C: 77.14%; H: 8.83%

Obtained: C: 76.94%; H: 8.88%

2.4.2 Synthesis of 8-(4'-pentylbiphenyl-4-yloxy)octane-1-thiol

(3) 4'-pentylbiphenyl-4-ol

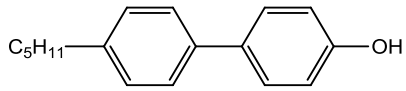

Under nitrogen, 4-bromo-4'-pentylbiphenyl (7) (10 g, 0.033 mol) was dissolved in dry tetrahydrofuran (150 mL) and stirred at -78°C; *n*-butyllithium (15.6 mL, 2.5 M in hexane, 0.039 mol) was added dropwise and the mixture stirred at -78 °C for 2 h. Trimethyl Borate (6.27 mL, 0.068 mol) was added and the reaction mixture allowed to reach room temperature overnight. The mixture was diluted with hydrochloric acid (100 mL, 10 %) and stirred for 30 min before extraction in diethyl ether. The crude product was used in the next reaction step.

Hydrogen peroxide (50 mL, 30% solution) and diethyl ether (75 mL) were added to 4'-pentylbiphenyl-4-ylboronic acid (4.025 g, 15 mmol) and the solution heated under gentle reflux for 3 h with vigorous stirring. The ether layer was separated and washed with saturated sodium metabisulphite solution (75 mL), dilute HCl (75 mL, 20 %) and water (75 mL), dried ($MgSO_4$) and concentrated under reduced pressure before purification *via* column chromatography (ethyl acetate : hexane, 1 : 4) to yield a white crystalline solid (2.56 g, 72%).

Melting point: 126.0 – 128.0 °C

^{1}H NMR (400MHz, $CDCl_3$) δ:

0.90 (3H, t, J = 7 Hz), 1.32 – 1.37 (2H, sext, J = 7 Hz), 1.32 – 1.37 (2H, quint, J = 7 Hz), 1.64 (2H, quint, J = 7 Hz), 2.63 (2H, t, J = 7 Hz), 6.89 (2H, d, J = 8.2 Hz), 7.23 (2H, t, J = 8.2 Hz), 7.42 – 7.48 (4H, m).

^{13}C NMR (100 MHz, $CDCl_3$) δ:

14.04 (1C, *CH_3*), 22.55 (1C, *CH_2*), 31.19 (1C, *CH_2*), 31.54 (1C, *CH_2*), 35.52 (1C, *CH_2*), 115.56 (2C, *Ar*), 126.52 (2C, *Ar*), 128.18 (2C, *Ar*), 128.76 (2C, *Ar*), 133.99 (1C, *Ar*), 138.04 (1C, *Ar*), 141.51 (1C, *Ar*), 154.77 (1C, *Ph*).

Combustion analysis:

Expected: C: 84.96%; H: 8.39%; O: 6.66%

Obtained: C: 84.52%; H: 8.12%; O: 6.44%

(9) S-8-hydroxyoctyl ethanethioate

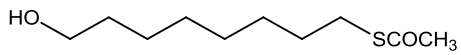

8-bromo-1-octanol (8) (3.0 mL, 0.017 mol), triethylamine (3.7 mL, 0.025 mol) and thioacetic acid (1.9 mL, 0.025 mol) were added to tetrahydrofuran (150 mL) and stirred for 15 h at room temperature. The crude product was diluted with water, extracted in ethyl acetate, washed with brine and then dried over magnesium sulphate. Purification was achieved *via* column chromatography (silica gel, ethyl acetate : hexane, 1 : 9) to yield a pale yellow oil (2.90 g, 84%).

^{1}H NMR (400 MHz, $CDCl_3$) δ:

1.32 - 1.35 (2H, quint, J = 7 Hz), 1.32 - 1.35 (2H, quint, J = 7 Hz), 1.49 - 1.56 (2H, quint, J = 7 Hz), 1.49 - 1.56 (2H, quint, J = 7 Hz), 1.49 - 1.56 (2H, quint, J = 7 Hz), 1.98 (2H, quint, 7 Hz), 2.31 (3H, s), 3.39 (2H, t, J = 6.8 Hz), 3.62 (2H, t, J = 6.8 Hz).

Combustion analysis:

Expected: C: 58.78%; H: 9.87%; O: 15.66%; S: 15.69%

Obtained: C: 59.02%; H: 9.53%; O: 15.21%

(10) S-8-bromooctyl ethanethioate

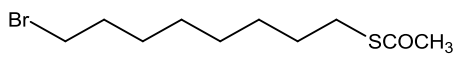

A mixture of S-8-hydroxyoctyl ethanethioate (9) (2.9 g, 0.0142 mol), and carbon tetrabromide (5.18 g, 0.0156 mol) in dichloromethane (50 ml) was cooled to 0 °C. Triphenylphosphine

(4.095 g, 0.0156 mol) was added over 30 min under vigorous stirring (1200 rpm), turning the solution from colourless to pale brown, then the mixture was stirred for 3 h at room temperature. The solvent was removed under reduced pressure and the mixture quickly added to stirred hexane (100 mL). Triphenylphosphine oxide formed as a white precipitate and was removed by filtration and the hexane removed under vacuum. Kugelrohr distillation (170 °C, 1.5 mmHg) yielded a clear, pale yellow oil (2.13 g, 56%).

^{1}H NMR (400 MHz, $CDCl_3$) δ:

1.32 - 1.35 (2H, quint, J = 7 Hz), 1.32 - 1.35 (2H, quint, J = 7 Hz), 1.49 - 1.56 (2H, quint, J = 7 Hz), 1.49 - 1.56 (2H, quint, J = 7 Hz), 1.49 - 1.56 (2H, quint, J = 7 Hz), 1.85 (2H, quint, J = 7 Hz), 2.31 (3H, s), 3.20 (2H, t, J = 6.8 Hz) 3.41 (2H, t, J = 6.8 Hz).

Combustion analysis:

Expected: C: 44.95%; H: 7.17%; O: 5.99%; S: 12.00%

Obtained: C: 45.12%; H: 7.03%; O: 5.91%

(11) S-8-(4'-pentylbiphenyl-4-yloxy)octyl ethanethioate

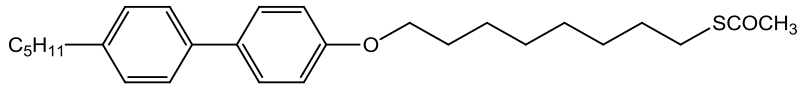

A solution of 4'-pentylbiphenyl-4-ol (3) (1.5 g, 6.24 mmol) and potassium carbonate (1.29 g, 9.36 mmol) in dimethylformamide (50 mL) was stirred under reflux conditions for 2 hours before the addition of S-8-bromooctyl ethanethioate (10) (1.85 g, 6.9 mmol) after which the solution was stirred under reflux overnight. The mixture was allowed to cool to room temperature before removal of potassium carbonate via filtration and the addition of water (250 mL). The product was extracted into diethyl ether (100 mL) washed with brine (100 mL), dried over magnesium sulphate, filtered and concentrated under reduced pressure. The crude product was purified *via* column chromatography (silica gel, ethyl acetate : hexane, 1 : 4) to yield a white crystalline solid (1.64 g, 61%).

Melting point: 69.6 - 71.1 °C

^{1}H NMR (400 MHz, $CDCl_3$) δ:

0.89 (3H, t, J= 7 Hz), 1.15 - 1.49 (2H, quint, J = 7 Hz), 1.15 - 1.49 (2H, quint, J = 7 Hz), 1.15 - 1.49 (2H, quint, J = 7 Hz), 1.15 - 1.49 (2H, quint, J = 7 Hz), 1.15 - 1.49 (2H, quint, J = 7 Hz), 1.15 - 1.49

(2H, quint, J = 7 Hz), 1.79 (2H, quint, J = 7 Hz), 1.90 - 1.96 (2H, quint, J = 7 Hz), 2.32 (3H, s), 2.71 (2H, t, J = 7 Hz), 3.30 (2H, t, J = 6.8 Hz), 3.98 (2H, t, J = 6.8 Hz), 6.91 - 6.94 (d, J = 8.2 Hz), 7.38 - 7.45 (4H, m), 7.98 - 8.01 (2H, m).

Combustion analysis:

Expected: C: 76.01%; H: 8.98%; O: 7.50% S: 7.52%

Obtained: C: 75.49%; H: 9.12%; O: 7.59%

(12) 8-(4'-pentylbiphenyl-4-yloxy)octane-1-thiol

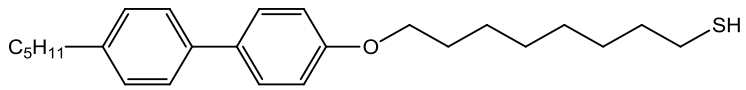

To a solution of S-8-(4'-pentylbiphenyl-4-yloxy)octyl ethanethioate (11) (1.0 g**,** 2.3 mmol) in ethanol (100 mL) was added hydrochloric acid (10 mL, 36%) and the mixture stirred under reflux in a nitrogen atmosphere for 5 h. The solution was extracted with diethyl ether, washed with sodium carbonate and dried over magnesium sulphate before removal of solvent under reduced pressure. The crude product was purified *via* column chromatography (silica gel, ethyl acetate : hexane, 1 : 9) to yield a white solid (0.80 g, 91%).

Melting point: 97.4 - 98.6 °C

^{1}H NMR (400 MHz, $CDCl_3$) δ:

0.89 (3H, t, J= 7 Hz), 1.15 - 1.49 (2H, quint, J = 7 Hz), 1.15 - 1.49 (2H, quint, J = 7 Hz), 1.15 - 1.49 (2H, quint, J = 7 Hz), 1.15 - 1.49 (2H, quint, J = 7 Hz), 1.15 - 1.49 (2H, quint, J = 7 Hz), 1.15 - 1.49 (2H, quint, J = 7 Hz), 1.79 (2H, quint, J = 7 Hz), 1.90 - 1.96 (2H, quint, J = 7 Hz), 2.71 (4H, m), 3.98 (2H, t, J = 6.8 Hz), 6.91 - 6.94 (d, J = 8.2 Hz), 7.38 - 7.45 (4H, m), 7.98 - 8.01 (2H, m).

^{13}C NMR (100 MHz, $CDCl_3$) δ:

14.04 (1C, *CH_3*), 22.55 (1C, *CH_2*), 24.10 (1C, *CH_2-SH*), 25.46 (1C, *CH_2*), 28.03 (1C, *CH_2*), 29.55 (2C, *CH_2*), 31.19 (1C, *CH_2*), 31.54 (1C, *CH_2*), 32.13 (1C, *CH_2*) 34.20 (1C, *CH_2*), 35.52 (1C, *CH_2*), 66.41 (1C, O-*CH_2*), 115.56 (2C, *Ar*), 126.52 (2C, *Ar*), 128.18 (2C, *Ar*), 128.76 (2C, *Ar*), 133.99 (1C, *Ar*), 138.04 (1C, *Ar*), 141.51 (1C, *Ar*), 154.77 (1C, *Ar-O*).

Combustion analysis:

Expected: C: 78.07%; H: 9.43%; O: 4.16%; S: 8.34%

Obtained: C: 77.83%; H: 9.55%; O: 4.19%

2.4.3 Synthesis of 4-(4-propylcyclohexyl)phenol-based ligands

For the synthesis of 4-(4-propylcyclohexyl)phenol- and 4-(4-pentylcyclohexyl)phenol-based ligands where no mass is specified in the synthetic procedure the reagents were used in the molar equivalents described.

15a, b, c

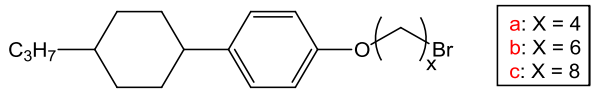

A solution of 4-(4-propylcyclohexyl)phenol (13) (2.00 g, 9.16 mmol) and potassium carbonate (2.53 g, 18.32 mmol) in methyl ethyl ketone (100 mL) was stirred at 80 °C under reflux for 2 h before the addition of dibromoalkane (14a, b, c) (27.48 mmol), after which the solution was stirred under reflux overnight. The mixture was allowed to cool to room temperature before removal of potassium carbonate via filtration and concentrated under reduced pressure. The crude product was purified *via* column chromatography (silica gel, ethyl acetate : hexane, 1 : 9) to yield 15a, b, c.

(15a) 1-(4-bromobutoxy)-4-(4-propylcyclohexyl)benzene

Yield: 2.20 g, 68%

Melting point: 53.9 °C

^{1}H NMR (400 MHz, $CDCl_3$) δ:

0.90 (3H, t, J = 7 Hz), 1.04 (2H, sext, J = 7 Hz), 1.19 - 1.45 (2H, quint, J = 7 Hz), 1.19 - 1.45 (4H, m), 1.79 - 1.94 (4H, m), 1.79 - 1.94 (1H, sept, J = 6.8 Hz), 2.01 - 2.06 (2H, quint, J = 7 Hz), 2.01 - 2.06 (2H, quint, J = 7 Hz), 2.40 (1H, quint, J = 6.8 Hz), 3.48 (2H, t, J = 6.8 Hz), 3.96 (2H, t, J = 6.8 Hz), 6.80 - 6.82 (2H, d, J = 8.2 Hz), 7.10 - 7.12 (2H, d, J = 8.2 Hz).

Combustion analysis:

Expected: C: 64.59%; H: 8.27%; O: 4.53%

Obtained: C: 64.49%; H: 8.43%

(15b) 1-((6-bromohexyl)oxy)-4-(4-propylcyclohexyl)benzene

Yield: 0.89 g, 26%

Melting point: 111.4 °C

^{1}H NMR (400 MHz, $CDCl_3$) δ:

0.90 (3H, t, J = 7 Hz), 1.04 (2H, sext, J = 7 Hz), 1.19 - 1.48 (9H, m), 1.73 - 1.89 (10H, m), 2.40 (1H, quint, J = 6.8 Hz), 3.39 (2H, t, J = 6.8 Hz), 3.93 (2H, t, J = 6.8 Hz), 6.79 - 6.81 (2H, d, J = 8.2 Hz), 7.09 - 7.11 (2H, d, J = 8.2 Hz).

Combustion analysis:

Expected: C: 66.13%; H: 8.72%; O: 4.20%

Obtained: C: 67.41%; H: 9.05%

(15c) 1-((8-bromooctyl)oxy)-4-(4-propylcyclohexyl)benzene

Yield: 2.14 g, 57%

Melting point: 40.3 °C

^{1}H NMR (400 MHz, $CDCl_3$) δ:

0.90 (3H, t, J = 7 Hz), 1.04 (2H, sext, J = 7 Hz), 1.19 - 1.45 (16H, m), 1.74 - 1.89 (8H, m), 2.40 (1H, quint, J = 6.8 Hz), 3.41 (2H, t, J = 6.8 Hz), 3.92 (2H, t, J = 6.8 Hz), 6.80 - 6.82 (2H, d, J = 8.2 Hz), 7.10 - 7.12 (2H, d, J = 8.2 Hz).

Combustion analysis:

Expected: C: 67.47%; H: 9.11%; O: 3.91%

Obtained: C: 66.55%; H: 9.04%

16a, b, c

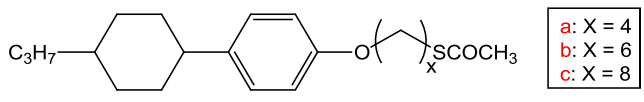

15a, b, c (0.017 mol), triethylamine (3.7 mL, 0.025 mol) and thioacetic acid (1.9 mL, 0.025 mol) were added to tetrahydrofuran (100 mL) and stirred for 15 h at room temperature. The crude product was diluted with water, extracted in ethyl acetate, washed with brine and then dried

over magnesium sulphate. Purification was achieved *via* column chromatography (silica gel, ethyl acetate : hexane, 1 : 9)

(16a) S-(4-(4-(4-propylcyclohexyl)phenoxy)butyl) ethanethioate

Yield: 1.42 g, 85%

Melting point: 47.2 °C

^{1}H NMR (400 MHz, $CDCl_3$) δ:

0.90 (3H, t, J = 7 Hz), 1.04 (2H, sext, J = 7 Hz), 1.19 - 1.45 (2H, quint, J = 7 Hz), 1.19 - 1.45 (4H, m), 1.79 - 1.94 (4H, m), 1.79 - 1.94 (2H, sept, J = 6.8 Hz), 2.01 - 2.06 (2H, quint, J = 7 Hz), 2.01 - 2.06 (2H, quint, J = 7 Hz), 2.30 (3H, s), 2.40 (1H, quint, J = 6.8 Hz), 2.96 (2H, t, J = 6.8 Hz), 3.96 (2H, t, J = 6.8 Hz), 6.80 - 6.82 (2H, d, J = 8.2 Hz), 7.10 - 7.12 (2H, d, J = 8.2 Hz).

Combustion analysis:

Expected: C: 72.37%; H: 9.25%; O: 9.18%; S: 9.20%

Obtained: C: 71.96%; H: 10.03%

(16b) S-(6-(4-(4-propylcyclohexyl)phenoxy)hexyl) ethanethioate

Yield: 0.25 g, 51%

Melting point: 87.8 °C

^{1}H NMR (400 MHz, $CDCl_3$) δ:

0.89 (3H, t, J = 7 Hz), 1.04 (2H, sext, J = 7 Hz), 1.19 - 1.45 (2H, quint, J = 7 Hz), 1.19 - 1.45 (2H, quint, J = 7 Hz), 1.19 - 1.45 (2H, quint, J = 7 Hz), 1.19 - 1.45 (4H, m), 1.76 - 1.89 (4H, m), 1.76 - 1.89 (2H, sept, J = 6.8 Hz), 1.76 - 1.89 (2H, quint, J = 7 Hz), 1.76 - 1.89 (2H, quint, J = 7 Hz), 2.30 (3H, s), 2.40 (1H, quint, J = 6.8 Hz), 2.88 (2H, t, J = 6.8 Hz), 3.91 (2H, t, J = 6.8 Hz), 6.79 - 6.81 (2H, d, J = 8.2 Hz), 7.08 - 7.10 (2H, d, J = 8.2 Hz).

Combustion analysis:

Expected: C: 73.35%; H: 9.64%; O: 8.50%; S: 8.51%

Obtained: C: 72.96%; H: 9.88%

(16c) S-(8-(4-(4-propylcyclohexyl)phenoxy)octyl) ethanethioate

Yield: 1.63 g, 83%

Melting point: 76.9 °C

^{1}H NMR (400 MHz, $CDCl_3$) δ:

0.88 (3H, t, J = 7 Hz), 1.04 (2H, sext, J = 7 Hz), 1.19 - 1.88 (23H, m), 2.28 (3H, s), 2.39 (1H, quint, J = 6.8 Hz), 2.84 (2H, t, J = 6.8 Hz), 3.88 (2H, t, J = 6.8 Hz), 6.78 - 6.80 (2H, d, J = 8.2 Hz), 7.07 - 7.09 (2H, d, J = 8.2 Hz).

Combustion analysis:

Expected: C: 74.20%; H: 9.96%; O: 7.91%; S: 7.92%

Obtained: C: 74.05%; H: 9.99%; O: 8.03

17a, b, c

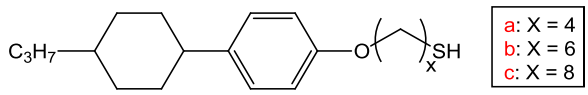

To a solution of 16a, b, c (3.16 mmol) in ethanol (100 mL) was added hydrochloric acid (20 mL, 36 %) and the mixture stirred under reflux in a nitrogen atmosphere for 5 h. The solution was extracted with diethyl ether, washed with sodium carbonate and dried over magnesium sulphate before removal of solvent under reduced pressure. The crude product was purified *via* column chromatography (silica gel, ethyl acetate : hexane, 1 : 9) to yield 17a, b, c.

(17a) 4-(4-(4-propylcyclohexyl)phenoxy)butane-1-thiol

Yield: 0.9 g, 93%

Melting point: 44.8 °C

^{1}H NMR (400 MHz, $CDCl_3$) δ:

0.90 (3H, t, J = 7 Hz), 1.04 (2H, sext, J = 7 Hz), 1.19 - 1.45 (2H, quint, J = 7 Hz), 1.19 - 1.45 (4H, m), 1.79 - 1.94 (5H, m), 1.79 - 1.94 (2H, sept, J = 6.8 Hz), 2.01 - 2.06 (2H, quint, J = 7 Hz), 2.01 -

2.06 (2H, quint, J = 7 Hz), 2.40 (1H, quint, J = 6.8 Hz), 2.60 (2H, quart, J = 6.8 Hz), 3.95 (2H, t, J = 6.8 Hz), 6.80 - 6.82 (2H, d, J = 8.2 Hz), 7.10 - 7.12 (2H, d, J = 8.2 Hz).

^{13}C NMR (100 MHz, $CDCl_3$) δ:

14.40 (1C, *CH_3*), 20.03 (1C, *CH_2*), 24.42 (1C, *CH_2*), 28.06 (1C, *CH_2*), 30.67 (1C, *CH_2*), 33.61 (2C, *2xCH_2*), 34.57 (2C, *2xCH_2*), 37.02 (1C, *CH*), 39.73 (1C, *CH_2*), 43.72 (1C, *Ar-CH*), 67.21 (1C, *O-CH_2*), 114.20 (2C, *Ar*), 127.62 (2C, *Ar*), 140.15 (1C, *Ar*), 157.00 (1C, *Ar-O*).

Combustion analysis:

Expected: C: 74.45%; H: 9.87%; O: 5.22%; S: 10.46%

Obtained: C: 74.24%; H: 9.99%

(17b) 6-(4-(4-propylcyclohexyl)phenoxy)hexane-1-thiol

Yield: 0.1 g, 11 %

Melting point: 104-105 °C

^{1}H NMR (400 MHz, $CDCl_3$) δ:

0.89 (3H, t, J = 7 Hz), 1.04 (2H, sext, J = 7 Hz), 1.19 - 1.45 (2H, quint, J = 7 Hz), 1.19 - 1.45 (2H, quint, J = 7 Hz), 1.19 - 1.45 (2H, quint, J = 7 Hz), 1.19 - 1.45 (4H, m), 1.76 - 1.89 (4H, m), 1.76 - 1.89 (2H, sept, J = 6.8 Hz), 1.76 - 1.89 (2H, quint, J = 7 Hz), 1.76 - 1.89 (2H, quint, J = 7 Hz), 2.40 (1H, quint, J = 6.8 Hz), 2.52 (2H, quart, J = 6.8 Hz), 3.91 (2H, t, J = 6.8 Hz), 6.79 - 6.81 (2H, d, J = 8.2 Hz), 7.08 - 7.10 (2H, d, J = 8.2 Hz).

^{13}C NMR (100 MHz, $CDCl_3$) δ:

14.40 (1C, *CH_3*), 20.03 (1C, *CH_2*), 24.42 (1C, *CH_2*), 28.06 (1C, *CH_2*), 28.25 (1C, *CH_2*), 29.21 (1C, *CH_2*), 30.67 (1C, *CH_2*), 33.61 (2C, *2xCH_2*), 34.57 (2C, *2xCH_2*), 37.02 (1C, *CH*), 39.73 (1C, *CH_2*), 43.72 (1C, *Ar-CH*), 67.21 (1C, *O-CH_2*), 114.20 (2C, *Ar*), 127.62 (2C, *Ar*), 140.15 (1C, *Ar*), 157.00 (1C, *Ar-O*).

Combustion analysis:

Expected: C: 75.39%; H: 10.24%; O: 4.78%; S: 9.58%

Obtained: C: 75.14%; H: 10.33%

(17c) 8-(4-(4-propylcyclohexyl)phenoxy)octane-1-thiol

Yield: 0.50 g, 87%

Melting point: 86.4-87.9 °C

^{1}H NMR (400 MHz, $CDCl_3$) δ:

0.90 (3H, t, J = 7 Hz), 1.04 (2H, sext, J = 7 Hz), 1.19 - 1.45 (2H, quint, J = 7 Hz), 1.19 - 1.45 (2H, quint, J = 7 Hz), 1.19 - 1.45 (2H, quint, J = 7 Hz), 1.19 - 1.45 (2H, quint, J = 7 Hz), 1.19 - 1.45 (2H, quint, J = 7 Hz), 1.19 - 1.45 (4H, m), 1.79 - 1.94 (5H, m), 1.79 - 1.94 (2H, sept, J = 6.8 Hz), 2.01 - 2.06 (2H, quint, J = 7 Hz), 2.01 - 2.06 (2H, quint, J = 7 Hz), 2.40 (1H, quint, J = 6.8 Hz), 2.51 (2H, quart, J = 6.8 Hz), 3.91 (2H, t, J = 6.8 Hz), 6.80 - 6.82 (2H, d, J = 8.2 Hz), 7.09 - 7.11 (2H, d, J = 8.2 Hz).

^{13}C NMR (100 MHz, $CDCl_3$) δ:

14.40 (1C, *CH_3*), 20.00 (1C, *CH_2*), 24.57 (1C, *CH_2*), 25.98 (1C, *CH_2*), 28.06 (1C, *CH_2*), 28.25 (1C, *CH_2*), 28.96 (1C, *CH_2*), 29.21 (1C, *CH_2*), 30.67 (1C, *CH_2*), 33.61 (2C, *2xCH_2*), 34.57 (2C, *2xCH_2*), 37.02 (1C, *CH*), 39.73 (1C, *CH_2*), 43.72 (1C, *Ar-CH*), 67.21 (1C, *O-CH_2*), 114.20 (2C, *Ar*), 127.62 (2C, *Ar*), 140.15 (1C, *Ar*), 157.00 (1C, *Ar-O*).

Combustion analysis:

Expected: C: 76.18%; H: 10.56%; O: 4.41%; S: 8.84%

Obtained: C: 75.55%; H: 11.02%; S: 9.51%

2.4.4 Synthesis of 4-(4-pentylcyclohexyl)phenol-based ligands

19a, b, c

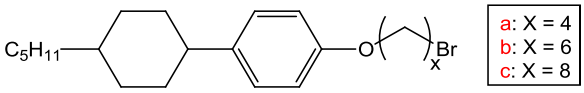

A solution of 4-(4-pentylcyclohexyl)phenol (18) (2.50 g, 10.15 mmol) and potassium carbonate (2.80 g, 20.30 mmol) in methyl ethyl ketone (100 mL) was stirred at 80 °C under reflux for 2 h before the addition of dibromoalkane (14a, b, c) (30.44 mmol), after which the solution was stirred under reflux overnight. The mixture was allowed to cool to room temperature before removal of potassium carbonate via filtration and concentrated under reduced pressure. The crude product was purified via column chromatography (silica gel, ethyl acetate : hexane, 1 : 9) to yield 19a, b, c.

(19a) 1-(4-bromobutoxy)-4-(4-pentylcyclohexyl)benzene

Yield: 2.03 g, 52%

Melting point: 52.9 °C

^{1}H NMR (400 MHz, $CDCl_3$) δ:

0.89 (3H, t, J = 7 Hz), 1.04 (2H, quint, J = 7 Hz), 1.19 - 1.45 (2H, sext, J = 7 Hz), 1.19 - 1.45 (2H, quint, J = 7 Hz), 1.19 - 1.45 (2H, quint, J = 7 Hz), 1.19 - 1.45 (5H, m), 1.84 - 1.94 (2H, quint, J = 7 Hz), 1.84 - 1.94 (4H, m), 2.06 (2H, quint, J = 7 Hz), 2.40 (1H, quint, J = 6.8 Hz), 3.48 (2H, t, J = 6.8 Hz), 3.96 (2H, t, J = 6.8 Hz), 6.80 - 6.82 (2H, d, J = 8.2 Hz), 7.10 - 7.12 (2H, d, J = 8.2 Hz).

Combustion analysis:

Expected: C: 66.13%; H: 8.72%; O: 4.20%

Obtained: C: 66.02%; H: 8.84%

(19b) 1-((6-bromohexyl)oxy)-4-(4-pentylcyclohexyl)benzene

Yield: 0.33 g, 8%

Melting point: 123-125 °C

^{1}H NMR (400 MHz, $CDCl_3$) δ:

0.89 (3H, t, J = 7 Hz), 1.04 (2H, quint, J = 7 Hz), 1.19 - 1.45 (2H, sext, J = 7 Hz), 1.19 - 1.45 (2H, quint, J = 7 Hz), 1.19 - 1.45 (2H, quint, J = 7 Hz), 1.19 - 1.45 (2H, quint, J = 7 Hz), 1.19 - 1.45 (2H, quint, J = 7 Hz), 1.19 - 1.45 (5H, m), 1.79 - 1.86 (2H, quint, J = 7 Hz), 1.79 - 1.86 (6H, m), 2.40 (1H, quint, J = 6.8 Hz), 3.42 (2H, t, J = 6.8 Hz), 3.94 (2H, t, J = 6.8 Hz), 6.81 - 6.83 (2H, d, J = 8.2 Hz), 7.10 - 7.12 (2H, d, J = 8.2 Hz).

Combustion analysis:

Expected: C: 67.47%; H: 9.11%; O: 3.91%

Obtained: C: 67.11%; H: 9.43%

(19c) 1-((8-bromooctyl)oxy)-4-(4-pentylcyclohexyl)benzene

Yield: 2.43 g, 59%

Melting point: 45.1 °C

^{1}H NMR (400 MHz, $CDCl_3$) δ:

0.89 (3H, t, J = 7 Hz), 1.04 (2H, quint, J = 7 Hz), 1.19 - 1.45 (2H, sext, J = 7 Hz), 1.19 - 1.45 (2H, quint, J = 7 Hz), 1.19 - 1.45 (2H, quint, J = 7 Hz), 1.19 - 1.45 (2H, quint, J = 7 Hz), 1.19 - 1.45 (2H, quint, J = 7 Hz), 1.19 - 1.45 (2H, quint, J = 7 Hz), 1.19 - 1.45 (5H, m), 1.79 - 1.86 (2H, quint, J = 7 Hz), 1.79 - 1.86 (6H, m), 2.40 (1H, quint, J = 6.8 Hz), 3.42 (2H, t, J = 6.8 Hz), 3.94 (2H, t, J = 6.8 Hz), 6.81 - 6.83 (2H, d, J = 8.2 Hz), 7.10 - 7.12 (2H, d, J = 8.2 Hz).

Combustion analysis:

Expected: C: 68.63%; H: 9.45%; O: 3.66%

Obtained: C: 68.55%; H: 9.49%

20a, b, c

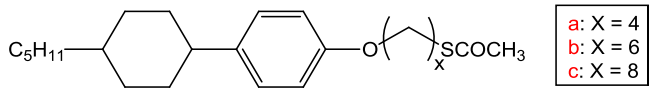

19a, b, c (0.017 mol), triethylamine (3.7 mL, 0.025 mol) and thioacetic acid (1.9 mL, 0.025 mol) were added to tetrahydrofuran (100 mL) and stirred for 15 h at room temperature. The crude product was diluted with water, extracted in ethyl acetate, washed with brine and then dried

over magnesium sulphate. Purification was achieved via column chromatography (silica gel, ethyl acetate : hexane, 1 : 9).

(20a) S-(4-(4-(4-pentylcyclohexyl)phenoxy)butyl) ethanethioate

Yield: 1.55 g, 87%

Melting point: 49.1 °C

^{1}H NMR (400 MHz, $CDCl_3$) δ:

0.89 (3H, t, J = 7 Hz), 1.04 (2H, quint, J = 7 Hz), 1.19 - 1.45 (2H, sext, J = 7 Hz), 1.19 - 1.45 (2H, quint, J = 7 Hz), 1.19 - 1.45 (2H, quint, J = 7 Hz), 1.19 - 1.45 (5H, m), 1.84 - 1.94 (2H, quint, J = 7 Hz), 1.84 - 1.94 (4H, m), 2.06 (2H, quint, J = 7 Hz), 2.30 (3H, s), 2.40 (1H, quint, J = 6.8 Hz), 2.92 (2H, t, J = 6.8 Hz), 3.96 (2H, t, J = 6.8 Hz), 6.80 - 6.82 (2H, d, J = 8.2 Hz), 7.10 - 7.12 (2H, d, J = 8.2 Hz).

Combustion analysis:

Expected: C: 73.35%; H: 9.64%; O: 8.50%; S: 8.51%

Obtained: C: 73.30%; H: 9.73%; S: 8.30%

(20b) S-(6-(4-(4-pentylcyclohexyl)phenoxy)hexyl) ethanethioate

Yield: 0.08 g, 27%

Melting point: 112-114 °C

^{1}H NMR (400 MHz, $CDCl_3$) δ:

0.89 (3H, t, J = 7 Hz), 1.04 (2H, quint, J = 7 Hz), 1.19 - 1.45 (2H, sext, J = 7 Hz), 1.19 - 1.45 (2H, quint, J = 7 Hz), 1.19 - 1.45 (2H, quint, J = 7 Hz), 1.19 - 1.45 (2H, quint, J = 7 Hz), 1.19 - 1.45 (2H, quint, J = 7 Hz), 1.19 - 1.45 (5H, m), 1.84 - 1.94 (2H, quint, J = 7 Hz), 1.84 - 1.94 (4H, m), 2.06 (2H, quint, J = 7 Hz), 2.32 (3H, s), 2.40 (1H, quint, J = 6.8 Hz), 2.87 (2H, t, J = 6.8 Hz), 3.92 (2H, t, J = 6.8 Hz), 6.80 - 6.82 (2H, d, J = 8.2 Hz), 7.10 - 7.12 (2H, d, J = 8.2 Hz).

Combustion analysis:

Expected: C: 74.20%; H: 9.96%; O: 7.91%; S: 7.92%

Obtained: C:74.08%; H: 10.04%

(20c) S-(8-(4-(4-pentylcyclohexyl)phenoxy)octyl) ethanethioate

Yield: 1.61 g, 84%

Melting point: 38.3 °C

^{1}H NMR (400 MHz, $CDCl_3$) δ:

0.89 (3H, t, J = 7 Hz), 1.04 (2H, quint, J = 7 Hz), 1.19 - 1.45 (2H, sext, J = 7 Hz), 1.19 - 1.45 (2H, quint, J = 7 Hz), 1.19 - 1.45 (2H, quint, J = 7 Hz), 1.19 - 1.45 (2H, quint, J = 7 Hz), 1.19 - 1.45 (2H, quint, J = 7 Hz), 1.19 - 1.45 (2H, quint, J = 7 Hz), 1.19 - 1.45 (5H, m), 1.84 - 1.94 (2H, quint, J = 7 Hz), 1.84 - 1.94 (4H, m), 2.06 (2H, quint, J = 7 Hz), 2.30 (3H, s), 2.40 (1H, quint, J = 6.8 Hz), 2.92 (2H, t, J = 6.8 Hz), 3.96 (2H, t, J = 6.8 Hz), 6.80 - 6.82 (2H, d, J = 8.2 Hz), 7.10 - 7.12 (2H, d, J = 8.2 Hz).

Combustion analysis:

Expected: C: 74.95%; H: 10.25%; O: 7.40%; S: 7.41%

Obtained: C: 74.79%; H: 10.33%; O: 7.52%

21(a, b, c)

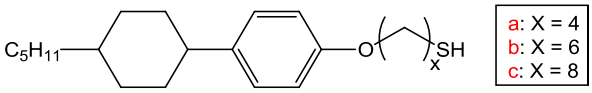

a: X = 4
b: X = 6
c: X = 8

To a solution of 20a, b, c (3.16 mmol) in ethanol (100 mL) was added hydrochloric acid (20 mL, 36 %) and the mixture stirred under reflux in a nitrogen atmosphere for 5 h. The solution was extracted with diethyl ether, washed with sodium carbonate and dried over magnesium sulphate before removal of solvent under reduced pressure. The crude product was purified via column chromatography (silica gel, ethyl acetate : hexane, 1 : 9) to yield 21a, b, c.

(21a) 4-(4-(4-pentylcyclohexyl)phenoxy)butane-1-thiol

Yield: 1.99 g, 93%

Melting point: 39.9 °C

^{1}H NMR (400 MHz, $CDCl_3$) δ:

0.89 (3H, t, J = 7 Hz), 1.04 (2H, quint, J = 7 Hz), 1.19 - 1.45 (2H, sext, J = 7 Hz), 1.19 - 1.45 (2H, quint, J = 7 Hz), 1.19 - 1.45 (2H, quint, J = 7 Hz), 1.19 - 1.45 (5H, m), 1.84 - 1.94 (2H, quint, J = 7 Hz), 1.84 - 1.94 (4H, m), 2.06 (2H, quint, J = 7 Hz), 2.40 (1H, quint, J = 6.8 Hz), 2.61 (2H, quart, J = 6.8 Hz), 3.96 (2H, t, J = 6.8 Hz), 6.80 - 6.82 (2H, d, J = 8.2 Hz), 7.10 - 7.12 (2H, d, J = 8.2 Hz).

^{13}C NMR (100 MHz, $CDCl_3$) δ:

14.11 (1C, *CH_3*), 22.70 (1C, *CH_2*), 24.42 (1C, *CH_2*), 26.65 (1C, *CH_2*), 28.05 (1C, *CH_2*), 30.67 (1C, *CH_2*), 32.21 (1C, *CH_2*), 33.65 (2C, *2xCH_2*), 34.57 (2C, *2xCH_2*), 37.31 (1C, *CH*), 37.40 (1C, *CH_2*), 43.72 (1C, *Ar-CH*), 67.21 (1C, *O-CH_2*), 114.20 (2C, *Ar*), 127.62 (2C, *Ar*), 140.15 (1C, *Ar*), 157.00 (1C, *Ar-O*).

Combustion analysis:

Expected: C: 75.39%; H: 10.24%; O: 4.78%; S: 9.58%

Obtained: C: 75.53%; H: 10.86%; S: 9.00%

(21b) 6-(4-(4-pentylcyclohexyl)phenoxy)hexane-1-thiol

Yield: 0.05 g, 71%

Melting point: 96.8-98.2 °C

^{1}H NMR (400 MHz, $CDCl_3$) δ:

0.89 (3H, t, J = 7 Hz), 1.04 (2H, quint, J = 7 Hz), 1.19 - 1.45 (2H, sext, J = 7 Hz), 1.19 - 1.45 (2H, quint, J = 7 Hz), 1.19 - 1.45 (2H, quint, J = 7 Hz), 1.19 - 1.45 (9H, m), 1.84 - 1.94 (2H, quint, J = 7 Hz), 1.84 - 1.94 (4H, m), 2.06 (2H, quint, J = 7 Hz), 2.40 (1H, quint, J = 6.8 Hz), 2.55 (2H, quart, J = 6.8 Hz), 3.92 (2H, t, J = 6.8 Hz), 6.80 - 6.82 (2H, d, J = 8.2 Hz), 7.10 - 7.12 (2H, d, J = 8.2 Hz).

^{13}C NMR (100 MHz, $CDCl_3$) δ:

14.11 (1C, *CH_3*), 22.70 (1C, *CH_2*), 24.42 (1C, *CH_2*), 26.65 (1C, *CH_2*), 28.05 (1C, *CH_2*), 29.24 (1C, *CH_2*), 32.20 (1C, *CH_2*), 33.65 (2C, *2xCH_2*), 34.57 (2C, *2xCH_2*), 37.31 (1C, *CH*), 37.40 (1C, *CH_2*), 43.72 (1C, *Ar-CH*), 67.21 (1C, *O-CH_2*), 114.20 (2C, *Ar*), 127.62 (2C, *Ar*), 140.15 (1C, *Ar*), 157.00 (1C, *Ar-O*).

Combustion analysis:

Expected: C: 76.18%; H: 10.56%; O: 4.41%; S: 8.84%

Obtained: C: 76.01%; H: 10.79%

(21c) 8-(4-(4-pentylcyclohexyl)phenoxy)octane-1-thiol

Yield: 0.74 g, 91%

Melting point: 38.4 °C

^{1}H NMR (400 MHz, $CDCl_3$) δ:

0.89 (3H, t, J = 7 Hz), 1.04 (2H, quint, J = 7 Hz), 1.19 - 1.45 (2H, sext, J = 7 Hz), 1.19 - 1.45 (2H, quint, J = 7 Hz), 1.19 - 1.45 (2H, quint, J = 7 Hz), 1.19 - 1.45 (2H, quint, J = 7 Hz), 1.19 - 1.45 (2H, quint, J = 7 Hz), 1.19 - 1.45 (2H, quint, J = 7 Hz), 1.19 - 1.45 (2H, quint, J = 7 Hz), 1.19 - 1.45 (5H, m), 1.84 - 1.94 (2H, quint, J = 7 Hz), 1.84 - 1.94 (4H, m), 2.06 (2H, quint, J = 7 Hz), 2.40 (1H, quint, J = 6.8 Hz), 2.55 (2H, quart, J = 6.8 Hz), 3.94 (2H, t, J = 6.8 Hz), 6.81 - 6.83 (2H, d, J = 8.2 Hz), 7.10 - 7.12 (2H, d, J = 8.2 Hz).

^{13}C NMR (100 MHz, $CDCl_3$) δ:

14.11 (1C, *CH_3*), 22.70 (1C, *CH_2*), 24.42 (1C, *CH_2*), 26.65 (1C, *CH_2*), 28.05 (1C, *CH_2*), 28.92 (1C, *CH_2*), 29.24 (1C, *CH_2*), 30.67 (1C, *CH_2*), 32.20 (1C, *CH_2*), 33.65 (2C, *2xCH_2*), 34.57 (2C, *2xCH_2*), 37.31 (1C, *CH*), 37.40 (1C, *CH_2*), 43.72 (1C, *Ar-CH*), 67.21 (1C, *O-CH_2*), 114.20 (2C, *Ar*), 127.62 (2C, *Ar*), 140.15 (1C, *Ar*), 157.00 (1C, *Ar-O*).

Combustion analysis:

Expected: C: 76.86%; H: 10.84%; O: 4.10%; S: 8.21%

Obtained: C: 76.63%; H: 11.05%; S: 8.48%

2.5 Gold Nanorods

2.5.1 Synthesis of Gold Nanorods

Method 1 (AuS1)

The seed-mediated synthesis of gold nanorods as performed by Murphy *et al.*[43] was carried out:

A seed solution was prepared by adding aqueous hydrogen tetrachloroaurate (1 mL, 0.01 M) and sodium citrate (1 mL, 0.01 M) to water (36 mL) and stirring. Freshly prepared aqueous sodium borohydride (1 mL, 0.1 M) was added, causing a colour change from colourless to orange, and the solution was left undisturbed for 2 then used within 2-6 hours of production. Growth solutions A and B were prepared, consisting of aqueous CTAB (18 mL, 0.1 M), hydrogen tetrachloroaurate (0.5 mL, 0.01 M), ascorbic acid (100 µL, 0.1 M) and sodium hydroxide (100 µL, 0.1 M). Growth solution C was prepared, consisting of aqueous CTAB (180 mL, 0.1 M), hydrogen tetrachloroaurate (5 mL, 0.01 M), ascorbic acid (1 mL, 0.1 M) and sodium hydroxide (1 mL, 0.1 M).

Seed solution (2 mL) was added to solution A and shaken for 4 s and then 2 mL of A was added to B and shaken for a further 4 s. All of solution B was added to solution C, causing a colour change from colourless to reddish-brown, and the solution was left to sit overnight. Separation of nanorods from spherical nanoparticles was attempted *via* centrifugation (1500 rpm, 20 min); however, the resulting solutions were dominated by CTAB precipitate.

UV-vis absorbance: 539.14 nm (TPB), 726.52 nm (LPB), $A_{LPB}/A_{TPB} = 0.18$

Method 2 (AuS2)

The scaled up adaptation of the above synthesis, as performed by Zubarev *et al.* was carried out:[53]

A seed solution was prepared by adding sodium citrate (1.47 mg, 5.70 µmol) and hydrogen tetrachloroaurate (1.97 mg, 5.00 µmol) to water (20 mL). To this solution, ice-cold sodium borohydride solution (0.6 mL, 0.1 M) was added with vigorous stirring (1200 rpm) turning the solution brownish-red. The seed solution was used within 10 min of preparation.

CTAB (64.06 g, 0.18 mol) was dissolved in water (880 mL) upon gentle heating (35 °C). In a separate flask, hydrogen tetrachloroaurate (173.4 mg, 0.44 mmol) was dissolved in water (880 mL) then mixed with the CTAB solution. 45, 140, and 1575 mL of this solution was placed into flasks labelled A, B, and C respectively, and kept at 27 °C. An ascorbic acid solution (0.1 M) was prepared by dissolving ascorbic acid (176 mg, 1.0 mmol) in water (10 mL). 0.25, 0.77, and 8.75 mL of 0.1 M ascorbic acid was added into flasks A, B, and C, respectively. The flasks were hand shaken and the solutions became colourless. Seed solution (4 mL) was added to flask A and shaken for 4 s. 12.4 mL of the resulting mixture was transferred from flask A to flask B and shaken for 4 s before transferring all of flask B into flask C then shaking for 4 s and left undisturbed overnight at 27 °C.

UV-vis absorbance: 538.00 nm (TPB), 634.50 nm (LPB), $A_{LPB}/A_{TPB} = 1.37$

Method 3(AuS3)

The seed-mediated Ag(I)-assisted synthesis of gold nanorods in a surfactant mixture, as performed by El-Sayed *et al*.,[45] was carried out:

A seed solution was prepared by adding hydrogen tetrachloroaurate (5 mL, 0.5 mM) to CTAB (5 mL, 0.20 M) with stirring. Ice-cold sodium borohydride (0.6 mL, 0.01 M) was added, resulting in the formation of a brownish yellow solution which was kept at 25 °C with vigorous stirring (1200 rpm) for 2 min.

A surfactant mixture was prepared by adding CTAB to a solution of benzyldimethylammonium chloride (BDAC) (5 mL, 0.15 M), stirring for at 40 °C for 20 min to give a BDAC/CTAB molar ratio of 2.7. Silver nitrate (200 µL, 4 mM) was added followed by hydrogen tetrachloroaurate (5 mL, 1 mM) with gentle stirring. Ascorbic acid (70 µL, 0.0778 M) was added followed by seed solution (12 µL). The growth process was completed after 1 h, the solution being kept at 25 °C, and then left to age for 7 days in order to increase the aspect ratio of nanorods.

UV-vis absorbance: 546.79 nm (TPB), 836.02 nm (LPB), $A_{LPB}/A_{TPB} = 2.11$

Method 4 (AuS4)

The gram-scale synthesis of gold nanorods without use of a seed solution, as performed by Jana[55] was carried out:

Hydrogen tetrachloroaurate (0.5 g, 1.27 mmol) was dissolved in water (15 mL) and CTAB (0.91 g, 2.5 mmol), aqueous silver nitrate (1 mL, 0.25 M) and sodium chloride (0.15 g, 2.56 mmol) were added and the mixture stirred for 5 min in order to form a suspension. Ascorbic acid (0.44 g, 2.50 mmol) in water (2.5 mL) was added and the mixture stirred for 5 min giving rise to a colour change from orange to white. Aqueous sodium borohydride (0.5 mL, 0.01 M) was added with stirring, changing the solution colour to purple within a few minutes.

For solvent extraction, the nanorod solution (1 mL) was mixed with decanoic acid (100 mg, 0.5 mmol) and mixed thoroughly. Chloroform (1 mL) was added and the mixture shaken in order to extract gold nanoparticles into the organic phase.

UV-vis absorbance: 528.75 nm (TPB), 714.40 nm (LPB), $A_{LPB}/A_{TPB} = 1.44$

Method 5 (AuS5)

The Ag(I)-assisted synthesis of gold nanorods, as performed by Zubarev *et al.*[89] was carried out:

A seed solution was prepared by mixing CTAB (364 mg, 1 mmol) in water (5 mL) with hydrogen tetrachloroaurate (1 mg, 2 µmol) in water (5 mL) at room temperature. An aqueous solution of ice-cold sodium borohydride (0.6 mL, 0.01 M) was added with vigorous stirring (1200 rpm). A colour change from yellow to brown was observed and stirring continued for 2 min. CTAB-coated gold nanoparticle seed solutions were used within 5 min of preparation.

Growth Solution:

Silver nitrate (25.5 mg 0.15 mmol) was dissolved in water (37.5 mL) and added to a solution of CTAB (54.66 g 0.15 mol) in water (750 mL) then mixed before leaving at 25 °C for 10 min without stirring. Hydrogen tetrachloroaurate (295.5 mg 0.75 mmol) was dissolved in 750 mL water and added to the CTAB/$AgNO_3$ mixture, then after 3 min ascorbic acid (10.5 mL, 0.0788 M) was added and the mixture was hand stirred for 3-5 sec becoming colourless. Growth solutions were typically used immediately after preparation.

Seed solution (2.4 mL) was added to the growth solution and stirred for 30 s before placing in a water bath at 27 °C without stirring. A reddish-brown colour developed within 10 min and solution was left for 1 h for reaction to reach completion.

UV-vis absorbance: 507.18 nm (TPB), 863.73 nm (LPB), $A_{LPB}/A_{TPB} = 4.49$

Attempts were also made at concentrating aqueous nanorod solutions *via* rotary evaporation.

Method 6 (AuS6)

The seed-mediated synthesis of gold nanorods with addition of nitric acid, as performed by Huang *et al.*[46] was carried out.

A seed solution was prepared by dissolving hydrogen tetrachloroaurate (0.0098 g, 0.025 mmol) in 2.5 mL water then adding CTAB (3.645 g, 0.01 mol) and water to bring the total solution volume to 100 mL. Ice-cold sodium borohydride (3.5 mL, 0.01 M) was transferred to the CTAB-hydrogen tetrachloroaurate solution and the mixture stirred for 3 min. The solution changed from yellow to colourless with the addition of CTAB and then became brown with addition of sodium borohydride.

Growth solutions:

Hydrogen tetrachloroaurate (0.098 g, 0.25 mmol) was dissolved in water (1000 mL) and CTAB (36.4 g, 0.01 mol) was added with stirring. 3 flasks were labelled A, B and C:

A: Growth solution (45 mL) and ascorbic acid (0.25 mL, 0.1 M).

B: Growth solution (45 mL) and ascorbic acid (0.25 mL, 0.1 M).

C: Growth solution (450 mL), ascorbic acid (2.5 mL, 0.1 M) and nitric acid (3 mL, 0.1 M).

4 mL of the seed solution was added to flask A and stirred for 3 s then 4 mL of this solution was transferred to flask B and stirred for 5 s. 40 mL of solution B was transferred to flask C and stirred for 5 s. Flask C was left undisturbed in a water bath at 27 °C for 12 h for the reaction to complete.

Purification

The supernatant containing only spherical nanoparticles was removed, leaving only a precipitate of high aspect nanorods. Water was added to redisperse the precipitate and nanorods were concentrated *via* centrifugation (2000 rpm, 20 min), carefully removing excess CTAB with a pipette.

UV-vis absorbance: 553.63 nm (TPB), 733.53 nm (LPB), $A_{LPB}/A_{TPB} = 0.27$

Method 7 (AuS7)

The 5-step, seed-mediated synthesis of gold nanorods, as performed by Li *et al.*[51] was carried out:

A seed solution was prepared by mixing CTAB (10 mL, 0.2 M) with hydrogen tetrachloroaurate (10 mL, 0.5 mM). Ice-cold sodium borohydride (0.6 mL, 0.01 M) was added with vigorous stirring which was continued for 2 min and the seed solution was used between 2 and 48 h of preparation.

Growth solution:

Five test tubes were labelled A, B, C, D, and E, each containing 9 mL growth solution, consisting of hydrogen tetrachloroaurate (0.25 mM) and CTAB (0.1 M). Ascorbic acid (0.2 mL, 0.03 M) was added to each tube and sodium hydroxide (60 µL, 0.1 M) was added to B.

Seed solution (1 mL) was added to A and stirred for 20 s, then A (1 mL) was added to B and stirred for 20s. Solution B (1 mL) was added to C and stirred for 20 s, then C (1 mL) C was added to D and stirred for 20 s. Finally, solution D (1 mL) and seed solution (10 µL) were added to E and left overnight without stirring.

UV-vis absorbance: 553.96 nm (TPB), 737.07 nm (LPB), $A_{LPB}/A_{TPB} = 0.64$

Method 8 (AuS8)

The seed-mediated synthesis as performed by Tollan *et al.,*[52] in which sodium borohydride and ascorbic acid are replaced by acetylacetone as reducing agent, was carried out:

A sodium carbonate buffer (0.1 M, pH 10) is used in conjunction with CTAB (10 mL, 0.2 M) to form the aqueous solution in which nanorod formation takes place. Hydrogen tetrachloroaurate (0.1 mL, 0.1 M) was added with stirring and an orange solution was observed. This was followed by silver nitrate (0.018 mL, 0.1 M) and finally, acetylacetone (0.1 mL, 0.35 M) which changes the solution from orange to colourless. This was followed by gradual appearance of purple colour indicative of nanorod formation.

UV-vis absorbance: 511.29 nm (TPB), 898.00 nm (LPB), $A_{LPB}/A_{TPB} = 2.80$

Method 9 (AuS9)

The Ag(I)-assisted synthesis of gold nanorods with dropwise addition of seed solution to growth solution, as performed by Drezek *et al.*[54] was carried out:

A seed solution was prepared by first mixing CTAB (10 mL, 0.2 M) and hydrogen tetrachloroaurate (10 mL, 0.01 M). Ice-cold sodium borohydride (1.2 mL, 0.01 M) was added to the mixture causing the colour to change to brown, indicating the formation of gold colloid seeds. The seed solution was immersed in a 40 °C water bath for 15 min then kept at room temperature.

Growth Solution and Scaled-Up Synthesis of Au Nanorods

CTAB (300 mL, 0.2 M), silver nitrate (6 mL, 0.01 M) and hydrogen tetrachloroaurate (30 mL, 0.01 M) were mixed and the yellow solution became colourless upon addition of ascorbic acid (4.6 mL, 0.1 M). Seed solution (15 mL) was added dropwise to the growth solution over a period of 15 min in order to initiate nanorod growth and the solution was left overnight for the reaction to complete.

UV-vis absorbance: 518.98 nm (TPB), 824.85 nm (LPB), $A_{LPB}/A_{TPB} = 2.23$

2.5.2 Shape Separation of Nanorods

Initial Investigations

Aqueous gold nanorod solutions prepared *via* method 5 (AuS5) were initially centrifuged at both 5000 rpm and 10000 rpm for 10 min using both conical- and spherical-bottomed centrifuge tubes. Precipitates were redispersed in water for UV-vis absorbance measurements and supernatants were measured as collected. Concentrated aqueous gold nanorod solutions prepared *via* method 4 (AuS4) were diluted by factors of 5x to 700x using deionised water and centrifuged (10000 rpm, 10 min) using spherical-bottomed centrifuge tubes. Precipitates were redispersed in water for UV-vis absorbance measurements and supernatants were measured as collected.

Nanorods prepared *via* method 4 (AuS4) were transferred from aqueous solution (1 ml) to chloroform (1 mL) *via* the addition of decanoic acid (0.1 g, 0.6 mmol) and sodium phosphate

monobasic (0.1 g, 0.8 mmol)[55] and centrifuged (10000 rpm, 10 min). A slight decrease in the TPB was observed in the UV-vis spectra for the supernatant, therefore an increase in A_{LPB}/A_{TPB} and the relative yield of nanorods, and so multiple centrifugations were performed with removal of the precipitate after each in order to determine whether this could be used to achieve shape separation.

Supernatants obtained from centrifuged solutions of gold nanoparticles were analysed by UV-vis absorbance spectrometry and an increase in A_{LPB}/A_{TPB} was observed, implying an increase in the yield of nanorods relative to spherical nanoparticles. For this reason the supernatants from future centrifugations of nanorod solutions were collected for analysis.

Variation of rpm, Time and Number of Cycles of Centrifugation on Shape Separation

Centrifugation of aqueous nanorod samples was typically carried out for 10 min at 10000 rpm. In order to determine the effects of rpm, time and number of cycles of centrifugation on shape separation these three parameters were systematically varied. Samples prepared using method 5 (AuS5) were centrifuged for 10 min at 2000, 4000, 6000, 8000 and 10000 rpm and the resulting supernatants analysed using UV-vis absorbance spectrometry. Identical samples were also centrifuged at 10000 rpm for 5, 10, 15 and 20 min and another set of identical samples were centrifuged at 10000 rpm for one, two and three 10 minute cycles, and the resulting supernatants analysed using UV-vis absorbance spectrometry.

In accordance with the work on centrifugation carried out by Sharma *et al*.,[59] see above, investigations into side wall and bottom precipitates were also carried out. Aqueous solutions of gold nanorods synthesised using method 5 (AuS5) were centrifuged (10000 rpm, 10 min) and the resulting side wall and bottom precipitates as well as supernatants were analysed using UV-vis absorbance spectrometry.

2.5.3 Addition of Sodium and Potassium Phosphates to Gold Nanoparticles

The addition of sodium and potassium phosphate monobasic and dibasic salts to aqueous gold nanorod solutions was investigated and compared with the studies of Huang *et al*.[60] Typically,

100 mg of phosphate was added to gold nanorod solutions produced using method 5 (AuS5), and any decrease in the LPB and/or TPB absorbance in the UV-vis spectrum was monitored.

Investigations into varying the concentrations of sodium phosphate monobasic were carried out. 500 and 1000 mg were added to gold nanorod solutions prepared using method 5 (AuS5), with the aim of increasing the rate and/or extent of the decrease of the TPB in the UV-vis absorption spectra.

2.6 Cadmium Sulphide Nanorods

2.6.1 Synthesis of Cadmium Sulphide Nanorods

Method 1 (CdS1)

The surfactant-templated synthesis of cadmium sulphide nanoparticles in a hexagonal liquid crystal system, adapted from the work of Fendler *et al.*[148] and Wan *et al.*,[76] was carried out:

Cadmium chloride (0.14 g, 0.764 mmol) was added to a solution of Triton X-100 in (42 wt% in 100 mL water) and the mixture stirred at 40 °C for 10 min before returning to room temperature.

In another flask, connected to the first with glass tubing, sodium sulphide (0.136 g, 1.743 mmol) was dissolved in water (100 mL), and hydrochloric acid (100 mL, 0.5 M) was added *via* syringe at a rate so as to provide a steady flow of hydrogen sulphide bubbles to the cadmium chloride solution, which was gently stirred throughout the reaction (200 rpm). Cadmium sulphide formation was indicated by a yellow colour and the addition of hydrochloric acid was continued until the increase in colour intensity ceases. Excess hydrogen sulphide was left until bubbling stopped then the flasks were opened and left to vent before addition of hydrogen peroxide (20 %, 50 mL) to both flasks. Triton X-100 was removed by dilution and washing with excess water. Cadmium sulphide nanostructures were isolated by centrifugation at 10000 rpm for 10 min.

Hydrogen sulphide reacts with cadmium chloride to form cadmium sulphide nanoparticles templated by the hexagonal lyotropic liquid crystalline Triton X-100 phase.

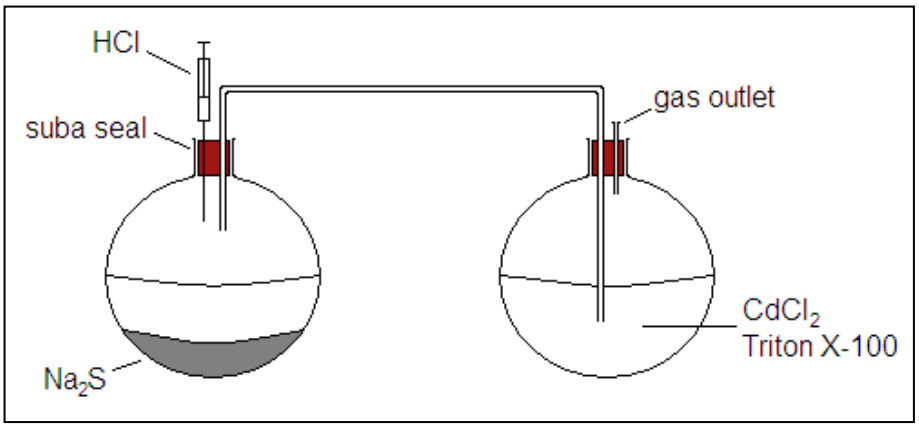

Figure 2.3 Method 1 (CdS1) experimental setup.

Method 2 (CdS2)

The aqueous, CTAB-templated synthesis of CdS nanoparticles, as performed by Chen *et al.*,[64] was carried out:

CTAB (5.00 g, 13.7 mmol) was dissolved in water (200 mL) as a standard micellar solution. Cadmium chloride (0.14 g, 0.764 mmol) and sodium sulphide (0.136 g, 1.743 mmol) were dissolved in micellar solution (32 and 72 mL) to make solutions A and B respectively.

Cyclohexane (1 mL) was added to solution A (20 mL) and solution B (20 mL) at room temperature and under nitrogen, with stirring for 10 min to give solutions A' and B'. Solution B' was injected slowly into solution A' with continued stirring at 35 °C causing a colour change from cloudy white to yellow/orange. After injection was completed the resulting solution C was stirred for 10 min then centrifuged (10000 rpm, 10 min).

Method 3 (CdS3)

The one-pot synthesis of cadmium sulphide nanorods, with oleylamine as a capping agent, as performed by Prasad *et al.*,[75] was carried out:

(i) High-Yield Synthesis of CdS Nanorods with AR of ~6.2

An oleylamine-sulphur solution was prepared by dissolving sulphur (0.3852 g, 12 mmol) in oleylamine (10 mL). Separately, cadmium chloride (0.366 g, 2.0 mmol) was dissolved in oleylamine (20 mL), trioctylphosphine oxide (2.0 g, 51.6 mmol) was added, and the mixture stirred at 100 °C under a nitrogen flow for 30 min. The oleylamine-sulphur solution was injected into the hot reaction mixture with gentle stirring and then stirred at 100 °C for 19 h.

^{1}H NMR ($CDCl_3$) δ:

0.81 (3H, t, J = 6.78), 1.16 - 1.38 (22H, m), 1.51 (2H, m), 1.92 - 1.95 (4H, m), 2.60 - 2.64 (2H, m), 5.27 - 5.29 (2H, m).

(ii) High Yield Synthesis of Highly Uniform CdS Nanorods with an AR of 5

An oleylamine-sulphur solution was prepared by dissolving sulphur (0.3852 g, 12 mmol) in oleylamine (10 mL). Separately, cadmium chloride (0.366 g, 2 mmol) was dissolved in oleylamine (20 mL), concentrated hydrochloric acid (1 mL, 36%) was added, and the mixture stirred at 100 °C under a nitrogen flow for 30 min. The oleylamine-sulphur solution was injected into the hot reaction mixture with gentle stirring and then stirred at 100 °C for 19 h.

In order to retrieve nanorods, the reaction mixtures were transferred into toluene (500 mL) at room temperature. Nanorods were precipitated by the addition of ethanol (100 mL) and centrifugation (10000 rpm, 10 min) and the yellow nanorod precipitate redispersed in hexane.

Method 4 (CdS4)

The synthesis of cadmium sulphide nanorods, catalysed by gold nanoparticles, as performed by Zhang *et al.*,[77] was carried out:

Thiol-coated gold nanospheres were first synthesised using the method described by Brust *et al.*[29]:

An aqueous solution of hydrogen tetrachloroaurate (30 mL, 30 mM) was mixed with tetradodecylammonium bromide in toluene (80 mL, 50 mM). The two-phase mixture was stirred vigorously and dodecanethiol (0.20 mL, 0.84 mmol) was added.

Sodium borohydride (25 mL, 0.4 M) was slowly added with vigorous stirring, and after 3 h the organic phase was separated, evaporated to 10 mL and mixed with ethanol (400 mL). The mixture was kept at -18 °C for 4 h and the dark brown precipitate filtered and washed with ethanol before dissolving in toluene (10 mL) and precipitating with ethanol (400 mL) ethanol (yield: 214 mg, ~93%).

In a typical synthesis, cadmium oxide (1 mmol, 0.1284 g) and oleic acid (2 mL) were mixed with octadecene (20 mL). Under nitrogen flow, the mixture was heated to 200 °C until a cadmium-oleate complex was formed in the solution, which became colourless. After cooling the mixture to 100 °C, gold nanoparticles in hexane (1 mL) were injected, and the hexane distilled out.

Sulphur solution (2.5 mL, 0.1 M) (sulphur in a 1:4 v/v oleylamine to phenyl ether mixture) was then injected and the mixture was kept at 120 °C for 30 min, and then at 300 °C for 3 h. After

cooling to room temperature, the mixture was treated with ethanol to precipitate the nanorods and then centrifuged. The precipitate was redispersed in hexane.

Method 5 (CdS5)

The synthesis of cadmium sulphide nanorods using trioctylphosphine as both solvent and stabiliser, as performed by Zhang *et al.*,[79] was carried out:

Cadmium acetate (40 mg, 0.15 mmol) was dissolved in hot trioctylphosphine (3 mL, 6.73 mmol) under nitrogen flow. Separately, sulphur (24.0 mg, 0.75 mmol) was dissolved in trioctylphosphine (1 mL, 2.24 mmol) with vigorous stirring. The sulphur solution was injected into the cadmium solution and stirred at 260 °C for 6 h. The resulting yellow solution was cooled to 50 °C and methanol was added to give a fine deposit of cadmium sulphide nanorods, which was separated by centrifugation and redissolved in toluene.

2.6.2 Cadmium Sulphide Nanorods as Lyotropic Liquid Crystals

In an approach similar to that carried out by Alivisatos *et al.*,[30] the formation of lyotropic liquid crystalline phases through dissolution of cadmium sulphide nanorods in organic solvent was investigated:

Cadmium sulphide nanorods synthesised using method 3i (CdS3i) were dissolved in hexane to form a 10% w/v solution. The solution was deposited onto a glass slide and rubbed under a glass cover slip before examining under an optical microscope.

A small amount of the solution was then placed into a sealed capillary tube and again viewed under an optical microscope, allowing the concentration to gradually increase as hexane was evaporated due to slow heating from the light source.

2.7 Functionalisation of Gold Nanorods

2.7.1 Functionalisation with Commercially Available Thiols

Initially, reactions were performed using commercially obtained aqueous gold nanorod solutions ("Nanorodz").

Method 1 (AuF1)

A standard procedure for the formation of self-assembled thiol monolayers on gold surfaces, as described by Whitesides *et al*.,[80] was carried out:

Aqueous gold nanorods (10 mL) were added to a solution of dodecanethiol (2 mL) in ethanol (10 mL) and stirred under nitrogen for 48 hours. A colour change from purple to clear was observed in the solution. A precipitate was separated and purified by centrifugation (2000 rpm, 20 min) then redispersed in ethanol. This process was repeated several times in order to remove excess dodecanethiol and finally the product was redispersed in deuterated chloroform.

Method 2 (AuF2)

An aqueous solution of gold nanorods prepared using method 9 (AuS9) (40 mL) was added to a solution of dodecanethiol (5 mL, 0.3 mmol) in acetone (40 mL) and stirred (700 rpm) overnight at room temperature. The organic layer was extracted into chloroform, and the solvent removed under reduced pressure.

^{1}H NMR (400 MHz, $CDCl_3$) δ:

0.88 (3H, t), 1.26 - 1.42 (18H, m), 1.56 (2H, m), 2.64 (2H, t, J = 6.8 Hz).

2.7.2 Functionalisation of Gold Nanorods with Synthesised Ligands

Method 1 (AuF3)

The reaction using dodecanethiol in AuF2 was repeated using 6:

Aqueous gold nanorods (10 mL) were added to a solution of 6 (2 mg, 5.8 µmol) in ethanol (10 mL) and stirred under nitrogen for 48 hours. A colour change from purple to clear was observed in the solution. A precipitate was separated and purified by centrifugation (2000 rpm, 20 min) then redispersed in ethanol. This process was repeated several times in order to remove excess 6 and finally the product was redispersed in deuterated chloroform.

Method 2 (AuF4)

The functionalisation of gold nanorods as performed by Thomas *et al*.,[85] in which an alkanethiol monolayer is initially formed, displacing the CTAB bilayer and subsequently undergoing ligand-exchange with other thiol ligands, was carried out:

A 2 : 3 : 4 mixture of aqueous gold nanorods : octadecanethiol : acetone (18 mL) was mixed for 5 h to allow nanorods to transfer from the aqueous to the organic layer. The organic layer was dried over magnesium sulphate and 6 (10 mg, 29 µmol) dissolved in acetone (10 mL) and stirred at room temperature for 24 h. Purification was achieved by washing with dichloromethane followed by centrifugation (2000 rpm, 20 min). This was repeated several times in order to remove excess 6 and finally the product was redispersed in deuterated chloroform.

Reactions were then performed using aqueous gold nanorod solutions synthesised using the methods described above.

Method 3 (AuF5)

The functionalisation of gold nanorods as performed by Li *et al*.,[86] was carried out:

An aqueous solution of gold nanorods prepared using method 5 (AuS5) (2 mL), was added to a solution of 6 (100 mg, 0.3 mmol) in dry tetrahydrofuran (50 mL) under a nitrogen atmosphere.

The mixture was stirred for 4 days at room temperature and the solvent was removed under reduced pressure. Dichloromethane (50 mL) was added, followed by centrifugation (10000 rpm, 10 min) in order to remove free CTAB and 6. The resulting gold nanorods were treated with excess 6 in dichloromethane, stirred overnight, and again centrifuged. This procedure was repeated 3 times to ensure that gold nanorods were completely coated by thiol molecules. Finally the gold nanorods were again centrifuged and then washed with dichloromethane several times to remove any remaining free 6.

Method 4 (AuF6)

In a similar manner to AuF2, an aqueous solution of gold nanorods prepared using method 9 (AuS9) (40 mL) was added to a solution of 6 (100 mg, 0.3 mmol) in acetone (40 mL) and stirred (700 rpm) overnight at room temperature. The organic layer was extracted into chloroform, and the solvent removed under reduced pressure.

^{1}H NMR (400 MHz, $CDCl_3$) δ:

0.90 (3H, t, J = 6.78 Hz), 1.33 – 1.36 (4H, m), 1.57 - 1.64 (4H, m), 1.74 - 1.86 (2H, m), 2.60 - 2.64 (2H, t, J = 7.78), 2.71 - 2.75 (2H, t, J = 7.24), 3.99 (2H, t, J = 6.42 Hz), 6.95 (2H, d, J = 5.58 Hz), 7.23 (2H, t, J = 8.04), 7.45 – 7.50 (4H, m).

17a (0.06 g, 0.20 mmol) in acetone (20 mL) was added to an aqueous solution of gold nanorods (20 mL) and stirred at 700 rpm for 48 h. A loss of purple colouration was observed in the solution as well as the formation of purple-coloured aggregates and a dark sediment on the inside of the reaction vessel surface.

The colourless liquid was removed by decanting and chloroform (40 mL) was added to redisperse the nanorods, with the reappearance of a blue-purple colour to the solution observed.

^{1}H NMR (400 MHz, $CDCl_3$) δ:

0.90 (3H, t, J = 7 Hz), 1.04 (2H, sext, J = 7 Hz), 1.19 - 1.45 (2H, quint, J = 7 Hz), 1.19 - 1.45 (4H, m), 1.79 - 1.94 (5H, m), 1.79 - 1.94 (2H, sept, J = 6.8 Hz), 2.01 - 2.06 (2H, quint, J = 7 Hz), 2.01 - 2.06 (2H, quint, J = 7 Hz), 2.40 (1H, quint, J = 6.8 Hz), 2.76 (2H, t, J = 6.8 Hz), 3.95 (2H, t, J = 6.8 Hz), 6.80 - 6.82 (2H, d, J = 8.2 Hz), 7.10 - 7.12 (2H, d, J = 8.2 Hz).

21a (0.06 g, 0.20 mmol) in acetone (20 mL) was added to an aqueous solution of gold nanorods (20 mL) and stirred at 700 rpm for 48 h. A loss of purple colouration was observed in the solution as well as the formation of purple-coloured aggregates and a dark sediment on the inside of the reaction vessel surface.

The colourless liquid was removed by decanting and chloroform (40 mL) was added to redisperse the nanorods, with the reappearance of a blue-purple colour to the solution observed.

^{1}H NMR (400 MHz, $CDCl_3$) δ:

0.89 (3H, t, J = 7 Hz), 1.04 (2H, quint, J = 7 Hz), 1.19 - 1.45 (2H, sext, J = 7 Hz), 1.19 - 1.45 (2H, quint, J = 7 Hz), 1.19 - 1.45 (2H, quint, J = 7 Hz), 1.19 - 1.45 (5H, m), 1.84 - 1.94 (2H, quint, J = 7 Hz), 1.84 - 1.94 (4H, m), 2.06 (2H, quint, J = 7 Hz), 2.40 (1H, quint, J = 6.8 Hz), 2.76 (2H, t, J = 6.8 Hz), 3.96 (2H, t, J = 6.8 Hz), 6.80 - 6.82 (2H, d, J = 8.2 Hz), 7.10 - 7.12 (2H, d, J = 8.2 Hz).

2.8 Functionalisation of Cadmium Sulphide Nanorods

2.8.1 Functionalisation with Commercially Available Thiols

Functionalisation with dodecanethiol

Oleylamine-coated CdS nanorods synthesised using method 3 (CdS3i) (400 mg) were dissolved in hexane (50 mL) and dodecanethiol (2 mL) was added. The mixture was stirred overnight, then the solvent removed under reduced pressure and the product redispersed in a 50:50 mixture of hexane and ethanol before centrifugation (10000 rpm, 10 min) to remove excess dodecanethiol and oleylamine.

A blank reaction, in which no dodecanethiol was added, was also performed.

Dodecanethiol ^{1}H NMR (400 MHz, $CDCl_3$) δ:

0.88 (3H, t), 1.26 - 1.42 (18H, m), 1.56 (2H, m), 2.58 (2H, quart, J = 6.8 Hz).

Product ^{1}H NMR (400 MHz, $CDCl_3$) δ:

0.88 (3H, t), 1.27 - 1.42 (18H, m), 1.57 (2H, m), 2.65 (2H, t, J = 6.8 Hz).

Functionalisation with 6-(ferrocenyl)hexanethiol

Oleylamine-coated CdS nanorods synthesised using method 3 (CdS3i) (50 mg) and 6-(ferrocenyl)hexanethiol (100 mg) were mixed in dichloromethane (30 mL) over 48 h. The solvent was removed under reduced pressure and the product redispersed in a 50:50 mixture of hexane and ethanol before centrifugation (10000 rpm, 10 min) to remove excess 6-(ferrocenyl)hexanethiol and oleylamine. 100 mg of product was obtained after centrifugation.

6-(ferrocenyl)hexanethiol ^{1}H NMR (400 MHz, $CDCl_3$) δ:

1.34 (4H, m), 1.50 (2H, quint, J = 7 Hz), 1.62 (2H, quint, J = 7 Hz), 2.32 (2H, t, J = 7.6 Hz), 2.52 (2H, quart, J = 6.8 Hz), 4.04 - 4.09 (9H, m).

Product ^{1}H NMR (400 MHz,$CDCl_3$) δ:

1.34 (4H, m), 1.50 (2H, quint, J = 7 Hz), 1.62 (2H, quint, J = 7 Hz), 2.32 (2H, t, J = 7.6 Hz), 2.68 (2H, t, J = 6.8 Hz), 4.04 - 4.09 (9H, m).

2.8.2 Functionalisation with Synthesised Ligands

Functionalisation of CdS Nanorods with 17a

Oleylamine- coated CdS nanorods synthesised using method 3 (CdS3i) (360 mg) and 17a (500 mg, 1.60 mmol) were mixed in dichloromethane (50 mL) over 48 h. The solvent was removed under reduced pressure and the product redispersed in a 50:50 mixture of hexane and ethanol before centrifugation (10000 rpm, 10 min) to remove excess 17a and oleylamine. 280 mg of a yellow solid was obtained after centrifugation.

^{1}H NMR (400 MHz, $CDCl_3$) δ:

0.90 (3H, t, J = 7 Hz), 1.04 (2H, sext, J = 7 Hz), 1.19 - 1.45 (2H, quint, J = 7 Hz), 1.19 - 1.45 (4H, m), 1.79 - 1.94 (5H, m), 1.79 - 1.94 (2H, sept, J = 6.8 Hz), 2.01 - 2.06 (2H, quint, J = 7 Hz), 2.01 - 2.06 (2H, quint, J = 7 Hz), 2.40 (1H, quint, J = 6.8 Hz), 2.76 (2H, t), 3.95 (2H, t, J = 6.8 Hz), 6.80 - 6.82 (2H, d, J = 8.2 Hz), 7.10 - 7.12 (2H, d, J = 8.2 Hz).

^{13}C NMR (100 MHz, $CDCl_3$) δ:

14.40 (1C, *CH_3*), 20.04 (1C, *CH_2*), 22.65 (1C, *CH_2*), 27.05 (1C, *CH_2*), 31.59 (1C, *CH_2*), 33.62 (2C, *2xCH_2*), 34.58 (2C, *2xCH_2*), 37.02 (1C, *CH*), 39.74 (1C, *CH_2*), 43.73 (1C, *Ar-CH*), 67.24 (1C, *O-CH_2*), 114.22 (2C, *Ar*), 127.61 (2C, *Ar*), 140.16 (1C, *Ar*), 157.02 (1C, *Ar-O*).

Functionalisation of CdS Nanorods with 17b

Oleylamine-coated CdS nanorods synthesised using method 3 (CdS3i) (150 mg) and 17b (80 mg, 0.24 mmol) were mixed in dichloromethane (50 mL) over 48 h. The solvent was removed under reduced pressure and the product redispersed in a 50:50 mixture of hexane and ethanol before centrifugation to remove excess 17b and oleylamine. 25 mg of a yellow solid was obtained after centrifugation.

^{1}H NMR (400 MHz, $CDCl_3$) δ:

0.90 (3H, t, J = 7 Hz), 1.04 (2H, sext, J = 7 Hz), 1.19 - 1.45 (2H, quint, J = 7 Hz), 1.19 - 1.45 (2H, quint, J = 7 Hz), 1.19 - 1.45 (2H, quint, J = 7 Hz), 1.19 - 1.45 (2H, quint, J = 7 Hz), 1.19 - 1.45 (2H, quint, J = 7 Hz), 1.79 - 1.94 (5H, m), 1.79 - 1.94 (2H, sept, J = 6.8 Hz), 2.01 - 2.06 (2H, quint, J = 7 Hz), 2.01 - 2.06 (2H, quint, J = 7 Hz), 2.40 (1H, quint, J = 6.8 Hz), 2.69 (2H, t, J = 6.8 Hz), 3.91 (2H, t, J = 6.8 Hz), 6.80 - 6.82 (2H, d, J = 8.2 Hz), 7.09 - 7.11 (2H, d, J = 8.2 Hz).

^{13}C NMR (100 MHz, $CDCl_3$) δ:

14.40 (1C, *CH_3*), 20.00 (1C, *CH_2*), 22.61 (1C, *CH_2*), 26.15 (1C, *CH_2*), 28.25 (1C, *CH_2*), 29.21 (1C, *CH_2*), 30.67 (1C, *CH_2*), 33.61 (2C, *2xCH_2*), 34.57 (2C, *2xCH_2*), 37.02 (1C, *CH*), 39.73 (1C, *CH_2*), 43.72 (1C, *Ar-CH*), 67.21 (1C, *O-CH_2*), 114.20 (2C, *Ar*), 127.62 (2C, *Ar*), 140.15 (1C, *Ar*), 157.00 (1C, *Ar-O*).

Functionalisation of CdS Nanorods with 17c

Oleylamine-coated CdS nanorods synthesised using method 3 (CdS3i) (180 mg) and 17c (280 mg, 0.77 mmol) were mixed in dichloromethane (50 mL) over 48 h. The solvent was removed under reduced pressure and the product redispersed in a 50:50 mixture of hexane and ethanol before centrifugation to remove excess 17c and oleylamine. 165 mg of a yellow solid was obtained after centrifugation.

^{1}H NMR (400 MHz, $CDCl_3$) δ:

0.90 (3H, t, J = 7 Hz), 1.04 (2H, sext, J = 7 Hz), 1.19 - 1.45 (2H, quint, J = 7 Hz), 1.19 - 1.45 (2H, quint, J = 7 Hz), 1.19 - 1.45 (2H, quint, J = 7 Hz), 1.19 - 1.45 (2H, quint, J = 7 Hz), 1.19 - 1.45 (2H, quint, J = 7 Hz), 1.19 - 1.45 (4H, m), 1.79 - 1.94 (5H, m), 1.79 - 1.94 (2H, sept, J = 6.8 Hz), 2.01 - 2.06 (2H, quint, J = 7 Hz), 2.01 - 2.06 (2H, quint, J = 7 Hz), 2.40 (1H, quint, J = 6.8 Hz), 2.68 (2H, t, J = 6.8 Hz), 3.91 (2H, t, J = 6.8 Hz), 6.80 - 6.82 (2H, d, J = 8.2 Hz), 7.09 - 7.11 (2H, d, J = 8.2 Hz).

^{13}C NMR (100 MHz, $CDCl_3$) δ:

14.40 (1C, *CH_3*), 20.00 (1C, *CH_2*), 22.61 (1C, *CH_2*), 25.98 (1C, *CH_2*), 26.16 (1C, *CH_2*), 28.25 (1C, *CH_2*), 28.96 (1C, *CH_2*), 29.21 (1C, *CH_2*), 30.67 (1C, *CH_2*), 33.61 (2C, *2xCH_2*), 34.57 (2C, *2xCH_2*), 37.02 (1C, *CH*), 39.73 (1C, *CH_2*), 43.72 (1C, *Ar-CH*), 67.21 (1C, *O-CH_2*), 114.20 (2C, *Ar*), 127.62 (2C, *Ar*), 140.15 (1C, *Ar*), 157.00 (1C, *Ar-O*).

Functionalisation of CdS Nanorods with 21a

Oleylamine-coated CdS nanorods synthesised using method 3 (CdS3i) (100 mg) and 21a (200 mg, 0.60 mmol) were mixed in dichloromethane (50 mL) over 48 h. The solvent was removed under reduced pressure and the product redispersed in a 50:50 mixture of hexane and ethanol before centrifugation to remove excess 21a and oleylamine. 135 mg of a yellow solid was obtained after centrifugation.

^{1}H NMR (400 MHz, $CDCl_3$) δ:

0.89 (3H, t, J = 7 Hz), 1.04 (2H, quint, J = 7 Hz), 1.19 - 1.45 (2H, sext, J = 7 Hz), 1.19 - 1.45 (2H, quint, J = 7 Hz), 1.19 - 1.45 (2H, quint, J = 7 Hz), 1.19 - 1.45 (5H, m), 1.84 - 1.94 (2H, quint, J = 7 Hz), 1.84 - 1.94 (4H, m), 2.06 (2H, quint, J = 7 Hz), 2.40 (1H, quint, J = 6.8 Hz), 2.75 (2H, t, J = 6.8 Hz), 3.96 (2H, t, J = 6.8 Hz), 6.80 - 6.82 (2H, d, J = 8.2 Hz), 7.10 - 7.12 (2H, d, J = 8.2 Hz).

^{13}C NMR (100 MHz, $CDCl_3$) δ:

14.09 (1C, *CH_3*), 22.68 (1C, *CH_2*), 25.82 (1C, *CH_2*), 26.63 (1C, *CH_2*), 28.09 (1C, *CH_2*), 32.19 (1C, *CH_2*), 33.62 (2C, *2xCH_2*), 34.55 (2C, *2xCH_2*), 37.28 (1C, *CH*), 37.36 (1C, *CH_2*), 38.70 (1C, *CH_2*), 43.70 (1C, *Ar-CH*), 67.24 (1C, *O-CH_2*), 114.19 (2C, *Ar*), 127.58 (2C, *Ar*), 140.09 (1C, *Ar*), 156.98 (1C, *Ar-O*).

Functionalisation of CdS Nanorods with 21b

Oleylamine-coated CdS nanorods synthesised using method 3 (CdS3i) (10 mg) and 21b (0.05 mg, 0.15 µmol) were mixed in dichloromethane (50 mL) over 48 h. The solvent was removed under reduced pressure and the product redispersed in a 50:50 mixture of hexane and ethanol before centrifugation to remove excess 21b and oleylamine. 9 mg of a yellow solid was obtained after centrifugation.

^{1}H NMR (400 MHz, $CDCl_3$) δ:

0.89 (3H, t, J = 7 Hz), 1.04 (2H, quint, J = 7 Hz), 1.19 - 1.45 (2H, sext, J = 7 Hz), 1.19 - 1.45 (2H, quint, J = 7 Hz), 1.19 - 1.45 (2H, quint, J = 7 Hz), 1.19 - 1.45 (2H, quint, J = 7 Hz), 1.19 - 1.45 (2H, quint, J = 7 Hz), 1.19 - 1.45 (5H, m), 1.84 - 1.94 (2H, quint, J = 7 Hz), 1.84 - 1.94 (4H, m), 2.06 (2H, quint, J = 7 Hz), 2.40 (1H, quint, J = 6.8 Hz), 2.62 (2H, t, J = 6.8 Hz), 3.94 (2H, t, J = 6.8 Hz), 6.81 - 6.83 (2H, d, J = 8.2 Hz), 7.10 - 7.12 (2H, d, J = 8.2 Hz).

^{13}C NMR (100 MHz, $CDCl_3$) δ:

14.11 (1C, *CH_3*), 22.70 (1C, *CH_2*), 24.42 (1C, *CH_2*), 26.65 (1C, *CH_2*), 28.92 (1C, *CH_2*), 29.24 (1C, *CH_2*), 29.35 (1C, *CH_2*), 32.20 (1C, *CH_2*), 33.65 (2C, *2xCH_2*), 34.57 (2C, *2xCH_2*), 37.40 (1C, *CH_2*), 43.72 (1C, *Ar-CH*), 67.21 (1C, *O-CH_2*), 114.20 (2C, *Ar*), 127.62 (2C, *Ar*), 140.15 (1C, *Ar*), 157.00 (1C, *Ar-O*).

Functionalisation of CdS Nanorods with 21c

Oleylamine-coated CdS nanorods synthesised using method 3 (CdS3i) (100 mg) and 21c (50 mg, 0.13 mmol) were mixed in dichloromethane (50 mL) over 48 h. The solvent was removed under reduced pressure and the product redispersed in a 50:50 mixture of hexane and ethanol before centrifugation to remove excess 21c and oleylamine. 60 mg of a yellow solid was obtained after centrifugation.

^{1}H NMR (400 MHz, $CDCl_3$) δ:

0.89 (3H, t, J = 7 Hz), 1.04 (2H, quint, J = 7 Hz), 1.19 - 1.45 (2H, sext, J = 7 Hz), 1.19 - 1.45 (2H, quint, J = 7 Hz), 1.19 - 1.45 (2H, quint, J = 7 Hz), 1.19 - 1.45 (2H, quint, J = 7 Hz), 1.19 - 1.45 (2H, quint, J = 7 Hz), 1.19 - 1.45 (2H, quint, J = 7 Hz), 1.19 - 1.45 (2H, quint, J = 7 Hz), 1.19 - 1.45 (5H, m), 1.84 - 1.94 (2H, quint, J = 7 Hz), 1.84 - 1.94 (4H, m), 2.06 (2H, quint, J = 7 Hz), 2.40 (1H, quint, J = 6.8 Hz), 2.68 (2H, t, J = 6.8 Hz), 3.94 (2H, t, J = 6.8 Hz), 6.81 - 6.83 (2H, d, J = 8.2 Hz), 7.10 - 7.12 (2H, d, J = 8.2 Hz).

^{13}C NMR (100 MHz, $CDCl_3$) δ:

14.11 (1C, *CH_3*), 22.70 (1C, *CH_2*), 24.42 (1C, *CH_2*), 26.65 (1C, *CH_2*), 28.92 (1C, *CH_2*), 29.24 (1C, *CH_2*), 29.35 (1C, *CH_2*), 30.67 (1C, *CH_2*), 32.20 (1C, *CH_2*), 33.65 (2C, *2xCH_2*), 34.57 (2C, *2xCH_2*), 36.12 (1C, *CH*), 37.40 (1C, *CH_2*), 43.72 (1C, *Ar-CH*), 67.21 (1C, *O-CH_2*), 114.20 (2C, *Ar*), 127.62 (2C, *Ar*), 140.15 (1C, *Ar*), 157.00 (1C, *Ar-O*).

2.9 Zinc Sulphide and Cadmium Sulphide Alkylamine-Functionalised Nanorods

Zinc sulphide nanorods with an octadecylamine surface coating were synthesised using the procedures described by Acharya *et al.*:[96]

Initially, the zinc ethylxanthate precursor was prepared *via* the method used by Golan *et al.*:[149]

A solution of zinc chloride (7.5 mmol, 1.02 g) in water (30 ml) was mixed with a solution of potassium ethyl xanthogenate (15 mmol, 2.40 g) in water (30 ml) under constant stirring. The resulting zinc ethylxanthate precipitate (2.02 g, 87.5%) was filtered, washed with water and dried in vacuum.

Zinc ethylxanthate (0.11 g, 0.34 mmol) was then dissolved in molten octadecylamine (2.02 g, 7.5 mmol, 22x molar excess) at 100 °C for 5 min before annealing at 130 °C for 8 min. After cooling to 40 °C, ODA-coated zinc sulphide particles were harvested by flocculation of the sample with methanol (10 mL) followed by washing of the precipitate with methanol then centrifugation and redispersion in toluene.

The above procedure was modified in order to prepare cadmium sulphide nanorods with an octadecylamine surface coating:

A solution of cadmium chloride (7.5 mmol, 1.37 g) in water (30 ml) was mixed with a solution of potassium ethyl xanthogenate (15 mmol, 2.40 g) in water (30 ml) under constant stirring. The resulting cadmium ethylxanthate precipitate (2.13 g, 80.0%) was filtered, washed with water and dried in vacuum.

Cadmium ethylxanthate (0.12 g, 0.34 mmol) was then dissolved in molten octadecylamine (2.02 g, 7.5 mmol, 22x molar excess) at 100 °C for 5 min before annealing at 130 °C for 8 min. After cooling to 40 °C, ODA-coated cadmium sulphide particles were harvested by flocculation of the sample with methanol (10 mL) followed by washing of the precipitate with methanol then centrifugation and redispersion in toluene.

2.10 Lyotropic Liquid Crystalline Phases in Metal (II) Phthalocyanines

Concentrated solutions and chromonic liquid crystals were prepared by mixing the required mass of tetrasulfonated-phthalocyanine with water/aqueous solution in the appropriate wt.% ratio in screw-capped vials, followed by heating with stirring to approximately 345 K for between 30-60 min in order to achieve sample homogenisation. Samples were then allowed to cool to ambient temperature (296 ±2 K) with further experimentation carried out at this temperature. Solution resistivity was measured using a CDM210 conductivity meter equipped with a four-pole CDC511T conductivity cell (Radiometer).

X-ray scattering measurements were undertaken through filling capillary tubes with the viscous sample, placed into a MAR345 diffractometer with a 2D image plate detector (Cu K_{α} radiation, graphite monochromator, λ=1.54 Å, 130-300 mm detector-sample distance, with exposure time of 30 min). Samples were heated between 297-355 K using a home-built capillary furnace in the presence of a magnetic field.

Electrochemical experiments were performed using a μAutolab Type III potentiostat, with a silver/silver chloride reference electrode, a nickel counter electrode, and a glassy carbon or platinum working electrode (of diameter 3.0 mm or 10.0 μm). Samples were degassed with argon for reductive electrochemistry, and working electrodes were cleaned and polished before every experiment, so that a clean surface was exposed to different locations of the sample for every change in experimental variable. Chronoamperometric transients were averaged over at least two runs prior to data analysis.

3 Results and Discussion

3.1 Synthetic Discussion

Organic synthesis of the below compounds was performed with the aim of obtaining suitable materials, as described above, for use in the surface modification of inorganic nanorods. Appropriate synthetic routes were investigated in order to achieve optimal yields for each step and any observed liquid crystalline phases were analysed for characterisation. MM2 energy minimisation was carried out using ChemBio3D Ultra 12.0 for the 3-dimensional representations of final products seen below.

3.1.1 Scheme 1: 5-(4'-pentylbiphenyl-4-yloxy)pentane-1-thiol

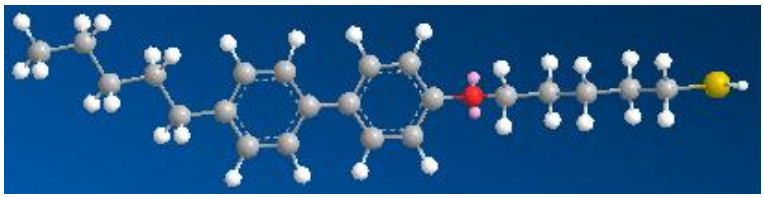

The compound 5-(4'-pentylbiphenyl-4-yloxy)pentane-1-thiol (6) was selected for synthesis due to the convenient availability of precursors 1 and 2 in the laboratory as well as the presence of a biphenyl ring, which typically may act as a rigid 'backbone' and is therefore conducive to the formation of calamitic liquid crystalline phases. Standard organic preparations were used to first form the phenol 3 and then in the addition of an alky chain with terminal double bond for conversion to the thioester and corresponding thiol, which would then be used as the binding group for attachment to gold and cadmium sulphide nanoparticles.

An overall yield of 41% was obtained for the 3-step reaction procedure after initial problems with the formation of 5 were overcome by replacing UV radiation with reflux of 4, the radical initiator and thioacetic acid. Whilst making melting point measurements using a heating stage in conjunction with an optical microscope, an intermediate state between isotropic liquid and crystalline solid was observed, see figure 3.1.

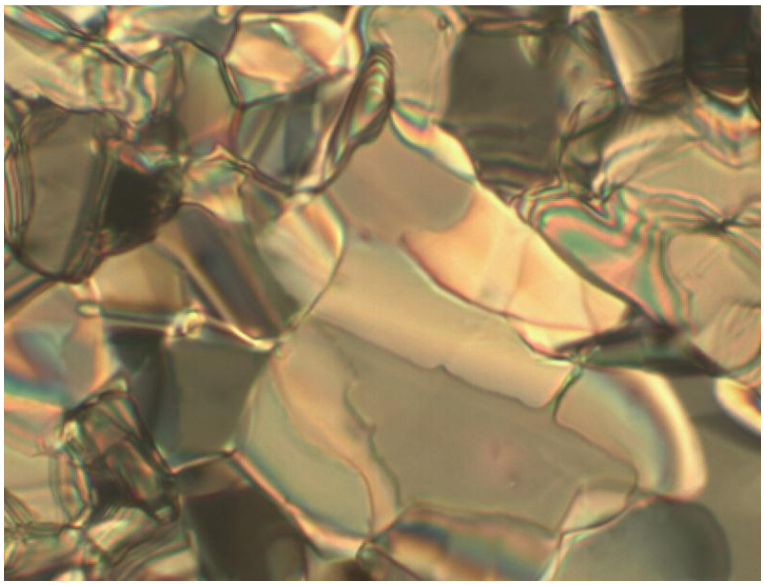

Figure 3.1 Polarised optical microscope image of 5 cooling from 50 to 40 °C.

The DSC curve below indicates the presence of a metastable phase when the thioester-terminated material (5) is cooled from the isotropic liquid, however no such phase was observed whilst the material underwent heating.

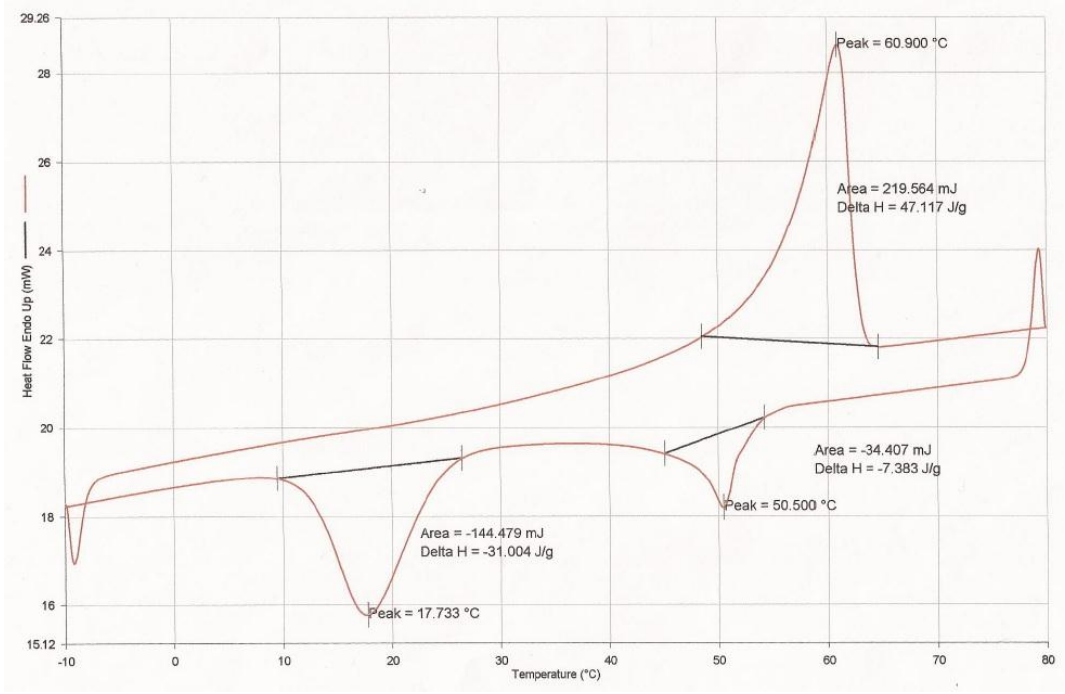

Figure 3.2 DSC curve for 5 showing metastable phase upon cooling.

No such metastable phase was observed within the DSC curve or polarised optical microscope images for the thiol-terminated material (6).

3.1.2 Scheme 2: 8-(4'-pentylbiphenyl-4-yloxy)octane-1-thiol

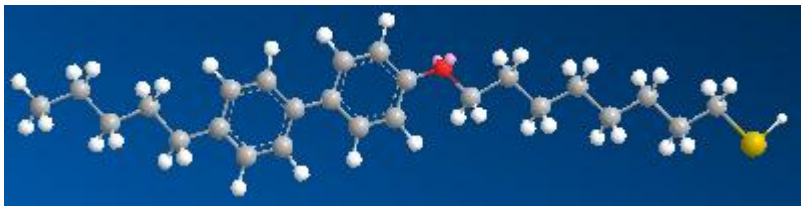

Structurally a similar material to 6, the compound 8-(4'-pentylbiphenyl-4-yloxy)octane-1-thiol (12) was synthesised using an alternative route in an attempt to increase the yields and flexibility of each reaction step. The length of alkyl 'spacer' chain was increased from five to eight carbons in order to investigate the effect on any liquid crystalline phases formed as well as the effect when used in the surface modification of nanorods. It was hoped that parallel synthesis could be employed to provide a more efficient route to varying both the rigid core section and the length of alky spacer within target materials.

However, the overall yield of 19% was lower when compared to scheme 1, largely due to the poor conversion of the hydroxyl group to the alkyl bromide (51% yield) and the extra reaction step required. Synthesis of compound 3 was also found to be more time-consuming than the Suzuki-Miyaura coupling process used previously, and for these reasons scheme 1 was preferred as the basis for future reactions involving the addition of a thiol-terminated alkyl chain to phenols. Unlike the intermediate 5 in scheme 1, no liquid crystalline or metastable phases were found in the synthesis of 12.

3.1.3 Scheme 3: 4-(4-propylcyclohexyl)phenol-based ligands

4-(4-propylcyclohexyl)phenol-based materials were selected for both their similarity to 6 and 12 as well as the availability of 4-(4-propylcyclohexyl)phenol within the laboratory. The addition of bromide-terminated alkyl chains *via* Williamson ether synthesis using a range of dibromoalkanes allowed for variation of the alkyl spacer between phenol and thiol groups. Reactions proceeded in a similar manner to those presented in scheme 1, with only the series incorporating the C_6 alkyl spacer exhibiting a vast reduction in the overall yield.

(17a) 4-(4-(4-propylcyclohexyl)phenoxy)butane-1-thiol

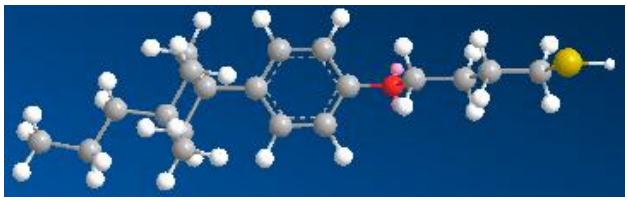

An overall yield of 54% compares favourably with that of scheme 1, with one less reaction step likely proving significant in the 13% increase. No liquid crystalline or metastable phases were observed upon heating and cooling, with figure 3.3 showing the texture observed of the crystalline solid under an optical microscope.

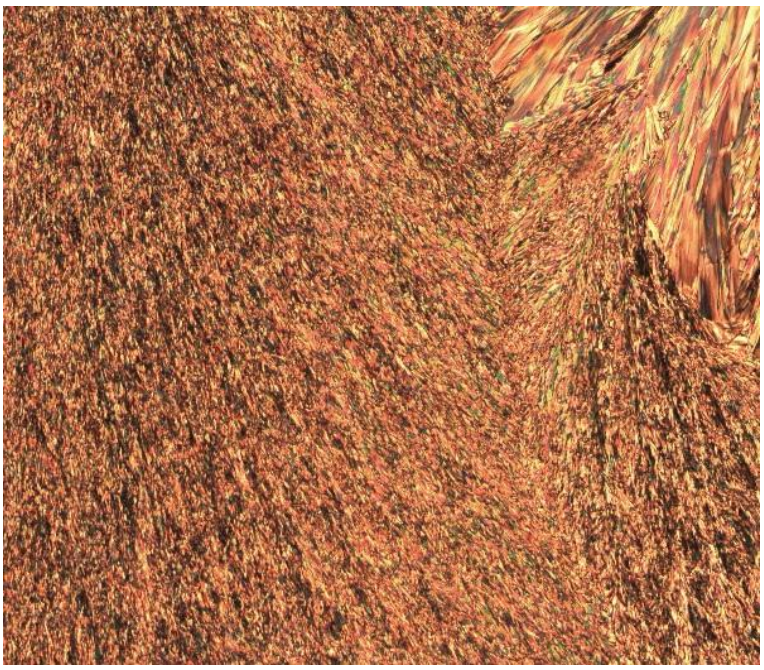

Figure 3.3 Polarised optical microscope image of 17a cooled to room temperature.

(17b) 6-(4-(4-propylcyclohexyl)phenoxy)hexane-1-thiol

With an overall yield of 1.5%, despite repetition of the synthetic route, only a tiny amount of the end product was obtained. Figures 3.4 - 3.7 show some of the textures observed using polarised optical microscopy during the heating and cooling of 17b and its intermediates:

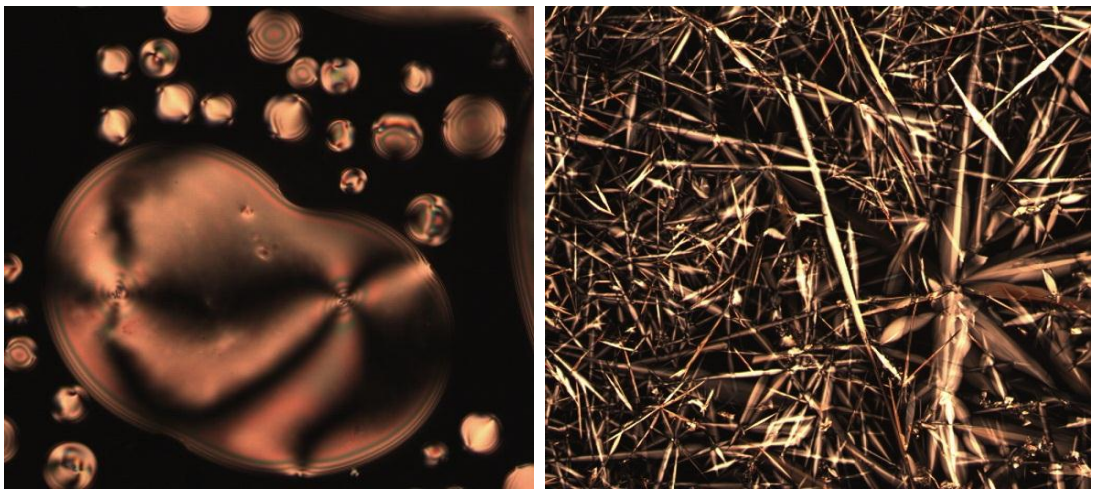

Figure 3.4 Polarised optical microscope images of (L) 15b cooling at 116 °C and (R) 16b after cooling.

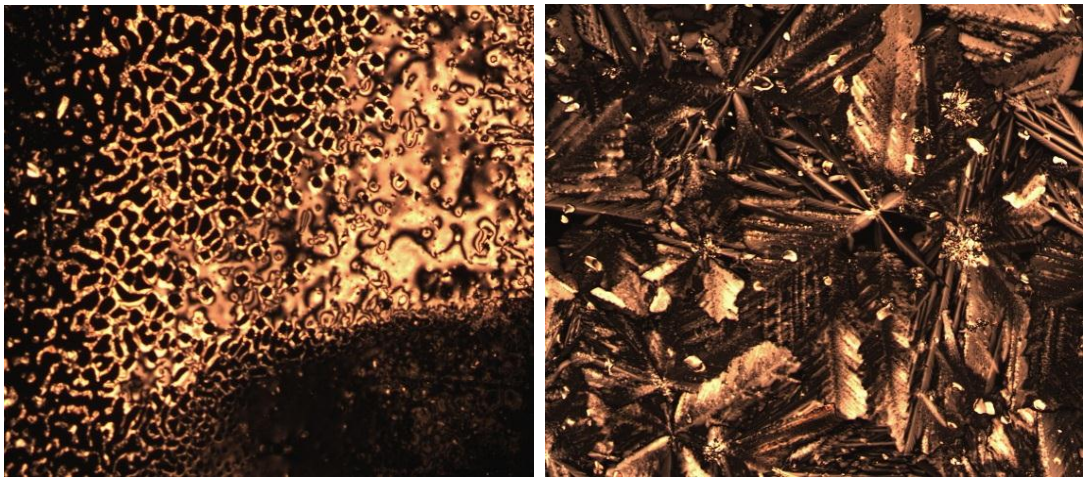

Figure 3.5 Polarised optical microscope images of (L) 17b at 30 °C and (R) 17b cooling to room temperature.

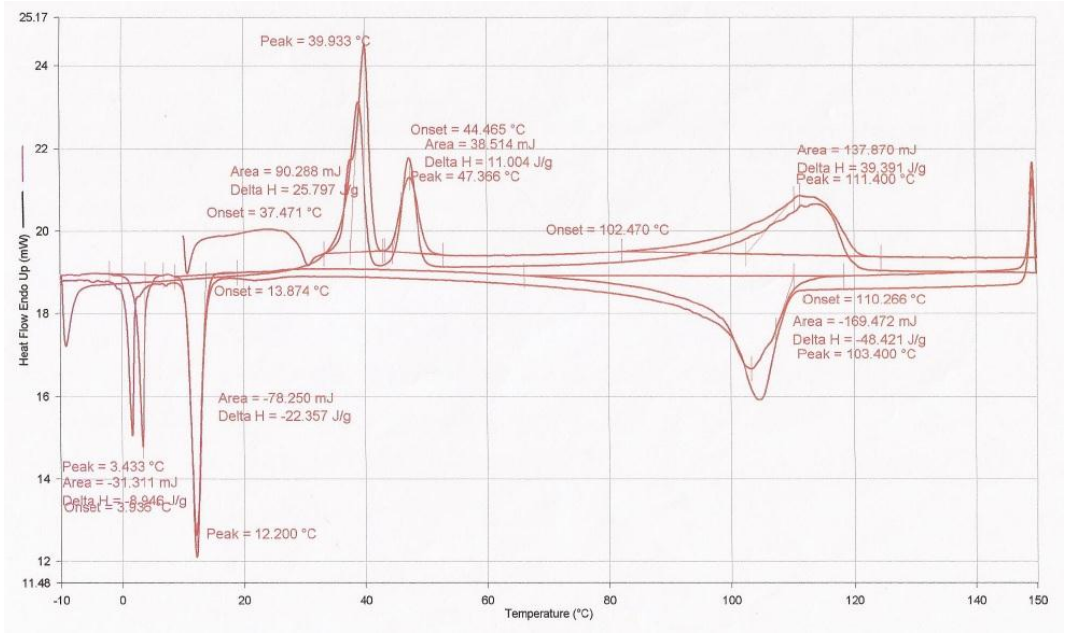

Figure 3.6 DSC curve for 15b showing multiple phase transitions.

The low yields made purification and analysis of each material less straightforward, and smaller amounts had to be used for the preparation of optical microscope slides as well as DSC samples, possibly leading to the formation of some of the 'textures' seen above. Surface point defects observed for 15b indicate the presence of a nematic or nematic-like liquid crystalline phase, and this was suggested by the DSC curve (figure 3.6) which showed phase transitions on heating at 39.9, 47.3 and 111.4 °C, and on cooling at 103.4, 12.2 and 3.9 °C.

Again, possible point defects were observed for 17b, as well as a 'leaf-like' texture was observed when the sample was left to cool from approximately 30 °C to room temperature, though the latter may have been owing to the low yield and therefore reduced amount of material used in preparation of microscope slides.

(17c) 8-(4-(4-propylcyclohexyl)phenoxy)octane-1-thiol

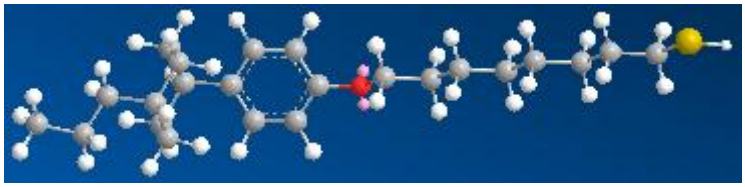

In a similar manner to 17a, no additional phases were seen upon heating and cooling of 17c or its intermediates. An overall yield of 41% was slightly lower than reactions involving the C_4 alky spacer, though none of the issues associated with the C_6 spacer were evident.

3.1.4 Scheme 4: 4-(4-pentylcyclohexyl)phenol-based ligands

Using the same approach as the synthesis of 17, 4-(4-pentylcyclohexyl)phenol-based materials were selected for both their similarity to 6 and 12 as well as the availability of 4-(4-pentylcyclohexyl)phenol within the laboratory. The main aim was to look at the effect of replacing the propylcyclohexyl moiety with the pentylcyclohexyl variant in terms of any changes in properties of the materials formed as well as the eventual effect when used in the surface modification of inorganic nanorods. Reactions proceeded in an almost identical manner to scheme 3, albeit with a slight reduction in the overall yields obtained, and similar difficulties were faced when reactions involving the C_6 spacer were investigated.

(21a) 4-(4-(4-pentylcyclohexyl)phenoxy)butane-1-thiol

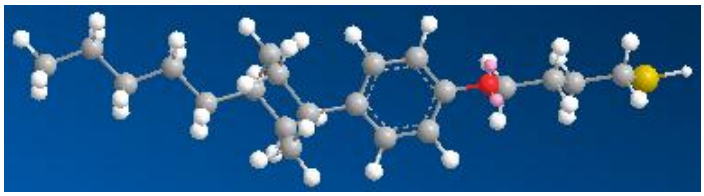

An overall yield of 41% is less than the yields obtained during the synthesis of materials 6 and 17a, and can possibly by attributed to the change from propyl to alkyl chain. The first step in which the bromide-terminated alky chain is added exhibited a significant drop in the yield obtained when compared to previous reactions.

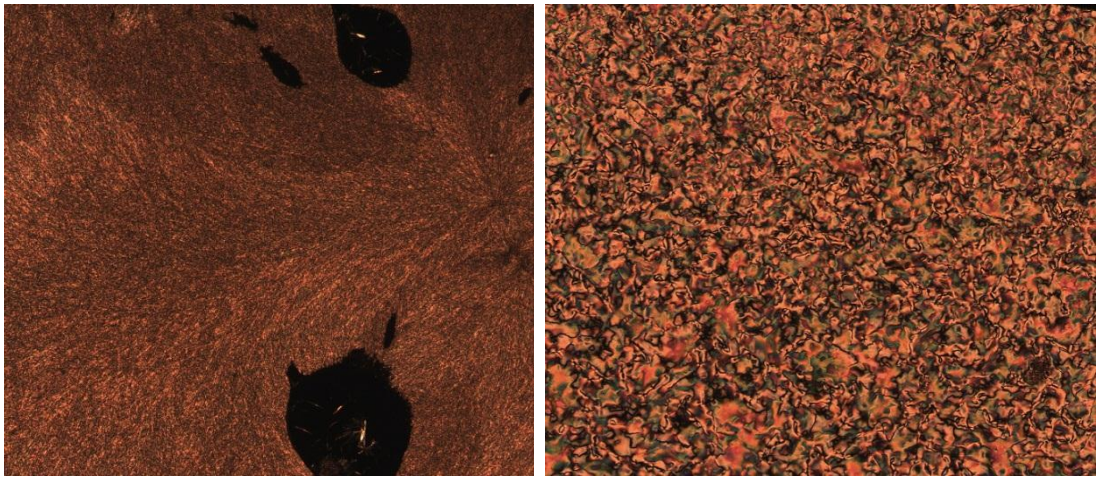

Figure 3.7 Polarised optical microscope images of 21a (L) at room temperature and (R) cooling at 30°C.

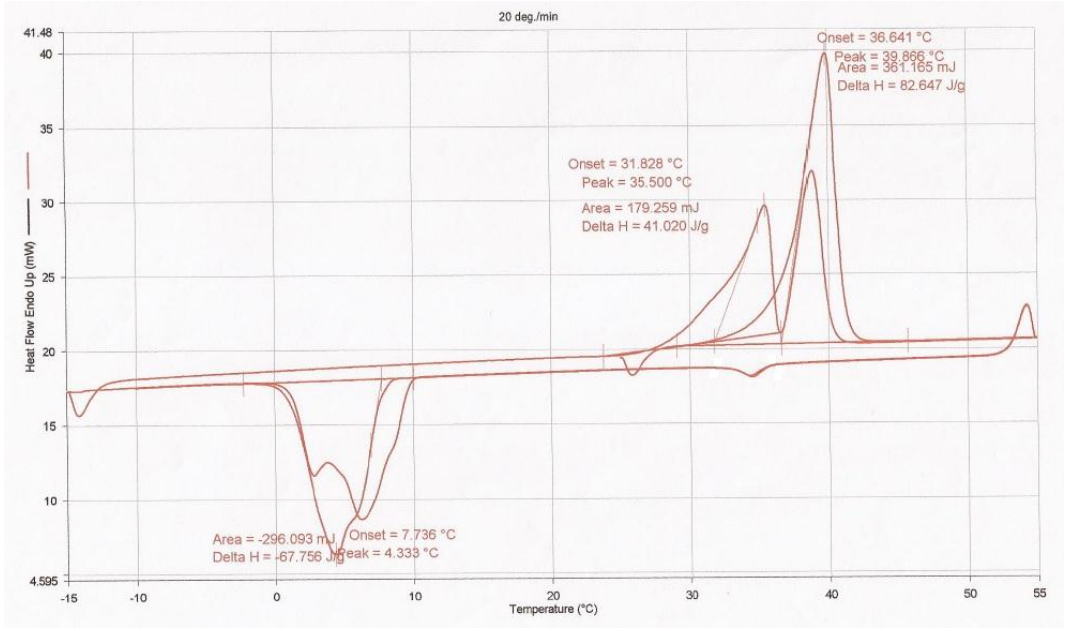

Figure 3.8 DSC curve for 21a indicating metastable phase on cooling.

Figure 3.7 illustrates the different textures observed for 21a at both room temperature and whilst being cooled from the isotropic phase. The second image shows a fluid, metastable phase with increased birefringence, with the sample having to be cooled to below room temperature to regain the crystalline texture originally observed. The DSC thermogram indicates the presence of a metastable phase when the material was cooled below 34.4 °C, however no such phase was observed whilst the material underwent heating, making it likely that the initial crystal structure of 21a differs from that of the same material after being heated to form an isotropic liquid.

(21b) 6-(4-(4-pentylcyclohexyl)phenoxy)hexane-1-thiol

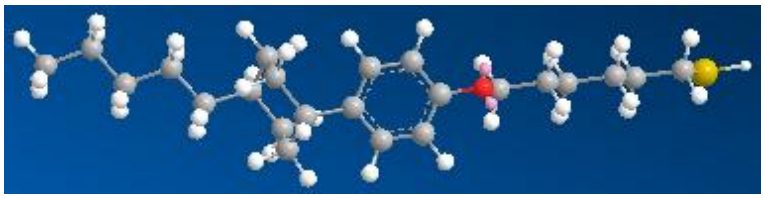

Much like the synthesis of 17b, the overall yield of 21b was very low at 1.5%, with just an 8% yield of 19b suggesting incompatibility between the 4-(4-pentylcyclohexyl)phenol and 14b. Even with repetition of the synthesis, the small amount of material produced led to difficulties in the purification and analysis of each material, especially noticeable in the DSC curves obtained which again showed a number of phase transitions along with obvious impurities.

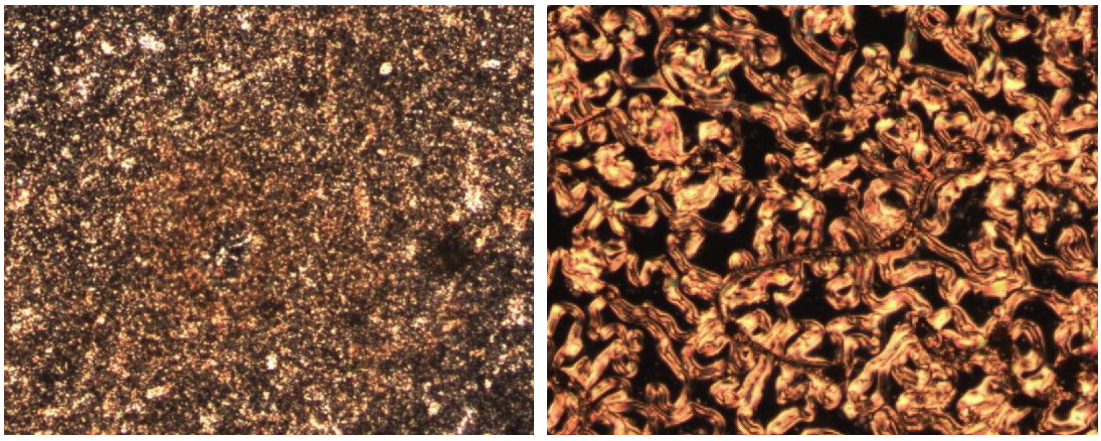

Figure 3.9 Polarised optical microscope images of 21b (L) at room temperature and (R) cooling at 30°C.

Figure 3.9 demonstrates that very similar differences in observed textures as 21a are observed when the material is cooled after initially heating to form the isotropic liquid. On cooling, a fluid, metastable phase with increased birefringence is again formed; however no DSC analysis was carried out due to the production of insufficient material.

(21c) 8-(4-(4-pentylcyclohexyl)phenoxy)octane-1-thiol

In a similar manner to scheme 3, the relative amount of the C_8 (21c) material produced was lower than that of the C_4 (21a), with an overall yield of 35% obtained. Addition of the dibromoalkane (14c) led to a material exhibiting a similar phase transition to those described previously, with a metastable phase observed between 29.5 and 15.8 °C whilst cooling from the isotropic liquid (figure 3.10).

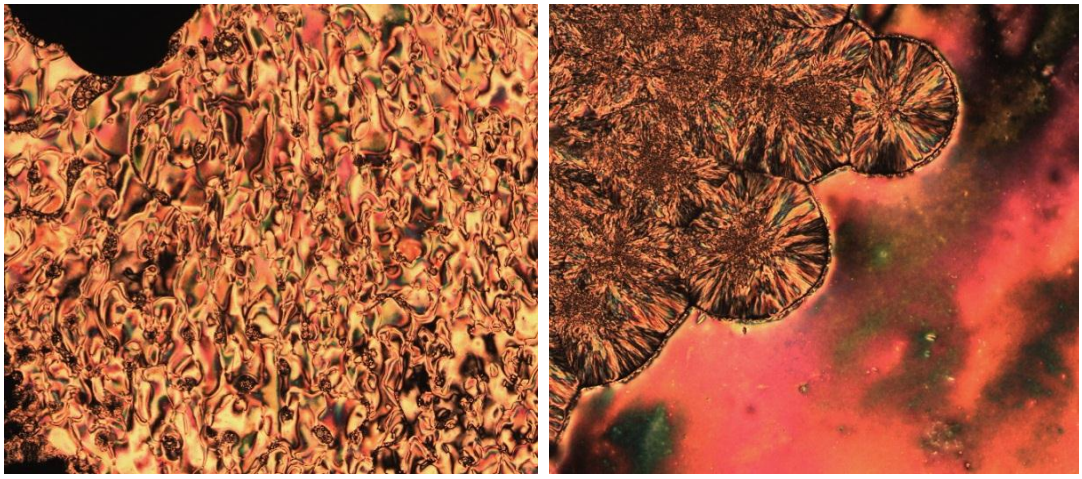

Figure 3.10 Polarised optical microscope images of 19c cooling from 30 °C.

Figure 3.11 shows 20c having cooled to room temperature after being heated to form the isotropic liquid (initially the surface texture looked almost identical to those seen for 21a and 21b at room temperature). However, once cooled to below approximately 15.8 °C, segregated focal conic domains typical of liquid crystalline mesophases can be observed, which on further cooling to 2.2 °C crystallise to re-form the original crystal structure.

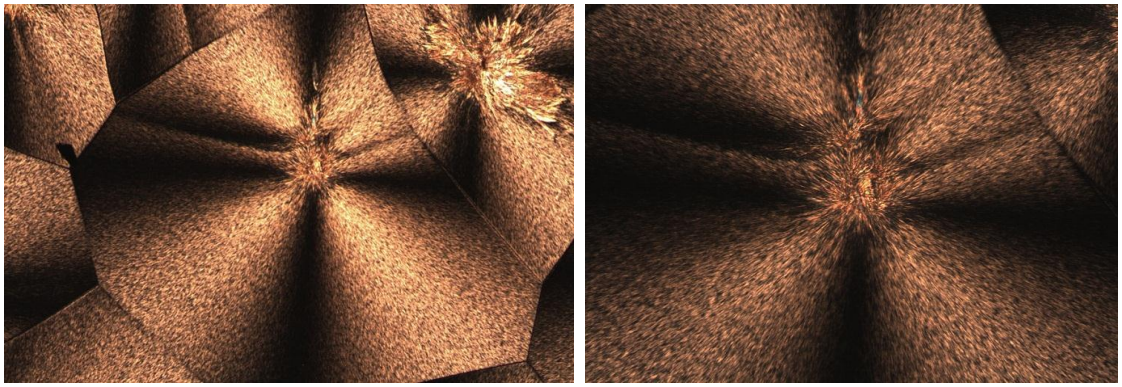

Figure 3.11 Polarised optical microscope images of 20c cooling to room temperature.

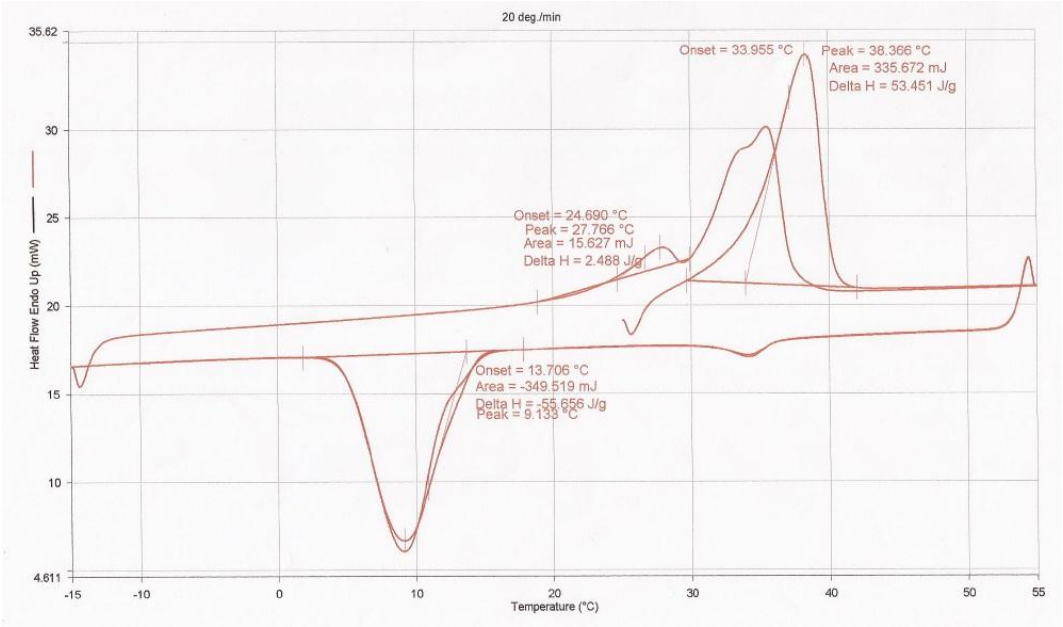

Figure 3.12 DSC curve for 21c indicating the presence of a metastable phase on cooling.

Finally, 21c showed similar behaviour to the previous final products, with a metastable phase observed on cooling below 34.2 °C and a return to the crystalline solid below 9.1 °C. The surface texture was again fluid and highly birefringent, and the DSC curve was comparable to those of the previous materials, with a small peak when cooling below the melting point indicating the transition from isotropic liquid to a fluid metastable phase.

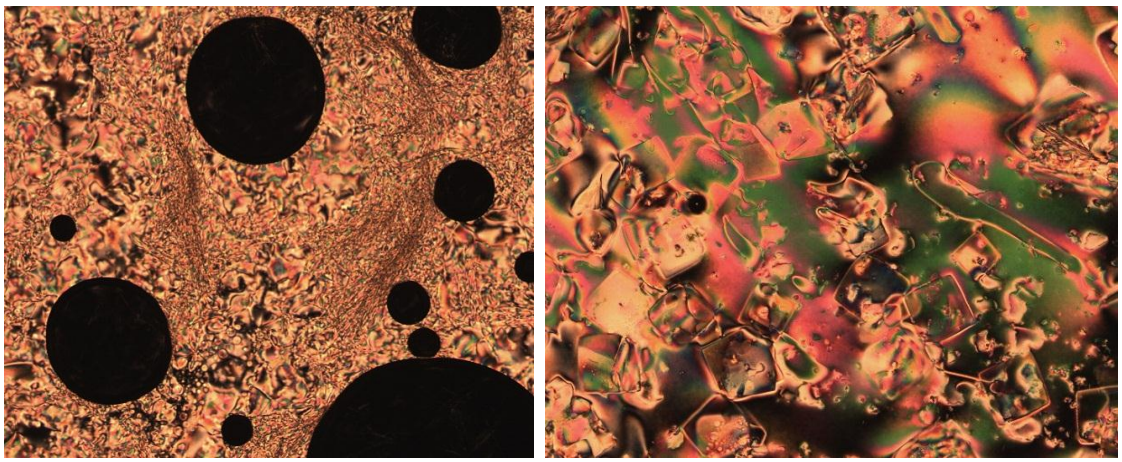

Figure 3.13 Polarised optical microscope images of 21c (L) at room temperature after cooling below 5 °C and (R) cooling at 25 °C.

3.2 Synthesis of Gold Nanorods

Gold nanorods were synthesised according to the solution-based seed-mediated methods described in section 2.5.1. UV-vis absorbance measurements were used to identify the λ_{max} and relative absorbance of the TPB and LPB, as well as the absorbance max ratio, A_{LPB}/A_{TPB}.

Figure 3.14 below shows a typical UV-vis absorbance spectrum for gold nanorods. In most cases the TPB and LPB were clearly resolved and an absorbance attributed to CTAB, by means of a blank CTAB in water UV-vis investigation, was observed between 950 and 1000 nm.

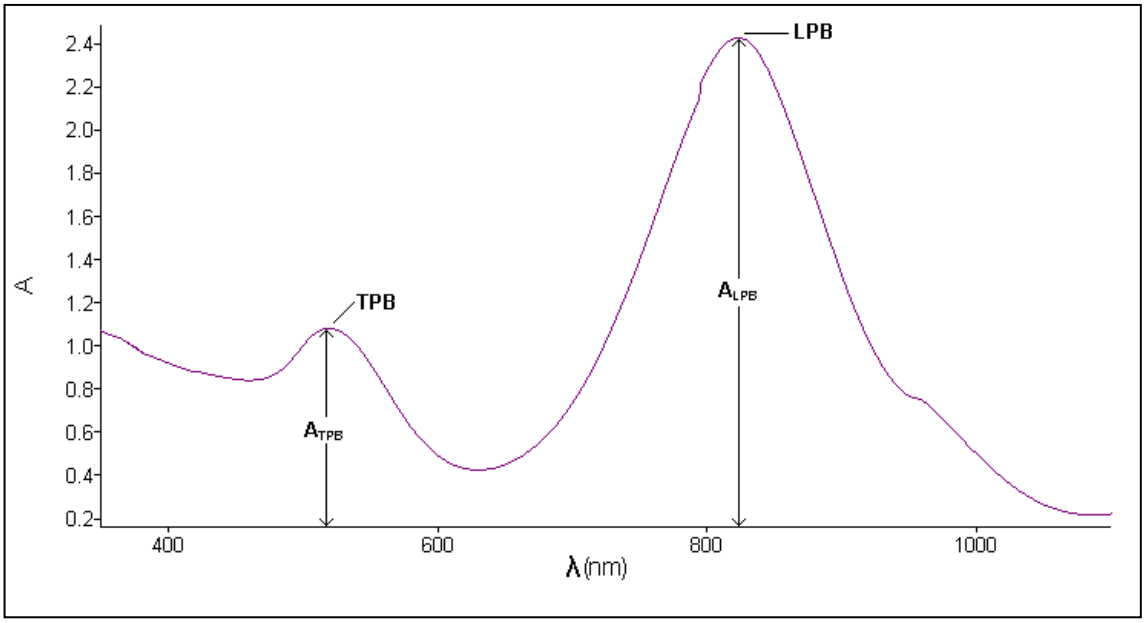

Figure 3.14 Sample UV-vis absorbance spectrum for synthesised aqueous gold nanorods (AuS9).

3.2.1 Seed-mediated Gold Nanorod Synthesis

Table 3.1 below provides a summary of the UV-vis data for the different syntheses of gold nanorods, including the ratio A_{LPB}/A_{TPB} as a measure of the relative proportion of nanorods formed compared to spherical nanoparticles. Also included are theoretical estimates of the aspect ratio, calculated using the wavelength of maximum absorption for the LPB in Equation 1.1, along with the mean values for aspect ratio measured from TEM images of each sample. For method AuS6 the UV-vis absorbance spectra indicated little or no nanorods in the sample which was confirmed by TEM. The data below obtained from TEM images represents nanorods, with spherical nanoparticles typically being excluded from mean values of nanorod dimensions and aspect ratios as well as the standard deviation.

Method	λ_{TBP} (nm)	λ_{LPB} (nm)	A_{LPB}/A_{TPB}	AR (calc)	AR (TEM)
AuS1	539.14	726.52	0.18	3.21	2.39
AuS2	538.00	634.50	1.37	2.26	3.64
AuS3	546.79	836.02	2.11	4.35	4.76
AuS4	528.75	714.40	1.44	3.09	3.18
AuS5	507.18	863.73	4.49	4.64	4.73
AuS6	553.63	733.53	0.27	3.29	-
AuS7	553.96	737.07	0.64	3.32	6.07
AuS8	511.29	898.00	2.80	5.00	4.05
AuS9	518.98	824.85	2.23	4.24	4.26

Table 3.1 Summary of UV-vis absorbance spectra for synthesised gold nanorods.

Table 3.2 below provides a summary of the TEM data and statistical analysis performed for the different syntheses of gold nanorods performed. The percentage yield of nanorods, "NRs %", is the percentage of nanoparticles observed in the TEM images which could be classed as nanorods, having aspect ratios of approximately 2 or higher.

Method	Length (nm)	Width (nm)	AR	SD (AR)	%RSD (AR)	NRs %
AuS1	44.63	19.01	2.39	0.59	24.69	8.70
AuS2	47.90	13.55	3.64	1.83	50.27	25.08
AuS3	39.82	8.69	4.76	1.30	27.25	68.82
AuS4	21.73	6.91	3.18	0.63	19.81	62.73
AuS5	36.53	7.82	4.73	1.08	22.83	90.10
AuS6	-	-	-	-	-	n/a
AuS7	79.71	13.25	6.07	2.13	35.12	21.43
AuS8	27.98	6.85	4.05	0.92	22.72	57.63
AuS9	30.29	7.18	4.26	0.83	19.48	52.52

Table 3.2 Mean values of length, width and aspect ratio, standard deviation and relative standard deviation of aspect ratios, and the percentage of nanorods from statistical analysis of TEM images.

Method 1 (AuS1)

The UV-vis spectra obtained for gold nanorods produced *via* method 1 showed that nanorods were produced in low yield relative to spherical nanoparticles, giving an absorbance max ratio of 0.18. This was confirmed by TEM, Figure 3.15 below shows many more spherical particles than anisotropic particles, which is somewhat expected due to the reported lower yields of nanorods when using citrate-capped seeds and a three-step synthesis without the assistance of silver nitrate.[14]

In addition, this synthesis was unknowingly performed using CTAB obtained from Aldrich which has been found to contain an iodide impurity concentration which is detrimental to nanorod formation.[34]

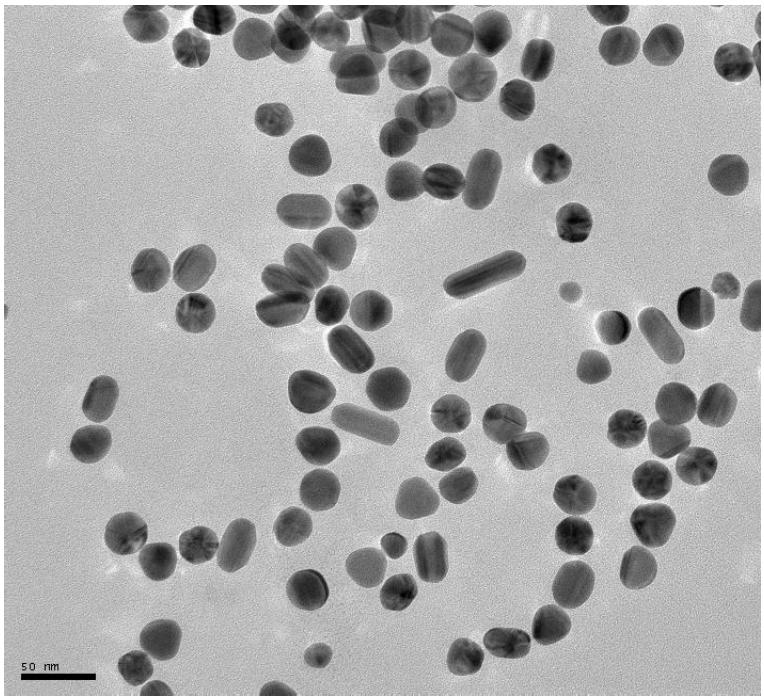

Figure 3.15 TEM image of gold nanoparticles synthesised using method 1.

The spherical nanoparticles observed in TEM images were large in size compared to the nanorods which is consistent with literature reports of citrate-capped gold seeds, which are typically found to be larger in diameter than CTAB-capped seeds.[14]

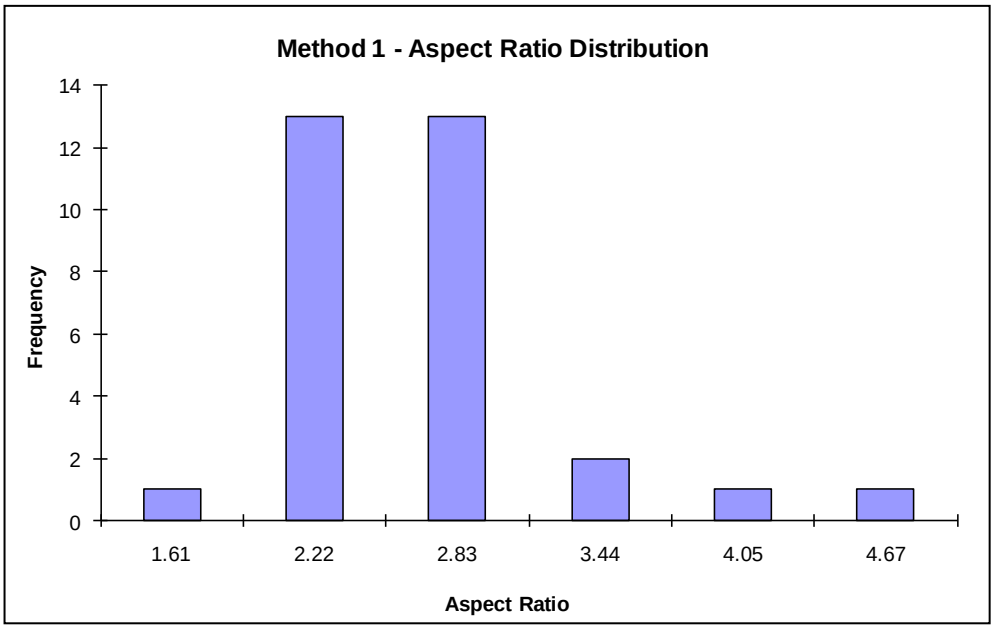

Figure 3.16 Aspect ratio distribution for gold nanorods synthesised using method 1.

Figure 3.16 shows the distribution of aspect ratios for gold nanorods synthesised using this method. Due to a relatively low amount of nanorods produced, 8.70% yield compared to the total number of nanoparticles observed in TEM images, the distribution does not fit the normal distribution, and no localised alignment is observed. UV-vis absorbance spectra obtained two months after synthesis showed a dramatic reduction in the absorbance max ratio, indicating a decrease in nanorod concentration due to their instability in aqueous solution, most likely transforming to more stable spherical nanoparticles.

Method 2 (AuS2)

A 'scaled up' version of method 1 was performed. The UV-vis spectra obtained for gold nanorods produced *via* method 2 showed that nanorods were produced in greater yield than spherical nanoparticles, giving an absorbance max ratio of 1.37. The predicted aspect ratio of 2.26 was lower than the average aspect ratio calculated from TEM images, 3.64. The paper by Zubarev *et al*.[53] mentions a "barely noticeable thin film" of precipitated nanorods formed around the insides of the glassware during the reaction, which was not noticeable in our reaction, possibly due to an excess of CTAB. The CTAB in this experiment and all future experiments was obtained from Sigma and so according to the work mentioned above contained low enough iodide impurity concentrations so as not to inhibit the formation of gold nanorods.

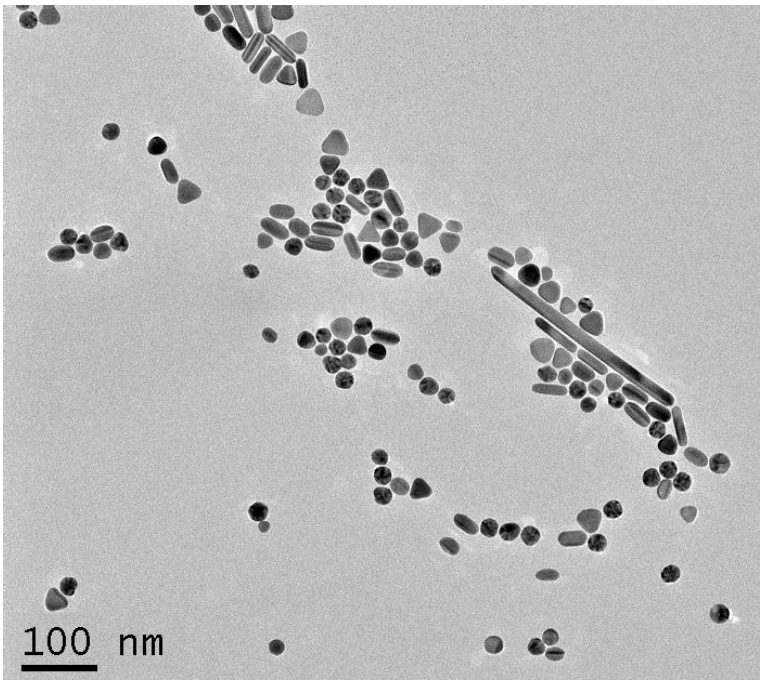

Figure 3.17 TEM image of gold nanoparticles synthesised using method 2.

Some localised alignment of nanorods was observed in the TEM images as nanorods with a higher average aspect ratio of 3.64 and a higher absorbance max ratio of 1.37 compared to method 1 were observed. The distribution of aspect ratios from TEM images showed that although most nanorods were close to the mean aspect ratio, some with much greater aspect ratios were produced.

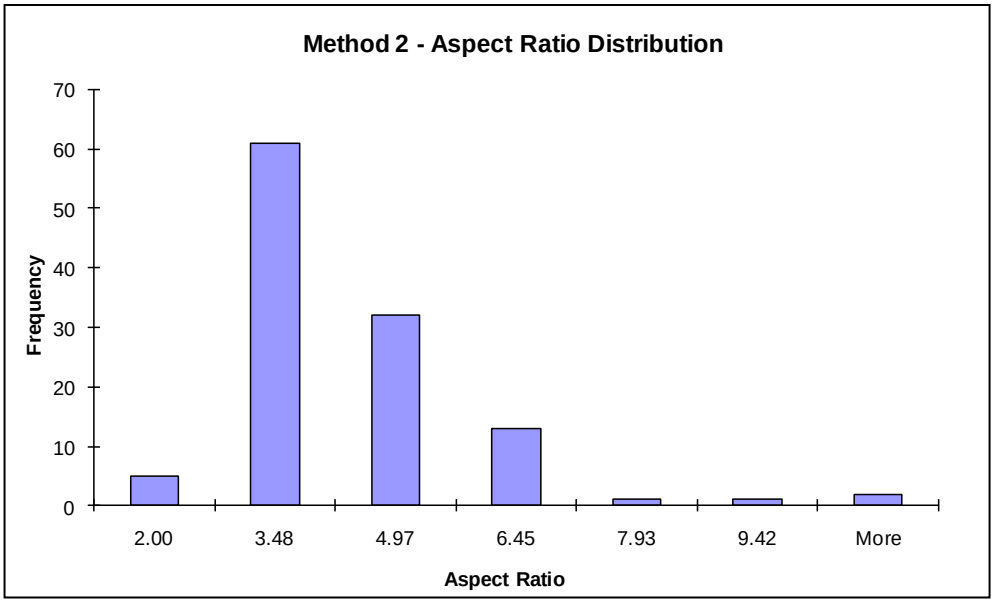

Figure 3.18 Aspect ratio distribution for gold nanorods synthesised using method 2.

Method 3 (AuS3)

An increase in the absorbance maximum ratio was observed compared to non-Ag(I)-assisted approaches, indicating an increase in the amount of nanorods produced relative to the number of spherical nanoparticles. This was later confirmed by TEM analysis, which returned a relative nanorod yield of 68.8% and showed areas of localised nanorod alignment, although the overall concentration of nanorods was not high enough to allow alignment over relatively large areas.

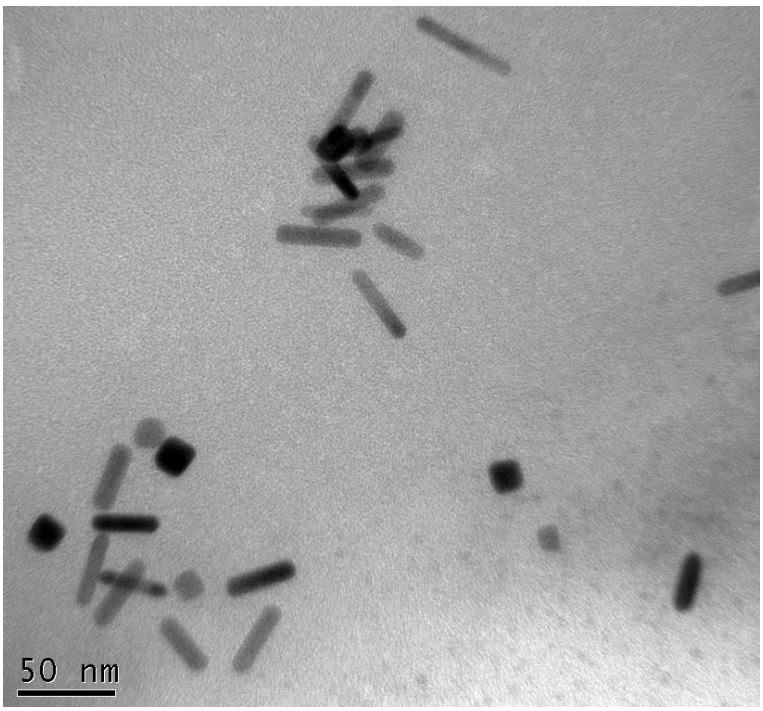

Figure 3.19 TEM image of gold nanoparticles synthesised using method 3.

Aqueous nanorod solutions prepared using this approach were also left to age for seven days in order to further increase the nanorod aspect ratio, as detailed in the original publication,[45] however, no further increase in aspect ratio was seen in the absorbance maximum ratio or TEM images. Figure 3.20 indicates that the nanorods synthesised using method 3 showed an improvement in monodispersity compared to the previously investigated stepwise approach, with a %RSD of 27.25 compared to 50.27 for method 2.

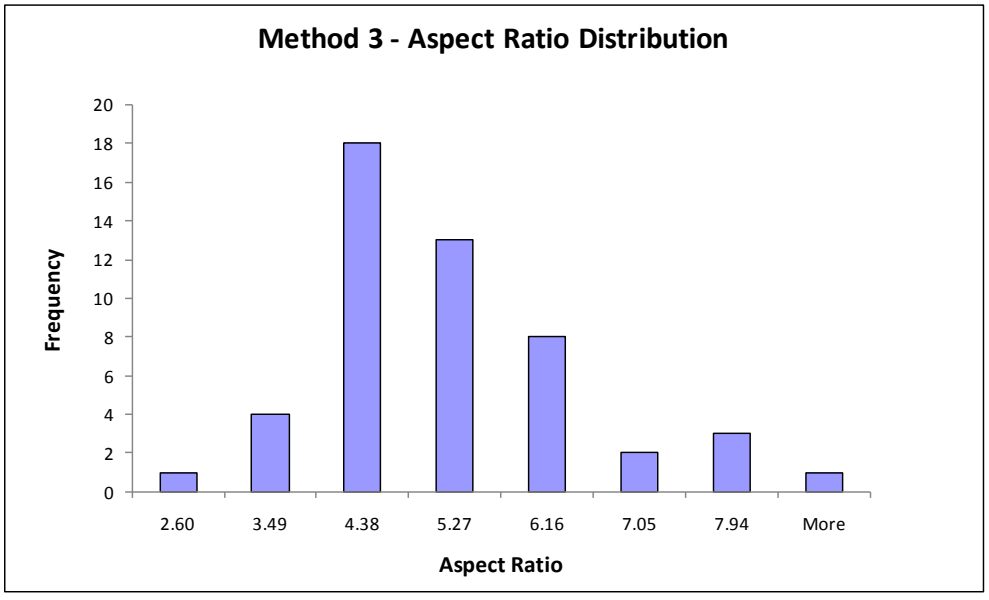

Figure 3.20 Aspect ratio distribution for gold nanorods synthesised using method 3.

Experiments were performed in a similar manner to those described within the literature, with variation of the ratio of BDAC to CTAB in the surfactant mixture, and it was observed that this ratio played a key role in the aspect ratio and relative yield of nanorods formed. However, it was also determined that the use of a surfactant mixture of BDAC and CTAB did not lead to any significant improvement over the Ag(I)-assisted synthesis of gold nanorods using only CTAB, as discussed below.

Method 4 (AuS4)

Optimisation of the gram-scale synthesis of gold nanorods was carried out. Table 3.3 below shows the effects of varying the concentrations of silver nitrate, sodium chloride and cyclohexane, as well as modifications to the procedure. Previous work investigated various different reducing agents in place of sodium borohydride and ascorbic acid, however these were generally found to be unsuitable due to the increased temperatures required leading to a reduction in the number of anisotropic CTAB micelles formed.[55]

For reactions in which gold nanorods were not obtained, i.e. no TPB was observed in the UV-vis absorbance spectrum, the final three columns read “n/a”. Although other samples showed an increase in aspect ratio or absorbance maximum ratio, the parameters used in the preparation of sample 2 appeared to yield the optimum combination of nanorod aspect ratio as well as number and relative yield of nanorods produced. However, over the course of repeating the experiment multiple times in order to vary different parameters or produce nanorod solutions for surface modification reactions, it was found that results using the same method were difficult to reproduce. Many reactions were unsuccessful and produced a large majority of thermodynamically-favoured spherical nanoparticles, and so it was decided that overall this method was unsuitable for nanorod synthesis; the lack of reproducibility probably due to the highly specific reaction conditions required to allow growth kinetics that favour the formation of anisotropic nanoparticles mentioned above.

Sample	AgNO3	NaCl	NaBH4	C6H12	Notes	λ_{LPB}	A_{LPB}/A_{TPB}	AR (calc)
	M	eqv.	M	M		nm		
1	**0.025**	2	0.01	0	**sonication**	n/a	n/a	n/a
2	0.25	2	0.01	0	stirring	700.20	1.159	2.94
2b	0.25	2	0.01	0	**stirring**	696.09	1.200	2.90
3	0.25	2	0.01	0	**sonication**	n/a	n/a	n/a
4	**0.59**	2	0.01	0		702.84		2.97
5	**0.1**	2	0.01	0		691.77		2.86
6	**0.3**	2	0.01	0		n/a	n/a	n/a
7	0.25	2	0.01	**0.1**		648.94	1.114	2.41
8	0.25	2	0.01	**0.05**		682.81	1.087	2.76
9	0.25	2	0.01	**1**		n/a	n/a	n/a
10	0.25	2	0.01	**0.01**		706.00	1.016	3.01
11	0.25	2	0.01	**0.005**		714.40	1.436	3.09
11b	0.25	2	0.01	**0.005**		702.95	0.980	2.97
12	0.25	2	0.01	**0.001**		692.27	0.820	2.86
13	0.25	2	0.01	0	**$NaBH_4$ (ice)**	n/a	n/a	n/a
14	0.25	**2**	0.01	0.005	**NaBr instead of NaCl**	747.95		3.45
15	0.25	**4**	0.01	0		682.87		2.76
16	0.25	**1**	0.01	0		692.07	1.398	2.86
17	0.25	2	0.01	0.005	**1/2 $HAuCl_4$**	682.87		2.76

Table 3.3 Variables in synthesis of gold nanorods using method 4.

Although the literature method specified the use of sonication during the reaction, sample 1 produced no LPB in the UV-vis absorption spectrum and no nanorods were observed in TEM images. Therefore stirring was used in place of sonication leading to the production of nanorods. Samples 7 to 12 looked at the effect of cyclohexane concentration on the aspect ratios and relative concentrations of nanorods produced, in accordance with investigations carried out by Törnblom *et al.* on the effects of solubilisation of aliphatic hydrocarbons on the size and shape of cylindrical CTAB micelles.[44] For sample 17, the note "1/2 $HAuCl_4$" signifies that the reaction was performed on a 50% scale compared to the other samples. In sample 14,

sodium bromide was used in place of sodium chloride in order to determine whether there was any benefit in the presence of additional bromide ions in the selective adsorption of CTAB to the growing gold nanorod surfaces, however, no improvement was observed. Figure 3.21 shows that nanorods produced using this approach displayed localised alignment, as sufficient nanorods were produced of high enough aspect ratio for Onsager theory (see above) to apply.

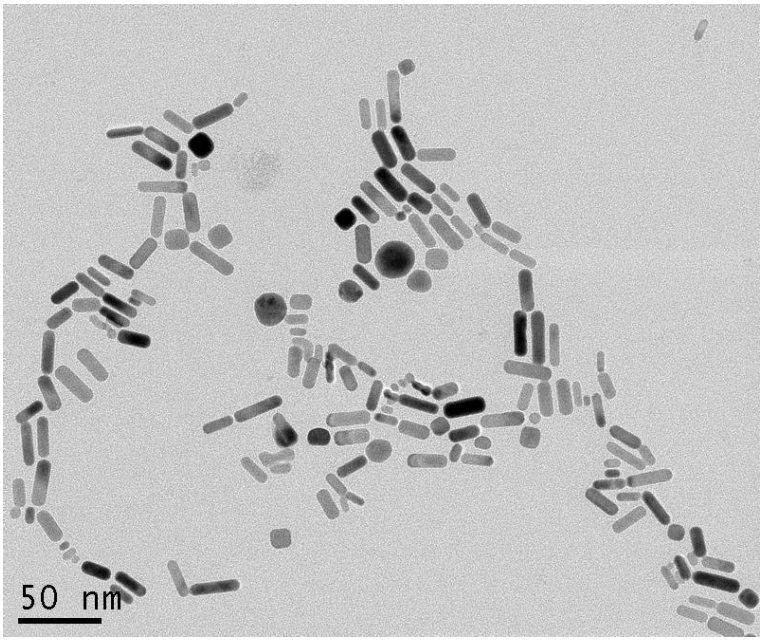

Figure 3.21 TEM image of gold nanoparticles synthesised using method 4.

Figure 3.22 (below) demonstrates that although there was a large spread of data, the normal distribution can be said to be approximately followed, probably due to the larger number of nanorods produced using this approach.

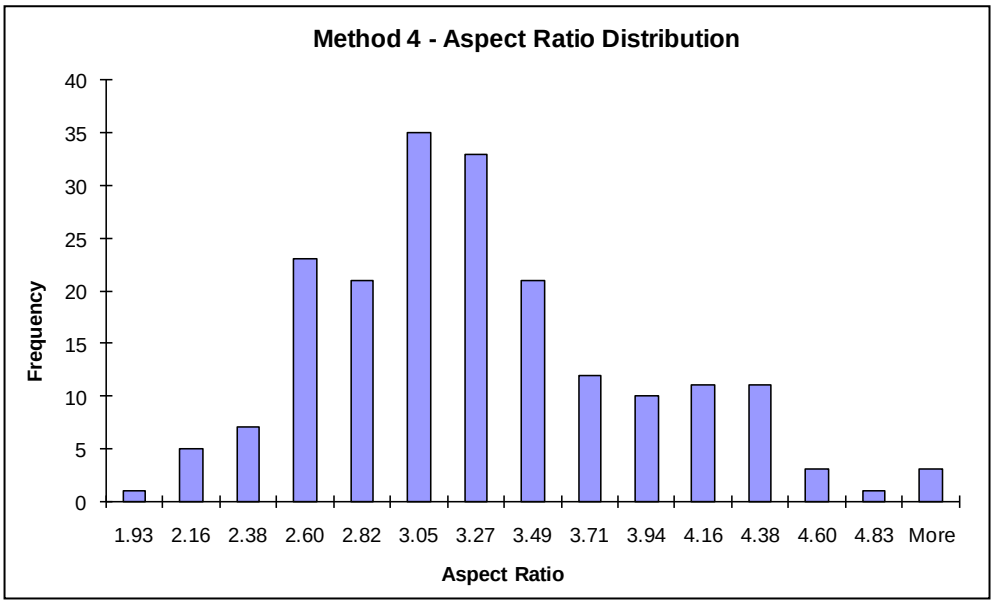

Figure 3.22 Aspect ratio distribution for gold nanorods synthesised using method 4.

Investigations into the stability of the aqueous gold nanorod solutions prepared at these higher concentrations were also carried out by means of UV-vis absorbance spectroscopy. UV-vis absorbance spectra obtained after one month indicated a reduction in the absorbance max ratio and therefore the concentration of nanorods relative to spheres. After three months of storage at room temperature, approximately 21 °C, the LPB corresponding to nanorod absorbance in the UV-vis spectra had almost completely disappeared, indicating substantial conversion of nanorods to more thermodynamically stable spherical nanoparticles. It is also possible that by keeping the solutions still over the time periods mentioned above, CTAB may have sedimented leading to a reduction in solution concentration and therefore a possible reduction in cylindrical micelles along with an increase in spherical micelles.

Method 5 (AuS5)

Another Ag(I)-assisted gold nanorod synthesis was performed, again leading to a high proportion of nanorods compared to spherical nanoparticles and an average aspect ratio approaching 5. This has the effect, as seen in figure 3.23, of allowing some localised alignment of the nanorods; however, the concentration was not sufficient so that larger areas of ordered nanorods were observed.

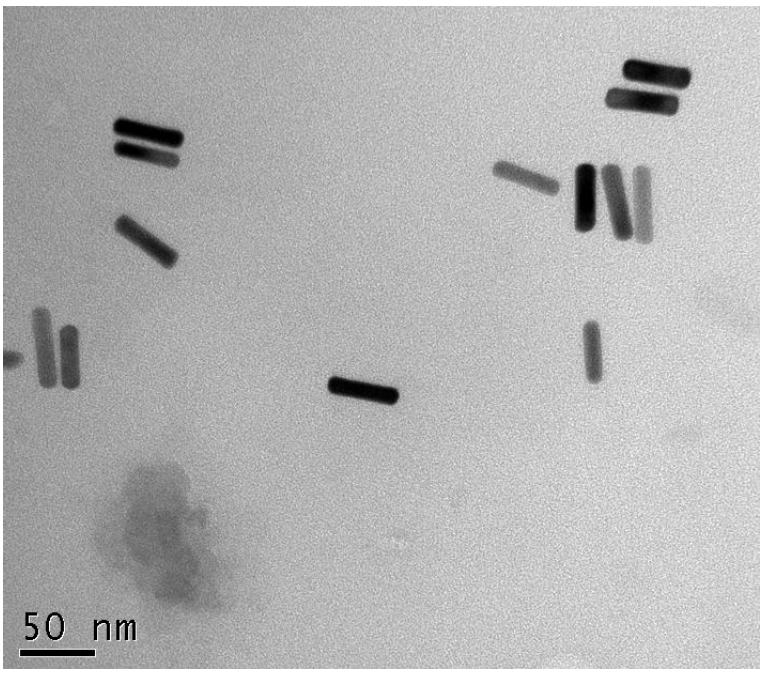

Figure 3.23 TEM image of gold nanoparticles synthesised using method 5.

The relative yield of nanorods compared to the total number of nanoparticles, taken from TEM images was the highest of the gold nanorods synthesis methods investigated at 90.1%. However, this was taken from only 112 nanoparticles counted from the series of ten TEM images acquired, and as figure 3.23 indicates, the concentration of nanorods produces was low compared to the gram-scale method described above. Figure 3.24 shows that the aspect ratio distribution favours nanorods of aspect ratio greater than 4, with few low-aspect ratio (< 3) nanorods produced.

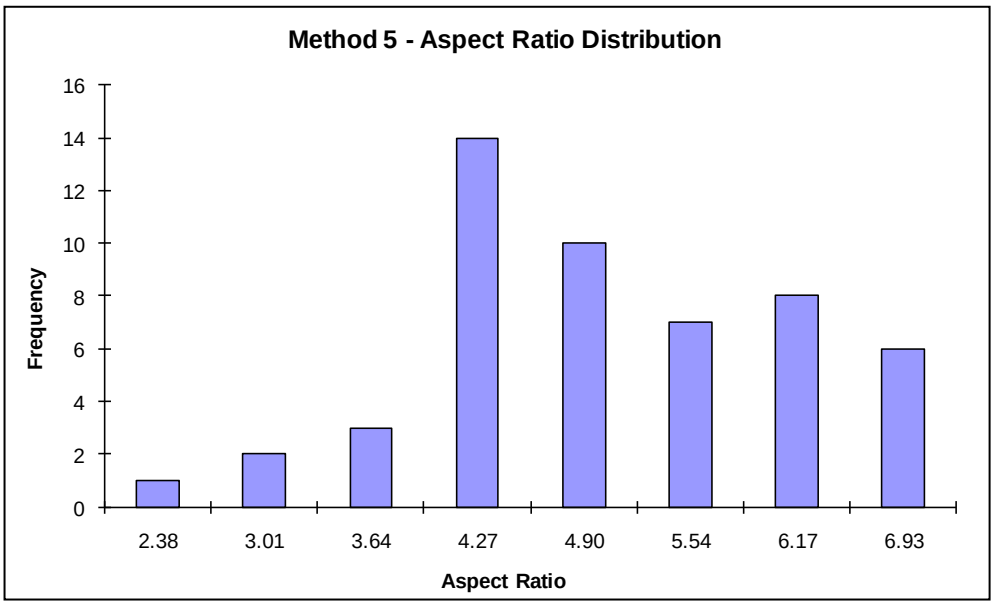

Figure 3.24 Aspect ratio distribution for gold nanorods synthesised using method 5.

The experimental procedure was modified to investigate the effects of dropwise addition of seed solution as carried out in method 9, and a significant increase in the absorbance max ratio and slight red-shift of LPB was observed in the UV-vis absorbance spectra.

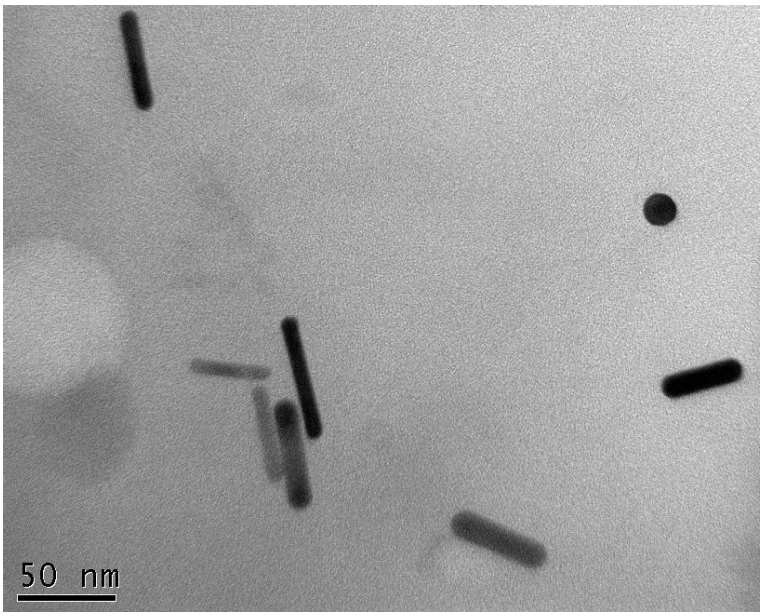

Figure 3.25 TEM image of gold nanoparticles synthesised using method 5 modified with dropwise addition of seed solution to growth solution.

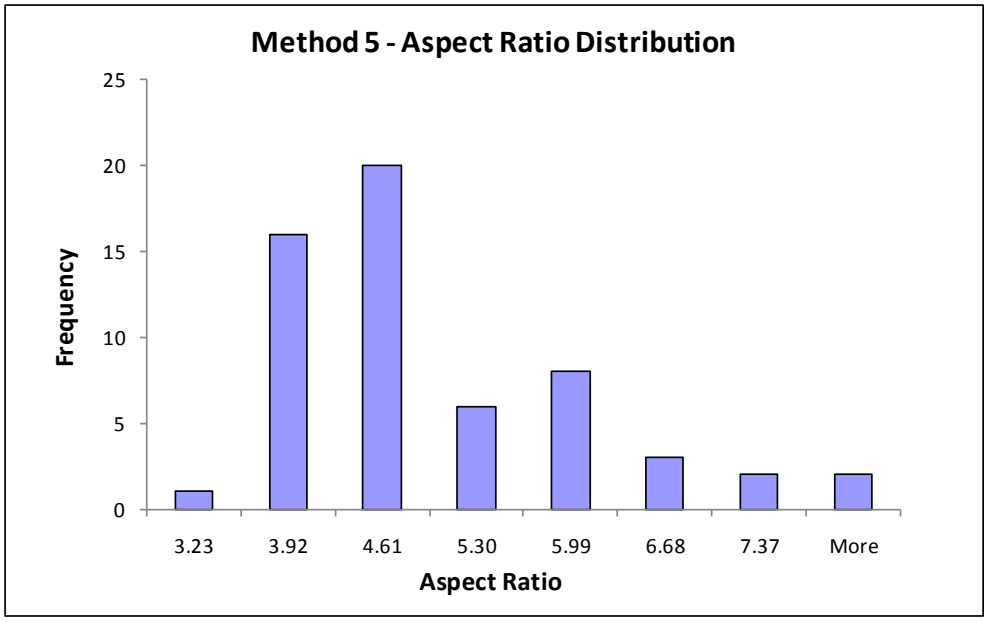

Figure 3.26 Aspect ratio distribution for gold nanorods synthesised using method 5 modified with dropwise addition of seed solution to growth solution.

In addition, attempts were made at increasing the concentration of nanoparticles in aqueous solution *via* rotary evaporation. UV-vis spectroscopy showed an increase in the absorbance compared to unconcentrated solutions, however a blue shift of the longitudinal plasmon band

of up to 10 nm was observed, indicating a slight reduction in the nanorod aspect ratios. A slight decrease in the absorbance max ratio was also observed, indicating a decrease in the percentage yield of nanorods relative to the total number of nanoparticles. As CTAB was visibly seen to be removed from the nanorod solution, along with water, it is possible that the concentration of CTAB was reduced enough so as to hinder the formation of cylindrical micelles or even to remove CTAB from the bilayer coating nanoparticles. This combined with the raised temperature necessary to evaporate the water would explain the reduction in the number of nanorods either *via* the formation of thermodynamically more stable spherical nanoparticles or aggregation of particles; therefore, further efforts into improving the concentration of nanorod solutions focused on improvement of the synthetic procedures.

Method 6 (AuS6)

A very low yield of nanorods relative to spherical nanoparticles was observed in both UV-vis absorbance spectra and TEM images. This may be due to unfavourable reaction kinetics or deviations from the experimental method used in the literature, and hence statistical analysis of the TEM images was not carried out for this approach.

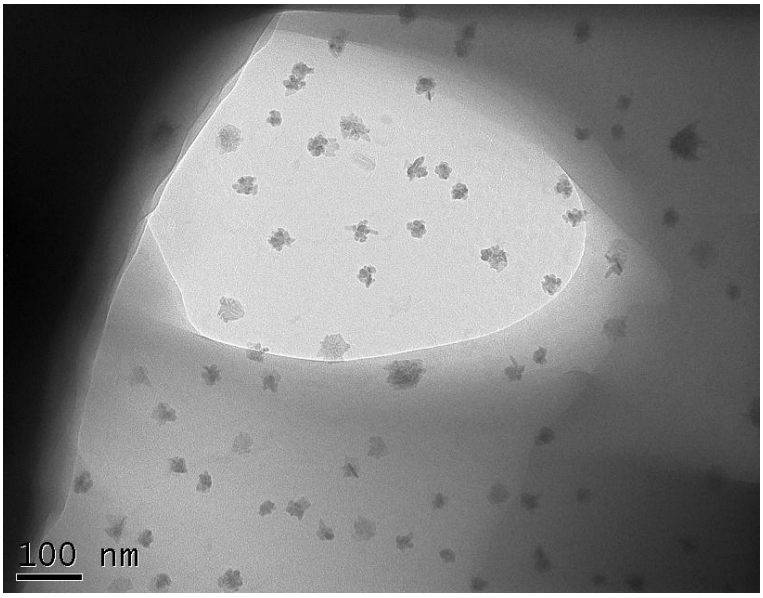

Figure 3.27 TEM image of gold nanoparticles synthesised using method 6.

Method 7 (AuS7)

A very low yield of nanorods relative to spherical nanoparticles was observed in both UV-vis absorbance spectra and TEM images. A mean aspect ratio of 6.07 from statistical analysis

indicates that this method was useful in the synthesis of high aspect ratio gold nanorods, however due to the low relative nanorod yield only five nanorods were present in the range of ten TEM images obtained and so further statistical analysis was not attempted. Again this was possibly due to unfavourable reaction kinetics or deviations from the experimental method used in the literature.

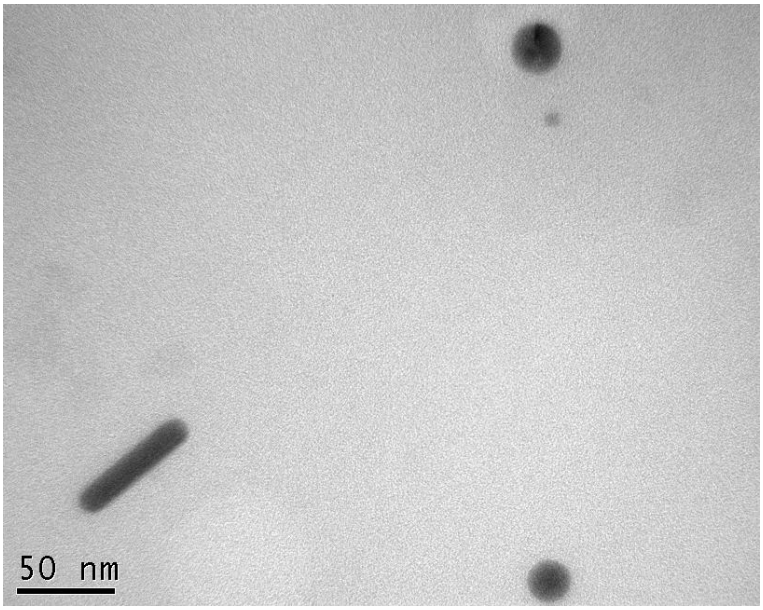

Figure 3.28 TEM image of gold nanoparticles synthesised using method 7.

Due to the difficulty associated with achieving control over the reaction conditions and sensitive kinetics of nanorod growth, increasing the number of steps is likely to increase the margin for error associated with the overall synthesis.

Method 8 (AuS8)

The one-step synthesis of gold nanorods using acetylacetone as reducing agent was found to be a much more straightforward and reproducible method, and as seen in figures 3.29 and 3.30, the nanorods aspect ratios were reasonably monodisperse and some localised alignment was observed. The mean aspect ratio of 4.05 compared well with nanorods synthesised using the standard sodium borohydride-ascorbic acid combination of reducing agents as did monodispersity with a %RSD of 22.7, however a relatively large amount of spherical nanoparticles were also produced.

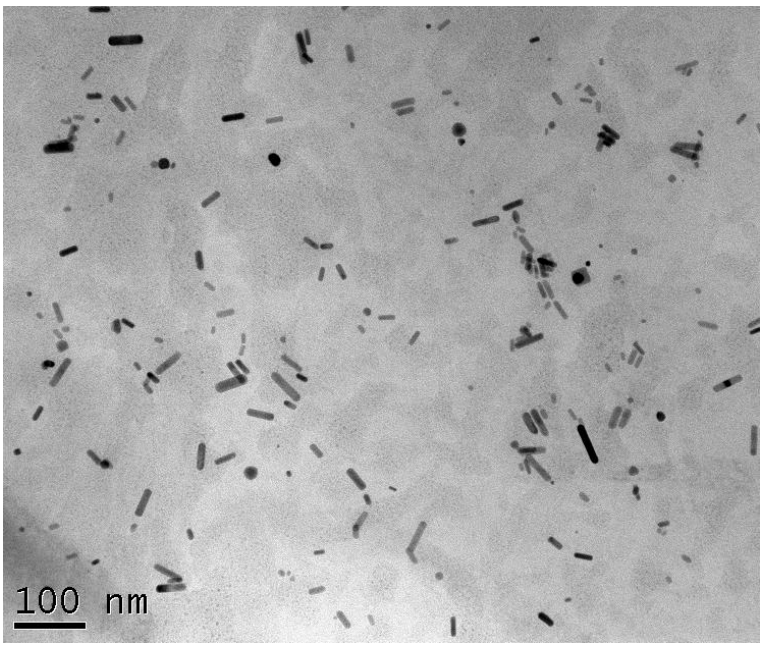

Figure 3.29 TEM image of gold nanoparticles synthesised using method 8.

Using this method, nanorods may be synthesised at different values of pH, which play a significant role in control over the rate of anisotropic growth as well as the shape and physical dimensions of the nanorods produced. Additionally, the concentrations of silver nitrate and acetylacetone used relative to the gold salt were found to affect the nanorod aspect ratio; and so this route may prove exciting as large-scale nanorod synthesis undergoes further development.

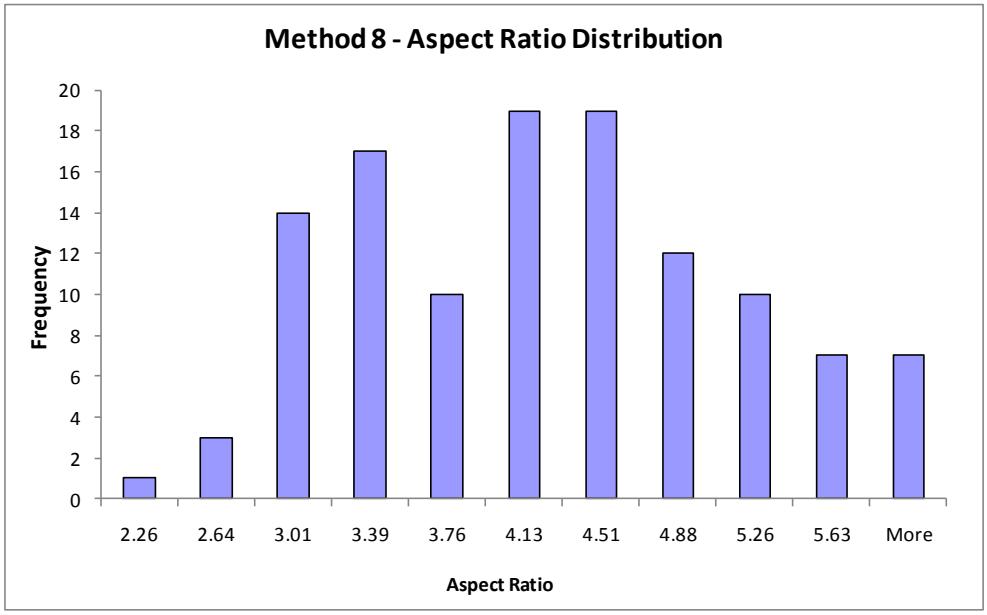

Figure 3.30 Aspect ratio distribution for gold nanorods synthesised using method 8.

Method 9 (AuS9)

The scaled-up synthesis of gold nanorods using standard Ag(I)-assisted growth method with higher gold salt concentrations and dropwise addition of seed solution led to a higher relative concentration of nanoparticles compared to most of the above approaches. The procedure was originally attempted with single-step addition of seed solution to growth solution; however this gave a much lower yield of nanorods, potentially due to changes in the growth rates of nanoparticles. It was noticed that keeping the seed solution at 40 °C for 15 minutes was important in this synthesis, with lower times leading to a reduction in the aspect ratios and relative yields of nanorods formed.

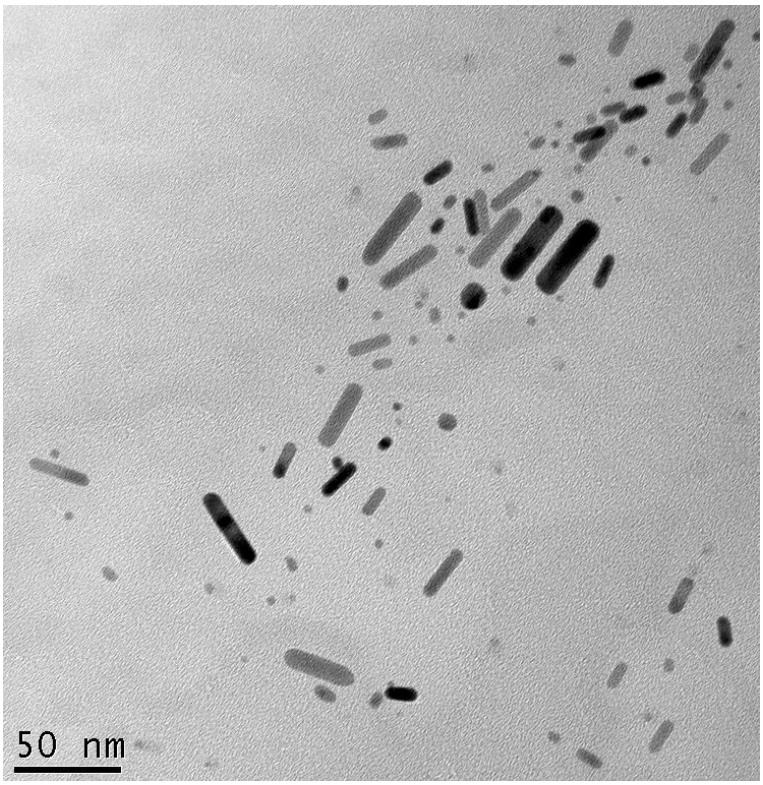

Figure 3.31 TEM image of gold nanoparticles synthesised using method 9.

Although figure 3.31 above shows nanorods of different sizes, the majority of nanorods produced using this approach were very similar in aspect ratio, with a %RSD of 19.48, the lowest of all of the gold nanorod synthetic approaches investigated. In addition, figures 3.32 and 3.33 show a good correlation between the normal distribution and the distribution of aspect ratios of nanorods produced using this method.

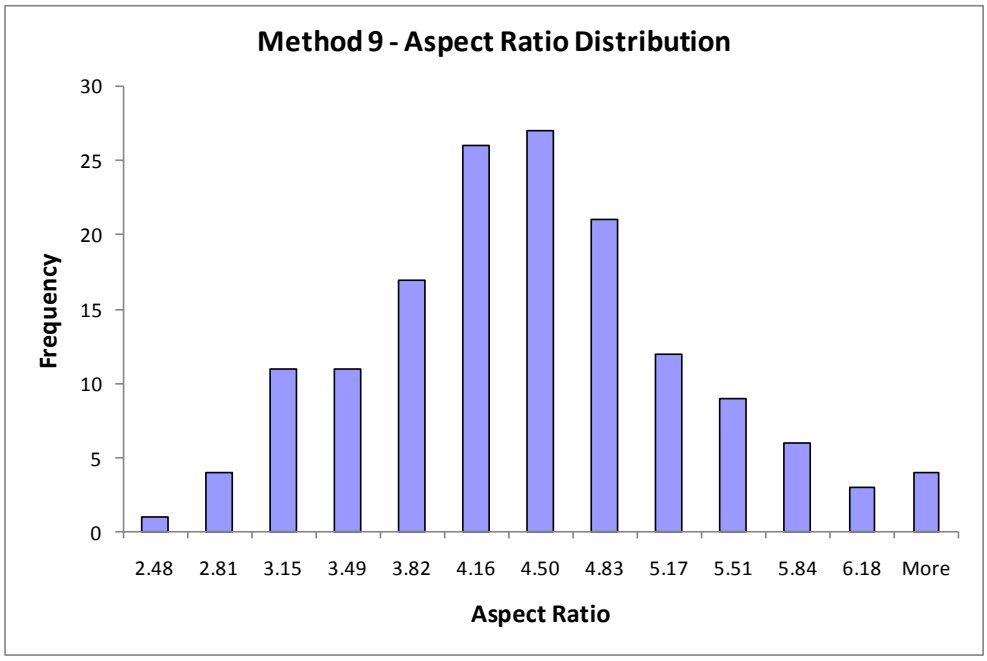

Figure 3.32 Aspect ratio distribution for gold nanorods synthesised using method 9.

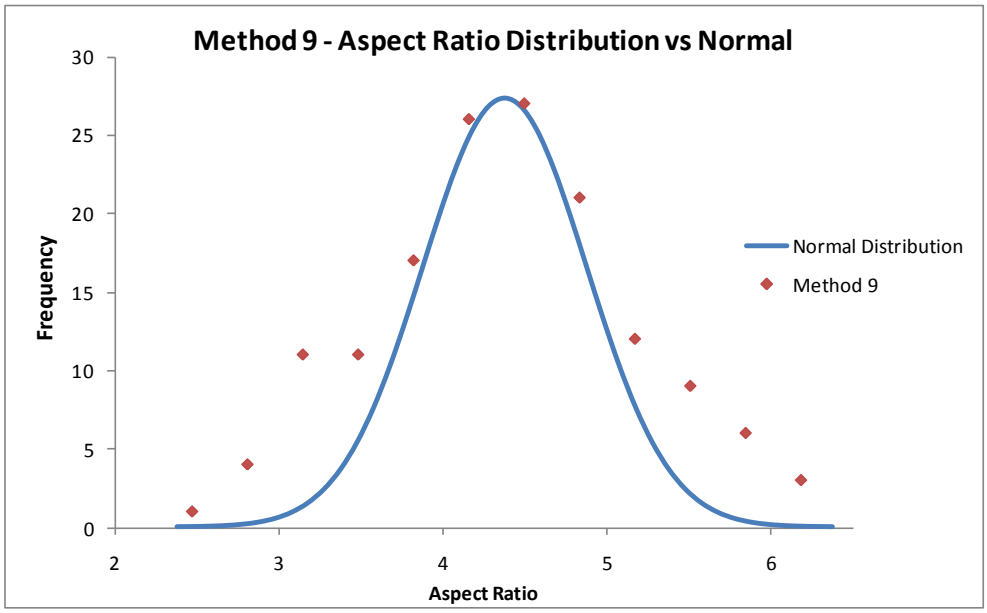

Figure 3.33 Comparison of gold nanorod aspect ratio distribution for method 9 with the normal distribution shows good fit of theoretical to experimental data.

Figure 3.33 compares the distribution of nanorod aspect ratios with the normal distribution, giving the best agreement of all synthesised gold nanorods in the investigations carried out. Due to the above factors, along with the relatively straightforward and time-efficient experimental procedure, nanorods synthesised using this approach were preferred for investigations into the surface functionalisation of gold nanorods.

3.2.2 Comparison of Theoretical and Measured Aspect Ratios

Aspect ratios of gold nanorods synthesised using methods described above were calculated from λ_{LPB} values obtained from UV-vis absorbance spectra using equations 1.1 (calc1) and 1.2 (calc2) from section 1.2.2 in order to compare with aspect ratios measured from TEM images.

Method	λ_{LPB} (nm)	AR (TEM)	AR (calc1)	AR (calc2)	NPs	NRs %
AuS2	634.50	3.64	2.26	2.57	327	25.08
AuS4	714.40	3.18	3.09	3.40	440	62.73
AuS1	726.52	2.39	3.21	3.52	276	8.70
AuS7	737.07	6.07	3.32	3.63	28	21.43
AuS9	824.85	4.26	4.24	4.54	417	52.52
AuS3	836.02	4.76	4.35	4.65	93	68.82
AuS5	863.73	4.73	4.64	4.94	122	90.10
AuS8	898.00	4.05	5.00	5.29	321	57.63

Table 3.4 Theoretical and measured gold nanorod aspect ratios in order of increasing λ_{LPB}.

Data was plotted in the below chart in order to better compare theoretical to experimental results:

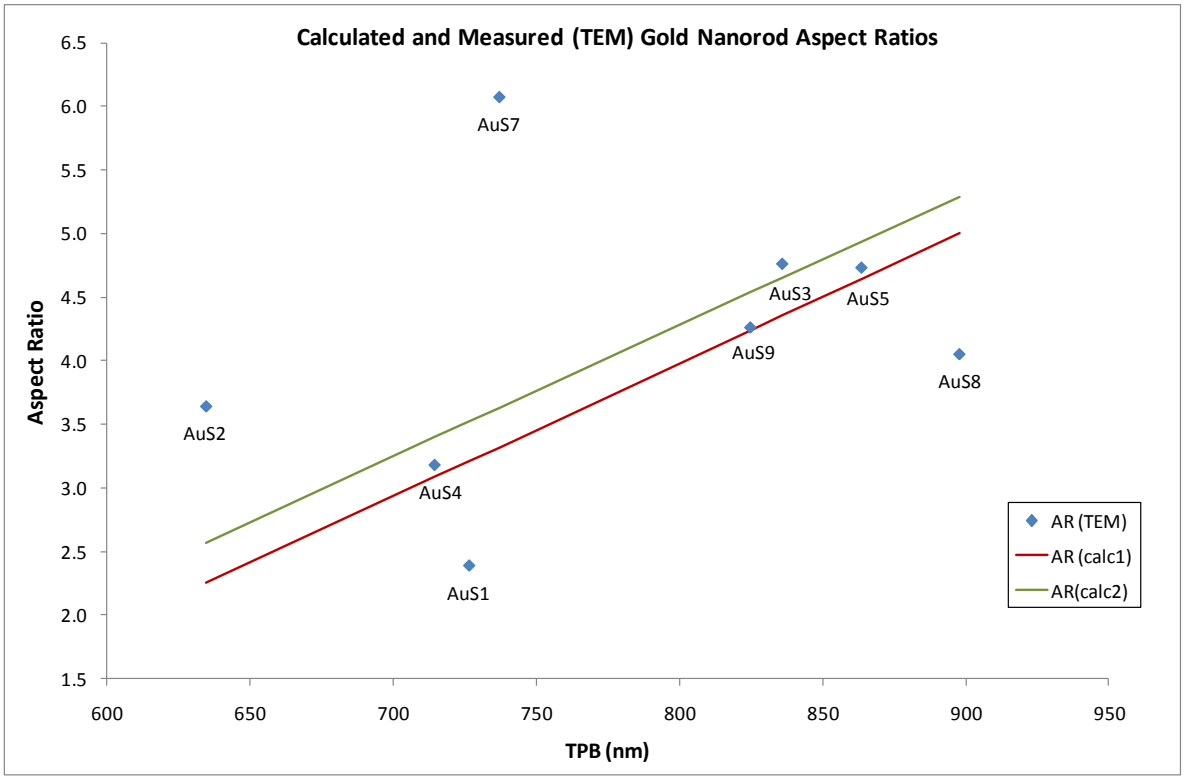

Figure 3.34 Aspect ratios measured using TEM images of gold nanorods synthesised compared to theoretical aspect ratios calculated using equation 1.1 (calc1) and 1.2 (calc2).

Lower nanorod yields relative to total number of nanoparticles or lower overall nanoparticle yields seemed to lead to larger deviations from the calculated aspect ratios. As demonstrated above, lower yields also contributed to poorer correlation between the normal distribution and the distribution of nanorod aspect ratios observed, therefore it comes as no great surprise that the higher relative yield syntheses were closer to the theoretically calculated values.

3.2.3 Purification of Gold Nanorods *via* Centrifugation

Initial Investigations

Attempts at purification *via* centrifugation were initially unsuccessful, with a decrease in the LPB absorbance observed in the UV-vis spectra, implying a reduction in the concentration of nanorods. Much of the literature contains little detail on the procedures used, usually implying that any precipitates consist of nanorods, which are larger and heavier than nanospheres and therefore sediment faster. An increase in the LPB was observed for all such cases in which the precipitate was redispersed in water and investigated using UV-vis absorbance spectroscopy.

Nanorods synthesised using method 4 were transferred from aqueous to organic solutions *via* the addition of decanoic acid and sodium phosphate monobasic and centrifuged using the same parameters as above.[55] A slight decrease in the TPB was observed in the UV-vis absorbance spectra for the supernatant (an increase in A_{LPB}/A_{TPB}) and so multiple centrifugations were performed with removal of the precipitate after each in order to determine whether this could be used to achieve shape separation. No further decrease in the TPB was observed after the second centrifugation.

Variation of rpm, time and number of cycles of centrifugation on shape separation

Samples prepared using method 5 (AuS5) centrifuged for 10 min at 2000, 4000, 6000, 8000 and 10000 rpm (the maximum limit of the centrifuge) showed an increase in absorbance maximum ratio with an increase in rpm in the UV-vis absorbance spectra. Samples centrifuged at 10000 rpm for 5, 10, 15 and 20 min showed an increase in absorbance maximum ratio with an increase in time, up to 10 min, after which no further increase was observed. Samples centrifuged at 10000 rpm for one, two and three 10 minute cycles showed a negligible increase in absorbance maximum ratio, and so overall the optimum centrifugation conditions were 10000 rpm for a single 10 min cycle.

For investigations into 'bottom' and 'side wall' precipitates resulting from centrifugation of aqueous gold nanorods, in both cases the UV-vis spectra demonstrated that the supernatant contained mostly rods and the bottom precipitate mostly spheres. The precipitate taken from the side wall contained a similar ratio of rods to spheres as the supernatant. Using centrifuge tubes with rounded ends it was found that discarding the precipitate left a nanorod solution of much greater absorbance maximum ratio, increasing from 1.82 to 3.45. Solution colours remained similar for 'bottom' and 'side' precipitates, unlike the observations made by Sharma *et al.*,[59] seen in figure 1.9. The UV-vis absorption spectra below show the difference in nanoparticle content for the precipitates, supernatant and the original solution before centrifugation.

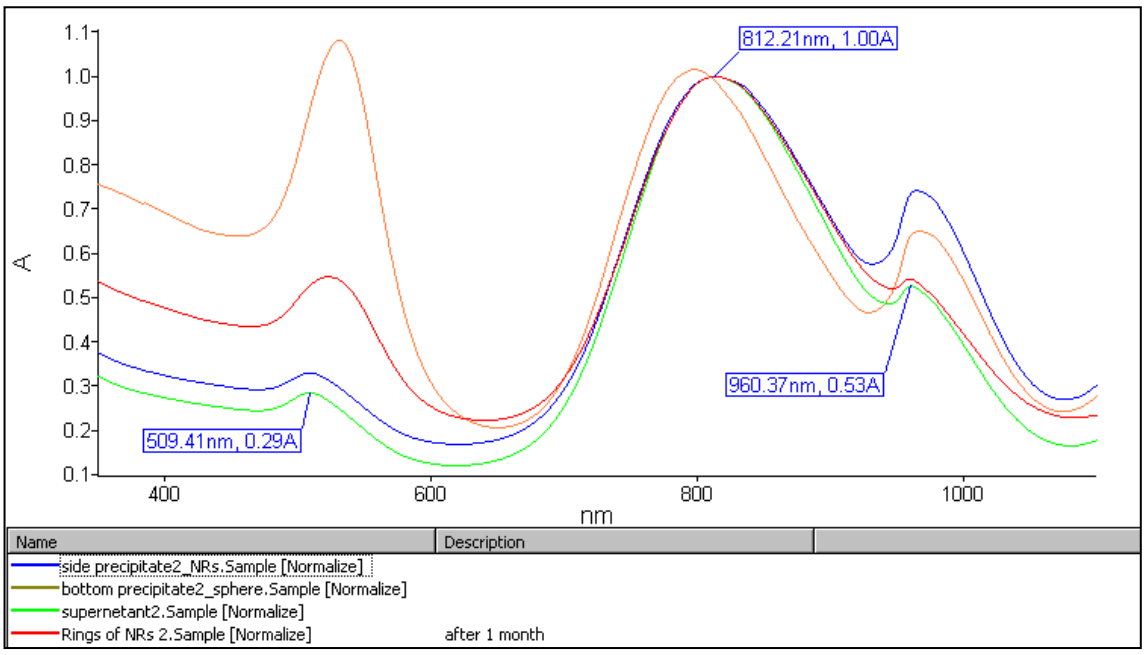

Figure 3.35 UV-vis absorbance spectra of gold nanoparticles shape-separated *via* centrifugation.

However, the arguments put forward in the above publication are "strictly applicable in dilute regime only" and when the same principles were applied to centrifugation of more concentrated nanorod solutions, produced using the method 4 (AuS4), a precipitate was formed but no shape-separation was observed. Since the solutions contain a much higher concentration of gold nanorods, they are a deep purple colour, and it is impossible to differentiate between precipitate and supernatant after centrifugation. For these reasons dilutions of 5x to 700x were made, however still no shape separation was observed, only a slight red shift of the LPB for supernatant solutions.

3.2.4 Addition of Sodium and Potassium Phosphates to Gold Nanoparticles

Addition of both sodium and potassium phosphate dibasic led to a reduction in the absorbance of both the TPB and LPB in the UV-vis spectra over time, as shown in figure 3.36 (below). For this reason no further investigations were carried out using dibasic phosphates.

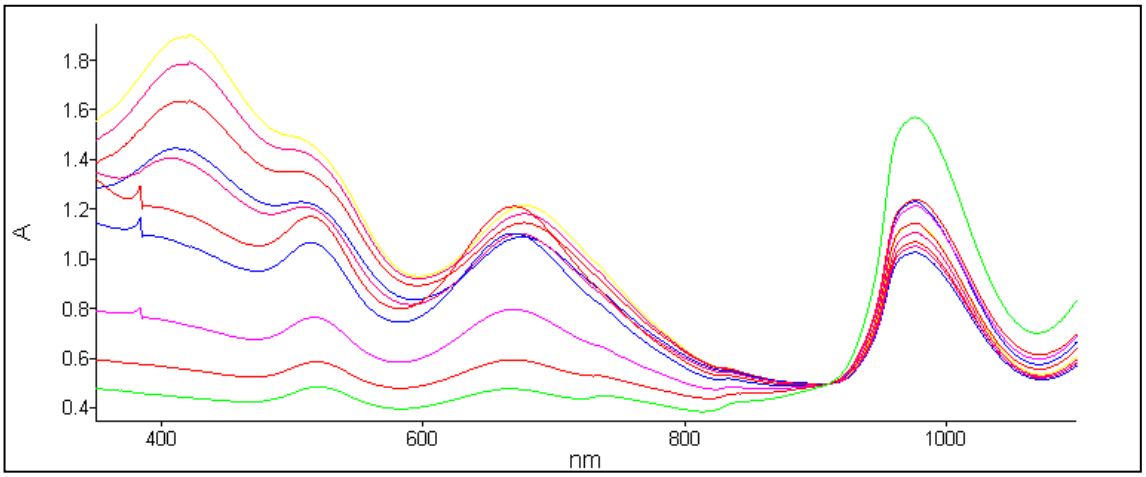

Figure 3.36 Addition of sodium phosphate dibasic to gold nanorods led to reduction of TPB and LPB absorbances in the UV-vis spectra.

In a similar manner to the literature,[60] the addition of sodium phosphate monobasic appears to selectively reduce the absorbance observed for the TPB whilst maintaining the absorbance for the LPB, as shown in the spectra below.

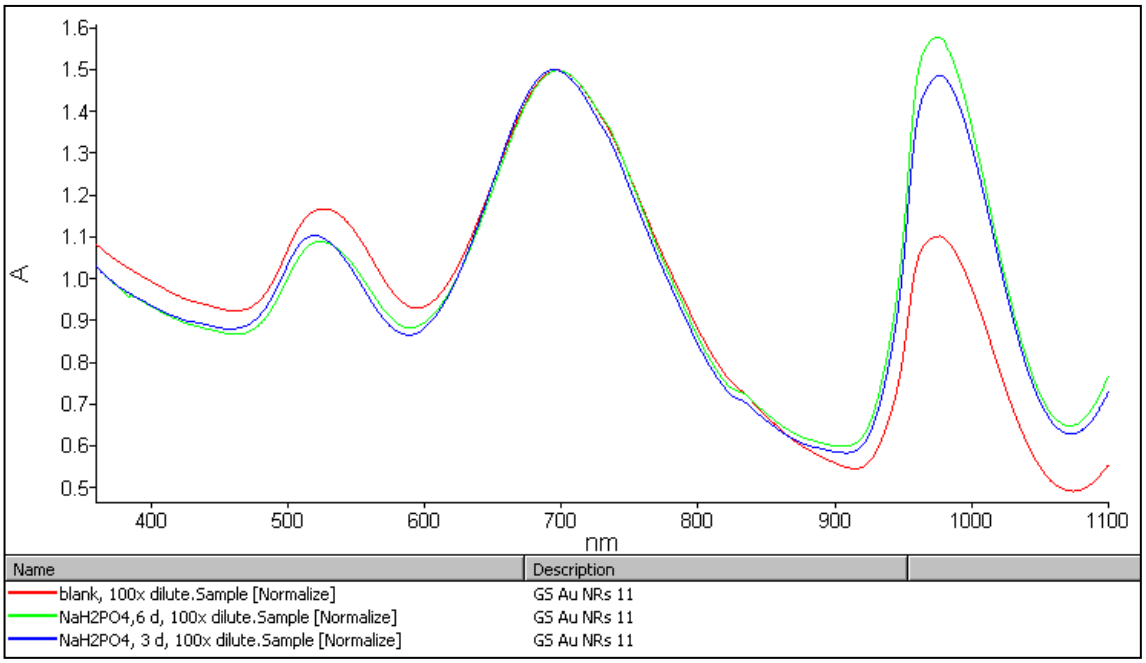

Figure 3.37 Addition of sodium phosphate monbasic to gold nanorods led to slight reduction of TPB in the UV-vis absorption spectra.

Investigations using increased concentrations of sodium phosphate monobasic were carried out, 500 and 1000 mg were added to aqueous nanorod solutions with the aim of increasing the rate and/or extent of the decrease in the TPB. However, with increased concentrations of sodium phosphate monobasic it was observed that both the TPB and LPB decreased in absorbance and broadened slightly, with the LPB decreasing more than the TPB, indicating that a higher relative yield of nanorods compared to nanospheres was not being achieved.

Furthermore, TEM images revealed no discernible change in the dimensions or proportions of gold nanoparticles after the above chemical additions, and so it is possible that the effects observed in the UV-vis absorbance spectra may merely be due to the phosphates forming complexes with the particles in solution.

Due to the minor improvements in relative nanorod yield compared to the time and inconvenience of carrying out these procedures, as well as the unknown effects of sodium phosphate addition on the surface modification reactions, it was deemed that the most suitable means of obtaining nanorods in higher concentrations would be through careful variation of the initial synthetic procedures, and so no further additions of sodium or potassium phosphates were performed.

3.3 Functionalisation of Gold Nanorods

Attempts at nanorod functionalisation were carried out using alkanethiols and liquid crystalline ligand groups in order to encourage formation of hybrid organic-inorganic particles, capable of self-assembly into calamitic liquid crystalline phases. Initial reactions were carried out using commercially obtained nanorods, and then further reactions used gold nanorods synthesised using the methods described above, optimised to give the best combinations of aspect ratio, relative yield and concentration of nanorods in solution.

3.3.1 Functionalisation with Commercially Available Thiols

Dodecanethiol and octadecanethiol were used in attempts to modify the surface coating of gold nanorods, with the former providing more success, possibly due to increased solubility in the solvent mixtures used. ^{1}H NMR studies of dodecanethiol yielded a signal at approximately 2.5 ppm for the carbon adjacent to the thiol functional group, shown in figure 3.38 below.

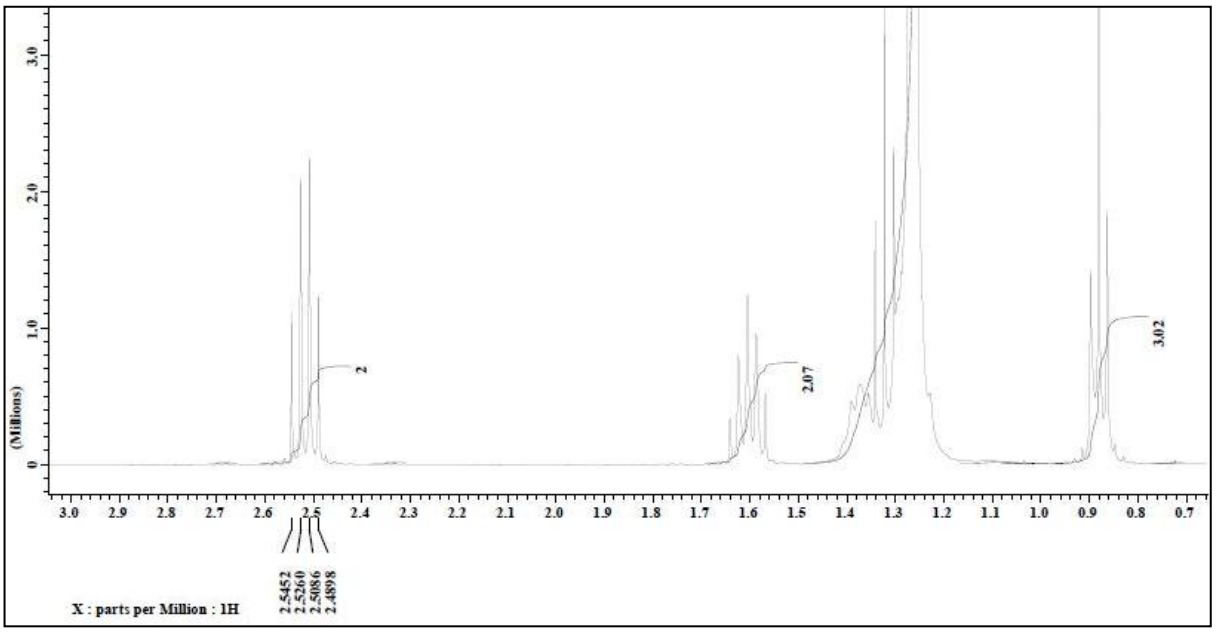

Figure 3.38 H^{1}NMR spectrum of dodecanethiol in deuterated chloroform.

However, the predicted signal for the protons in this position is a triplet, as there are two protons on the adjacent carbon, with the thiol functional group on the other side. After functionalisation reactions with nanorods, this signal is shifted by approximately 0.15 ppm and becomes a triplet. ^{1}H NMR spectra for dodecanethiol were acquired several times using

freshly cleaned or new NMR tubes and in all instances a quartet was observed. The presence of a quartet may be due to impurities within the compound, and has also been observed in the literature; [29, 150] however; no clear explanation appears to have been presented thus far.

Method 1 (AuF1)

The change in solution colour from purple to clear indicates that nanorods are no longer dispersed in solution. This was probably due to irreversible aggregation of gold nanorods as the CTAB bilayer was displaced by dodecanethiol or instability in the organic solvent. No clear ^{1}H NMR or UV-vis absorption data was obtained.

Method 2 (AuF2)

Figure 3.39 below shows the solutions obtained from the blank reaction (A) and the reaction with dodecanethiol (B). In the former, the solution is colourless, indicating a lack of stable, dispersed gold nanoparticles, probably due to irreversible aggregation as acetone is added to the aqueous solution. In the latter, the purple colouration remains in solution after the addition of acetone and dodecanethiol, indicating that nanoparticles were stablised in a mixture of organic and aqueous solvent. The organic phase was extracted into deuterated chloroform and a blue-purple colour was observed, indicating the presence of gold nanoparticles dispersed in organic solvent. ^{1}H NMR spectra confirmed the presence of dodecanethiol.

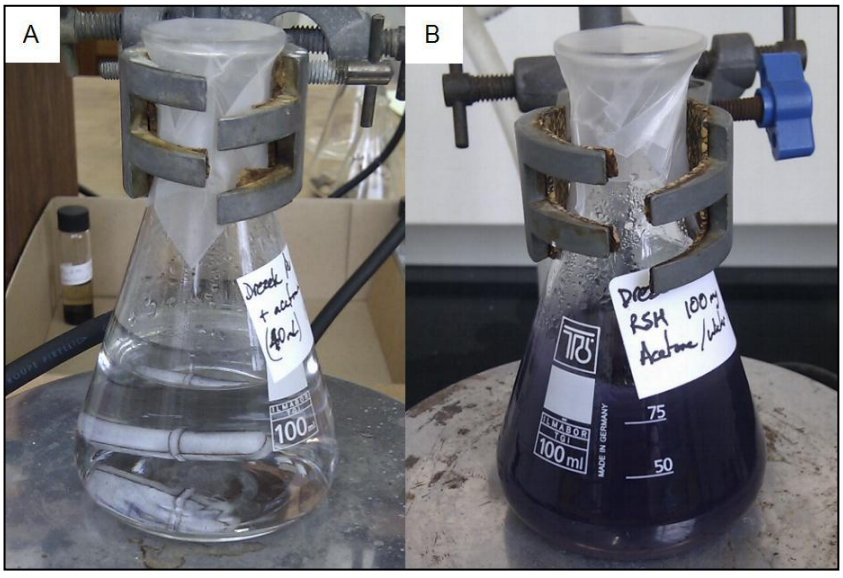

Figure 3.39 Gold nanorod solutions prepared using method 9 (AuS9) mixed with acetone (A) and acetone with dodecanethiol (B).

3.3.2 Functionalisation with Synthesised Ligands

Initially, attempts were made at estimation of the surface coverage of nanorods with organic ligands after surface modification reactions had been carried out, using a typical maximum coverage of self-assembled monolayers for alkanethiols value of $4.5_{x10}{}^{14}$ molecules/cm^{2}.[80] However, only values for the surface coverage of flat substrates were available, and translating these to calculations for an approximately cylindrical nanorod with different crystal faces, combined with the use of synthesised ligands and difficulty gauging what proportion of the initial surface coating had been replaced, made obtaining any degree of accuracy a very challenging prospect.

Method 1 (AuF3)

The reaction using dodecanethiol was repeated using synthesised ligand 6:

Again the change in solution colour from purple to clear indicates that nanorods are no longer dispersed in solution, and as in the reaction above no clear ^{1}H NMR or UV-vis absorption data was obtained. This was probably due to irreversible aggregation of gold nanorods as the CTAB bilayer was displaced by 6 or instability in the organic solvent.

Method 2 (AuF4)

The change in solution colour from purple to clear indicates that nanorods are no longer dispersed in solution. This was probably due to irreversible aggregation of gold nanorods as the CTAB bilayer was displaced by 6 or instability in the organic solvent. Obtaining coherent ^{1}H NMR and UV-vis absorption data again proved irresolvable.

Reactions were then performed using aqueous gold nanorod solutions synthesised using the methods described above.

Method 3 (AuF5)

Even after extending the reaction time, a colourless solution was obtained, and the lack of clear data within ^{1}H NMR or UV-vis absorption spectroscopy indicated that irreversible aggregation of the gold nanorods had taken place.

Method 4 (AuF6)

As with the reaction using dodecanethiol, see above, the solution remained purple in colour after the addition of acetone and 6, indicating nanoparticles stabilised in a mixture of organic and aqueous solvent. Again, as the organic phase was extracted into deuterated chloroform, the blue-purple colour remained, and ^{1}H NMR spectra confirmed the presence of 6 with a weak signal for the ligand showing a slight shift in the peak for the -CH_2- protons next to the thiol group and a change in splitting pattern from a quartet to a triplet.

Figure 3.40 was obtained from a sample of gold nanorods after treatment with 6 as specified above. The sample was dispersed in deuterated chloroform and was the same as that used in obtaining H^{1}NMR spectra, and clearly shows the presence of gold nanorods. The nanorods are much more closely packed than in the as-prepared samples seen in figure 3.18, which could be due to the surface modification or some aggregation resulting from the removal of CTAB. An attempt at purification *via* column chromatography was made, however only compound 6 was recovered, demonstrated by the ^{1}H NMR spectra, indicating a possible low surface coverage of gold nanorods, with remaining CTAB causing them to stick to the silica gel.

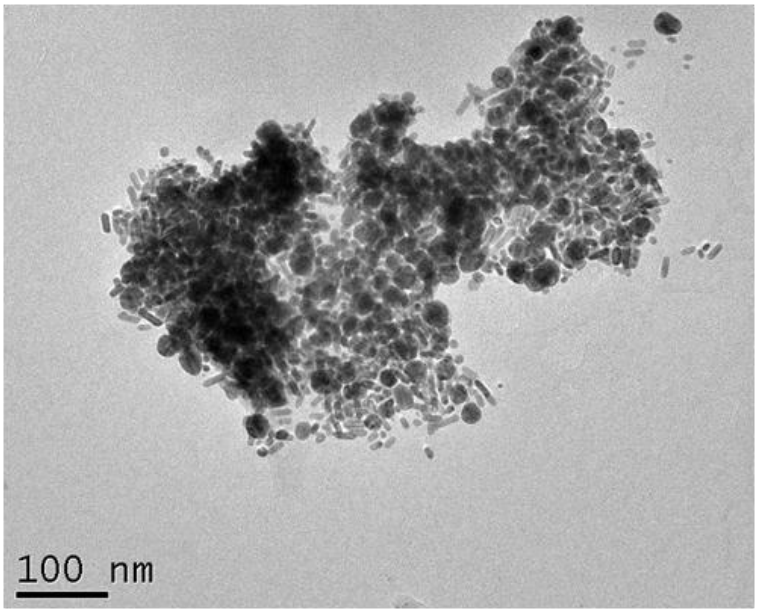

Figure 3.40 TEM image of functionalised gold nanorods produced using method 4 (AuF6).

AuF7

The initial loss of purple colour in the solution demonstrates that as the CTAB bilayer coating of the gold nanoparticles is replaced by the organic ligand 17a, the nanoparticles become unstable in aqueous solutions. This is further demonstrated by the formation of purple-

coloured aggregates and the dark sediment coating the bottom of the reaction flask. Upon removal of the aqueous solution and addition of chloroform, the nanorods are redispersed and the typical blue-purple colour of nanoparticles in solution is observed, implying that the nanorods are now coated with the organic ligand and therefore become soluble in organic solvents.

The ^{1}H NMR spectra confirmed the presence of 17a with a shift of the signal for the -CH_2- protons next to the thiol group from 2.60 to 2.76 ppm as well as a change in splitting pattern from a quartet to a triplet.

The λ_{max} of the LPB in the UV-vis absorption spectrum shifted from 690.46 nm for CTAB-coated gold nanorods to 631.49 nm after surface functionalisation with 17a, and the absorption also became broader with an apparent loss of the TPB.

For the reaction between aqueous gold nanorods and organic ligand 21a, a shift of the signal for the -CH_2- protons next to the thiol group from 2.60 to 2.76 ppm as well as a change in splitting pattern from a quartet to a triplet was again observed in the ^{1}H NMR spectra. However, the quartet at 2.60 ppm was maintained and possessed an integration value of roughly 5 times that of the triplet at 2.76 ppm, indicating that an excess of unreacted 21a was still present along with the product.

3.4 Synthesis of Cadmium Sulphide Nanorods

For all syntheses of cadmium sulphide nanoparticles, an absorbance was observed in the UV-vis absorption between 420 and 500 nm. EDS performed in conjunction with TEM imaging confirmed the presence of both cadmium and sulphur in the reaction products.

Method 1 (CdS1)

Figure 3.41 below shows the only rod-like particles observed from the series of ten TEM images, with a far greater number of spherical particles. However, these particles, approximately 500 nm in length, when viewed at greater magnification, were found to be aggregates of smaller, spherical particles. For this reason statistical analysis of the TEM images was not performed.

The synthesis involved the use of an aqueous Triton X-100 solution as a reverse hexagonal phase template therefore, although cadmium sulphide rods were unable to form as they may have done in a hexagonal phase template, the rod-shaped aggregations may have been templated in the reverse hexagonal phase. It is likely that any templating effect was not sufficient to prevent the formation of more thermodynamically favourable spherical nanoparticles, possibly due to changes in the constitution of the reaction mixture as hydrogen sulphide was bubbled through, or a lack of control over reaction kinetics, vital to the formation of anisotropic cadmium sulphide nanoparticles.

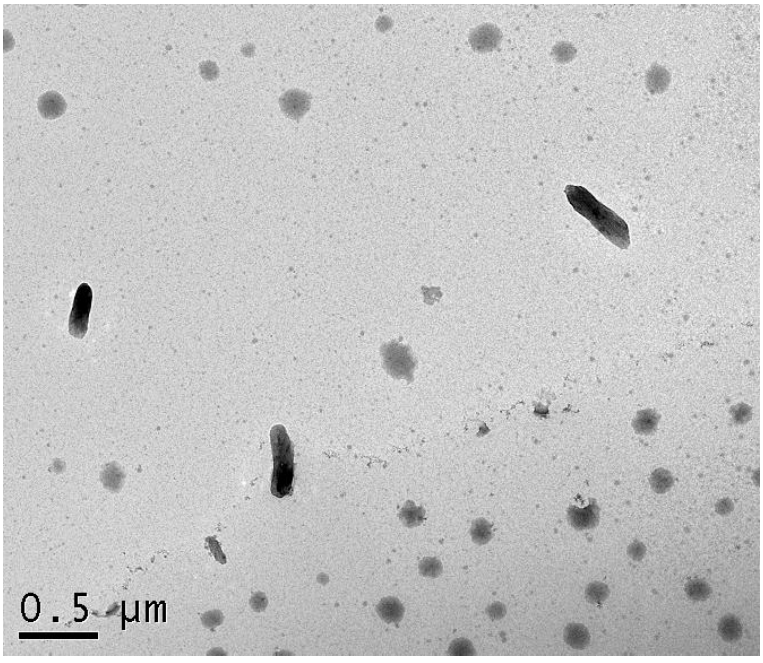

Figure 3.41 TEM image of cadmium sulphide nanoparticles synthesised using method 1.

It is also reasonable to suggest that since larger rod-shaped aggregates of nanoparticles were produced, the reverse hexagonal phase of the surfactant was either not successfully obtained or maintained, or was of much larger dimensions compared to the nanoparticles and therefore was unsuitable for the aims of this reaction.

Method 2 (CdS2)

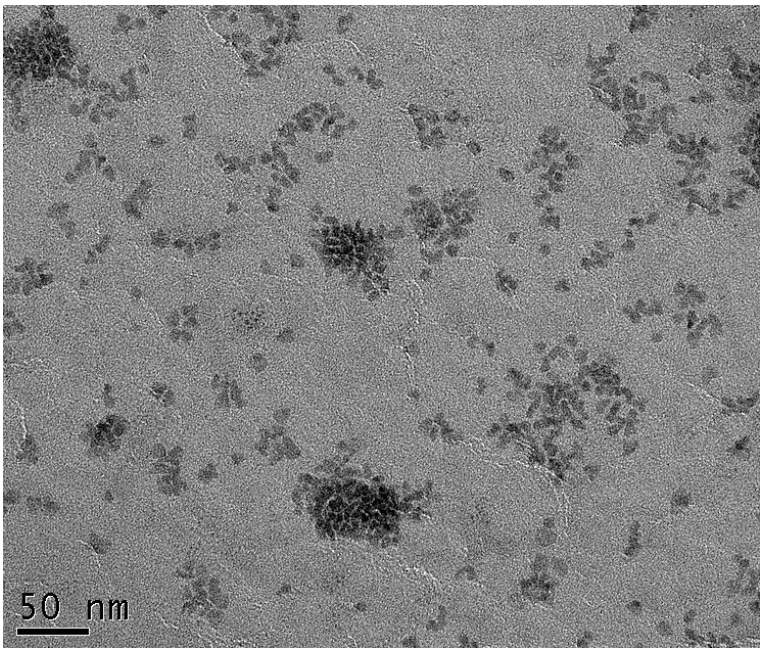

Figure 3.42 TEM image of cadmium sulphide nanoparticles synthesised using method 2.

Figure 3.42 above, shows roughly spherical cadmium sulphide nanoparticles produced using the second synthetic route. Although TEM images show that no nanorods were produced during this reaction, it was observed that cadmium sulphide nanoparticles may be synthesised using CTAB as a surfactant in a similar fashion to the gold nanorod syntheses described above. However, as no anisotropic nanoparticles were produced, possibly due to unfavourable reaction kinetics or deviations from the experimental method used in the literature, statistical analysis of the TEM images was not performed.

Method 3 (CdS3)

(CdS3i) For the reaction involving trioctylphosphine oxide and oleylamine, cadmium sulphide nanorods were produced, as seen in the TEM image below. A mean aspect ratio of 5.08 and a standard deviation of 1.24 were observed, giving %RSD of 24.41. The mean aspect ratio is lower than that reported in the literature,[75] possibly due to deviations in the experimental

procedure brought about by insufficient details of the exact conditions required, however figure 3.43 indicates that it was still sufficient for some localised alignment to occur.

EDS analysis was also performed, with nanorods produced using this method being used in further reactions - see below (section 3.6) for data and comparison between synthesised cadmium sulphide nanorods and those having undergone surface modification.

Figure 3.44 shows the spread of aspect ratios and can be seen to approximately follow the normal distribution, providing the best fit of all attempted synthetic routes to cadmium sulphide nanorods attempted in this research.

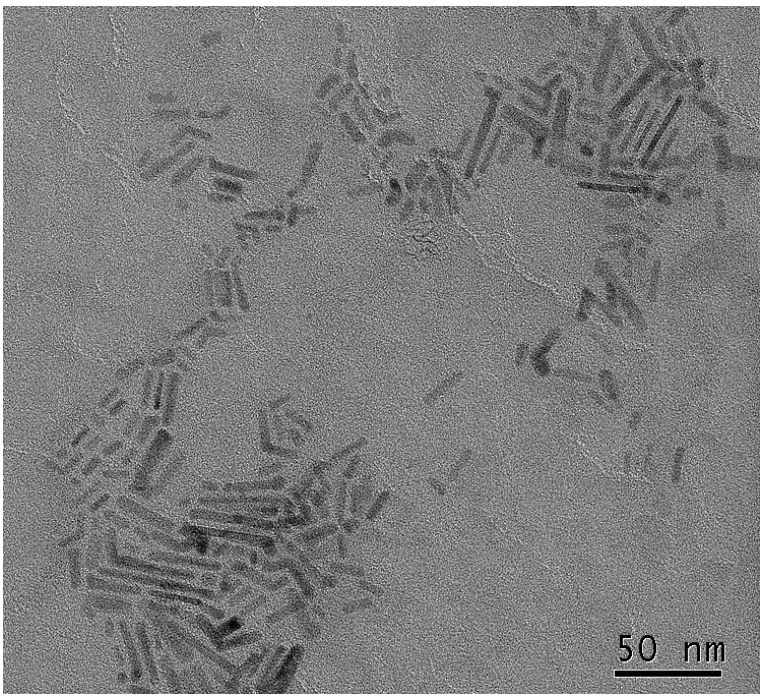

Figure 3.43 TEM image of cadmium sulphide nanoparticles synthesised using method 3i.

Ensuring that the sulphur was fully dissolved in the oleylamine was necessary for good nanorod aspect ratios and relative yields. Initially the oleylamine solution was used without heating to fully dissolve sulphur and lower aspect ratios and nanorod yields relative to spherical nanoparticles than those observed above were seen. Again this was not mentioned in the literature and resulted from a trial-and-error-style optimisation approach to the synthesis.

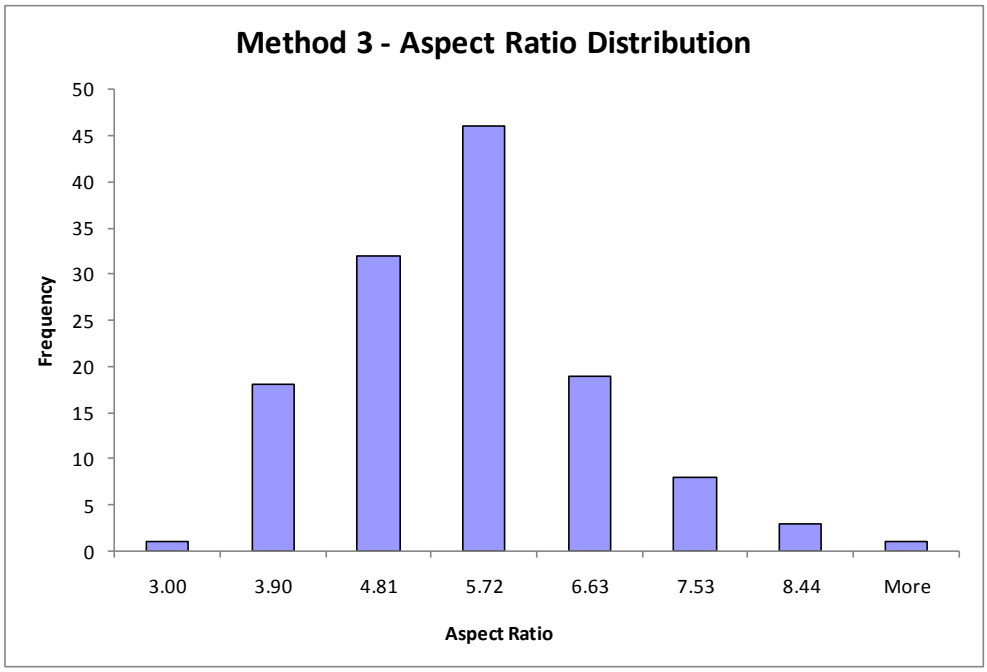

Figure 3.44 Aspect ratio distribution for cadmium sulphide nanorods synthesised using method 3i.

(CdS3ii) The same reaction was performed with the addition of hydrochloric acid in place of trioctylphosphine oxide with the intention of achieving an increase in the monodispersity of nanorod aspect ratios. However, shorter, nanorods of lower aspect ratio along with a higher proportion of thermodynamically-favourable spherical nanoparticles were obtained, as seen in figure 3.45.

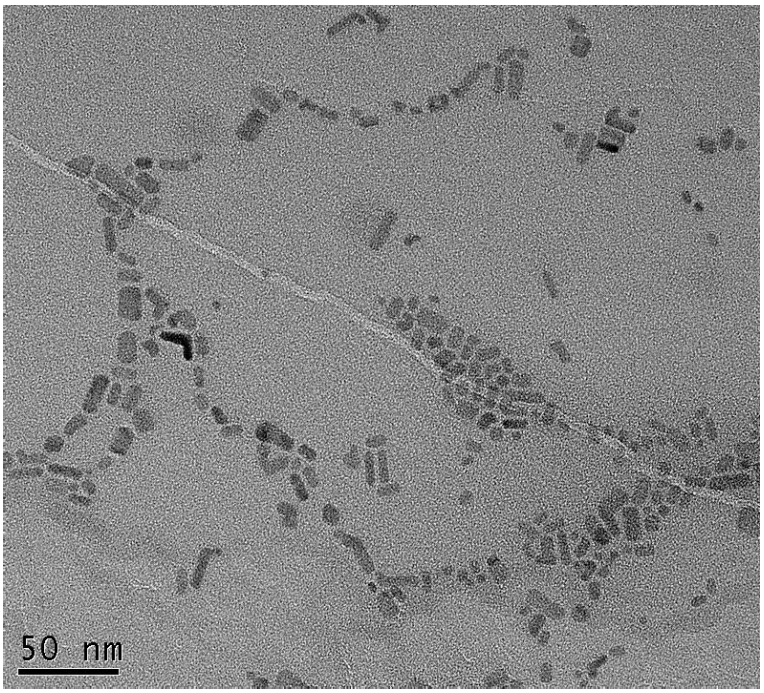

Figure 3.45 TEM image of cadmium sulphide nanoparticles synthesised using method 3ii.

Cadmium sulphide nanorods produced in the presence of hydrochloric acid in place of trioctylphosphine oxide were inferior in aspect ratio as well as nanorod yield relative to spherical and other nanoparticle shapes. Therefore, as they were unsuitable for further use when compared with nanorods synthesised using method CdS3i, statistical analysis of TEM images was not performed. These findings are in agreement with the work done by Prasad *et al.*, who found that using hydrochloric acid decreased the mean aspect ratio from 6.2 to 5, but increased the monodispersity. Since the cadmium sulphide nanorods synthesised in the above reactions were lower in aspect ratio than the literature reports, it follows that no increase in monodispersity is observed due to a reduction in the number of nanorods that formed compared to spherical nanoparticles.

Method 4 (CdS4)

The fact that spherical gold nanoparticles first had to be synthesised, combined with a less straightforward experimental procedure meant that this approach was less trivial when compared to the trioctylphosphine oxide-assisted approach described in method 3 (CdS3i). Cadmium sulphide nanorods with mean aspect ratio of 5.63, a standard deviation of 1.82 and a %RSD of 32.33 were obtained according to TEM imaging.

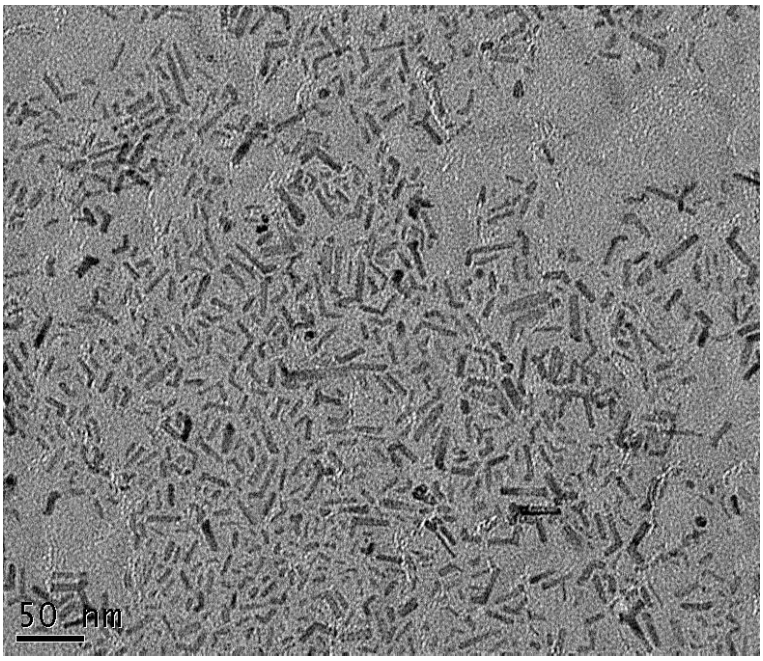

Figure 3.46 TEM image of cadmium sulphide nanoparticles synthesised using method 4.

One of the other factors in this approach was the high temperature required, with nucleation of cadmium sulphide occurring at a relatively low temperature and crystalline nanorod formation occurring at approximately 300 °C. This compares unfavourably with the reaction temperatures of around 100 °C used above.

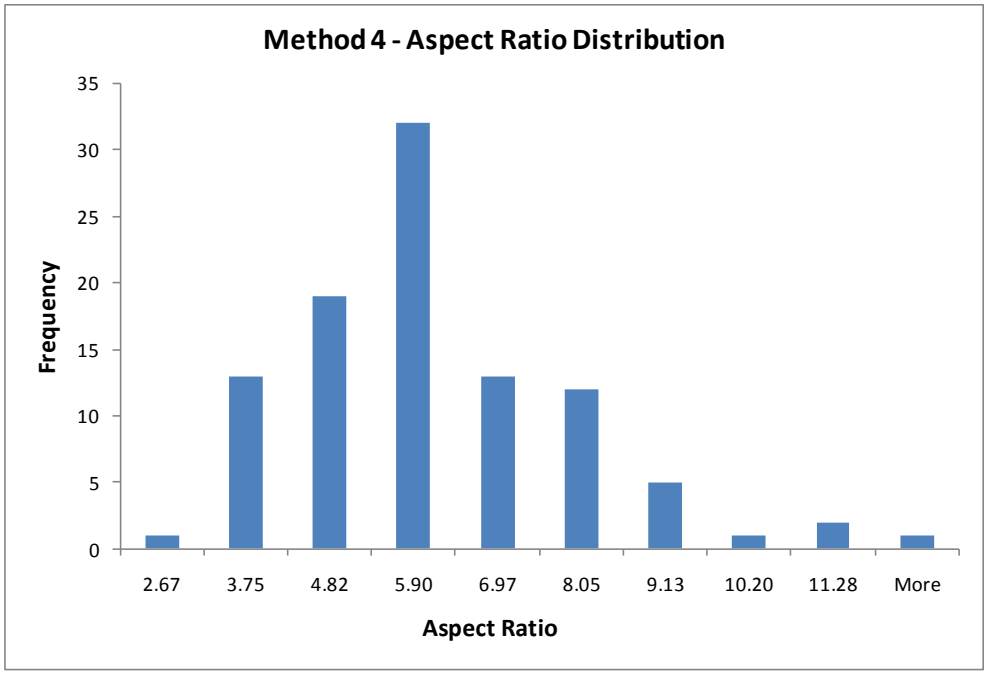

Figure 3.47 Aspect ratio distribution for cadmium sulphide nanorods synthesised using method 3.

Again the aspect ratios approximately follow the normal distribution, though are more polydisperse than cadmium sulphide nanorods synthesised in method 3 (CdS3i). An absorbance band at around 546 nm in the UV-vis spectrum was observed, possibly corresponding to the spherical gold nanoparticles used as seeds in this reaction. It can also be observed in figure 3.46 that some spherical gold nanoparticles remain amongst the cadmium sulphide nanorods, though it may be possible to separate these *via* liquid-liquid extraction or column chromatography following a surface modification process.

Method 5 (CdS5)

Use of trioctylphosphine as both solvent and stabiliser led to the formation of roughly spherical cadmium sulphide nanoparticles, as seen in the TEM image below, again possibly due to unfavourable reaction kinetics or deviations from the experimental method used in the literature. There was also difficulty in obtaining TEM images due to a dark background and

some beam damage to the sample, which is sensitive to high velocity electrons, therefore images had to be obtained quickly making it more difficult to focus on the nanoparticles.

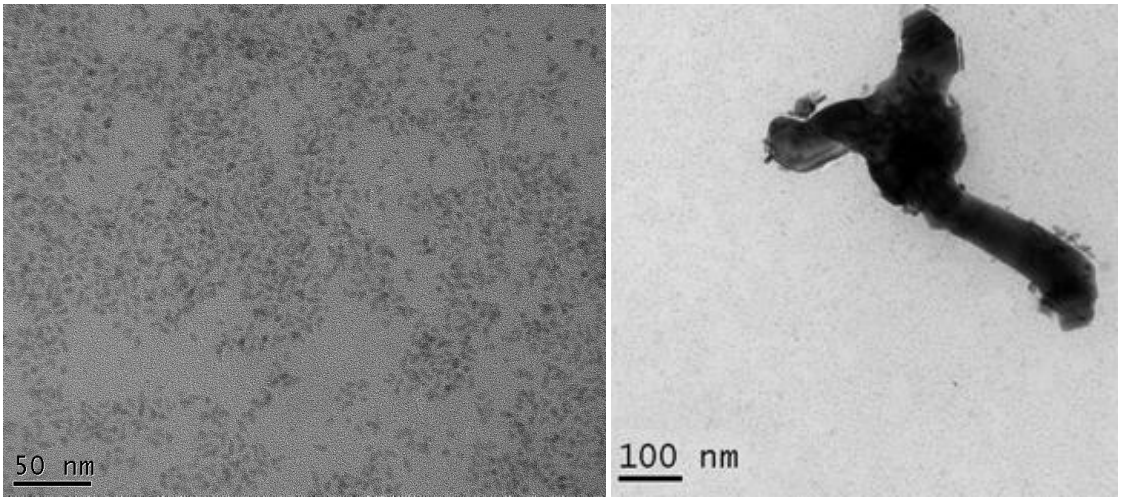

Figure 3.48 TEM images of cadmium sulphide nanoparticles synthesised using method 5.

The image on the right shows the only nanorods observed using TEM, however they are difficult to distinguish and appear to be of relatively low aspect ratio. For this reason statistical analysis was not carried out.

3.5 Cadmium Sulphide Nanorods as Lyotropic Liquid Crystals

Proceeding in a similar manner to the work of Alivisatos *et al*. in the formation of lyotropic liquid crystalline phases from solutions of cadmium selenide nanorods,[30] solutions of cadmium sulphide nanorods in hexane (CdS3i), were investigated.

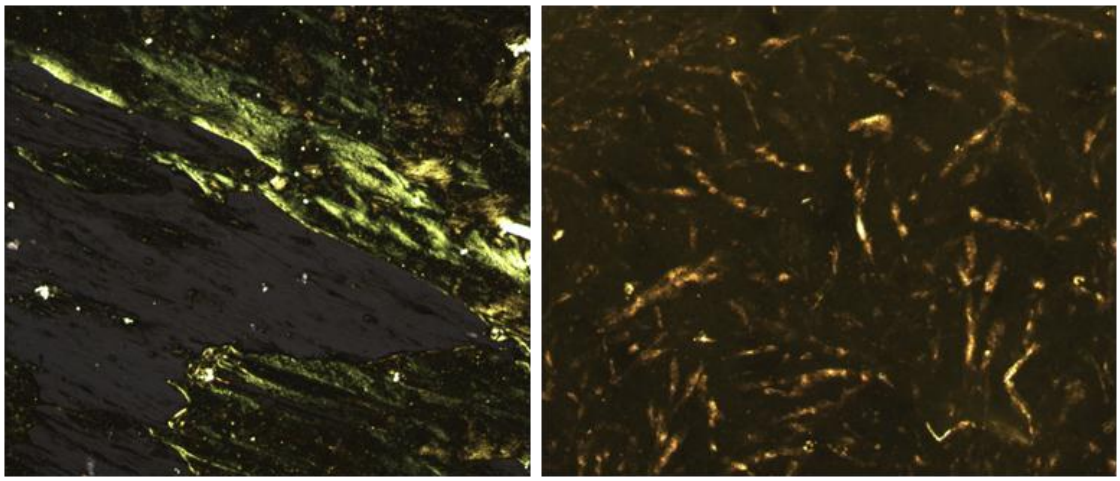

Figure 3.49 Birefringence of cadmium sulphide nanorods viewed under crossed polarisers.

The images above provide an example of the birefringence exhibited when a thin layer of cadmium sulphide nanorod solution was viewed within the confines of a microscope slide and cover plate *via* polarised optical microscopy. However, since the samples were unsealed, it was deemed likely that solvent evaporation may well have led to crystallisation and so the experiment was repeated with the solutions sealed inside glass capillary tubes.

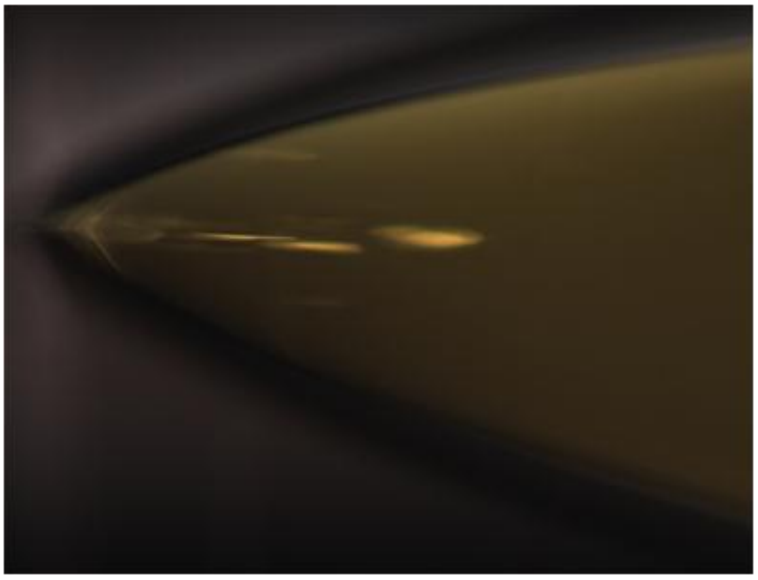

Figure 3.50 Microscope image showing birefringence of cadmium sulphide nanorods inside capillary tube viewed under crossed polarisers.

Figure 3.50 indicates that birefringence was observed in samples sealed within capillary tubes, though there was some difficulty in ascertaining whether the bright 'dashes' were due to the capillary tube surface - through careful manipulation and observation of the samples it was possible to determine that these features where in fact due to the cadmium sulphide nanorod solution. The 'textures' or 'features' observed were not as conclusive as those obtained when cadmium selenide solutions were used,[30] however this may be due to a reduction in the yield and monodispersity of nanorods synthesised *via* differing experimental procedures. Again, referring to Onsager's theory on the ordered alignment of rods at sufficient concentration, it is likely that the concentrations and aspect ratios of nanorods used were not sufficient for the formation of better defined liquid crystalline-like phases. For this reason, as well as the problems associated with solvent evaporation, XRD measurements were unable to be obtained for the above samples.

3.6 Functionalisation of Cadmium Sulphide Nanorods

Following a similar pathway as for the surface modification of gold nanorods, both commercially available and synthesised thiol-terminated organic materials were used to replace the amine-terminated compounds coating the nanorod surface. Unlike gold nanorods, no commercially available cadmium sulphide nanorods were available at the time of investigation, and so all surface modification experiments were carried out using nanorods synthesised within the laboratory, specifically those produced using method CdS3i (see above).

3.6.1 Functionalisation with Commercially Available Thiols

Functionalisation with Dodecanethiol

In an identical manner to the investigations carried out using gold nanorods, the ^{1}H NMR spectra reveals that the signal for the methyl group adjacent to the sulphur shifts downfield by approximately 0.07 ppm, from 2.58 to 2.65 ppm after the reaction with CdS nanorods, indicating a change in the environment as the thiol group is attached to the nanorod surface. A change in splitting pattern from quartet to triplet was observed as the -SH proton is lost and it can be reasoned that dodecanethiol has replaced the majority of the oleylamine at the nanorod surface.

Functionalisation with 6-(ferrocenyl)hexanethiol

Examining the ^{1}H NMR spectra reveals that the signal for the methyl group adjacent to the sulphur shifts downfield by approximately 0.16 ppm, from 2.52 to 2.68 ppm for 6-(ferrocenyl)hexanethiol after reaction with CdS nanorods, indicating a change in the environment as the thiol group is attached to the nanorod surface. A change in splitting pattern from quartet to triplet was observed as the -SH proton is lost, and so it can be supposed that a similar thiol-nanorod bond as in previous reactions is formed.

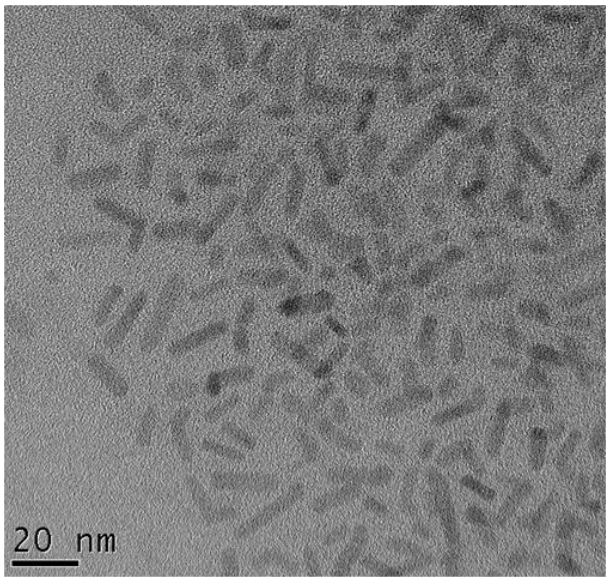

Figure 3.51 TEM images of cadmium sulphide nanorods coated with 6-(ferrocenyl)hexanethiol.

The appearance of nanorods in the TEM images along with the ^{1}H NMR data obtained from the same sample demonstrates that 6-(ferrocenyl)hexanethiol-coated cadmium sulphide nanorods were successfully prepared. Alongside TEM measurements, EDS data was also obtained in order to compare the functionalised nanorods with those synthesised in oleylamine. Comparison of the data shown in table 3.6 with that in table 3.5 demonstrates the presence of iron in the 6-(ferrocenyl)hexanethiol-coated cadmium sulphide nanorods as well as an increase in the carbon content which is to be expected after exchange with oleylamine.

Element	Weight%	Atomic%
C	46.30	76.46
O	5.53	6.49
Si	6.20	4.07
S	8.37	5.55
Cu	8.01	2.62
Cd	25.61	4.83

Table 3.5 EDS analysis of oleylamine-coated cadmium sulphide nanorods.

Element	Weight%	Atomic%
C	58.68	84.03
O	3.60	4.09
Si	2.94	1.15
S	8.04	4.67
Cu	7.90	2.27
Cd	15.93	2.67

Table 3.6 EDS analysis of cadmium sulphide nanorods coated with 6-(ferrocenyl)hexanethiol.

Also observed in the EDS for CdS nanorods coated with 6-(ferrocenyl)hexanethiol (above) is a decrease in the relative amount of oxygen, which is again consistent with the displacement of oleylamine by the 6-(ferrocenyl)hexanethiol which does not contain oxygen.

3.6.2 Functionalisation with Synthesised Ligands

The table below describes the relative yields obtained for the surface modification of cadmium sulphide nanorods using the range of synthesised ligands in an effort to compare how successful each reaction.

	Before			After			
	CdS (mg)	Ligand (mg)	ratio	CdS-ligand (mg)	"yield" A	"yield" B	"yield" C
17a	100	200	2.00	135	1.35	0.68	0.45
17b	10	0.05	0.01	9	0.90	180.00	0.90
17c	100	50	0.50	60	0.60	1.20	0.40
21a	360	500	1.39	280	0.78	0.56	0.33
21b	150	80	0.53	25	0.17	0.31	0.11
21c	180	280	1.56	165	0.92	0.59	0.36

Table 3.7 Comparison of mass of nanorods and ligands used to product retrieved (A = with respect to CdS, B = with respect to Ligand, C = with respect to CdS + Ligand).

Typically, relative yields of 0.3 to 0.5 (relative mass of product compared to amount of CdS and organic ligand used) were observed, though due to the centrifugation procedures employed to separate and purify the end products, these values are only a rough evaluation of the actual yields obtained. For example, it is highly likely that due to the small amount of 17b used, the "high" yields may actually be due to nanorods retaining their original surface coating; this is made even more apparent by the reaction involving 21b in which again a lower amount of ligand was available, yet in this instance a far lower yield was gauged to have been obtained.

Functionalisation of CdS Nanorods with 17a

The ^{1}H NMR spectrum showed that the signal for the methyl group adjacent to the sulphur shifted from 2.61 to 2.76 ppm for 17a after reaction with CdS nanorods, indicating a change in the environment as the thiol group is attached to the nanorod surface. Although the signal was weaker than for unreacted 17a, possibly due to a lower concentration or incomplete

surface modification, a change in splitting pattern from quartet to triplet was observed as the -SH proton is lost. This is consistent with previous chemical shifts.

In the ^{13}C NMR spectrum signals for the carbon environments closest to and adjacent to the sulphur atom are shifted by up to 1.8 ppm when compared to their values in the ^{13}C NMR spectrum for 17a, indicating a change in their environment.

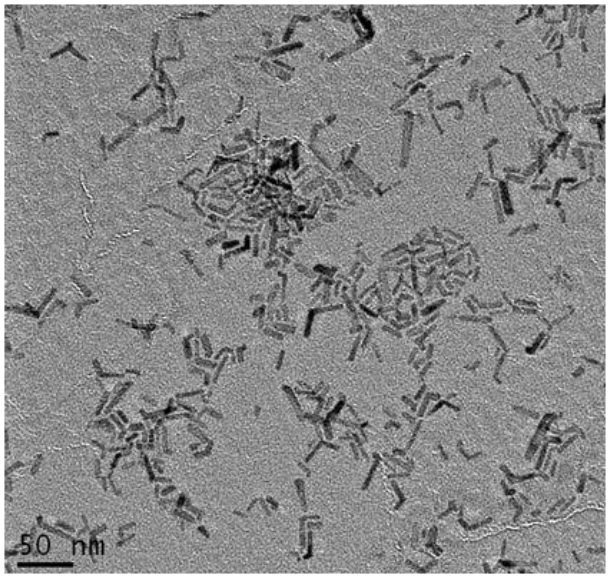

Figure 3.52 TEM image of cadmium sulphide nanorods coated with 17a.

TEM images show that CdS nanorods are present in the sample after reacting with 17a, with no noticeable aggregation of nanoparticles.

Element	Weight%	Atomic%
C	59.34	80.39
O	8.37	8.45
Si	9.82	5.65
S	2.72	1.42
Cu	9.60	2.52
Cd	9.94	1.47

Table 3.8 EDS analysis of cadmium sulphide nanorods functionalised with 17a.

Analysis of the EDS spectra revealed an increase in the relative amounts of carbon and oxygen present compared to oleylamine-coated CdS nanorods (see table 3.5 above) which is consistent with the addition of the organic ligand.

Variation in the amounts of Cu, Si, Cr and Al are due to the mounting grids used to obtain the TEM and EDS. In both EDS for the CdS nanorods functionalised with 17a, a decrease in the amount of Cd and S is observed. This may indicate a lower concentration of CdS nanorods in the product when compared to the EDS for non-functionalised CdS nanorods, or a possible excess of organic ligand.

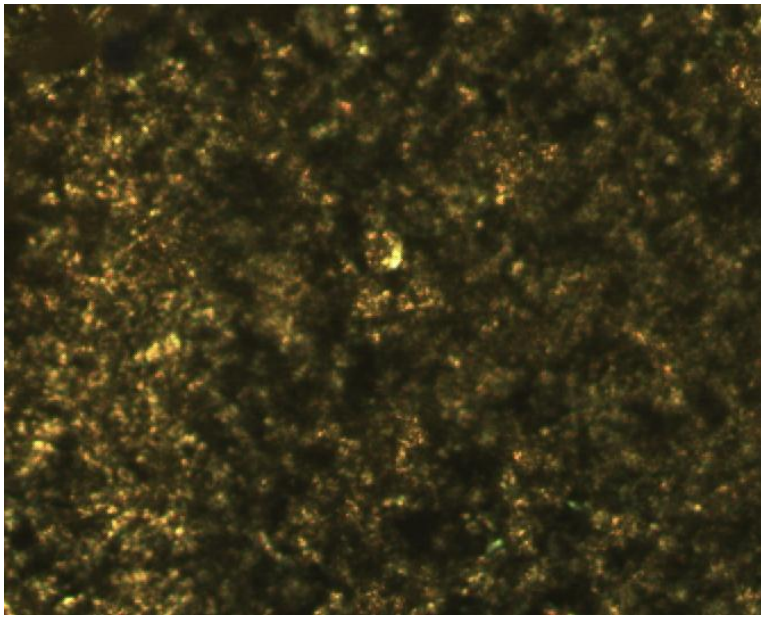

Figure 3.53 Optical microscope image (crossed-polarisers, 100x magnification) of cadmium sulphide nanorods coated with 17a.

Optical microscopy and DSC measurements revealed that the functionalised nanorods exhibited a single melting point, differing with that of pure 17a. The increase from 44 to 92 °C seen in figure 3.54 below confirmed that the properties of the 17a-functionalised nanorods differed from those for the ligand on its own, as well as oleylamine (which itself has a melting point of approximately 21 °C. A single melting point was observed for all subsequent functionalised cadmium sulphide nanorods in this series of experiments, with no liquid crystalline phases present within the hybrid inorganic-organic systems produced.

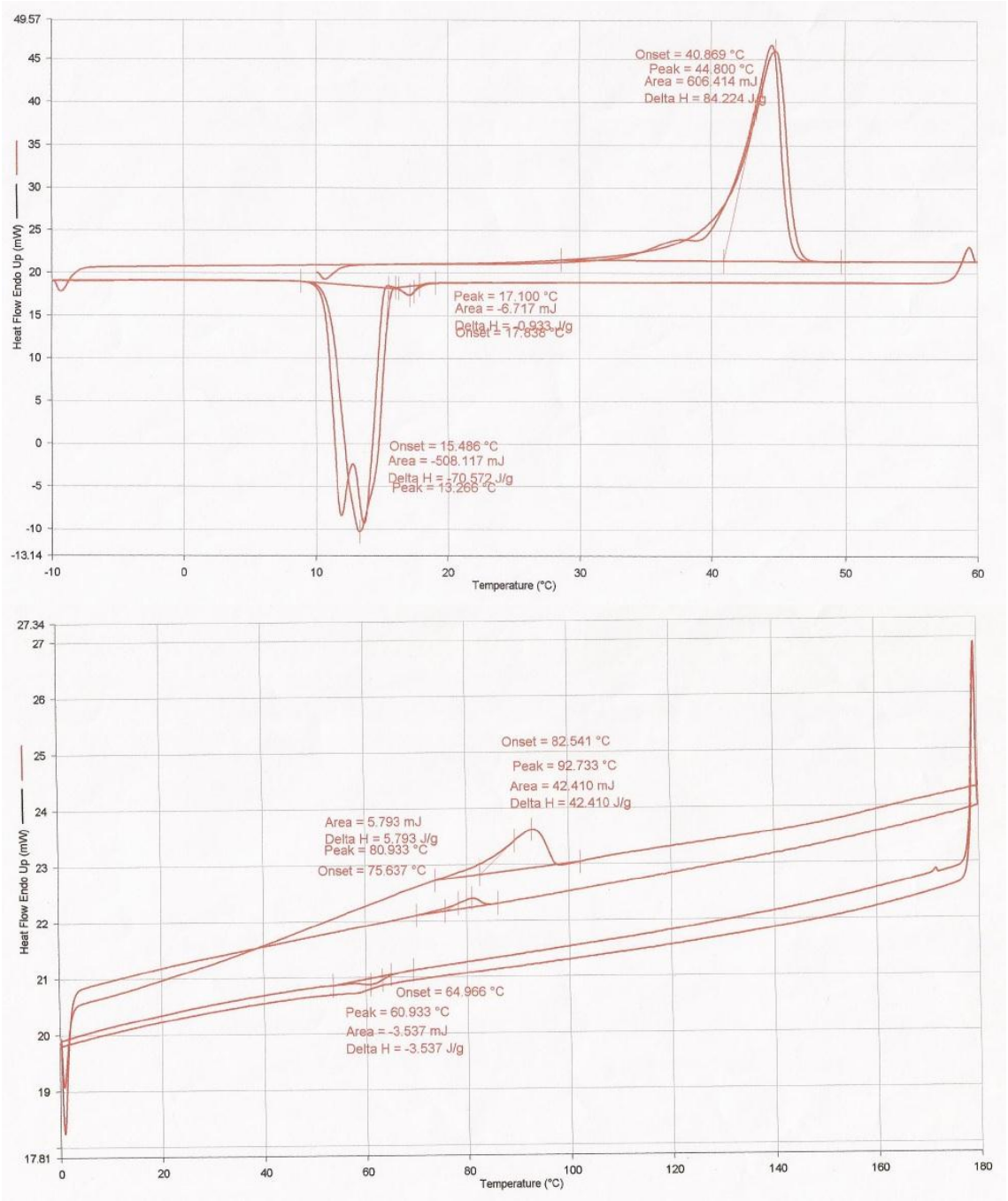

Figure 3.54 DSC curve for 17a (top) and CdS nanorods functionalised with 17a (bottom).

Photoluminescence measurements were also obtained for cadmium sulphide nanorods coated with 17a, however much like the UV-vis absorbance performed, the nanorods were found to be highly absorbing in the 400 - 410 nm region of the electromagnetic spectrum.

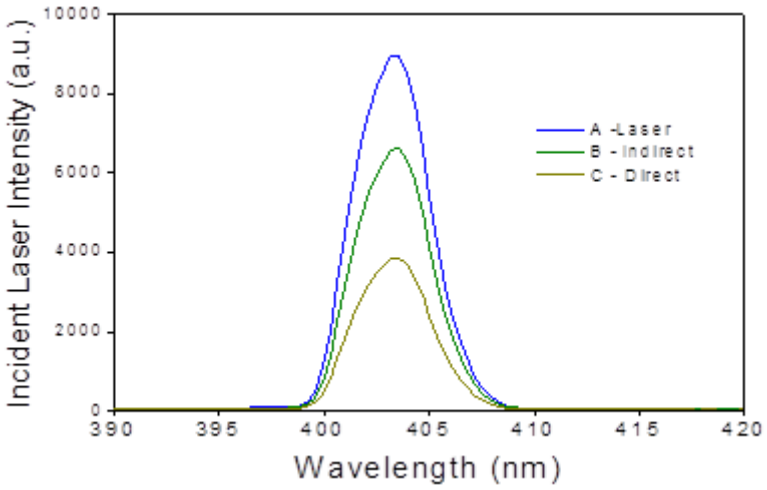

Figure 3.55 Photoluminescence measurements of CdS nanorods functionalised with 17a.

Functionalisation of CdS Nanorods with 17b

The NMR spectra were less well resolved than for CdS nanorods functionalised with 17a and 17c. This was possibly due to the lower yields observed in the synthesis of 17b and consequent reduced final mass of organic material that could be used in excess for effective surface modification of the nanoparticles.

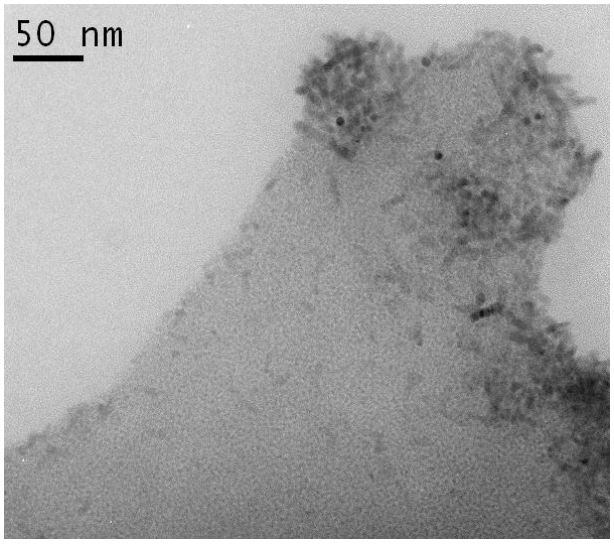

Figure 3.56 TEM image of cadmium sulphide nanorods coated with 17b.

The presence of nanorods within the TEM images combined with the NMR data obtained demonstrates that the cadmium sulphide nanorods were in fact functionalised with the organic material to a certain extent.

Element	Weight%	Atomic%
C	18.00	46.79
O	7.52	14.89
Si	5.42	6.12
S	9.09	8.88
Cu	26.95	13.31
Cd	31.71	8.85

Table 3.9 EDS analysis of cadmium sulphide nanorods functionalised with 17b.

The significant increase in Cu measured using EDS indicates the lower amount of material examined using this technique - the samples being prepared on copper grids. For this reason it is difficult to discern any conclusive analysis of the values obtained for the other elements, and in a similar manner microscope images were also inadequate due to the small amount of material available.

Functionalisation of CdS Nanorods with 17c

The ^{1}H NMR spectrum again showed a shift from 2.51 to 2.68 ppm compared to 17c after reaction with CdS nanorods, indicating bonding between the thiol group and nanorod surface. The now-typical change in splitting pattern from quartet to triplet was also observed, consistent with observations made after previous surface modification reactions. In an identical manner to the functionalisation with 17a, signals for the carbon environments close or adjacent to the sulphur atom are shifted by up to 1.8 ppm when compared to their values in the ^{13}C NMR spectrum for 17c.

TEM images demonstrated that CdS nanorods were present in the sample after reaction with 17c, although greater aggregation of nanoparticles was observed, possibly indicating poorer surface coverage than in previous investigations. This may also be inferred by the EDS measurements in which the amount of carbon again increased, which would be consistent with the addition of 17c; however, unlike in previous surface modification investigations, no such increase is seen for oxygen.

Element	Weight%	Atomic%
C	82.99	94.39
O	2.97	2.54
Si	0.57	0.28
S	1.13	0.48
Cu	8.09	1.74
Cd	4.02	0.49

Table 3.10 EDS analysis of cadmium sulphide nanorods functionalised with 17c.

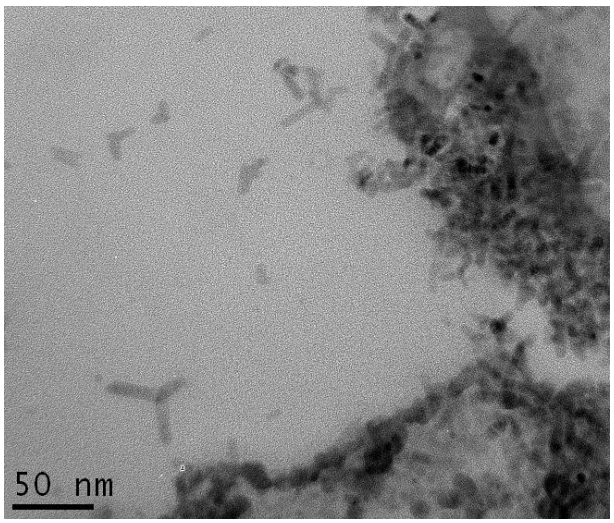

Figure 3.57 TEM image of cadmium sulphide nanorods coated with 17c.

Neither polarised optical microscopy nor DSC measurements revealed any phase transitions other than a melting point, which again differed from the pure organic ligand.

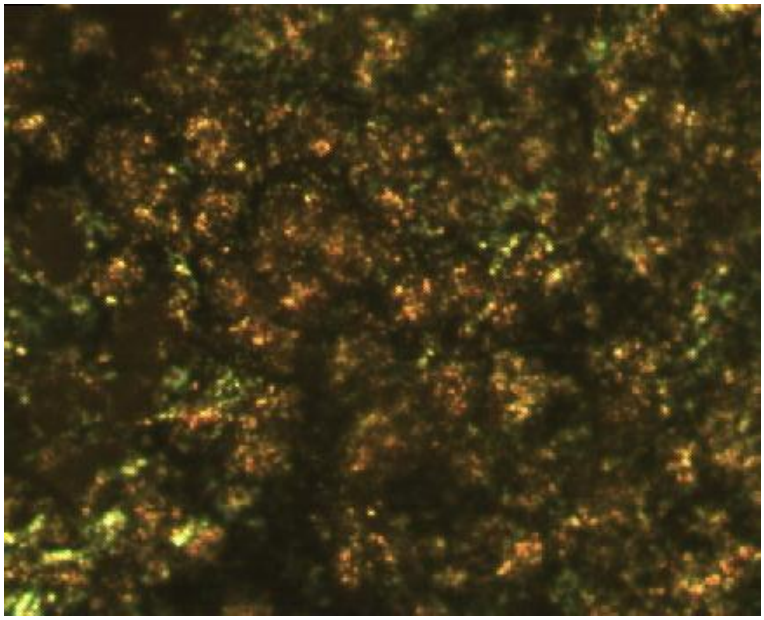

Figure 3.58 Optical microscope image (crossed-polarisers, 100x magnification) of cadmium sulphide nanorods coated with 17c.

Functionalisation of CdS Nanorods with 21a

The ^{1}H NMR spectrum shows that the signal for the methyl group adjacent to the sulphur shifted from 2.59 to 2.75 ppm for 21a after reaction with CdS nanorods, indicating a change in the environment as the thiol group is attached to the nanorod surface. A change in splitting pattern from quartet to triplet was observed as the -SH proton is lost and again the results were consistent with previous chemical shifts.

The ^{13}C NMR spectrum shows that there is a shift in some of the signals associated with the methyl groups near to the terminal thiol group, specifically the methyl group adjacent to the sulphur atom, indicating a change in their environment. A signal is lost at around 30.6 ppm and replaced by one at around 38.7 ppm.

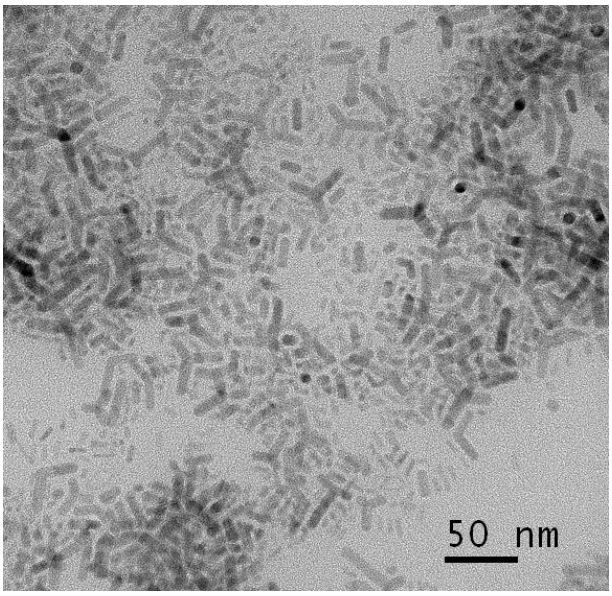

Figure 3.59 TEM image of cadmium sulphide nanorods coated with 21a.

TEM images show that CdS nanorods are present in the sample after reacting with 21a, however more tri-armed nanoparticles appear to be present. EDS measurements were inconclusive for this investigation, with no data for carbon or oxygen able to be determined.

Element	Weight%	Atomic%
Si	0.57	1.36
S	18.66	38.78
Cu	26.07	27.35
Cd	54.58	32.36

Table 3.11 EDS analysis of cadmium sulphide nanorods functionalised with 21a.

Again, only a single melting transition was observed *via* optical microscopy and DSC measurements, figure 3.60 shows the crystalline solid under crossed polarisers.

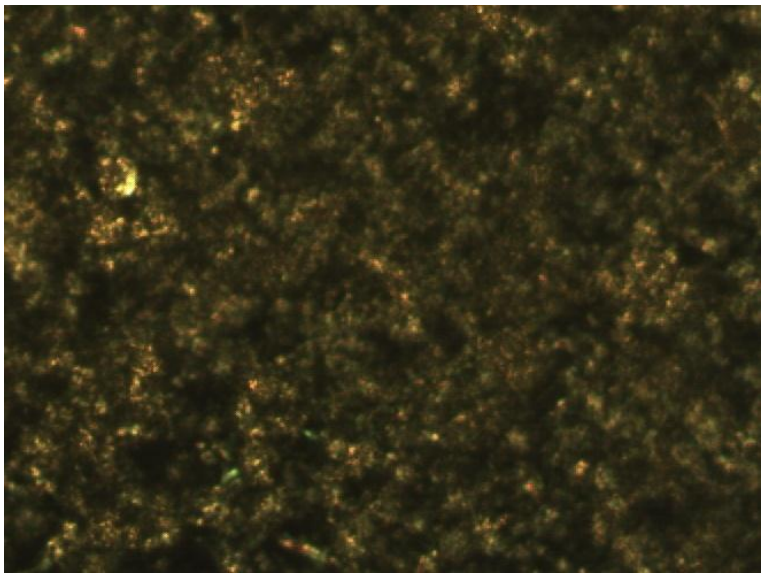

Figure 3.60 Optical microscope image (crossed-polarisers, 100x magnification) of cadmium sulphide nanorods coated with 21a.

Functionalisation of CdS Nanorods with 21b

Much like the investigations using 17b, the NMR data obtained wasn't as well resolved as with other samples but did indicate that successful surface modification had occurred. The TEM images indicated an increase in nanoparticle aggregation when compared with other samples, and EDS measurements were inconclusive with a decrease in the amount of carbon pointing towards poor surface modification yet an increase in oxygen implying the opposite.

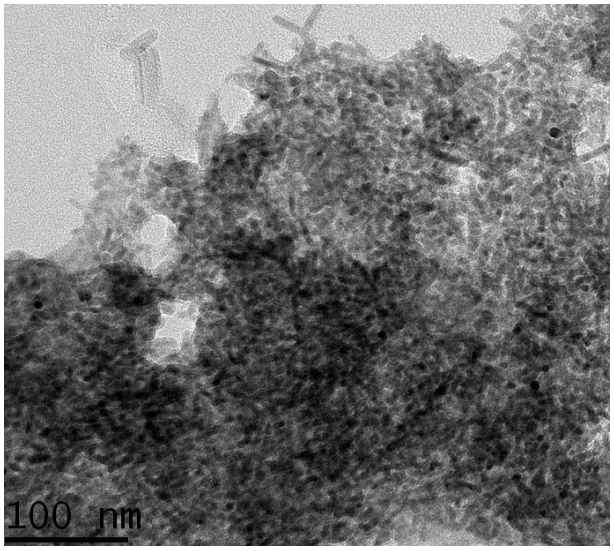

Figure 3.61 TEM image of cadmium sulphide nanorods coated with 21b.

Element	Weight%	Atomic%
C	19.10	46.78
O	8.16	14.62
Si	12.10	11.93
S	10.25	9.68
Cu	16.63	7.78
Cd	33.58	9.03

Table 3.12 EDS analysis of cadmium sulphide nanorods functionalised with 21b.

For this particular reaction, no optical microscope images or DSC analysis were acquired due to the restrictively small amount and questionable purity of material obtained.

Functionalisation of CdS Nanorods with 21c

In the final investigation into the surface modification of cadmium sulphide nanorods, the now-typical shift of approximately 0.13 nm and change in splitting pattern from quartet to triplet for the signal associated with protons adjacent to the thiol moiety was again observed in the ^{1}H NMR spectrum.

TEM imaging confirmed the presence of nanorods within the sample, and much like previous experiments an increase in the amount of 'tripod' nanoparticles was observed along with areas of localised alignment.

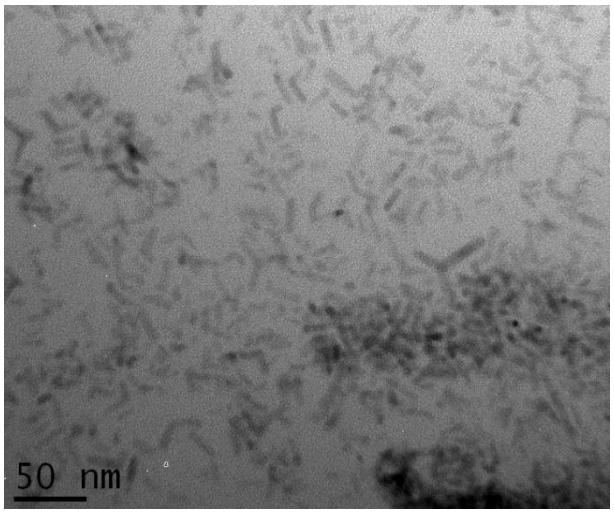

Figure 3.62 TEM image of cadmium sulphide nanorods coated with 21c.

EDS measurements were again unclear, with an increase in carbon, copper and silicon observed along with a decrease in cadmium, sulphur and oxygen, however since only two sets of data were obtained compared to three for other nanorod samples this wasn't entirely unexpected.

Element	Weight%	Atomic%
C	58.36	86.01
O	2.07	2.27
Si	0.99	0.62
S	6.03	3.36
Cu	19.30	5.45
Cd	12.44	2.01

Table 3.13 EDS analysis of cadmium sulphide nanorods functionalised with 21c.

Optical microscopy and DSC analysis again revealed a single melting transition, once more differing from that observed for 21c alone to give an indication that the product differed from the cadmium sulphide nanorods and organic ligand.

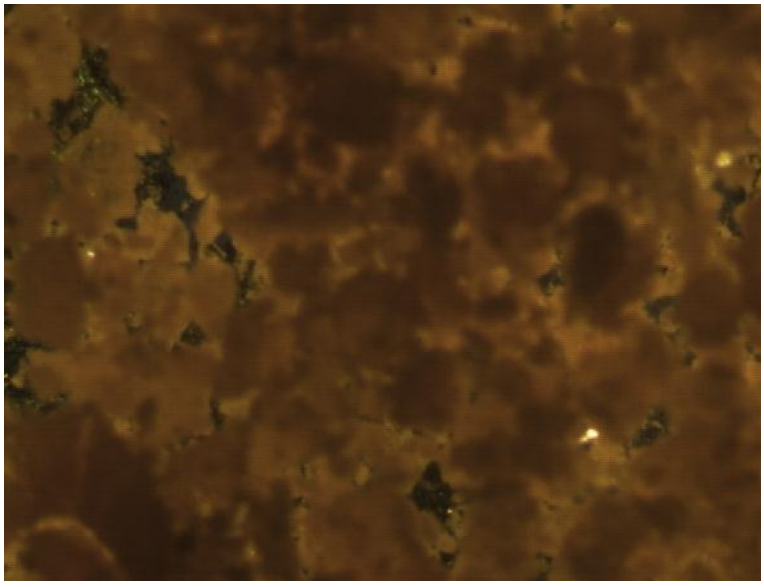

Figure 3.63 Optical microscope image (crossed-polarisers, 100x magnification) of cadmium sulphide nanorods coated with 21c.

3.7 Zinc Sulphide and Cadmium Sulphide Alkylamine-Functionalised Nanorods

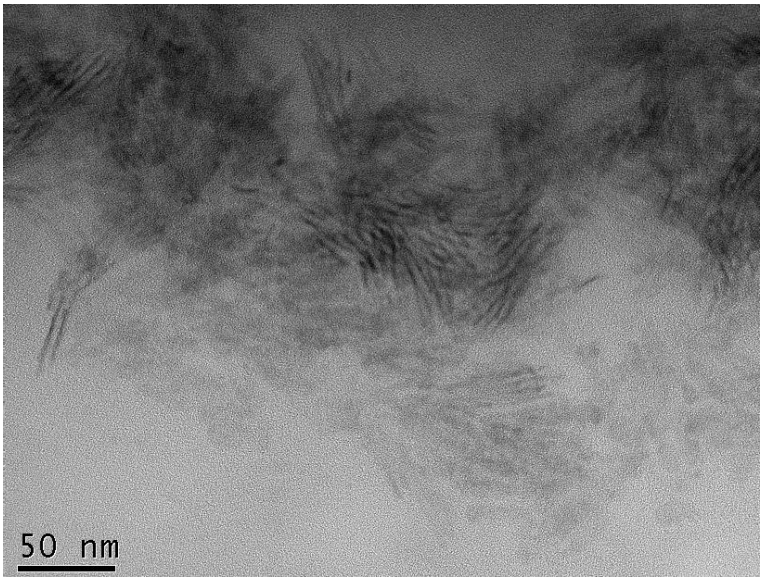

Figure 3.64 TEM image of octadecylamine-coated zinc sulphide nanorods.

Figure 3.64 shows zinc sulphide nanorods produced using the approach described in section 2.9 with some nanorods of aspect ratio above 5 clearly visible, as well as localised ordering.

Element	Weight%	Atomic%
C	76.83	92.86
O	1.31	1.08
S	3.04	1.43
Cu	16.27	4.08
Zn	2.57	0.57

Table 3.14 EDS analysis of octadecylamine-coated zinc sulphide nanorods.

This experiment was merely a repeat of the work carried out within the literature; following on the procedure was repeated with cadmium replacing the zinc compounds as a novel, single-step procedure for the synthesis of cadmium sulphide nanorods.

Figure 3.65 shows the cadmium sulphide nanorods produced using the approach described in section 2.8. Aspect ratios appear to be lower than those of the above zinc sulphide nanorods; however some localised alignment is still observed and much like earlier syntheses, tripod-shaped nanorods are also formed.

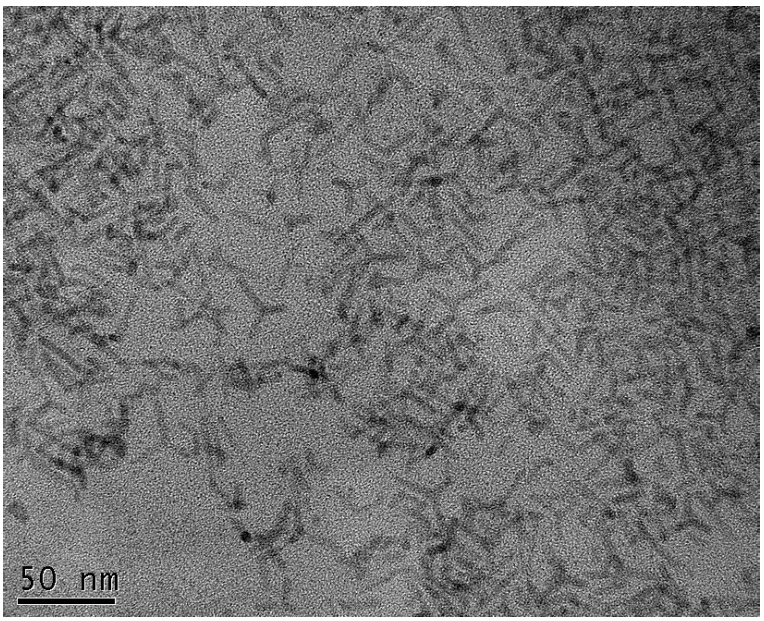

Figure 3.65 TEM image of octadecylamine-coated cadmium sulphide nanorods.

Element	Weight%	Atomic%
C	79.47	94.50
O	0.49	0.44
S	3.40	1.51
Cu	14.69	3.30
Cd	1.95	0.25

Table 3.15 EDS analysis of octadecylamine-coated cadmium sulphide nanorods.

Although experimental work was not carried out due to insufficient time, the potential exists for reactions in which the octadecylamine capping agent would be replaced with liquid-crystalline amine-terminated materials such as (4'-pentyl-[1,1'-biphenyl]-4-yl)methanamine:

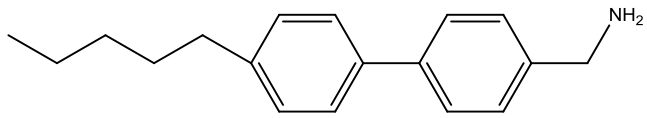

(4'-pentyl-[1,1'-biphenyl]-4-yl)methanamine

Figure 3.66 Liquid-crystalline compound with potential for use in CdS nanorod synthesis.

Such groups would be synthesised by the reduction, using lithium aluminium hydride, of corresponding nitriles in diethyl ether according to literature procedures.[151]

3.8 Lyotropic Liquid Crystalline Phases in Metal (II) Phthalocyanines

Two chromonic phases of copper(II)- and nickel(II)-phthalocyanine tetrasulfonic acid tetrasodium salt were characterised in terms of structure and electrochemical properties. Figures 3.67 and 3.68 show the roughly 'flat', disk-like, MM2-minimised structures of the phthalocyanines used in the subsequent investigations.

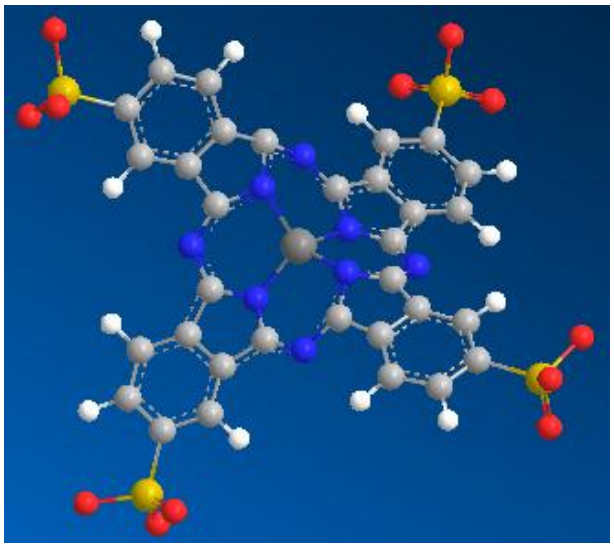

Figure 3.67 Nickel(II) compound MM2 energy minimisation in ChemBio3D

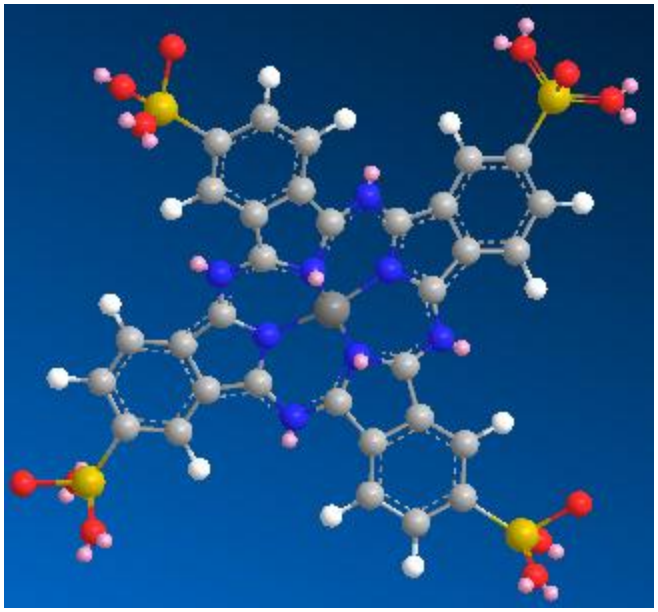

Figure 3.68 Copper(II) compound MM2 energy minimisation in ChemBio3D

3.8.1 Structural characterisation

Preliminary experiments in preparing aqueous-based lyotropic chromonic liquid crystals of the above revealed the presence of the N-phase for the nickel(II) complex at 0.26 M in aqueous solutions of sodium hydroxide at pH 8 (figure 3.70a illustrates the Schlieren textures observed through crossed-polarisers). Solutions of lower concentration formed an isotropic phase with systems appearing dark when viewed under crossed-polarisers, whilst solutions of higher concentration exhibited birefringence, but on closer inspection appeared to be crystal suspensions. The presence of oxygen within the system was not found to be critical for N phase formation. For the copper(II) system birefringence was only observed in samples of concentration above 0.38 M, with the M phase occurring at 0.88 M, a system visibly more viscous than the Ni(II) N-phase. For both phases the rapid evaporation of solvent proved problematic to control for samples in thin layers on microscope slides. The one-dimensional resistivity of both the N and M phases was observed to be comparable with 0.1 M aqueous KCl (table 3.16), indicating partial ionisation of the stacks.

UV-visible spectroscopy of the dark blue nematic phases indicated systems of very high optical absorbance, as expected for dye aggregates;[152] the use of dilute solutions in the concentration range 0.001 to 0.05 mM revealed extinction coefficients of 46970 M^{-1} cm^{-1} (λ_{max}=623 nm) for the Ni(II) system and 25236 M^{-1} cm^{-1} (λ_{max}=613 nm) for the Cu(II) system as shown in figure 3.69 below.

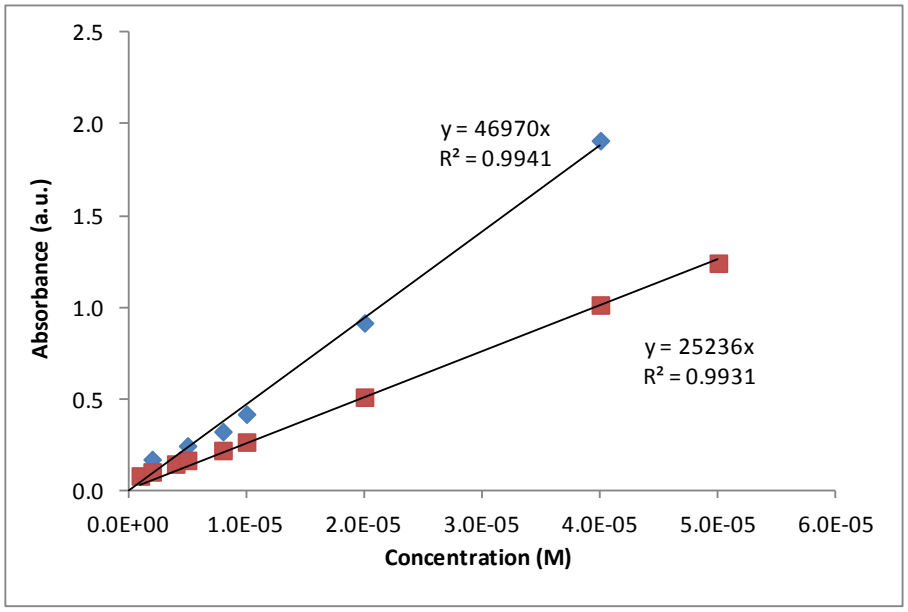

Figure 3.69 UV-visible absorption for dilute Ni (blue) and Cu (red) phthalocyanine solutions.

(a)

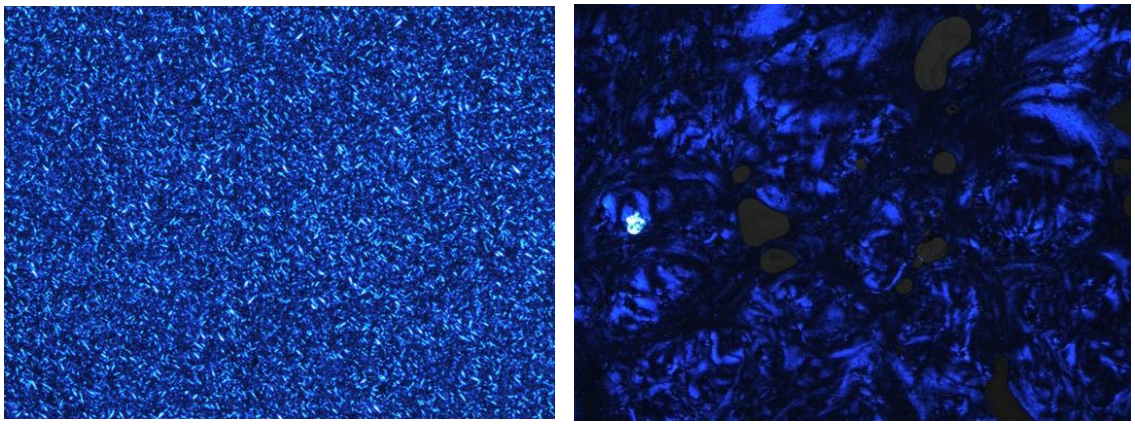

(b)

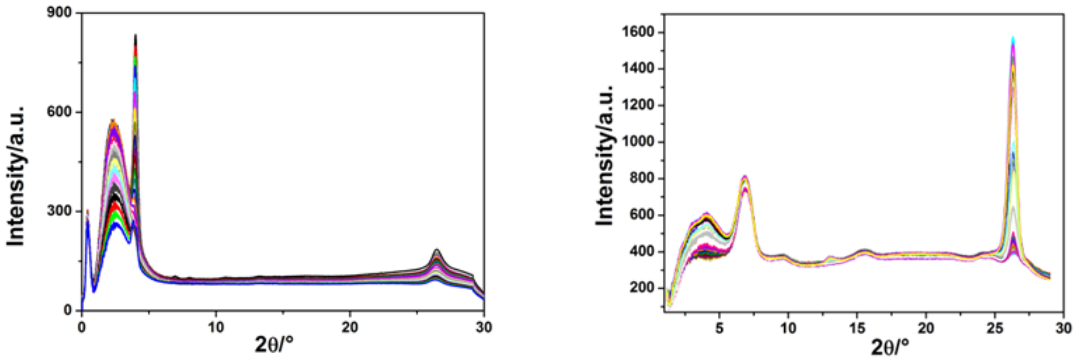

Figure 3.70

(a) Optical microscope images (crossed-polarisers, 100x magnification) of the N-phase of 0.26 M Ni(II) phthalocyanine tetrasulfonic acid tetrasodium salt in water at pH 8 (left), and the M-phase of 0.88 M Cu(II) phthalocyanine tetrasulfonic acid tetrasodium salt in water (right).

(b) X-Ray scattering patterns obtained from the samples in (a): N-phase (left) and M-phase (right). The primary beam is shown at $2\theta = 0.4^{o}$. Traces illustrate the change from low to high temperatures.

X-ray scattering measurements (see table 3.16) using Cu K_{α} radiation (1.54 Å) of the Ni(II) system revealed several features (figure 3.70b), as expected from measurements with similar systems,[131-133] which suggests the presence of the α-polymorph within the chromonic system.[132] Following the Bragg equation, it can be suggested that the wide-angle features represent the intramolecular macrocyle separation within aggregates (δ) as 3.4 Å, a value close to the packing distance observed within the solid state,[131, 133] with the small-angle data implying an aggregation correlation length of 43.5 Å (Ni) or 30.7 Å (Cu), suggesting that, on average, there are 13 (Ni) or 9 (Cu) molecules-per-aggregate, with stacks being of single molecule widths of 22.1-21.7 Å, in agreement with that estimated for the diameter of a single phthalocyanine molecule using ChemDraw 12.0. The temperature-independence of these data (figure 3.70b) indicates that the systems remain within the chromonic liquid crystal phase over

the range 298-325 K (Ni) and 297-355 K (Cu). For the M-phase, up to six orders of the hexagonal pattern are seen (table 3.16), although the higher orders are very weak, and diffuse.

Phase	ρ^a/ Ω cm	R^b/Ω	$C_d{}^c$/mF cm^{-2}	X-ray Scattering Data				
				2θ/°	d^d/Å	q^e/Å^{-1}	$^f q/q_0$	Assignment
N	12.70	5773	12.3	2.03	43.5			Aggregate length
Nickel(II)				3.99	22.1			Aggregate width
phthalocyanine				26.5	3.36			Aggregate spacing
tetrasulfonic acid								
tetrasodium salt								
(0.26 M in H_2O pH 8)								
M	9.17	4585	2.1	2.88	30.7			Aggregate length
Copper(II)				4.07	21.7			Aggregate width
phthalocyanine				6.81	13.0	0.485	1.00	q_0
tetrasulfonic acid				10.5	8.45	0.744	1.53	$q_0\sqrt{3}$
tetrasodium salt				13.0	6.78	0.926	1.91	$2q_0$
(0.88 M in H_2O)				15.6	5.68	1.11	2.28	$q_0\sqrt{7}$
				21.2	4.18	1.50	3.10	$3q_0$
				24.4	3.64	1.73	3.56	$2q_0\sqrt{3}$
				26.3	3.39			Aggregate spacing
Isotropic Solution	11.29							
(0.1 M aqueous KCl)								

[a]Resistivity measured at 293 ±1 K; [b]resistance determined using $R = \frac{\rho}{4r_0}$ with r_0 = 5.5 µm (N) or 5.0 µm (); [c]specific double-layer capacitance inferred from cyclic voltammetry; [d]fundamental crystal spacing determined using $d/A = \frac{1.54}{2\sin\theta}$; [e]scattering vector estimated using $q = \frac{2\pi}{d}$; [f]q_0 = fundamental repeat distance in the hexagonal system (centre-to-centre separation between aggregates).

Table 3.16 Physical characteristics of the N and M lyotropic chromonic liquid crystals.

3.8.2 Electrochemical characterisation

Figure 3.71 illustrates voltammograms corresponding to the oxidation of the two systems. For the Ni(II) system, two one-electron waves are observed, as in dilute solutions,[153, 154] attributed to phthalocyanine ligand-based oxidations. For the Cu(II) system a single oxidation wave is observed, also as in dilute aqueous solution,[153, 155] and also believed to originate from ligand-based oxidations in a complex, multi-electron process. For both systems, the voltammetry is consistent with quasi-reversible electrode kinetics, and of a diffusion-controlled nature (peak currents are directly proportional to the square-root of the scan rate). The data is consistent

with aggregate diffusion or charge transport between aggregate stacks, given that copper(II) phthalocyanine is considered to be a prototypical organic semiconductor,[155] so that intra-aggregate charge transport should be very fast. Reduction of the M phase at a Pt microelectrode afforded waves, which are not at steady-state (figure 3.71iii), but are consistent with a two-electron process, following a slow, irreversible chemical reaction,[153] with $\sqrt{D_r D_z} \sim 10^{-13}\ m^2\ s^{-1}$.[156]

In order to investigate the occurrence of diffusional anisotropy within such ordered, ionic aggregates, microdisc potential-step chronoamperometry was undertaken, potentiostating the electrode after the two-electron waves. Following previous work on the electrochemical characterisation of anisotropic diffusion,[156] the resulting current-time transients were fitted to the adimensional expression,

$$\psi = \frac{i}{4nFr_0c_0\sqrt{D_r D_z}} = 0.7854 + \frac{1}{2}\sqrt{\frac{\pi}{\tau}} + 0.214e^{-0.7824/\sqrt{\tau}}, \qquad \text{(Equation 3.1)}$$

where n=2, F=96484.6 C mol^{-1}, r_0 is the microelectrode radius, c_0 is the effective homogeneous concentration of the redox system, with diffusion coefficients in the directions normal (D_z) and tangential (D_r) to the electrode surface, and for a dimensionless time variable $\tau = 4\frac{D_r t}{r_0^2}$. The fitting procedure employed involved iterative optimisation of D_r and D_z *via* comparison of experimental data over the whole normalised temporal domain (of dummy variable s), subject to a difference-minimised parameter, $\wp = \frac{1}{\sum s}\sum_s \frac{\left|\psi^{\text{expt}} - \psi^{\text{theory}}\right|}{\psi^{\text{expt}}}$. The results are illustrated in figure 3.72 where it is apparent that both systems fit reasonably well over the whole temporal domain with, for the Ni(II) N-phase $D_r = 3.8 \pm 0.4 \times 10^{-8}$ cm^2 s^{-1} and $D_z = 2.2 \pm 1.5 \times 10^{-9}$ cm^2 s^{-1}, and for the seemingly more ordered Cu(II) M-phase, with $D_r = 1.2 \pm 0.9 \times 10^{-8}$ cm^2 s^{-1} and $D_z = 4.4 \pm 1.7 \times 10^{-11}$ cm^2 s^{-1}. Since both systems afford larger diffusion coefficients in the direction radial to the electrode surface compared to the perpendicular, with ratios of $\frac{D_r}{D_z} \sim 20$ (Ni) and 300 (Cu), it can be suggested that the presence of the electrical field at the electrode orients the stacks in a homogenously aligned manner within the electrochemical system, so that in both cases D_r represents transport along the stacks (on the same order of magnitude in both phases), and D_z indicates that lateral transport between columnar aggregates is important, with the smaller value for the M-phase indicating worse lateral aggregate electronic couplings.

Lower values of D compared with dilute aqueous solution are consistent with the higher viscosities of these highly concentrated redox liquid crystals. It is possible that the diffusion model utilised above overestimates the current at short times either because of adsorption, or due to an electro-induced orientation effect - the experimental data only match-up with the model after τ ~ 0.2 (Ni) or 0.5 (Cu), and are not attributable to Ohmic losses (table 3.16).

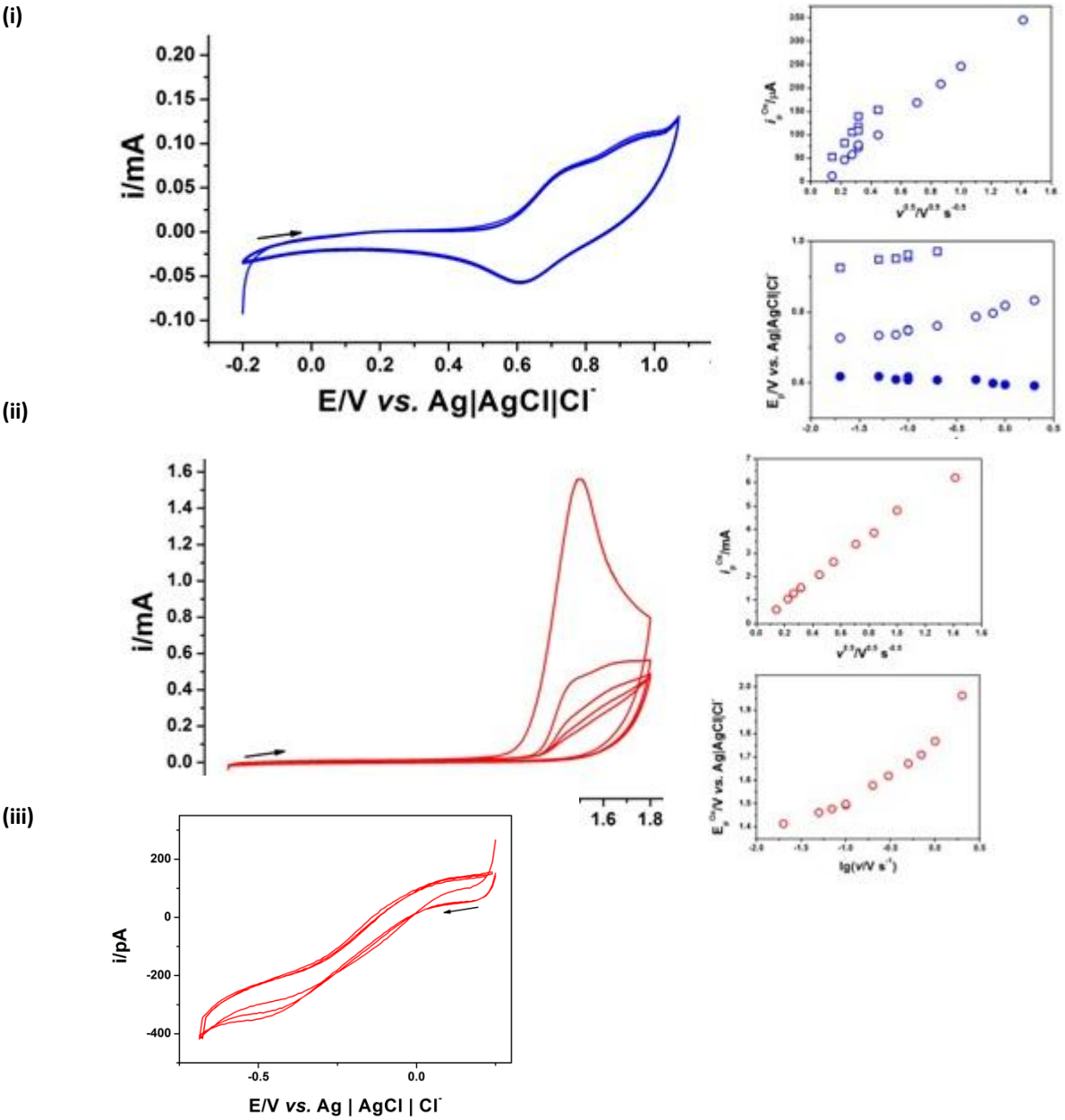

Figure 3.71 Cyclic voltammograms (v = 0.1 V s^{-1}, five cycles) for the oxidation of (i) the Ni(II) sample, and (ii, iii) the Cu(II) sample, at (i, ii) a 3.0 mm glassy carbon electrode or (iii) 10.0 µm platinum microdisc electrode (arrows indicate direction of initial sweep). Also shown in (i) and (ii) are the variation of the peak oxidative potential and current of the first cycle with experimental timescale (wave 1 = circles, wave 2 = squares; oxidative processes = open symbols, filled symbols =reductive signals).

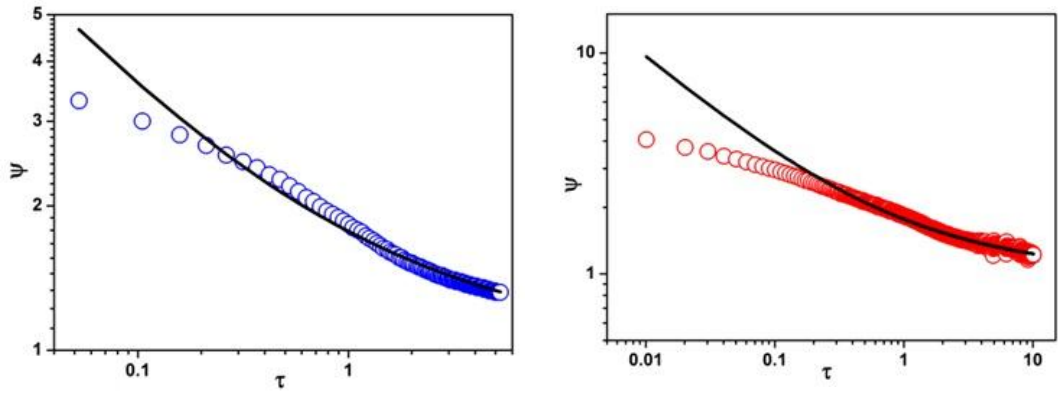

Figure 3.72 Reduced space chronoamperometric transients for (L) the two-electron oxidation of the Ni(II) sample in (a)(i), with a 10.0 µm glassy carbon microelectrode at 1.06 V *vs.* Ag/AgCl/Cl$^-$, and (R) the two-electron reduction of the Cu(II) sample in (a)(iii), with a 10.0 µm Pt microelectrode at -0.7 V *vs.* Ag/AgCl/Cl$^-$ (experimental data = open circles, theoretical fit = solid line).

Self-assembling chromonic liquid crystals in the nematic phase allow for diffusion in at least two dimensions *via* physical transport or through carrier hopping. Mobilities are likely affected by the size of the gaps between aggregates, mesogens stacks and stack defects. It is unclear whether the choice of metal centre is significant compared with the order of the structured liquid nanosystem; the established molecular semiconductor, copper(II) phthalocyanine is known to have a complex electronic structure caused by overlap of the metal 3d levels with the ligand 2p orbitals, leading to both localised and delocalised states at the Fermi level, which can be distorted by the presence of dioxygen.[155] The exact role played by peripheral group dissociation has not been unravelled; the extent of such effects may be controlled by the applied electric field, encouraging phase alignment and migrative structuring of the phase, in a manner similar to that proposed for room temperature ionic liquids,[157] or through localised variations in proton concentration.

4 Conclusions

4.1 Organic Synthesis

The synthesis of thiol-terminated organic materials for use in the surface modification of inorganic nanorods was successfully performed. Although phenol (3) synthesis exhibited a higher yield when the procedure employed in scheme 2 was used in place of Suzuki-Miyaura coupling (scheme 1), the subsequent step involving conversion of hydroxyl (9) to alkyl bromide (10) gave a prohibitively low yield, and so the use of 5-bromo-pent-1-ene (scheme 1) or dibromoalkanes in a similar manner to schemes 3 and 4 may be seen as the most efficient route towards synthesis of the desired organic 'ligand' materials.

It was found that the addition of 1,6-dibromoalkane (14b) the reaction yields were significantly lower and higher melting points were recorded (table 4.1) alongside additional phase transitions for both intermediates and final products, although these may have been at least partially attributable to the increased level of impurity present as a result of the less facile purification of the smaller amounts of material. It is possible that the elevated melting points could have contributed to the severe reduction in yields obtained, though no further investigation other than repetition of the synthetic process was undertaken.

	yield (%)	m.p. (°C)
17a	54	44.8
17b	1.5	104.5
17c	41	87.2
21a	41	39.9
21b	1.5	97.5
21c	35	38.4

Table 4.1 Overall yields and melting points of synthesised organic materials.

It was also observed that replacing the propylcyclohexyl (scheme 3) moiety with the pentylcyclohexyl (scheme 4) variant led to decreases in the reaction yields as well as a slight decrease in the melting points of final products. Overall, the lack of liquid crystalline phases in the majority of organic materials produced may have played some role in the absence of any observable calamitic liquid crystalline phases for nanorods functionalised with said materials.

4.2 Gold Nanorods

A systematic study and comparison of different literature methods of gold nanorod synthesis was performed leading to an increase in the understanding and control of the nanorod properties. The synthesis of anisotropic nanoparticles is far more complex than that of spherical particles which are thermodynamically favourable due to their maximisation of surface are per unit volume. The majority of the literature focuses on novel methods of synthesis which are typically carried out on a microgram to milligram scale with little scope for the practical production of nanorods on a large scale.

Commercially available nanorods are also provided in very low concentration (as described in section 2.1.10), as well as being prohibitively expensive if the target hybrid nanorods are to be used in cost effective, large-surface-area plastic solar cells. A higher concentration and therefore actual yield of nanorods was also required in order to fully characterise the new hybrid materials, and the process of investigating different organic ligands meant that a reproducible method was highly desirable. It was therefore necessary to scale up the very dilute concentrations used in the literature, requiring modification of the synthetic procedures, with reproducibility and practicality in mind. Gold nanorods were synthesised using seed-mediated solution-based methods, typically using CTAB as surfactant with sodium borohydride and ascorbic acid as reducing agents and in some instances Ag(I) ions present. The reproducibility of each reaction method was also investigated with practical applications in mind. Synthesised nanoparticle solutions were analysed using UV-vis absorbance spectrometry, TEM and EDS, all confirming the presence of gold nanorods.

Studies into optimised gold nanorod synthesis found that method 9 produced the best combination of relative nanorod yield, monodispersity, aspect ratio, and actual amounts of nanorods produced, as well as simplicity of procedure and a good fit of theoretical to measured data. For the above reasons, these nanorods (AuS9) were selected for investigations into surface modification.

The synthetic procedures for the preparation of gold nanorods were optimised in terms of the best combination of relative nanorod yield and actual amounts of nanorods produced, monodispersity and aspect ratio of the nanorods, as well as the simplicity, reproducibility and time taken to carry out the preparation, isolation, purification and characterisation. Variation in the duration and frequency of rotation of stirring as well as the timing and rate of addition of different reagents were also seen to have a dramatic impact on the yield and dimensions of nanoparticles formed. Such aspects of synthetic procedures are rarely reported in the

literature and hence had to be determined experimentally. At the conclusion of the investigations into the synthesis of gold nanorods, good control of the nanoparticle aspect ratios had been achieved *via* control of the nucleation and growth steps through variation in different reaction parameters as summarised below.

The basic principle for our optimised method of controlled gold nanorod synthesis involves two steps: firstly the preparation of small spherical gold nanoparticles and secondly the growth of gold nanorods nucleated by the pre-prepared spherical nanoparticles in a rod-like micellar environment. Several different methods have been used for the synthesis of gold nanorods during this thesis which can be grouped into involving a different number of steps. Modifications to the methods were carried out over a range of amounts of surfactant and reducing agents, and also through variation of the reaction conditions. The following discussion provides a brief comparison of these methods:

One-step preparations of gold nanorods

Method 4 (AuS4) was a one-step, gram-scale synthesis of gold nanorods, giving this method the potential to be simpler and easier to reproduce when compared to other, multi-step methods. The results demonstrated that a relatively large yield of rods were formed (63%), but also that the lowest aspect ratio (AR = 3.18) was produced in comparison with nanorods prepared using the other procedures, see table 3.2 for a collation of the results of the methods investigated in this thesis in terms of reaction yield and nanorod and aspect ratio. However, over the course of repeating the experiment multiple times in order to vary different parameters or produce nanorod solutions for surface modification, it was found that dimensions and yields of nanorods obtained using the same parameters were difficult to reproduce.

Method 8 (AuS8) employed acetylacetone as the reducing agent in a one-step synthesis using a sodium carbonate buffer solution with the surfactant CTAB as the aqueous solution in which nanorod formation occurred. Although a slightly higher average aspect ratio was observed (AR = 4.05), the yield of nanorods obtained (58%) is similar, but slightly lower than that obtained using method 4 (AuS4) above, in spite of the fact that method 8 is also a one-step procedure and might reasonably be expected to provide nanorods in high yield.

Two-step preparations of gold nanorods

The synthetic procedure described in method 5 (AuS5) was highly reproducible and produced gold nanorods high in both yield (90%) and aspect ratio (AR = 4.73). This is a two-step procedure in which first a 'seed' solution if prepared followed by preparation and addition of a 'growth' solution. The use of a massive excess of CTAB as surfactant in the growth solution meant that a large amount of CTAB precipitate was often mixed in with the final product, which in some cases made the isolation and characterisation of the nanorods more difficult compared to other methods. However, compared to the above one-step procedures, a much higher relative yield of nanorods was observed (90%). Unfortunately this method proved rather difficult to scale up and the absolute amount of nanorods produced was low compared to method 4. Methods 9 and 3 employ similar reaction conditions to method 5, but in method 9 after the preparation of seed solution, the reaction mixture was kept at 40°C for about 15 min and also different concentrations of starting materials were used. In method 3 a binary surfactant mixture of CTAB and BDAC was used and an average nanorod yield (53%) was achieved, whereas method 5 gave gold nanorods in good yield (69%). Interpretation of TEM images illustrates that gold nanorods synthesised using methods 3 and 9 have relatively high aspect ratios (AR = 4.76 and 4.26 respectively), which correlates well with the maximum wavelength of absorption attributable to the longitudinal plasmon band (λ_{LPB} = 869.02 and 824.85 nm respectively).

Methods 6 and 7 use multiple steps in the preparation of gold nanorods. In method 6, nitric acid was added to the synthesis of the gold nanorods in the absence of silver nitrate, leading to the formation of nanospheres rather than nanorods in our experiments. The relative yield of nanorods was also very low (21%) in method 7 compared to the large proportion of spherical particles formed. Nevertheless, this method did produce the longest nanorods with the highest mean aspect ratio (AR = 5.92) of all nanorods produced using the different procedures investigated.

Unfortunately, only a maximum of five nanorods were present in the series of ten separate TEM images obtained, due to a low relative concentration compared to the gold nanospheres predominately produced using this method, therefore further statistical analysis was not appropriate. This was possibly due to unfavourable reaction kinetics or deviations from the experimental method used in the literature. It was clear that the five-step reaction procedures used in methods 6 and 7 produced spherical gold nanoparticles rather than nanorods and that the reaction protocols were much more complex than the corresponding one-step and two-step procedures.

The one-step methods 4 and 8 were much simpler to carry out than the five-step methods and allowed for the production of gold nanorods in good yield. Unfortunately, the aspect ratios of nanorods produced were the lower than the other nanorod-producing methods. Consequently, it was concluded that attempts to further control and optimise the reaction conditions was better done using two-step reactions, which produced the best compromise between a good overall gold nanorod yield and a relatively high aspect ratio as well as possessing relatively simple and reproducible reaction procedures. These reactions also seem to have the potential to be scaled up in order to produce reasonable amounts of gold nanorods for further investigations into surface modification and use in photovoltaic cells. In addition, these methods also produced the most stable gold nanorods as determined *via* TEM and UV-vis measurements several months after preparation.

General Gold Nanorod Conclusions/Parameters for Gold Nanorod Preparation

- The use of ascorbic acid as a mild reducing agent in synthetic procedures appeared to assist the growth of gold nanorods and reduction of Au3+ ions, with the rate of reduction dependant on the concentration of reducing agent. As the amount of ascorbic acid or other reducing agents changes, the rate of reduction becomes faster or slower accordingly.
- The solution colour changes over time during each procedure depending on the nanoparticle dimensions.
- Nanorod aspect ratios can be controlled by the shape and size properties of the micellar template, and by the relative concentrations of gold salt and surfactant, typically CTAB, used in the reaction.
- The presence of the surfactant provides cylindrical micelles which may act as a nanorod template, constrains the particle growth in one dimension through surface adsorption, and stabilises the resultant particles.
- High temperatures are not required for the synthesis of gold nanorods, within the reaction a typical temperature is approximately 25 °C.
- The ratio of seed solution to growth solution plays an important role in determining the final product. Addition of unsuitable concentrations of seed solution to growth solutions typically leads to exclusively the formation of spherical nanoparticles, as less gold will be available for the anisotropic growth of each particle. Additionally, the correct growth conditions are critical for the production of nanorods of good quality and high yield in aqueous solution.

- Larger aspect ratios equate to greater red-shifting of the LPB in UV-vis absorption spectra, unlike the TPB which may be blue-shifted.
- Gold nanorods were typically purified, or separated from spherical particles, *via* three cycles of centrifugation (10000 rpm for 10 minutes). In order to determine the effects of rpm, duration and number of cycles of centrifugation on shape separation, these three parameters were systematically varied.
- Centrifuge-induced separation is only possible for larger nanorods, rendering the purification of smaller rods much less straightforward. Use of a solvent extraction procedure (transfer of nanorods from aqueous to organic solvent) may be useful in allowing purification of large amounts of shorter rods.
- The stability of the nanorods produced *via* different methods was investigated using UV-vis spectroscopy after 2 and 4 months and after 1 year from their preparation. The most stable nanorods were obtained using methods 5 and 8, and the most unstable nanorods were produced through method 2 for which it was observed that the rods had degraded significantly, typically forming spherical particles. It is also possible that by keeping the solutions motionless over the time periods, CTAB may have sedimented leading to a reduction in its concentration in solution and therefore a possible reduction in the amount of cylindrical micelles along with a subsequent increase in spherical micelles.
- The addition of sodium hydrogen and dihydrogen phosphate, and potassium hydrogen and dihydrogen phosphate salts to aqueous gold nanorod solutions was investigated and changes in the LPB and/or TPB absorbance observed in the UV-vis spectra were monitored. It was observed that addition of sodium hydrogen phosphate appeared to reduce the absorption associated with the TPB indicating a reduction in the amount of spherical gold nanoparticles; however this was not confirmed by TEM images and may have been due to the phosphates forming complexes with the particles in solution.
- There is still no simple and effective method available in the literature to produce high aspect ratio gold nanorods in high yield.

4.3 Cadmium Sulphide Nanorods

Cadmium sulphide nanoparticles including nanorods were synthesised using solution-based methods with a variety of different capping agents, again with analysis using UV-vis absorbance spectrometry, TEM and EDS in order to confirm the presence of cadmium sulphide nanoparticles. The intensity of absorbance measured *via* UV-vis spectroscopy were consistently too high for an accurate peak wavelength or intensity to be recorded, nevertheless the absorbances recorded fell within in the range expected for cadmium sulphide nanoparticles.

For investigations into cadmium sulphide nanorod synthesis, method 3i was found to produce the best combination of relative nanorod yield, monodispersity, aspect ratio, and actual amounts of nanorods produced, as well as being the most straightforward. Methods 3ii and 4 also produced cadmium sulphide nanorods, however these were either of lower aspect ratio and yield, or in the latter case required a more complicated and time consuming experimental procedure at higher temperatures with no substantial improvement in the resulting nanorods. Methods 1, 2 and 5 produced roughly spherical cadmium sulphide nanoparticles and therefore were unsuitable for this study.

Birefringence observed under a polarised optical microscope within samples of cadmium sulphide nanorods in hexane solutions indicate the potential presence of lyotropic liquid crystalline phases as the nanorods locally self-align into ordered phases. Further improvement to the synthetic procedure or the use of alternative routes in order to increase the aspect ratio and monodispersity of nanorods would likely increase the degree of birefringence and liquid crystalline features present according to Onsager's theory (see above).

Zinc sulphide and cadmium sulphide nanorods were successfully synthesised by following and subsequently adapting the approach employed by Acharya *et al.*[96] As mentioned above, one possible route for future investigations would be the replacement of octadecylamine with synthesised liquid crystalline amine-terminated materials of similar structure to the organic materials synthesised within this work.

4.4 Surface Modification of Inorganic Nanorods

Initial investigations into the surface modification of gold nanorods were unsuccessful, largely due to the low concentration of commercially obtained gold nanorods. The surface modification of synthesised gold nanorods was investigated using dodecanethiol and octadecanethiol, with the former proving more suitable, possibly due to its increased solubility in the solvents used. As mentioned in chapter 3, a downfield shift of approximately 0.10 ppm along with a change in splitting pattern from quartet to triplet, consistent with literature observations, was recorded in the ^{1}H NMR spectra for the methyl protons adjacent to the thiol functional group. This was repeated consistently for all thiol-functionalised nanorods, including when various synthesised organic ligands were used, giving a strong indication that successful surface modification had taken place. IR spectroscopy was also attempted in order to compare the nanorods and organic ligand materials before and after surface modification, however the absorption bands observed were largely unclear and inconsistent over repeated measurements. For these reasons as well as problems with equipment and time restraints no further IR spectroscopy was performed.

Despite an increase in localised alignment of nanorods after surface modification with organic materials had taken place, no liquid crystalline phases were detected for the hybrid materials. The increase in alignment is expected to be a result of the decreased repulsion between organic surface coatings when compared to ionic surfactants such as CTAB - though as various unsuccessful attempts at surface modification demonstrated, this process has to be carefully controlled in order to avoid irreversible aggregation of nanorods.

Cadmium sulphide nanorods (CdS3i) were successfully functionalised using commercially available dodecanethiol, as verified by the above NMR studies. The nanorods were also functionalised using ferrocene hexanethiol, with ligand exchange again confirmed by both NMR spectroscopy, TEM and EDS.

After initial reactions between cadmium sulphide nanorods and commercially available thiols, functionalisation with the synthesised organic ligands was successfully achieved. EDS revealed an increase in the relative amounts of C and O present, consistent with the addition of the organic ligand. Optical microscopy and DSC analysis confirmed differences of 20 °C upwards in the melting point of the organic ligands and functionalised CdS nanorods, although a large proportion of the cadmium sulphide nanorods themselves remained in the solid state upon

heating under a polarised optical microscope. Examination using EDS typically revealed an increase in the relative amount of carbon and oxygen in the functionalised nanorods compared to their "blank" equivalents, consistent with the addition of the organic surface ligand groups employed. However, such measurements were often less than conclusive, especially in the cases where only a small amount of organic material was available for surface modification.

Overall, it is easy to see why there is such a great imbalance between synthesis and surface modification of spherical nanoparticles compared to their anisotropic equivalents within the scientific literature. High yield synthesis of monodisperse, high aspect ratio, inorganic nanorods is much less straightforward than spherical particles, and in turn the nanorods are typically much less stable, making surface modification - especially the type required in order to meet the aims of this project - much more difficult to achieve.

4.5 Lyotropic Liquid Crystalline Phases in Metal (II) Phthalocyanines

Investigations were carried out using chromonic liquid crystalline systems, which provide an alternative approach to the formation of self-assembled organometallic nanorods. Copper(II)- and nickel(II)-phthalocyanine tetrasulfonic acid tetrasodium salt were dissolved in water at appropriate concentrations to produce lyotropic liquid crystalline phases which were then characterised in terms of structure and electrochemical properties. The XRD measurements obtained suggested "stack" dimensions in accordance with those calculated using chemical modelling software, and birefringent liquid crystalline textures were observed when the materials were examined using polarised optical microscopy.

The self-assembling chromonic liquid crystals that forming a nematic phase allowed for diffusion in at least two dimensions *via* physical transport or through carrier hopping, with mobility likely influenced by the space between aggregates, mesogens stacks as well as defects within the stacks. As discussed previously, it remains unclear whether changing the metal centre is significant compared with the order of the structured liquid nanosystem, and the precise effects of peripheral group dissociation have not been resolved although there are a number of possibilities in controlling the extent of any influence this may have.

Overall, the use of metal (II) phthalocyanines in the formation of chromonic liquid crystalline phases demonstrated the possibility an alternative route for the production of hybrid inorganic-organic nanorod-like systems.

5 Publications and Conference Presentations

5.1 Publications

1. J. E. Halls, R. W. Bourne, K. J. Wright, L. I. Partington, M. G. Tamba, Yan Zhou, T. Ramakrishnappa, G. H. Mehl, S. M. Kelly and J. D. Wadhawan, *Electrochem. Comm*., 2012, **19**, 50-54.

2. J. E. Halls, K. J. Wright, J. E. Pickersgill, J. P. Smith, A. A. Altalhi, R. W. Bourne, P. Alaei, T. Ramakrishnappa, S. M. Kelly, and J. D. Wadhawan, *Electrochimica Acta*, 2012, **70**, 215-227.

3. R. W. Bourne, S. M. Kelly and J. D. Wadhawan, J. Exp. Nanosci., **7**, 2012, 673–687.

4. J. E. Halls, R. W. Bourne, J. D. Wadhawan, Electrochemistry of liquid nanosystems, in R. G. Compton, J. D. Wadhawan (eds.), Specialist Periodical Reports in Electrochemistry, volume 11, RSC Publishing, 2012, in press.

5.2 Conference Presentations

1. "Preparation of Liquid Crystalline Nanorods" - Poster Presentation at the British Liquid Crystal Society Conference, 29th - 31st March 2010, University of Hull.

2. "Hybrid organic-inorganic nanorods and their potential use in photovoltaic cells" - Oral Presentation at RSC Postgraduate Symposium on Nanotechnology, 16th December 2011, University of Birmingham.

6 References

1 F. Reinitzer, *Monatshefte für Chemie*, 1888, **9**, 21.
2 L. Onsager, *Annals New York Academy of Sciences*, 1949, **51**, 627.
3 G. J. Vroege and H. N. W. Lekkerkerker, *Rep. Prog. Phys.*, 1992, **55**, 1241.
4 S. Kusabayashi and M. M. Labes, *Molecular Crystals and Liquid Crystals*, 1969, **7**, 11.
5 H. Kamei, Y. Katayama, and T. Ozawa, *Japanese Journal of Applied Physics*, 1972, **11**, 2.
6 G. W. Gray, K. J. Harrison, and J. A. Nash, *Electronics Letters*, 1973, **9**, 130.
7 D. Adam, P. Schuhmacher, J. Simmerer, L. Haussling, K. Siemensmeyer, K. H. Etzbach, H. Ringsdorf, and D. Haarer, *Nature*, 1994, **371**, 141.
8 M. Carrasco-Orozco, W. C. Tsoi, M. O'Neill, M. P. Aldred, P. Vlachos, and S. M. Kelly, *Adv Mater*, 2006, **18**, 1754.
9 P. J. Collings and M. Hird, 'Introduction to Liquid Crystals', Taylor & Francis Ltd., 2004.
10 A. M. van de Craats, J. M. Warman, K. Mullen, Y. Geerts, and J. D. Brand, *Adv Mater*, 1998, **10**, 36.
11 S. Middleman and A. K. Hochberg, 'Process Engineering Analysis in Semiconductor Device Fabrication', McGraw-Hill, 1993.
12 G. Mie, *Annalen der Physik*, 1908, **330**, 377.
13 V. Sharma, K. Park, and M. Srinivasarao, *Mat Sci Eng R*, 2009, **65**, 1.
14 T. K. Sau and A. L. Rogach, *Adv Mater*, 2009, **22**, 1781.
15 R. W. Murray, *Chem Rev*, 2008, **108**, 2688.
16 X. Huang, S. Neretina, and M. A. El-Sayed, *Adv Mater*, 2009, **21**, 4880.
17 X. H. Huang, I. H. El-Sayed, W. Qian, and M. A. El-Sayed, *Nano Lett*, 2007, **7**, 1591.
18 F. Manea, F. B. Houillon, L. Pasquato, and P. Scrimin, *Angewandte Chemie International Edition*, 2004, **43**, 6165.
19 S. A. Maier and H. A. Atwater, *J Appl Phys*, 2005, **98**, 011101.
20 S. A. Maier, *Curr Nanosci*, 2005, **1**, 17.
21 F. E. Wagner, S. Haslbeck, L. Stievano, S. Calogero, Q. A. Pankhurst, and P. Martinek, *Nature*, 2000, **407**, 691.
22 M. Faraday, *Philosophical Transactions of the Royal Society of London*, 1857, **147**, 145.
23 R. Zsigmondy, 'The Chemistry of Colloids', John Wiley & Sons, 1917.
24 R. Zsigmondy, 'Colloids and the Ultramicroscope', John Wiley & Sons, 1909.
25 T. Svedberg, 'The Formation of Colloids', D. Van Nostrod Company, Inc., 1921.
26 T. Svedberg, 'The Ultracentrifuge', Oxford University Press, 1940.
27 R. Gans, *Annalen der Physik*, 1912, **37**, 20.
28 M. A. El-Sayed, *Accounts Chem Res*, 2001, **34**, 257.
29 M. Brust, M. Walker, D. Bethell, D. J. Schiffrin, and R. Whyman, *J Chem Soc Chem Comm*, 1994, 801.
30 L. S. Li, J. Walda, L. Manna, and A. P. Alivisatos, *Nano Lett*, 2002, **2**, 557.
31 S. Link, M. B. Mohamed, and M. A. El-Sayed, *J Phys Chem B*, 1999, **103**, 3073.
32 A. Brioude, X. C. Jiang, and M. P. Pileni, *J Phys Chem B*, 2005, **109**, 13138.
33 S. Eustis and M. A. El-Sayed, *J Appl Phys*, 2006, **100**, 44324.
34 D. K. Smith, N. R. Miller, and B. A. Korgel, *Langmuir*, 2009, **25**, 9518.
35 J. S. Duan, K. Park, R. I. MacCuspie, R. A. Vaia, and R. Pachter, *J Phys Chem C*, 2009, **113**, 15524.
36 N. R. Jana, L. Gearheart, and C. J. Murphy, *J Phys Chem B*, 2001, **105**, 4065.
37 F. Kim, J. H. Song, and P. D. Yang, *J Am Chem Soc*, 2002, **124**, 14316.
38 Y. Y. Yu, S. S. Chang, C. L. Lee, and C. R. C. Wang, *J Phys Chem B*, 1997, **101**, 6661.
39 J. Zhu, Y. C. Wang, S. N. Yan, and Y. Lu, *Journal of Wuhan University of Technology - Mater. Sci. Ed.*, 2003, **18**, 6.
40 C. R. Martin, *Chem Mater*, 1996, **8**, 1739.
41 B. L. Cushing, V. L. Kolesnichenko, and C. J. O'Connor, *Chem Rev*, 2004, **104**, 3893.
42 T. K. Sau and C. J. Murphy, *Philosophical Magazine*, 2007, **87**, 2143.
43 B. D. Busbee, S. O. Obare, and C. J. Murphy, *Adv Mater*, 2003, **15**, 414.
44 M. Tornblom and U. Henriksson, *J Phys Chem B*, 1997, **101**, 6028.
45 B. Nikoobakht and M. A. El-Sayed, *Chem Mater*, 2003, **15**, 1957.
46 H. Y. Wu, W. L. Huang, and M. H. Huang, *Cryst Growth Des*, 2007, **7**, 831.

47 M. Hu, P. Hillyard, G. V. Hartland, T. Kosel, J. Perez-Juste, and P. Mulvaney, *Nano Lett*, 2004, **4**, 2493.
48 Liu and P. Guyot-Sionnest, *The Journal of Physical Chemistry B*, 2005, **109**, 22192.
49 D. K. Smith and B. A. Korgel, *Langmuir*, 2008, **24**, 644.
50 J. E. Millstone, W. Wei, M. R. Jones, H. J. Yoo, and C. A. Mirkin, *Nano Lett*, 2008, **8**, 2526.
51 Q. L. Li, T. Burgi, and H. Chen, *J Wuhan Univ Technol*, 2010, **25**, 104.
52 C. M. Tollan, J. Echeberria, R. Marcilla, J. A. Pomposo, and D. Mecerreyes, *J Nanopart Res*, 2009, **11**, 1241.
53 B. P. Khanal and E. R. Zubarev, *J Am Chem Soc*, 2008, **130**, 12634.
54 J. Cui, J. B. Fan, T. Zhao, A. Wang, R. A. Drezek, and M. Q. Zhu, *J Biomed Nanotechnol*, 2009, **5**, 573.
55 N. R. Jana, *Small*, 2005, **1**, 875.
56 F. Kim, K. Sohn, J. S. Wu, and J. X. Huang, *J Am Chem Soc*, 2008, **130**, 14442.
57 X. S. Kou, S. Z. Zhang, C. K. Tsung, M. H. Yeung, Q. H. Shi, G. D. Stucky, L. D. Sun, J. F. Wang, and C. H. Yan, *J Phys Chem B*, 2006, **110**, 16377.
58 Y. Xia, Y. J. Xiong, B. Lim, and S. E. Skrabalak, *Angew Chem Int Edit*, 2009, **48**, 60.
59 V. Sharma, K. Park, and M. Srinivasarao, *P Natl Acad Sci USA*, 2009, **106**, 4981.
60 H. W. Huang, C. C. He, Y. L. Zeng, X. D. Xia, and X. Y. Yu, *Colloid Surface A*, 2008, **317**, 56.
61 W. U. Huynh, J. J. Dittmer, N. Teclemariam, D. J. Milliron, A. P. Alivisatos, and K. W. J. Barnham, *Phys Rev B*, 2003, **67**, 115316.
62 J. T. Hu, L. S. Li, W. D. Yang, L. Manna, L. W. Wang, and A. P. Alivisatos, *Science*, 2001, **292**, 2060.
63 P. Li, L. Y. Wang, L. Wang, and Y. D. Li, *Chem-Eur J*, 2008, **14**, 5951.
64 C. C. Chen, C. Y. Chao, and Z. H. Lang, *Chem Mater*, 2000, **12**, 1516.
65 Q. Q. Wang, G. Xu, and G. R. Han, *J Solid State Chem*, 2005, **178**, 2680.
66 M. Salavati-Niasari, M. R. Loghman-Estarki, and F. Davar, *Chem Eng J*, 2008, **145**, 346.
67 F. Shieh, A. E. Saunders, and B. A. Korgel, *J Phys Chem B*, 2005, **109**, 8538.
68 S. Kan, T. Mokari, E. Rothenberg, and U. Banin, *Nat Mater*, 2003, **2**, 155.
69 Z. Tang, N. A. Kotov, and M. Giersig, *Science*, 2002, **297**, 237.
70 F. Shieh, A. E. Saunders, and B. A. Korgel, *The Journal of Physical Chemistry B*, 2005, **109**, 8538.
71 J. Yang, J.-H. Zeng, S.-H. Yu, L. Yang, G.-e. Zhou, and Y.-t. Qian, *Chem Mater*, 2000, **12**, 3259.
72 L. Manna, E. C. Scher, and A. P. Alivisatos, *J Am Chem Soc*, 2000, **122**, 12700.
73 Y. Yin and A. P. Alivisatos, *Nature*, 2005, **437**, 664.
74 A. E. Saunders, A. Ghezelbash, P. Sood, and B. A. Korgel, *Langmuir*, 2008, **24**, 9043.
75 K. T. Yong, Y. Sahoo, M. T. Swihart, and P. N. Prasad, *J Phys Chem C*, 2007, **111**, 2447.
76 Y. Li, J. H. Wan, and Z. N. Gu, *Acta Phys-Chim Sin*, 1999, **15**, 1.
77 H. W. Zhang, S. Delikanli, Y. L. Qin, S. L. He, M. Swihart, and H. Zeng, *Nano Res*, 2008, **1**, 314.
78 P. Buffat and J. P. Borel, *Physical Review A*, 1976, **13**, 2287.
79 S. T. Chen, X. L. Zhang, Q. H. Zhang, and W. H. Tan, *Nanoscale Res Lett*, 2009, **4**, 1159.
80 J. C. Love, L. A. Estroff, J. K. Kriebel, R. G. Nuzzo, and G. M. Whitesides, *Chem Rev*, 2005, **105**, 1103.
81 M. Brust, J. Fink, D. Bethell, D. J. Schiffrin, and C. Kiely, *J Chem Soc Chem Comm*, 1995, 1655.
82 B. Thierry, J. Ng, T. Krieg, and H. J. Griesser, *Chem Commun*, 2009, 1724.
83 K. Ikeda, A. Kanazawa, O. Tsutsumi, and N. Kanayama, *Chem Commun*, 2001, **2**, 2640.
84 L. Cseh and G. H. Mehl, *J Am Chem Soc*, 2006, **128**, 13376.
85 M. Jebb, P. K. Sudeep, P. Pramod, K. G. Thomas, and P. V. Kamat, *J Phys Chem B*, 2007, **111**, 6839.
86 J. M. El Khoury, X. L. Zhou, L. T. Qu, L. M. Dai, A. Urbas, and Q. Li, *Chem Commun*, 2009, 2109.
87 Q. Dai, J. Coutts, J. H. Zou, and Q. Huo, *Chem Commun*, 2008, 2858.
88 E. Dujardin, L. B. Hsin, C. R. C. Wang, and S. Mann, *Chem Commun*, 2001, 1264.
89 B. P. Khanal and E. R. Zubarev, *Angew Chem Int Edit*, 2007, **46**, 2195.
90 H. P. Xu, B. Y. Xie, W. Z. Yuan, J. Z. Sun, F. Yang, Y. Q. Dong, A. J. Qin, S. Zhang, M. Wang, and B. Z. Tang, *Chem Commun*, 2007, 1322.
91 B. C. Sih and M. Wolf, *J Phys Chem C*, 2007, **111**, 17184.
92 C. Lapointe, N. Cappallo, D. H. Reich, and R. L. Leheny, *J Appl Phys*, 2005, **97**.
93 T. Hegmann, H. Qi, and V. M. Marx, *J Inorg Organomet P*, 2007, **17**, 483.
94 B. M. I. van der Zande, G. J. M. Koper, and H. N. W. Lekkerkerker, *J Phys Chem B*, 1999, **103**, 5754.
95 Q. K. Liu, Y. X. Cui, D. Gardner, X. Li, S. L. He, and Smalyukh, II, *Nano Lett*, 2010, **10**, 1347.

96 S. Kundu, J. P. Hill, G. J. Richards, K. Ariga, A. H. Khan, U. Thupakula, and S. Acharya, *J Nanosci Nanotechno*, 2011, **11**, 7729.
97 in 'Renewables 2012 Global Status Report', www.ren21.net, 2012.
98 U. EPA, in 'Inventory of U.S. Greenhouse Gas Emissions and Sinks: 1990-1998', Washington DC, 2000.
99 M. Gratzel, *Nature*, 2001, **414**, 338.
100 M. A. Green, *Prog Photovoltaics*, 2001, **9**, 123.
101 S. R. Forrest, *Nature*, 2004, **428**, 911.
102 J. G. Xue, B. P. Rand, S. Uchida, and S. R. Forrest, *Adv Mater*, 2005, **17**, 66.
103 R. Kropp, in 'Solar Expected to Maintain its Status as the World's Fastest-Growing Energy Technology', 2009, SRI world group.
104 A. E. Becquerel, *Comptes rendus de l'Académie des sciences*, 1839, **9**.
105 A. Einstein, *Annalen der Physik*, 1905, **322**, 132.
106 H. Hoppe and N. S. Sariciftci, *J Mater Res*, 2004, **19**, 1924.
107 C. W. Tang, *Appl Phys Lett*, 1986, **48**, 183.
108 J. H. Schon, C. Kloc, and B. Batlogg, *Appl Phys Lett*, 2000, **77**, 2473.
109 P. Peumans, S. Uchida, and S. R. Forrest, *Nature*, 2003, **425**, 158.
110 W. C. Tsoi, M. O'Neill, M. P. Aldred, S. P. Kitney, P. Vlachos, and S. M. Kelly, *Chem Mater*, 2007, **19**, 5475.
111 A. C. Fisher, 'Electrode Dynamics', Oxford University Press, 1996.
112 P. W. Atkins and J. d. Paula, 'Physical Chemistry 7th Edition', Oxford University Press, 2002.
113 R. G. Compton and C. E. Banks, 'Understanding Voltammetry', World Scientific Publishing, 2007.
114 J. A. V. Butler, *Trans. Faraday Soc.*, 1924, **19**.
115 M. Volmer and T. E. Gruz, *Z. Physik. Chem.*, 1930, **150A**.
116 J. Tafel, *Z. Physik. Chem.*, 1905, **50A**.
117 J. Franck, *Trans. Faraday Soc.*, 1926, **21**.
118 E. Condon, *Physical Review*, 1926, **28**.
119 K. B. Oldham, J. C. Myland, C. G. Zoski, and A. M. Bond, *J. Electroanal. Chem.*, 1989, **270**, 79.
120 C. Amatore, E. Maisonhaute, and G. Simonneau, *J. Electroanal. Chem.*, 2000, **486**, 141.
121 J. Heinze, *Agnew. Chem. Int. Ed. Engl.*, 1991, **30**, 170.
122 A. Régis, P. Hapiot, and S. Servagent-Noinville, *Anal. Chem.*, 2000, **72**, 2216.
123 S. Bruckenstein, *Anal. Chem.*, 1987, **59**, 2098.
124 K. Štulík, C. Amatore, K. Holub, V. Mareček, and W. Kutner, *Pure and App. Chem.*, 2000, **72**, 1483.
125 C. P. Andrieux, P. Hapiot, and J. M. Saveant, *Chem. Rev.*, 1990, **90**, 723.
126 S. M. Kelly and M. O'Neill, *Advanced Materials,* 2011, **23**, 566.
127 C. R. Treadway, M. G. Hill, and J. K. Barton, *Chemical Physics*, 2002, **281**, 409.
128 V. G. Nazarenko, O. P. Boiko, M. I. Anisimov, A. K. Kadashchuk, Y. A. Nastishin, A. B. Golovin, and O. D. Lavrentovich, *Appl Phys Lett*, 2010, **97**.
129 D. Zigah, C. Herrier, L. Scheres, M. Giesbers, B. Fabre, P. Hapiot, and H. Zuilhof, *Angew Chem Int Edit*, 2010, **49**, 3157.
130 J. Lydon, *J Mater Chem*, 2010, **20**, 10071.
131 B. Donnio, *Curr Opin Colloid In*, 2002, **7**, 371.
132 N. V. Usoltseva and V. V. Bykova, *Molecular Crystals and Liquid Crystals*, 1992, **215**, 89.
133 N. V. Usoltseva, V. V. Bykova, N. M. Kormilitsyn, G. A. Ananieva, and V. E. Maizlish, *Nuovo Cimento Della Societa Italiana Di Fisica D-Condensed Matter Atomic Molecular and Chemical Physics Fluids Plasmas Biophysics*, 1990, **12**, 1237.
134 J. Gregory and K. C. Holmes, *Journal of Molecular Biology*, 1965, **13**, 796.
135 P. V. Braun, P. Osenar, and S. I. Stupp, *Nature*, 1996, **380**, 325.
136 X. G. Peng, L. Manna, W. D. Yang, J. Wickham, E. Scher, A. Kadavanich, and A. P. Alivisatos, *Nature*, 2000, **404**, 59.
137 W. U. Huynh, J. J. Dittmer, and A. P. Alivisatos, *Science*, 2002, **295**, 2425.
138 N. Miyaura and A. Suzuki, *J Chem Soc Chem Comm*, 1979, 866.
139 K. Matos and J. A. Soderquist, *J Org Chem*, 1998, **63**, 461.
140 A. Williamson, *Philosophical Magazine*, 1850, **37**, 7.
141 Y. Y. Luk, N. L. Abbott, J. N. Crain, and F. J. Himpsel, *J Chem Phys*, 2004, **120**, 10792.
142 R. Derda, D. J. Wherritt, and L. L. Kiessling, *Langmuir*, 2007, **23**, 11164.
143 S. Lightowler and M. Hird, *Chem Mater*, 2005, **17**, 5538.
144 J. Simon, S. Salzbrunn, G. K. S. Prakash, N. A. Petasis, and G. A. Olah, *J Org Chem*, 2001, **66**, 633.

145 M. Fibbioli, K. Bandyopadhyay, S. G. Liu, L. Echegoyen, O. Enger, F. Diederich, P. Buhlmann, and E. Pretsch, *Chem Commun*, 2000, 339.
146 T. W. Baughman, J. C. Sworen, and K. B. Wagener, *Tetrahedron*, 2004, **60**, 10943.
147 R. Appel, *Angewandte Chemie International Edition in English*, 1975, **14**, 801.
148 S. Baral and J. H. Fendler, *J Am Chem Soc*, 1989, **111**, 1604.
149 N. Belman, S. Acharya, O. Konovalov, A. Vorobiev, J. Israelachvili, S. Efrima, and Y. Golan, *Nano Lett*, 2008, **8**, 3858.
150 S. Frein, J. Boudon, M. Vonlanthen, T. Scharf, J. Barberá, G. Süss-Fink, T. Bürgi, and R. Deschenaux, *Helvetica Chimica Acta*, 2008, **91**, 2321.
151 L. H. Amundsen and L. S. Nelson, *J Am Chem Soc*, 1951, **73**, 242.
152 J. J. Gooding, R. G. Compton, C. M. Brennan, and J. H. Atherton, *Electroanalysis*, 1997, **9**, 759.
153 J. T. S. Irvine, B. R. Eggins, and J. Grimshaw, *Journal of Electroanalytical Chemistry*, 1989, **271**, 161.
154 J. H. Zagal, S. Griveau, J. F. Silva, T. Nyokong, and F. Bedioui, *Coordin Chem Rev*, 2010, **254**, 2755.
155 H. Abramczyk, B. Brozek-Pluska, K. Kurczewski, M. Kurczewska, I. Szymczyk, P. Krzyczmonik, T. Blaszczyk, H. Scholl, and W. Czajkowski, *Journal of Physical Chemistry A*, 2006, **110**, 8627.
156 J. E. Halls, N. S. Lawrence, and J. D. Wadhawan, *J Phys Chem B*, 2011, **115**, 6509.
157 A. A. Kornyshev, *J Phys Chem B*, 2007, **111**, 5545.